

University of Alberta

Design and applications of fluorescent protein-based biosensors for live cell imaging

by

Yidan Ding

A thesis submitted to the Faculty of Graduate Studies and Research
in partial fulfillment of the requirements for the degree of

Doctor of Philosophy

Department of Chemistry

©Yidan Ding
Spring 2014
Edmonton, Alberta

Permission is hereby granted to the University of Alberta Libraries to reproduce single copies of this thesis and to lend or sell such copies for private, scholarly or scientific research purposes only. Where the thesis is converted to, or otherwise made available in digital form, the University of Alberta will advise potential users of the thesis of these terms.

The author reserves all other publication and other rights in association with the copyright in the thesis and, except as herein before provided, neither the thesis nor any substantial portion thereof may be printed or otherwise reproduced in any material form whatsoever without the author's prior written permission.

Abstract

Fluorescent proteins (FPs) are essential tools of biochemical research. Traditionally, FPs have been utilized as markers of gene expression, protein localization, and organelle structure. In recent years, however, FPs have gained in popularity as active biosensors of cellular activity, in which the fluorescence intensity or colour of a FP chromophore is modulated in response to a change in its environment. Current methods for converting FPs into active biosensors of live cell biochemistry remain few in number and are technically challenging. In addition, a growing demand has emerged for spectrally orthogonal biosensors for monitoring multiple biological parameters in a single live cell. A challenge in realizing this goal is that the broad spectral profiles of FPs have limited the number of biosensors that can be used together.

In this thesis I describe the engineering of new FP-based biosensors and further validating them via live cell multiparameter imaging. The first class of FP-based biosensors addressed in this thesis is Förster resonance energy transfer (FRET) biosensors. I described our efforts to use optimized spectrally distinct FRET-based biosensors to image Ca^{2+} dynamics in two distinct subcellular compartments as well as Ca^{2+} and caspase-3 activity in the same subcellular compartment. Although the inherently ratiometric response of FRET biosensor permits quantitative measurements, the fact that two FPs are involved in each FRET pair present a challenge with respect to their application in multiparameter imaging. To overcome this issue, we engineered intensimetric biosensors based

on the recently introduced dimerization-dependent fluorescent protein (ddFP) technology. I demonstrate that ddFP-based protease biosensors enable the reporting of protease activity either by the intensimetric loss of the initially bright fluorescence or with dramatic green-to-red and red-to-green colour switches and translocation from the cytoplasm to the nucleus. In addition to detection of caspase activities, we also achieved specific highlighting of the mitochondria-associated membrane (MAM) using ddFP technology. Attempts to detect polyADP-ribose and polyubiquitin using ddFP technology were ultimately unsuccessful. Overall, this work serves to expand the scope of current FRET and ddFP-based biosensor designs and applications.

Table of Contents

Chapter 1: Introduction.....	1
1.1 Overview and premise.....	1
1.2 Fluorescent proteins	4
1.2.1 Natural sources	4
1.2.2 Primary sequence and structure.....	5
1.2.3 Chromophore formation.....	7
1.2.4 Engineered FP variants.....	9
1.2.4.1 Variants with colour diversity	10
1.2.4.2 Monomeric FP variants	12
1.2.4.3 Circularly permuted variants	14
1.2.4.4 Other engineered FPs	15
1.3 Applications of FPs: genetically encoded biosensors	16
1.3.1 Förster resonance energy transfer (FRET)	16
1.3.1.1 General considerations	17
1.3.1.2 Engineered FP pairs.....	19
1.3.1.3 Strategies to assemble FP-based FRET biosensor	20
1.3.2 Complementation-based biosensor.....	24
1.3.2.1 Split FP-based biosensor	24
1.3.2.2 Dimerization-dependent FP (ddFP)-based biosensor	25
1.3.3 Single FP-based biosensors	26
1.3.4 Conclusion for FP-based biosensors	28
1.4 Protein engineering	29
1.5 The scope of the thesis.....	32
Chapter 2: FRET biosensors for multiparameter imaging in live cells	35
2.1 Introduction	35
2.2 Results and discussion.....	37
2.2.1 Optimization of CaYang and CaYin by domain rearrangements.	37

2.2.2	Optimization of CaYin by linker length modification	41
2.2.3	Multiparameter imaging of Ca ²⁺ in different cellular compartments 43	
2.2.4	Multiparameter imaging with Ca ²⁺ and caspase biosensors.....	45
2.2.5	Correction factor for bleed through between FRET pairs	45
2.3	Conclusions	47
2.4	Materials and methods.....	49
2.4.1	General methods.....	49
2.4.2	Construction of Ca ²⁺ biosensors (CaYang and CaYin).....	49
2.4.3	Optimization of Ca ²⁺ biosensors by linker modification.....	50
2.4.4	Protein purification and characterization	50
2.4.5	Construction of mammalian expression vectors	51
2.4.6	General methods for live cell imaging.	51
2.4.7	Ca ²⁺ imaging and induction of apoptosis	52

Chapter 3: Dimerization dependent fluorescent protein-based

	biosensors for imaging of caspase activity	53
3.1	Introduction	53
3.2	Results and discussion.....	55
3.2.1	Protease activity monitored by a red ddFP (ddRFP)-based caspase-3 biosensor	55
3.2.2	Concurrently monitoring Ca ²⁺ flux and caspase-3 via a Ca ²⁺ biosensor and a ddRFP-based caspase-3 biosensor	57
3.2.3	Protease activity monitored by a green ddFP (ddGFP)- or a yellow ddFP (ddYFP)-based caspase-3 biosensor.....	58
3.2.4	Engineering a single colour translocation-based biosensor	59
3.2.5	Engineering a colour switch and translocation-based biosensor..	63
3.2.6	Detection of both caspase-8 and caspase-3 in single cells	66
3.2.7	Detection of caspase-3 activation during neuritic pruning.....	69
3.3	Conclusions	72
3.4	Materials and methods.....	73

3.4.1	General methods and materials	73
3.4.2	Construction of the ddFP caspase biosensor	73
3.4.3	HeLa cell culture and imaging	74

Chapter 4: Dimerization-dependent FP based indicator for close

contacts between membranes	76
4.1 Introduction	76
4.2 Results and discussion	79
4.2.1 ddGFP labeling of MAM in live cells	79
4.2.2 MAM labeling is dependent on the proximity	82
4.2.3 Investigating the localization of FACL4	86
4.3 Conclusion	90
4.4 Material and methods	91
4.4.1 General methods and materials	91
4.4.2 Construction of mammalian expression plasmids	92
4.4.3 Mammalian cell culture and imaging	92

Chapter 5: Biosensing strategies for PARP1 activity

5.1 Introduction	95
5.2 Results and discussion	97
5.2.1 Detection of PARP1 activity <i>in vitro</i>	97
5.2.2 Confirmation of PARP1 activity in live cells	101
5.2.3 Detection of PARP1 activity via FRET in live cells	105
5.2.4 Detection of PARP1 activity using dimerization-dependent fluorescent protein technology in live cells	108
5.2.5 Validation DNA damage with ATM and PARP1 inhibitors	111
5.2.6 Detection of polyubiquitin chains in live cells	113
5.3 Conclusion	116
5.4 Material and methods	117
5.4.1 General methods and materials	117
5.4.2 Construction of <i>in vitro</i> PARP1 biosensors	117
5.4.3 Protein purification	118

5.4.4	Construction of mammalian expression plasmids.....	119
5.4.5	Mammalian cell culture and imaging.....	120
Chapter 6: Conclusions and future directions.....		123
6.1	Summary of thesis	123
6.2	Future directions	126
6.2.1	FRET based biosensors in multiparameter imaging.....	126
6.2.2	DdFP-based biosensors for multiparameter imaging	127
6.3	Closing remarks.....	128
Appendix: Engineering fluorescent biosensors based on the photo-responsive domain, LOV2		130
A.1	Introduction	130
A.2	Results and discussion.....	133
A.2.1	Characterization of LOV2 domain from <i>Arabidopsis</i>	133
A.2.2	Attempted detection of LOV2 conformational change using FRET and ddFPs.....	135
A.2.3	Attempted engineering of an <i>Avena sativa</i> LOV2 sensor using a circularly permuted fluorescent protein.....	139
A.2.4	Attempted alternative design of LOV2 and cpFP fusions.....	142
A.3	Conclusion	145
A.4	Materials and methods.....	145
A.4.1	General methods and materials	145
A.4.2	Construction of LOV2 related fusions	146
A.4.3	Plasmid library screening	147
A.4.4	Protein Purification and Characterization	147
Bibliography.....		150

List of Tables

Table 2.1 Optimization of CaYang and CaYin constructs by domain swapping.	39
Table 2.2 Residues appended or deleted in the linker library.....	41
Table 2.3 Filter sets used for dual FRET imaging.	43
Table 2.4 Analysis of spectral crosstalk for calculation of correction factors.....	46
Table 3.1 Details of the gene constructs used in this work.....	75
Table 4.1 Cloning strategies for DNA constructs described in Chapter 4.....	94
Table 5.1 Comparison of DNA damage response with and without inhibitors ..	112
Table 5.2 Cloning strategies for DNA constructs described in Chapter 5.....	121
Table A.1 Cloning strategies for DNA constructs described in Appendix.....	149

List of Figures

Figure 1.1 Schematic representation of FP reporter fusion.	2
Figure 1.2 A cartoon representation of avGFP	6
Figure 1.3 Two proposed mechanisms (paths a and b) for chromophore formation in avGFP.	8
Figure 1.3 Proposed mechanisms for chromophore formation in DsRed.....	9
Figure 1.5 Unnatural chromophore structures in engineered FPs.....	11
Figure 1.6 Monomerizing tetrameric Anthozoa FPs.....	13
Figure 1.7 Circularly permuted FP.....	14
Figure 1.8 Spectral profiles for three representative FP pairs.	18
Figure 1.9 FP-based FRET biosensor design strategies.....	22
Figure 1.10 Split FP-based complementation strategies for protein-protein interaction.	24
Figure 1.11 DdFP-based complementation strategy.....	26
Figure 1.12 Schematic representations of single FP-based biosensor.	27
Figure 1.13 Schematic representation of the process of directed evolution.	30
Figure 2.1 Excitation and emission spectra of the FPs that compose the spectrally distinct FRET pairs used in this work.....	37
Figure 2.2 Domain arrangements tested during the optimization of CaYang and CaYin.	38
Figure 2.3 Characterization of optimized Ca ²⁺ biosensors.	40
Figure 2.4 Optimization of the CaYin emission ratio change by testing of selected combinations of two linkers.....	42
Figure 2.5 Dual FRET imaging of Ca ²⁺ concentration and caspase-3 activity.....	44
Figure 2.6 Dual FRET imaging of Ca ²⁺ concentration and caspase-3 activity with application of a correction factor for spectral crosstalk.....	47
Figure 3.1 Schematic of reversibly associated ddFPs.....	54
Figure 3.2 General design of ddFP-based protease biosensors.....	55
Figure 3.3 Imaging of caspase-3 activity with a ddRFPs.	56

Figure 3.4 Imaging of Ca ²⁺ concentration and caspase-3 activity.	58
Figure 3.5 Imaging of caspase-3 activity with a ddGFPs.	59
Figure 3.6 Biosensors based on translocation of fluorogenic ddGFP partner.	60
Figure 3.7 Biosensors based on translocation of fluorogenic ddRFP partner.....	61
Figure 3.8 Attempted caspase-dependent ddFP translocation from the nucleus to the cytoplasm.	62
Figure 3.9 Red to green colour-switching biosensors based on translocation of the dark ddFP partner.....	64
Figure 3.10 Green to red colour-switching biosensors based on translocation of the dark ddFP partner.....	65
Figure 3.11 Concurrent monitoring caspase-3 and caspase-8 activity	67
Figure 3.12 Concurrent monitoring of two caspase activities with a two-colour single polypeptide biosensor.....	68
Figure 3.13 Monitoring caspase-3 activity associated with neurite pruning.	70
Figure 3.14 Nuclear fragmentation and caspase-3 activation in apoptotic and NGF-deprived neurons.....	71
Figure 4.1 Schematic illustration of FAACL4's function in lipid metabolism.	78
Figure 4.2 Schematic of ddFP technology	78
Figure 4.3 ddGFP labeling of MAM in live cells.	80
Figure 4.4 ddGFP MAM label colocalizes with mitochondria (A) and ER (B)...	81
Figure 4.5 Tom20 truncation mutants delocalize from the mitochondria and prevent fluorescent labeling of the MAM.....	83
Figure 4.6 Control experiments with non-MAM proteins	84
Figure 4.7 Localization of FAACL4 in live HeLa cells.	87
Figure 4.8 Localization of FAACL4 isoform 2 in live HeLa cells.....	89
Figure 4.9 Schematic illustration of FAACL4 localization.	91
Figure 5.1 Schematic of the PARP1-assisted DNA repair pathway.....	96
Figure 5.2 Schematic for FRET-based PARP1 biosensor strategy.....	98
Figure 5.3 Proteolysis of PARP1 and mPARG expressed in <i>E. coli</i>	99
Figure 5.4 Recruitment of PARP1 and mPARG after microirradiation.	103

Figure 5.5 Recruitment of C-terminus FP fusions and catalytic domain of mPARG after microirradiation.	104
Figure 5.6 FRET analysis with protein fusions of FP and mPARG	107
Figure 5.7 FRET analysis of cells coexpressing EYFP-PAPP1 and mTFP1-mPARG before and after microirradiation.	108
Figure 5.9 Recruitment of ddFP-mPARG proteins after microirradiation.	110
Figure 5.8 Recruitment of PARP1 and mPARG fusions with the treatment of inhibitors.	112
Figure 5.10 Recruitment of fusions with Rap80 or SuperUIMs after microirradiation.....	115
Figure A.1 LOV2 domain and the photocycle.....	134
Figure A.2 Absorption and emission spectra of LOV2 mutants.....	135
Figure A.3 Characterization of FRET constructs with LOV2 mutants.	137
Figure A.4 Characterization of a red FRET (O/Ch) and ddRFP constructs with LOV2 mutants.....	138
Figure A.5 Sequence alignment of <i>Arabidopsis</i> and <i>Avena sativa</i> LOV2 domain.	139
Figure A.6 Characterization of LOV2-GECO.....	141
Figure A.7 Characterization of cpLOV2 and fusion of cpLOV2-GECO.	143

List of Abbreviations

ϵ	extinction coefficient
Φ	quantum yield
ActA	actin assembly inducing protein
Ala	alanine
Arg	arginine
ATM	ataxia telangiectasia mutated kinase
ATP	adenosine-triphosphate
avGFP	<i>Aequorea victoria</i> green fluorescent protein
Bcl2	Homo sapiens B-cell lymphoma 2
BFP	blue fluorescent protein
BiFC	bimolecular fluorescence complementation
bp	base pairs
B-PER	bacterial protein extraction reagent
CaM	calmodulin
cb5	cytochrome-b5
CCD	charge-coupled device
cm	centimeter
CFP	cyan fluorescent protein
cpFP	circularly permuted fluorescent protein
CyPet	cyan fluorescent protein for energy transfer

ddFP	dimerization-dependent fluorescent protein
ddFP-A	dimerization-dependent fluorescent protein copy A
ddFP-B	dimerization-dependent fluorescent protein copy B
ddGFP	dimerization-dependent green fluorescent protein
ddRFP	dimerization-dependent red fluorescent protein
ddYFP	dimerization-dependent yellow fluorescent protein
DSBs	double-stranded breaks
DDR	DNA damage response
DEVD	aspartate-glutamate-valine-aspartate
DMEM	Dulbecco's modified eagle media
DMSO	dimethylsulfoxide
DNA	deoxyribonucleic acid
dNTPs	deoxynucleotide triphosphates
DsRed	<i>Discosoma</i> species Red fluorescent protein
dTomato	dimeric Tomato fluorescent protein
<i>E. coli</i>	<i>Escherichia coli</i>
EGTA	ethylene glycol-bis(2-aminoethylether)-N,N,N',N'-tetraacetic acid
ELISA	enzyme-linked immunosorbent assay
ER	endoplasmic reticulum
EYFP	enhanced yellow fluorescent protein
FACL4	long chain fatty acid coenzyme A ligase 4
FACS	fluorescence activated cell sorting

FBS	fetal bovine serum
FMN	flavin mononucleotide
FRET	Förster resonance energy transfer
GFP	green fluorescent protein
Gly	glycine
GTPase	guanosine triphosphatase
HeLa	cervical cancer cell line originating from Henrietta Lacks
HHBSS	HEPES-buffered Hank's balanced salt solution
His	histidine
hr	hour
IETD	isoleucine-glutamate-threonine-aspartate
Ile	isoleucine
IPTG	isopropyl β -D-thiogalactopyranoside
kb	kilobases
kDa	kilodalton
Kd	dissociation constant
LB	Luria Bertani
LEHD	leucine-glutamate-histidine-aspartate
LOV	light, oxygen and voltage-sensing
MAM	mitochondria-associated ER membrane
MBSU	Molecular Biology Services Unit
MEF	mouse embryonic fibroblast

mg	milligram
mL	milliliter
mM	millimolar
mRNA	messenger ribonucleic acid
mTFP1	monomeric teal fluorescent protein version 1
MW	molecular weight
NAD ⁺	nicotinamide adenine dinucleotide
NES	nuclear export signal
ng	nanogram
NLS	nuclear localization sequence
nm	nanometer
nM	nanomolar
NTA	nitrilotriacetic acid
PAR	poly(ADP-ribose) polymerases
PARP	poly(ADP-ribose)
PARG	poly(ADP-ribose) glycohydrolase
PBS	phosphate buffered saline
PCR	polymerase chain reaction
PDB	protein data bank
Phe	phenylalanine
RAP80	receptor-associated protein 80
RFP	red fluorescent protein

SASG	Serine-alanine-serine-glycine
Ser	serine
SDS-PAGE	sodium dodecyl sulfate polyacrylamide gel electrophoresis
SR α/β	signal recognition particle receptor α/β
TNF- α	tumor necrosis factor- α
Tom20	translocase of outer membrane-20
Trp	tryptophan
Tyr	tyrosine
μg	microgram
μM	micromolar
UIMs	ubiquitin-interacting motifs
UV	ultraviolet
WT	wild type
YFP	yellow fluorescent protein
YPet	yellow fluorescent protein for energy transfer

Chapter 1: Introduction¹

1.1 Overview and premise

Fluorescence live cell imaging provides a platform for the noninvasive study of internal structure, gene expression, enzyme function, protein-protein interactions, cell signaling [1,2] and a large number of cellular processes [3-5]. As the basis for fluorescence live cell imaging, molecular fluorophores enable the visualization of cellular structures and dynamic cellular processes in real time without disrupting natural cell function. Molecular fluorophores are chemical moieties absorbing light at one wavelength and emitting light (fluorescence) at a longer wavelength. They are generally defined into two groups: non-genetically encoded fluorophores, such as small molecule dyes and quantum dots; and genetically encoded fluorophores, such as fluorescent proteins (FPs).

Both groups of molecular fluorophores are widely utilized in fluorescent labeling technology, which is a major application of fluorescence imaging. Due to the increasing availability of molecular fluorophores, the internal structure of a cell, or localization and movement of a protein of interest, can be revealed by the fluorescence signal. To achieve specificity for the targeted protein, non-genetically encoded molecular fluorophores are generally linked to the protein of interest (POI) by a chemical conjugation reaction. Another challenge associated with non-genetically encoded fluorophores is getting them through the cell membrane and into the cytoplasm of the cell [6,7]. In contrast, genetically encoded fluorophores are ribosomally synthesized polypeptides and thus can be attached to specific proteins in living cells or organisms by fusing the gene encoding the FP to the gene of interest, using standard molecular biology

¹ A version of the discussion on the FRET-based biosensor (Section 1.3.1) has been submitted for publication (H. Hoi, Y. Ding, and R. E. Campbell, “FRET with fluorescent proteins”, an invited book chapter for *Resonance Energy Transfer*, Ed. I. Medintz and N. Hildebrandt, Wiley VCH Publishing House).

techniques (**Figure 1.1**). The fusion gene can be introduced into the cell type of interest using standard transformation or transfection procedures.

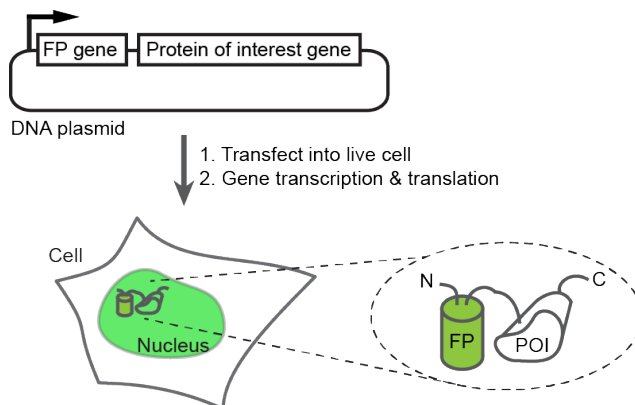


Figure 1.1 Schematic representation of FP reporter fusion.

A green FP (GFP) gene is fused to a gene encoding protein of interest (POI). The gene encoding the FP fusion is introduced into cells via transfection. After expression of this FP fusion, the fluorescence of the GFP marks the location of POI, in this case, in the nucleus.

In addition to fluorescent labeling, molecular fluorophores can be engineered into fluorescent probes or biosensors sensitive to analyte fluctuations, enzymatic activities or interactions of biomolecules. For example, the non-genetically encoded fluorophores fura-2 and indo-1 have been developed to interact with Ca^{2+} [8]. They are widely utilized to measure Ca^{2+} concentrations within cell compartments and quantitative changes during Ca^{2+} flux in the cytoplasm [9]. Likewise, genetically encoded fluorophores such as GCaMP, a FP-based Ca^{2+} sensor, is routinely utilized in sensing spatial and temporal changes of intracellular Ca^{2+} concentration in live cells [10].

Among all the molecular fluorophores commonly used in fluorescence imaging, fluorescent proteins (FPs) have been the most extensively studied and further developed in recent years. These developments include the enhancement of photophysical properties, the expansion of the colour palette, and the development of new biosensors. Wild type FPs, as compared to organic fluorophores, suffer from low brightness and are sensitive to photobleaching, which contributes to loss of fluorescence under illumination. After intensive

engineering, many FPs variants are now comparable or even superior to synthetic fluorophores. For example, relative to fluorescein, the engineered green variant EGFP is 24-fold more photostable [11]. The availability of a broad palette of FP hues now makes it possible to image the localization or activity of multiple proteins in a single cell. One impressive demonstration is that six different hues of FP were imaged in a single cell using a single excitation laser line [12]. The incredible development of FP related biosensing technology enables the imaging of analyte flux (*e.g.*, glutamate [13], Ca^{2+} [14], and cyclic nucleotides [15,16]), enzymatic activities (*e.g.*, protein kinase [17], protease [18,19]) and protein-protein interactions [20-22]. More details related to FP-based biosensors will be discussed in detail in Section 1.3.

Many FP-based biosensors have been created and proven to be powerful in visualizing biological dynamic processes in live cells. However, the number of newly created FP-based biosensors is relatively small compared to the freshly engineered FPs, which implies that the potential of FP-related biosensors has not yet been fully utilized in biological studies. Furthermore, as engineered FP-based biosensors are continuing to fill up the toolbox of biosensors, a trend of using multiple biosensors to achieve detection of multiple parameters has emerged in recent publications [23-27]. Yet, the primary challenge of designing and executing multiparameter imaging is to assign the relatively narrow range of visible wavelengths (~400–650 nm) to different parameters [28]. Regarding FPs, this resource is ultimately limited by the broad excitation and emission profiles of available FPs [29]. Due to the limited number of spectral distinct FP-based biosensors, the usage of multiple biosensors in single cells is currently limited [2].

For the research described in this thesis, we attempted to apply FP-based biosensors to monitor multiple dynamic processes with live cell imaging. We also aimed to improve the dynamic range of the existing biosensors and to create new biosensors that could indicate specific cellular activity upon extracellular stimulations. Our approach centers on utilizing Förster resonance energy transfer (FRET) and dimerization-dependent FPs (ddFPs). To provide the necessary background for understanding this work, this introductory chapter will first

introduce the properties of wild-type FPs and molecularly engineered FPs, followed by the overview of essential concepts related to designs of FP-based biosensors and their applications in live cell imaging.

1.2 Fluorescent proteins

Since the discovery of green fluorescent protein from *Aequorea victoria* jellyfish (avGFP), a variety of FP variants with distinctive characteristics have been discovered in nature and developed in the lab. Today, they are widely distributed among research labs as powerful tools for studying dynamic processes in live cells. In recognition of the significance in using FPs in modern research, the 2008 Nobel Prize in Chemistry was awarded to Osamu Shimomura, Martin Chalfie, and Roger Y. Tsien, three researchers who discovered and promoted FP technology [30].

1.2.1 Natural sources

In *Aequorea victoria* jellyfish, avGFP serves as an energy transfer acceptor from the accompanying bioluminescent protein aequorin. This energy transfer process effectively shifts the blue luminescence to longer wavelength green fluorescence. Since the first FPs had been discovered in bioluminescent organisms, it was generally thought that additional FP homologues would most likely be discovered in other bioluminescent species. Until 1999, a few more GFPs were discovered from other bioluminescent marine coelenterates, including hydrozoa such as *Obelia* and *Phialidium*, and Anthozoa such as *Renilla* [31,32].

As the first FP identified, avGFP was cloned and expressed alone to produce fluorescence in different organisms, such as *Escherichia coli* [33] and *Caenorhabditis elegans* [34]. Today, avGFP serves as the single most well characterized cofactor-independent fluorescent marker for cell biology studies. Variants of avGFP that fluoresce at red-shifted or blue-shifted wavelengths were later engineered to enable variety of biosensing applications. However, the peak

emission of the most red-shifted variant of avGFP only reached as far as the yellow region (~530nm) in the band of visible wavelengths.

The gap in the red region was filled up by the discovery of the red homologues of avGFP from nonbioluminescent reef corals of the Anthozoa class [35]. Rewardingly, these Anthozoa FPs come in variety of fluorescent hues that span the cyan to red regions of the visible spectrum [35,36]. The biological role of FPs in reef corals is still an open question, but it is likely that they have some role in providing photoprotection to photosynthetic related algae in shallow waters [37] and aiding identification by the cohabitating marine species [38]. Among these Anthozoa FPs, a red fluorescent protein (RFP) isolated from *Discosoma*, namely DsRed, was of particular interest for further engineering [35]. The excitation and emission wavelengths of DsRed are at 558 and 583 nm, respectively [35], which are quite distinctive from those of GFP. Accordingly, DsRed can easily be utilized in conjunction with GFP in multicolour imaging applications. Recently, the palette of FPs was further enriched by engineered FPs discovered in the lancelet *Branchiostoma lanceolatum* (phylum Chordata) with fluorescent hues ranging from green to red [39].

Together, avGFP, DsRed, and a handful of other naturally occurring FPs have served as the progenitors of the numerous engineered variants optimized for particular live cell imaging applications and widely distributed in the research community.

1.2.2 Primary sequence and structure

Using wild type avGFP as illustration, it is a protein of 238 amino acids with an approximate molecular mass of 27 kDa [32]. Following transcription of the 714 base pair gene, and subsequent translation, the protein spontaneously folds into a cylindrical 11-stranded antiparallel β -sheet structure that functions as a well-structured and rigid shell protecting the fluorophore from the surrounding environment [40,41]. This structure is often referred to as a β -barrel or β -can (**Figure 1.2**).

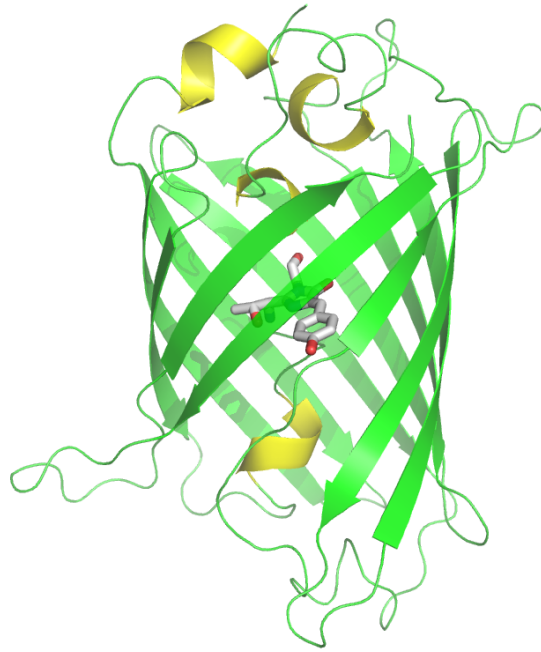


Figure 1.2 A cartoon representation of avGFP

Chromophore is shown in cartoon with carbon atoms coloured grey, nitrogen atoms coloured blue, and oxygen atoms coloured red. Image is derived from PDB ID 1EMA [40]).

In addition to the β -barrel structure, a primarily helical segment runs along the central long axis down the middle of this barrel. Residues Ser65–Try66–Gly67 are located within this helical region and close to the geometric center of the β -barrel structure. These three residues, facilitated by the surrounding protein environment, are posttranslationally modified to become the chromophore [40,41]. All known FPs, including those from jellyfish, coral and lancelet, share a homologous three-dimensional β -barrel structure, though they only share a sequence identity in the range of 20% to 30% [35]. The complete and proper folding of the β -barrel enables the next step in the maturation of FPs, which is the autogenic formation of chromophore.

1.2.3 Chromophore formation

Chromophore formation is a posttranslational modification that forms the conjugated system of the visible wavelength fluorophore. Given the intense interest in these proteins and the great number of researchers who have used them in their research, the precise details of the chromophore formation reactions have been extensively investigated. The widely accepted mechanism for the chromophore formation involves a three-step reaction: cyclization, dehydration and oxidation.

Although controversy exists between the sequence of the dehydration and oxidation steps, cyclization has been established as the initial step in the chromophore formation. After the proper folding of the polypeptide chain into a β -barrel, a distortion of the polypeptide backbone positions the carbonyl carbon of Ser65 into close proximity to the amide nitrogen of Gly67 in the precyclized state [42]. Then, Ser65-Tyr66-Gly67 undergo a cyclization of the main chain. One proposed mechanism is that cyclization is followed by the loss of a molecule of water and finally an oxidation of the C α -C β bond of Tyr66 with molecular oxygen (path **a** in **Figure 1.3**) [43]. This series of steps is designated as the cyclization-dehydration-oxidation mechanism. However, accumulating evidence has eroded support for the cyclization-dehydration-oxidation mechanism and increased support for the reaction pathway of cyclization–oxidation–dehydration as shown as path **b** in **Figure 1.3** [44].

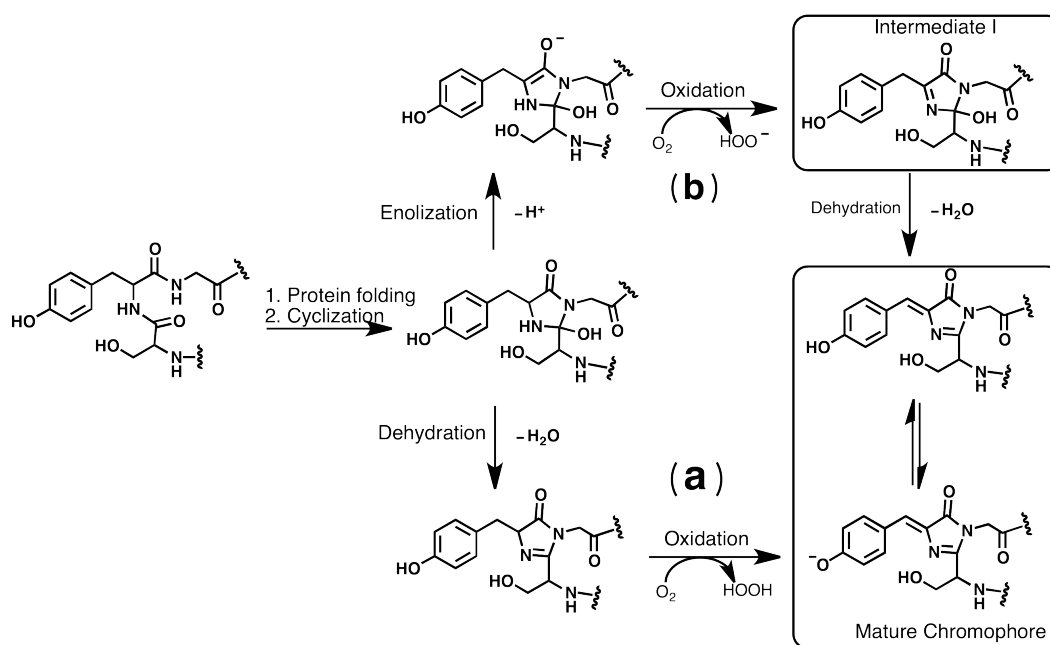


Figure 1.3 Two proposed mechanisms (paths a and b) for chromophore formation in avGFP.

The mechanism shown here was adapted from a recent review by Watcher [45]. Wiggly lines represent points of attachment to the remainder of the polypeptide chain.

Relative to avGFP, far fewer reports have been published regarding the mechanism of chromophore formation in the widely distributed coral FP, DsRed. The latest research has suggested that chromophore formation in both green and red FPs can be explained using a single mechanistic scheme that involves a branched pathway occurring at the first oxidation product in path **b** of **Figure 1.3**, designated as intermediate I [46]. In contrast to avGFP, the first oxidation product in DsRed, intermediate I, is subject to a loss of HO⁻ to form intermediate II (**Figure 1.4**). Followed by a second irreversible oxidation, intermediate II is then converted into a short lived blue emitting intermediate III, which has recently been trapped and structurally characterized by x-ray crystallography [47]. In the next step, the blue intermediate undergoes irreversible hydroxylation to form intermediated IV. Finally, a dehydration step converts the molecule into a phenolic form of the chromophore (**Figure 1.4**) [46], which exists in equilibrium

with the phenolate fluorophore that emits red fluorescence when excited by green light.

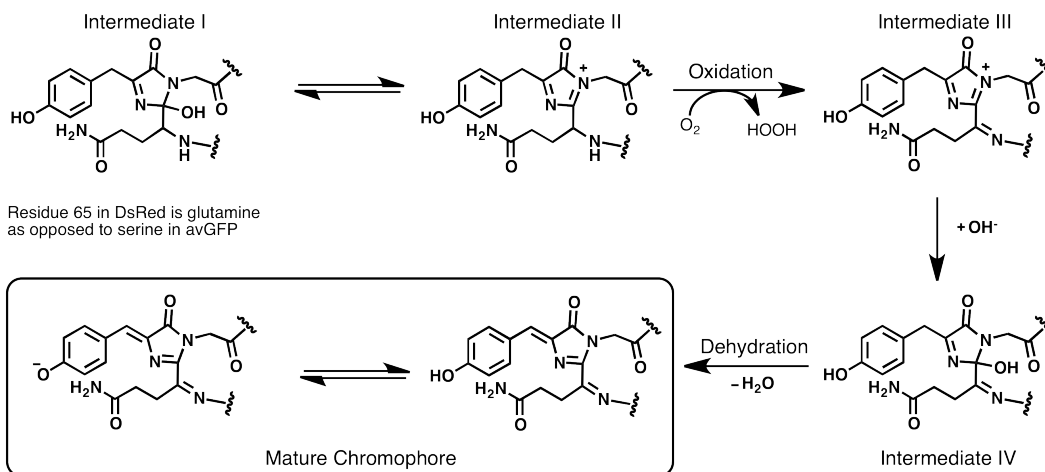


Figure 1.3 Proposed mechanisms for chromophore formation in DsRed.

A branched pathway occurring at the first oxidation product in path **b** (Figure 1.3) initiates DsRed chromophore formation.

1.2.4 Engineered FP variants

Although numerous naturally occurring FPs have been discovered, they generally suffer from slow maturation, poor photostability, low brightness or sensitivity to changes in the environment, which limit their usage as imaging tools. To improve the properties of FPs for imaging applications, researchers have engineered FP variants by altering their genetic sequence. Essentially all FPs currently used in research applications are engineered variants of the wild-type proteins [11,29]. After intensive engineering over last decade, these general drawbacks of FPs are, generally speaking, no longer issues for using FPs as imaging tools [11]. Therefore, in this Section, we focus on the directed evolution of FPs aimed at facilitating their application in imaging. For example, directed evolution can be used to expand the colour diversity, create monomeric version of naturally oligomeric proteins, and create circularly permuted versions of FPs.

The most obvious desirable property of an engineered FP is high fluorescent brightness. Higher FP brightness provides an improved signal-to-noise ratio and

sensitivity of detection in optical imaging measurements. Of particular relevance to fluorescence microscopy of live cells is that a brighter FP means less intense excitation light is required and thus there is reduced phototoxicity to cells. In addition, enhanced brightness allows the FPs or FP-tagged fusion proteins to be expressed at a low concentrations still yielding significant signal and thus minimizing the perturbation of the normal cell biology. When expressing FP-tagged fusion proteins in live cells, the concern is not so much for the absolute concentration of the introduced protein, but for the concentration of fusion protein relative to endogenous (normal) unfused protein that is normally present in the cell.

1.2.4.1 Variants with colour diversity

Since the limited number of spectral distinct FPs restricts the usage of multiple FP-based biosensors in single cells, one major goal of directed evolution of FPs is to enrich the colour diversity. Naturally occurring FPs provide a variety of templates for researchers to develop hue-shifted variants, which could have more optimal spectral profiles for particular imaging applications. Fortunately, the chromophore of FPs tends to be quite tolerant of mutation of the first two residues (the Gly is essential). Some mutations of the chromophore tripeptide can dramatically modify the conjugated system and alter the spectral properties of FPs. In this way, Tsien and coworkers produced some of the first colour variants of avGFP. For example, a mutation of residue 66 from tyrosine to tryptophan produced the initial versions of the cyan variant (**Figure 1.5A**). Likewise, a mutation Tyr66 to His66 [31] (**Figure 1.5B**) or Tyr66 to Phe66 (**Figure 1.5C**) [48] produced the first blue fluorescent variant. Much later, a handful of colour variants were also created from DsRed via similar chromophore mutation strategies. For example, mHoneydew was created by mutating Tyr67 to tryptophan (**Figure 1.5D**) and mBlueberry was made by mutating Tyr67 to phenylalanine (**Figure 1.5F**) [49]. The Tyr67His mutant of mCherry2 has been reported (**Figure 1.5E**), but has not proven useful for live cell imaging [50].

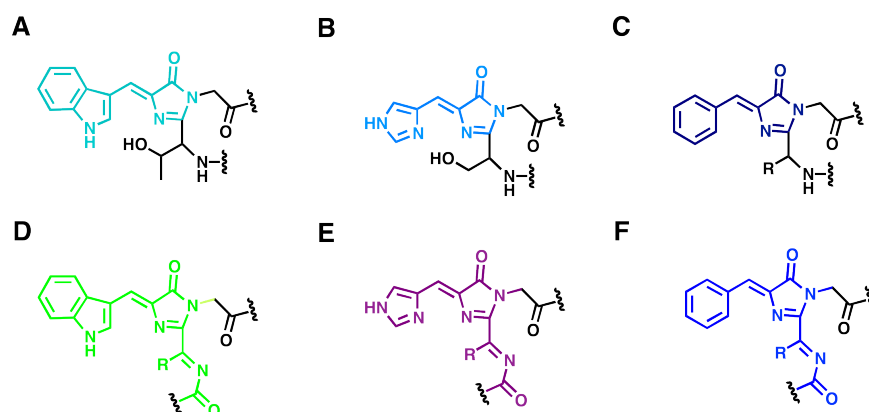


Figure 1.5 Unnatural chromophore structures in engineered FPs.

(A) Variant of avGFP with Tyr66Trp mutation is commonly known as Cyan FP (CFP). (B) The Tyr66His variant is commonly known as Blue FP (BFP). (C) Sirius is an optimized variant of Tyr66Phe mutant of avGFP and emits blue fluorescence. (D) The tryptophan analogue of the DsRed chromophore is found in the yellow fluorescent mHoneydew variant. (E) The histidine analogue of the DsRed chromophore is reported in a red fluorescent mCherry2 variant. (F) The phenylalanine analogue of the DsRed chromophore is found in the blue fluorescent mBlueberry variant.

In addition to chromophore structure modification, the adjustment of the non-covalent interactions between chromophore and buried amino acid side chains in the vicinity also lead to creation of hue-shifted variants. One famous illustration of this is the creation of yellow variants (YFP) from avGFP. With a mutation of residue 203 from threonine to tyrosine, the protein is converted into a yellow-emitting variant in spite of having the same chromophore structure as GFP [31]. The red-shifted spectral of this variant is the result of a π - π stacking interaction between the hydrophobic side chain and the phenolate moiety of chromophore, which presumably decreases the energy of excited state and allows more efficient electron delocalization. It has been proposed that the electric field within the β -barrel can also modify the spectral properties of the chromophore [51]. By interacting with inherent dipole moment of chromophore, the electric field inside the barrel alters the energy of the ground and excited states and contributes to spectral modulation, particularly, in the mFruit series of FPs (DsRed derivatives) [52].

1.2.4.2 Monomeric FP variants

With the engineering of hue-shifted variants, many new opportunities for using FPs in biosensing became available to researchers. However, naturally occurring FPs demonstrate some extent of self-association or oligomerization, typically dimerization and tetramerization, which often causes the artificial oligomerization of the fused POIs and hence alters their native function. As a well-known example, Anthozoa FPs are obligate tetrameric proteins in which four copies of the β -barrel must come together to form the native form of the FP [53].

The crystallographic study of DsRed illustrated that tetramer formation mediated by two chemically distinct interfaces, one of which is hydrophobic and one of which is hydrophilic (**Figure 1.6**). The first example of an engineered monomeric version of DsRed, known as mRFP1, was created by disrupting both of these interfaces. Interface disruption was followed by multiple rounds of random mutagenesis to rescue the fluorescence intensity and chromophore maturation rate [54]. Similar approaches have now been applied to a handful of other coral FPs, leading to an expansion of the toolbox of available colours of FPs for use in imaging applications [55,56].

In contrast, the issue of oligomerization is typically not relevant for avGFP and its derivatives, since their dissociation constants are approximate 100 μ M [58]. Under normal imaging conditions, where intracellular concentrations are kept at or below the low micromolar range, avGFP remains a monomer that does not influence target protein fusion.

Together, avGFP derivatives and monomerized coral FP variants have served as the templates for further modification and expansion of the FP palette [49,59]. A classic illustration of this kind of protein engineering would be the development of the mFruit variants [52], which are derivatives of mRFP1. After the intensive engineering over last decade, a wide selection of monomerized FPs is now available for biosensor construction and multicolour imaging, with a variety of colours ranging from blue to far-red.

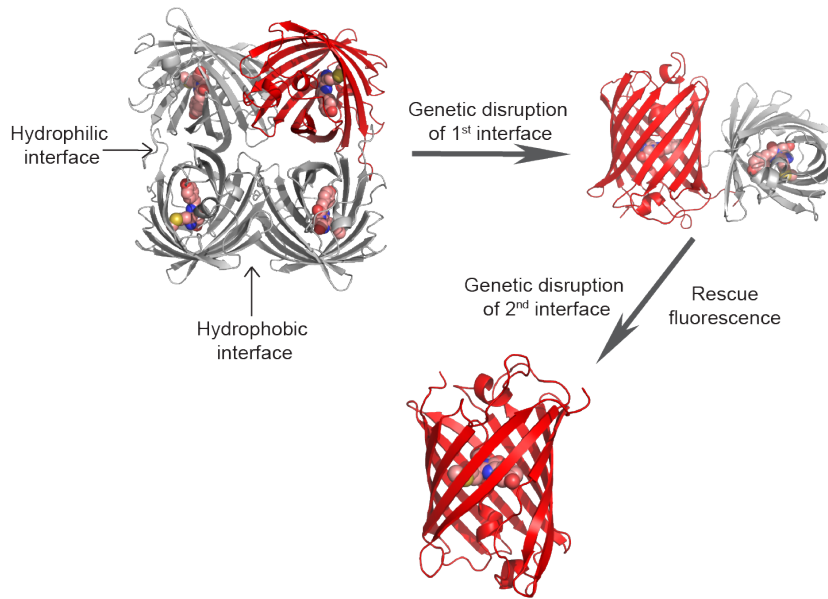


Figure 1.6 Monomerizing tetrameric Anthozoa FPs.

Shown is the crystal structure of a DsRed variant (PDB ID 2V4E) [57]. Wild-type derived FPs are homotetramers. However, dimeric and monomeric variants of Anthozoa FPs can be engineered by genetically disrupting the protein-protein interfaces. Cartoon spheres are used to represent the structure of the Met-Tyr-Gly chromophore, with carbon atoms coloured in pink, oxygen atoms coloured in red, nitrogen atoms coloured in blue and sulfur atoms coloured in yellow.

Although oligomerization is generally considered as a critical drawback for applications in fluorescent labeling, recently, some researchers have discovered the advantage of oligomerization in FP-based biosensor design. Notably, my colleague Dr. Spencer Alford utilized the inherent dimerization of coral FPs in the engineering of a dimerization-dependent FPs (ddFPs), which is considered as an alternative complementation biosensor [60,61]. Furthermore, by modulating the inherent dimerization interface between donor and acceptor FPs, researchers have engineered FRET pairs with enhanced efficiency of energy transfer [62]. It could be said that an emerging trend in FP engineering is to convert the disadvantage of FP oligomerization in fluorescent labeling into an advantage in FP-based biosensing.

1.2.4.3 Circularly permuted variants

As a key feature contributing to that popularity of FP technology, the robust folding of FPs from the nascent polypeptide into the complete β -barrel allows relatively dramatic modifications of the polypeptide chain, which in turn facilitate a variety of biosensor designs. One of the best know modifications is circular permutation of a FP (cpFP), in which the original N- and C-termini are linked by several inserted residues, and new N- and C-termini are created at a position elsewhere in the gene (**Figure 1.7**) [63,64]. Once a normal FP is correctly folded and the chromophore has formed, it is quite stable and quite resistant to a variety of environmental insults. In contrast to normal FPs, cpFPs are more sensitive to their environment, such as pH and temperature. As a result, this sensitivity can be explored as the basis for creating single FP-based biosensors.

CpFP-based biosensors are made by fusing with a sensing domain or a pair of interacting domains, whose activation can influence the fluorescence signal of the host cpFP. One classic example is the cpFP-based Ca^{2+} biosensors, which was created by fusing the calcium-sensitive domain calmodulin (CaM) and its binding partner M13 to the N- and C-termini of cpEGFP, respectively [65]. Likewise, cpEGFP was also concatenated between a kinase substrate peptide and a phosphotyrosine-binding domain to create biosensors for kinase activities [66]. This part will be discussed in detail with single FP-based biosensors in Section 1.3.3.

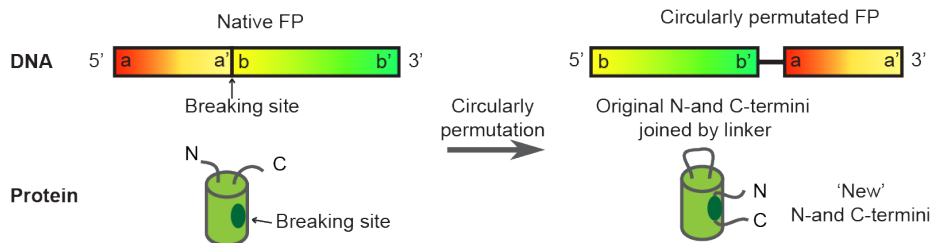


Figure 1.7 Circularly permuted FP.

Original N- and C-termini are joined by a linker and new termini are created in close proximity to the chromophore. The 3D structure of the β -barrel is retained whereas the primary sequence is permuted.

In addition to acting as template for single FP-based biosensor, cpFPs were also utilized to improve energy transfer within the FRET-biosensors. The rationale is that substituting normal FPs for cpFPs should alter the donor-acceptor dipole-dipole orientation and, accordingly, the FRET efficiency. Accordingly, a YFP variant Venus was circularly permuted to yield cpVenus. When using cpVenus with ECFP in a FRET-based Ca^{2+} biosensor, the dynamic range of FRET change was remarkably increased from 100% to 560% [67].

1.2.4.4 Other engineered FPs

The majority of interest in engineering FPs is focussed on developing new colour-hues, minimizing their oligomerization propensity, optimizing folding efficiency, improving photostability, and increasing brightness. However, some atypical properties were also discovered during FP engineering and have since been optimized for specific applications. For example, many FPs have been engineered that significantly change their fluorescence intensity (photoactivation) or colour (photoconversion) upon illumination with light of a specific wavelength [68]. One example is photoactivatable GFP (PA-GFP), whose green fluorescence intensity increases 100-fold after illumination with UV light at ~ 413 nm [69]. The photoconvertible FPs, mMaple [70] and Kaede [71], emit bright green fluorescence that shifts to red upon irradiation with UV or violet light. Photoactivatable and photoconvertible FPs are commonly utilized for highlighting a subpopulation of proteins and achieving single molecule tracking.

Furthermore, some atypical FP variants have been engineered to have a Stokes shift as large as 180 nm, while typical Stokes shift is approximate 30-60 nm [72]. Long Stokes shift FPs can be excited from the protonated ground state and then undergo excited-state proton transfer (ESPT) such that they emit from the lower energy anionic ground state. In contrast, typical FPs fluoresce from the same protonation state in which they were originally excited [72]. Examples of proteins that undergo ESPT are the green fluorescent T-Sapphire [73], the yellow fluorescent mAmetrine [28], and the red fluorescent mKeima [12], with Stokes

shifts of 112, 120, and 180 nm, respectively. The long Stokes shift variants have proven particularly useful as FRET donors to orange or red FP acceptors. An advantage of using long Stokes shift variants as FRET donors is the minimization of the direct excitation of the donor, which is often a problem in FP-based FRET experiments due to the fact that the excitation (and emission) peaks tend to be very broad.

1.3 Applications of FPs: genetically encoded biosensors

In addition to fluorescent labeling, FPs are widely used for engineering biosensors that enable researchers to study biological recognition, signal transduction, and enzyme activities in live cells. In this section, we introduce several strategies that commonly used in the design of biosensors, including FRET-, complementation-, and single FP-based strategies.

1.3.1 Förster resonance energy transfer (FRET)

FRET is the radiationless energy transfer through dipole-dipole interaction from a donor fluorophore to an acceptor chromophore. The efficiency of this energy transfer is highly dependent on the distance between donor and acceptor [74]. When the donor and acceptor are closer to each other (<10 nm) and have favourable orientations, energy transfer efficiency to the acceptor approaches 100%. If the acceptor is also a fluorophore, it will be sensitized to emit fluorescence at its characteristic emission wavelength. This energy transfer is often represented by FRET efficiency, which is proportional to the amount of donor quenching. Rather than quote FRET efficiency, researchers often use the shorthand of quoting the ratio of acceptor to donor fluorescence intensity, where a higher ratio indicates higher FRET efficiency. Since FRET efficiency depends on the signal from donor and acceptor individually, a major advantage of FRET technology is that it is inherently ratiometric, which permits quantitative measurement and minimizes variations from cell-to-cell [75].

1.3.1.1 General considerations

In FRET applications, the efficiency of energy transfer is dependent on the photophysical properties of FPs, including the wavelengths and shape of the absorption and emission spectra, the fluorescent brightness (i.e., the product of extinction coefficient ϵ and quantum yield Φ), the susceptibility to photobleaching, and the sensitivity to changes in the protein environment (e.g., pH or halide ion concentration) [75]. To achieve efficient energy transfer, a proper overlap between the emission spectrum of a donor fluorophore and excitation spectrum of an acceptor fluorophore is required. Relative to dye-based fluorophores, FPs tend to have quite broad excitation and emission spectral profiles (**Figure 1.8**). The substantial width of the fluorescence profiles is a double-edged sword with respect to the use of FPs for FRET applications.

On the one hand, practically any FP will have some substantial degree of spectral overlap with any other FP [76]. On the other hand, the wide excitation and emission profiles of FPs lead to a less-desirable consequence causing the spectral bleed through problem when using intensity-based methods for FRET imaging [75]. This problem manifests itself in two distinct ways. The first is when substantial donor emission occurs at the wavelengths that correspond to the acceptor (i.e., FRET) emission channel. The second is when there is substantial direct excitation of the acceptor at the donor excitation wavelength. Both these types of spectral bleed through complicate the quantitative analysis of FRET signals obtained using FPs. One solution to minimize the impact of the spectral bleed through problems is to use a long Stokes shift donor FP such as T-Sapphire paired with an orange or red FP acceptor [73]. Other practical solutions to minimize this problem include the use of narrow-band excitation/emission filters, single wavelength laser excitation, and/or linear unmixing [77] of the emission profile. Regardless of spectral bleed through, quantitative measurements of FRET efficiency are always possible by measuring the recovery of donor fluorescence after photo-bleaching the acceptor.

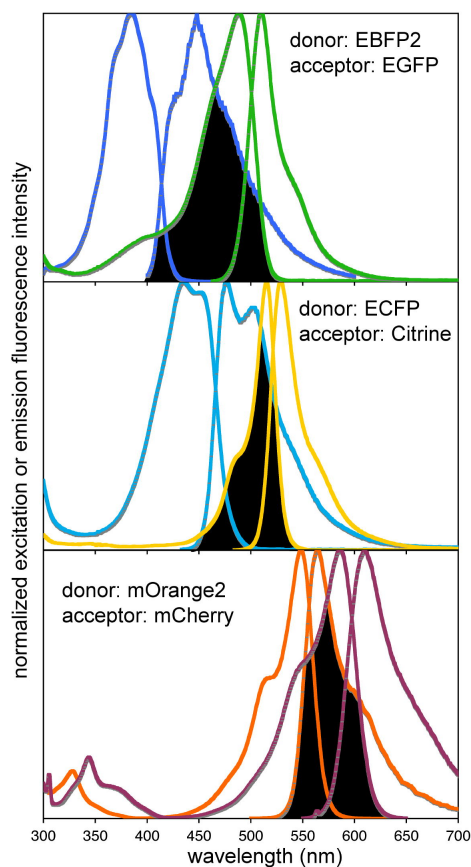


Figure 1.8 Spectral profiles for three representative FP pairs.

From top to bottom, the FRET donor/acceptor pairs represented in each panel are EBFP2/EGFP, ECFP/Citrine, and mOrange2/mCherry. For each FP, the excitation and emission peaks are coloured identically with the excitation profile occurring at lower wavelength and the emission peak at higher wavelength. The area shaded in black represents the region of overlap between the emission profile of the donor and the excitation profile of the acceptor. This figure is credit to Dr. Robert Campbell.

In addition to a larger overlap integral (J), a higher donor Φ and a higher acceptor ϵ are essential for a good FRET pair. FRET efficiency is critically dependent on the Förster radius, in which a larger Förster radius corresponds to a more efficient energy transfer. For example, although TagBFP has a poorer overlap integral (J) with YFP than does ECFP, the higher Φ of TagBFP (0.63 versus 0.40) compensates for this deficiency and both pairs (TagBFP/YFP and ECFP/YFP) have similar Förster radii of approximately 4.9 nm [78].

The other consideration in FRET design is the modulation of the distance or relative orientations (κ^2) between the fluorophores. In most cases, the assumption of random orientations is correct [75]. FPs are typically linked to a protein of interest genetically by fusing the two genes in frame, perhaps with a short flexible linker sequence (e.g., a sequence rich in Gly and Ser) between them. Even if a linker sequence is not added, the N- and C-terminal ends of FPs tend to get unstructured and thus act as “built-in” flexible linkers. This fact leads to a great deal of conformational freedom for the FP relative to its fused partner. Therefore, the FPs are very likely to adopt a wide range of orientations (i.e., static disorder) that will average out to a κ^2 of 2/3 [75]. As a relative rare case, the two FPs engage in heterodimer formation with each other, which brings the chromophores into closer proximity and produces a more favourable dipole alignment rather than random orientations [79]. The closer proximity and dipole alignment are thought to explain the particularly high FRET efficiency exhibited by the CyPet (Cyan FP for energy transfer) / YPet (yellow FP for energy transfer) FRET pair [80-82].

1.3.1.2 Engineered FP pairs

Taking all the factors discussed above into consideration, the available and suitable FRET pairs in biosensing are somewhat limited, although the ever-growing FP palette is always providing new candidates for assembling FRET pairs. Blue-Green pair was utilized as the first FRET pair in biosensor design [83], but its widespread acceptance was limited by the fact that the BFP-type variants were relatively dim and sensitive to photobleaching [84].

In contrast to the blue-green pair, the cyan-yellow (CFP-YFP) pair is much more popular in current FRET applications. CFP-YFP pair benefits from a larger spectral overlap [76] and the fact that CFP is brighter and more photostable than BFP. To improve this FRET pair, substantial effort has been invested in finding improved versions of CFP and YFP. Regarding to CFP variants, enhanced CFP (ECFP) [10,83], Cerulean [85] and mTurquoise [86] were engineered from avGFP derivatives with enhanced brightness (as a result of improved ϵ and Φ). In

addition, an Anthozoan-derived alternative to CFP, the protein known as monomeric teal fluorescent protein (mTFP1) [55], has been engineered in the Campbell lab. Relative to ECFP and Cerulean, mTFP1 has improved brightness, photostability, and pH resistance, and has been found to provide superior performance in a head-to-head comparison [87]. For YFP variants, Citrine [88] and Venus [89] are extremely bright and have proven more than sufficient for many applications in which they have been used.

In addition to Blue-Green and Cyan-Yellow pairs, researchers have great interests in searching for good red FRET pairs, since red variants lead to lower phototoxicity from excitation light, less red autofluorescence from endogenous fluorophores, and greater tissue penetration (for light up to ~1000 nm [90]) in live cell imaging. Unfortunately, the red FPs have so far proven to have relatively disappointing performance in FRET applications [91]. As an illustrative example, an effort to use the mOrange2/ mCherry FRET pair in a live cell imaging application concluded that the greater spectral overlap of the orange-red pair, relative to a cyan-yellow pair, led to large spectral bleed through and thus limited its general utility for FRET imaging [24]. To solve this issue, one solution is to use long Stokes shift variants (discussed in Section 1.2.3.4) as FRET donors to minimize the direct excitation of the acceptor. The other solution is to systematically develop new FPs with properties better suited to a wide range of FRET applications. As an illustration, the recently published green-red FRET pair, Clover and mRuby2 [92], is reported to have the highest Förster radius of any ratiometric FRET pair yet described and is proving to be a competitor to the classic cyan-yellow FRET pair.

1.3.1.3 Strategies to assemble FP-based FRET biosensor

The most straightforward approach for creating a FRET-based biosensor is to create an intermolecular biosensor, in which two FP variants are fused to two different proteins of interest that have been hypothesized to have a physiologically relevant small-molecule dependent interaction. Typically, the two FPs are fused to

two different polypeptide chains and are then brought into proximity by small molecule dependent protein–protein interaction (**Figure 1.9A**). For instance, intermolecular FRET has been applied to study the influence of the epitopes on the oligomerization state of dopamine D1 and D2 receptors from the G-protein-coupled-receptor (GPCR) superfamily [93]. In another example, researchers exploited FRET to investigate the kinetics of metabotropic glutamate receptor (mGluR) activation by monitoring glutamate induced subunit dimerization [94]. However, one general concern about the intermolecular FRET strategy is the possibility of false negatives due to the particularities of each fusion. That is, even though the proteins of interest undergo a true interaction, it is not recorded as an increase in FRET efficiency due to the fact that the termini where the FPs happen to be fused just happen to be distant from each in the interaction complex.

In addition to intermolecular FRET, biosensors could also be designed to undergo intramolecular FRET. Such biosensors are constructed by fusing a donor and an acceptor FP within a single polypeptide chain, where changes in the conformation of the non-FP portion of the polypeptide chain can result in a change in FRET efficiency (**Figure 1.9B,C,D**). The portion of the FRET construct that undergoes the conformational change is typically chosen (or designed) because its change in conformation occurs in response to a biochemical event of primary interest. The conformational changes to be discussed in this Section are generally related to small molecule binding, enzymatic modification, protein–protein interactions, or protease-substrate recognition.

Of the biosensors for small molecule dependent protein–protein interactions (**Figure 1.9B**), the best-known example is the ‘cameleon’-style biosensors for Ca^{2+} [10,14,95]. In a cameleon, donor and acceptor FPs was linked through a non-FP portion, which is generated by fusing the CaM Ca^{2+} binding domain to a M13 peptide [10]. Ca^{2+} -loaded CaM initiates the formation of a globular complex with M13 bringing donor and acceptor FPs into closer proximity. Consequently, FRET efficiency of these constructs is highly sensitive to Ca^{2+} concentrations. Likewise, by replacing CaM and M13 by protein domains that undergo conformational changes upon binding to other ions or small molecules, researchers have

generated a variety of intramolecular FRET-based biosensors, such as ones for Zn^{2+} [96], cAMP [15].

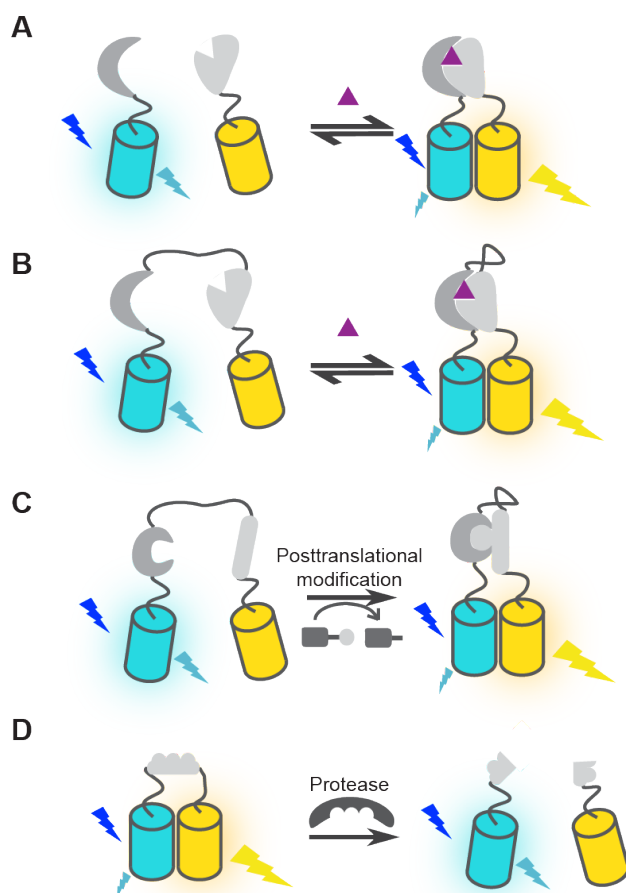


Figure 1.9 FP-based FRET biosensor design strategies.

For all examples the cyan barrel is the donor and yellow barrel is the acceptor. Intermolecular (A) and intramolecular (B) biosensors for a small molecule (magenta triangle) induced protein-protein interaction. (C) Intramolecular biosensors for enzymatic posttranslational modifications. The grey circle depicts a chemical functionality that is installed into a substrate domain by specific enzyme. (D) Protease biosensors. Donor and acceptor FPs are linked by the protease substrate sequence.

In addition to small molecule dependent protein-protein interactions, enzymatic modification induced protein-protein interactions have also been investigated by utilizing intramolecular FRET-based biosensors. In these biosensors, a substrate and molecular recognition domain are linked together with donor and acceptor FPs (Figure 1.9C). Once the substrate has been

posttranslationally modified by the enzyme activity of interest, it binds to the molecular recognition domain, which leads to a conformational change that alters the distance between FPs and changes the FRET efficiency. These biosensors are widely distributed in the study of kinases [17,23].

Another class of biosensors, intramolecular FRET-based protease biosensors, have facilitated the study of cell signaling and programmed cell death (apoptosis). Construction of protease biosensors involves a peptide containing a protease substrate sequence flanked by a pair of FPs (**Figure 1.9D**). Upon protease-substrate recognition, the protease cleaves the substrate sequence leading to the separation of FPs and thus a loss of FRET response (**Figure 1.9D**). This type of biosensor, a trypsin-cleavable sequence, was first used as to demonstrate that FRET between BFP and GFP was feasible [83]. Intramolecular FRET-based protease biosensors have since been used to detect many other proteases, such as caspase-3 [19,97] [27], caspase-6 [98], caspase-8 [26] and caspase-9 [98] in live cells.

The strategies described above are only some of the most popular designs, and do not represent an exhaustive list. Using an increasing number of clever designs, researchers have created a variety of sensitive protein domains that undergo conformational changes in the presence of analytes or stimuli and cause a change in FRET efficiency. Consequently, a vast number of FRET-based biosensors have been developed for specific applications. Given the advantages of ratiometric imaging and the dramatic expansion of FP pairs, the current trend for FRET-based biosensors is not limited to detecting individual biochemical events, but to be used in certain combinations for monitoring multiple independent physiological events concurrently [28]. Some successful examples of concurrent use of two biosensors include: imaging of dual caspase activities [26,27,97]; caspase-3 activity together with Ca^{2+} dynamics [14]; kinase activity together with cAMP dynamics [23]; and Src kinase activity in conjunction with membrane matrix metalloproteinase activity [24].

1.3.2 Complementation-based biosensor

Protein complementation is a process in which two protein fragments reconstitute into a complete functional protein. FP complementation is most commonly referred to using the abbreviation BiFC, which stands for biomolecular fluorescence complementation.

1.3.2.1 Split FP-based biosensor

Given that the chromophore of a FP requires the intact β -barrel in order to form and be fluorescent, the most basic strategy for designing a complementation-based biosensor relies on the reconstitution of non-functional split fragments of an FP, which are fused to interacting protein partners (**Figure 1.10A**). Through the interaction of protein partners, the proximity dependent reconstitution of the non-functional fragments restores the complete structure and the chromophore is able to form and emits fluorescence.

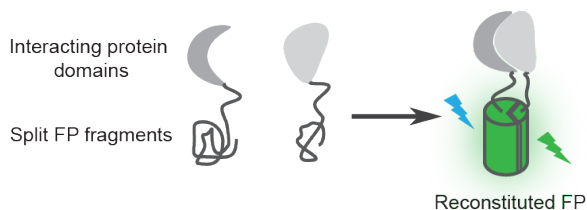


Figure 1.10 Split FP-based complementation strategies for protein-protein interaction.

Non-fluorescent split FP fragments are fused to interacting protein domains. The protein-protein interaction leads to irreversible reconstitution of two fragments and thus restores fluorescence.

Since the discovery of split avGFP fragments by Regan and coworkers in 2000 [99], other FP variants of different colour hues have been proven to be capable of being split and subsequently reconstituted into native FPs. Some examples include Cerulean [100], YFP [101], mRFP1 [102] and mCherry [103]. Essentially all split FP-based biosensors are utilized in screening or detecting protein-protein interaction. As an example, Hu and coworkers developed an

EYFP-based complementation biosensor to visualize subcellular localization of activator protein 1 dimers in mammalian cells [101]. Furthermore, the EYFP-based biosensor was utilized in conjunction with other split-FP-based biosensors in multiparameter imaging to visualize multiple interactions in the same cell [104].

Although split FP technology provides alternative solutions for screening protein-protein interactions, the more general application of this technology is limited by the slow kinetics of fluorescence development and the irreversible protein complementation [21].

1.3.2.2 Dimerization-dependent FP (ddFP)-based biosensor

As an alternative strategy for the design of complementation-based biosensors, my colleague Dr. Spencer Alford developed the dimerization-dependent FPs (ddFPs) that were inspired by the oligomerization of naturally occurring coral FPs [60,61]. Although oligomerization is generally considered a hindrance to the development of FP-based biosensor [53], Dr. Alford created a clever way to convert this disadvantage into an advantage. The key of ddFP technology is a pair of engineered dark monomeric FPs, whose fluorescence development depends on the formation of heterodimer (**Figure 1.11**). One of the dark monomers (copy A) contains a fully formed chromophore that is quenched in the monomeric state. The second dark monomer (copy B) does not form a chromophore itself and only acts to substantially increase the fluorescence of copy A upon formation of the AB heterodimer (**Figure 1.11**).

As will be discussed in detail in Chapters 3 and 4, I have shown that ddFP technology is particularly useful for the detection of associated membranes [61] and protease activities [60,61]. Given the expanded palette of ddFPs, including red (ddRFP), green (ddGFP) and yellow (ddYFP) variants, there is a promising future for the applications of ddFP technology in multiparameter imaging. Since ddFPs retain substantial affinity that favours the formation of heterodimers at intracellular concentrations in the low micromolar range, the effective

concentration of the ddFP partners must be taken into account when designing biosensors.

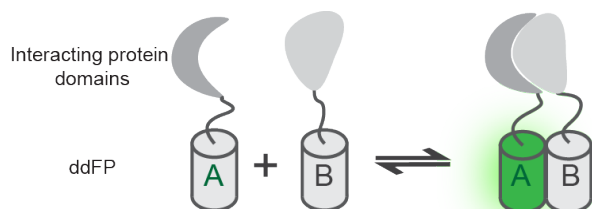


Figure 1.11 DdFP-based complementation strategy.

Using green ddFP as an illustration, a ddFP heterodimer is reversibly formed in the presence of a protein-protein interaction and fluorescence is restored.

In contrast to irreversible split FP-based biosensors, one of the major advantages of ddFP-based biosensors is their reversible nature, which allows researchers to probe dynamic events inside live cells [60]. The other advantage is the high solubility of the ddFP monomers resulting from a fully folded β -barrel, whereas split-FP fragments often suffer from poor solubility that limits their applications [105].

1.3.3 Single FP-based biosensors

Single FP-based biosensors utilize FPs that have been engineered such that the chromophore is spectrally responsive to its environment or to a conformational change caused by direct attachment to a domain of interest. In contrast to ratiometric FRET-based biosensors, single FP-based biosensors mainly report biochemical events as intensimetric signals, caused by a change in emission intensity [3]. Since most single FP-based biosensing involves a conversion between quenched and unquenched chromophores, the magnitude of an intensimetric change is typically greater than the change of a ratiometric FRET biosensor. Although most of the single FP-based biosensors are intensimetric, some ratiometric biosensors have also been reported [106].

One category of single FP-based biosensors are the intrinsic biosensing FPs. Without any external sensing domains, the unique interactions between chromophore and residues in the environment make these FPs sensitive to pH [107,108], or halides [109]. Protons and halide ions are small enough to penetrate the β -barrel and modulate the pK_a of the chromophore environment, which in turn alters the protonation state of the chromophore and thus tempers the fluorescence intensity (**Figure 1.12A**). In addition to the modifications within the chromophore environment, subtle modifications at the surface of the barrel are also utilized in the design of redox potential biosensors. In this design, cysteines were installed on the barrel of avGFP and the subsequent formation of disulfide bonds could cause a conformational distortion of the barrel and thus affect the chromophore environment [110,111].

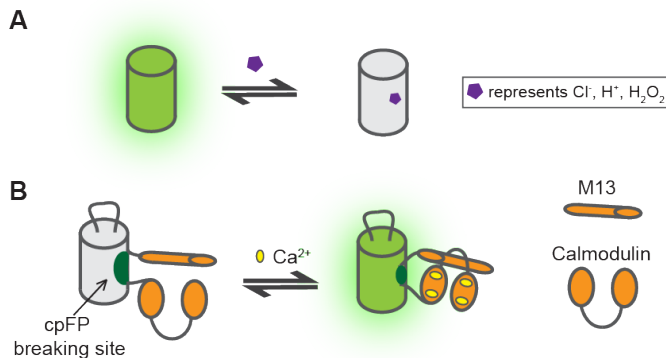


Figure 1.12 Schematic representations of single FP-based biosensor.

(A) Intrinsic biosensor. The fluorescence of the FP is related to the concentration of some small molecules in the chromophore environment. (B) cpFP-based Ca²⁺ biosensor. The chromophore is quenched due to the close proximity of the breaking site. In the presence of Ca²⁺, the conformational change with CaM and M13 seals the gap at the breaking site and thus restores the fluorescence.

The other major category of single FP-based biosensor is those constructed with circularly permutated FPs (cpFP, Section 1.2.3.2) and extrinsic sensing domains. By fusing cpFP to an extrinsic sensing domain, analyte-induced conformational changes of the sensing domain alters the chromophore environment of the cpFP and thus leads to a change in fluorescence emission. The

key to this strategy is that the position of the new cpFP termini must be in close proximity to the chromophore and fused to a sensing domain (**Figure 1.7**). Upon stimulation, conformational change occurs in the sensing domain and causes a perturbation of the chromophore environment of cpFP. One typical example is the design of the single FP-based Ca^{2+} biosensors such as GCaMPs [63,65] and GECOs [106]. In these biosensors, CaM and the M13 peptide are fused to the N- and C-termini of cpGFP (**Figure 1.12B**). The mechanism of fluorescent response to Ca^{2+} is revealed by a crystal structure of GCaMP [112]. In the absence of Ca^{2+} , CaM and M13 are unstructured, that allows the access of solvent to chromophore and quenches fluorescence. With the binding of Ca^{2+} , a globular structure formed by CaM and M13 seals the channel into the β -barrel and restores fluorescence [112]. Due to its intensimetric nature, each single FP-based biosensor will occupy a relative small range in the visible wavelength. Thus, the emerging trend is to engineer other single FP-based biosensors with different colour hues that could potentially be used in multiparameter imaging to monitor multiple physiological events concurrently.

1.3.4 Conclusion for FP-based biosensors

After almost 20 years of widespread awareness of FP technology, it has now earned a central place in the repertoire of tools for biological research. It is also important to emphasize that FP-based biosensors are not a remedy for all research problems in cell biology. It is easy for researchers to become overly enamoured by the idea of “seeing” biochemistry in live cells and pursue FP-based techniques at the expense of other traditional, and perhaps less glamorous, alternatives. This problem stems in a large part from the fact that, in our everyday life, images are the most compelling and convincing form of evidence that we have. As the adage states, “seeing is believing.” however, as scientists, we should be careful not to place undue weight on any one piece of evidence, no matter how aesthetically appealing it might be. There are a number of potential artefacts, such as photobleaching and photoactivation, that can conspire to make an image not what

it appears. Alternative lines of evidence, including *in vitro* tests of protein–protein interactions or conformational changes, are highly recommended.

Biosensing with FPs is the basis for a toolbox of powerful techniques, and new tools will continue to be added over the coming years and decades. These techniques will continue to be at the cutting edge of our ability to explore ever more intricate questions in biology and thus lead to countless new and breathtaking insights. Accordingly, there remain a tremendous number of opportunities for designing FP-based biosensors that are specific for probing biological activities and could be used in integration with other biosensors in multiparameter imaging.

1.4 Protein engineering

Protein engineering is the laboratory process of creating or altering protein properties and functions by making purposeful changes in its coding DNA sequence. Proper protein functions highly rely on the organized three-dimensional structure, which is determined by the primary amino acid sequences, thus, modulation of protein functions can be rationally or randomly installed via genetic manipulations of the genes encoding proteins of interest [113].

To facilitate protein engineering, theoretical computational simulation [114,115], advanced crystallographic data of progenitor proteins and published structure-function studies have been utilized as guidance for genetic modifications [116]. Since the decisions of the genetic modifications are derived from a rational analysis of existing data, this protein engineering strategy is often referred as “rational design”.

Alternatively, libraries of protein variants can be created and then subjected to a selection pressure, by which proteins exhibiting desired phenotypes are identified and isolated from a pool of candidates [117]. This protein engineering approach is known as “directed evolution” since it mimics the natural evolution, whose direction was determined by a competitive surviving selection. Directed evolution utilizes molecular biology techniques coupled with genetic or

phenotypic screens to generate and select altered proteins [117,118]. The first step of directed evolution focuses on generating a diverse gene library via DNA recombination, followed by the second step of introducing the library into an appropriate host (*e.g.*, *E. coli*). Third step involves selecting desired phenotype by screening the library of variants. The selected variants are then isolated for further characterization or serve as template of the next round of directed evolution (**Figure 1.13**). During the last few decades, directed evolution is widely applied in the area of enzyme engineering, in which candidates with altered activity, improved specificity and stability are effectively selected from libraries of great diversity [119].

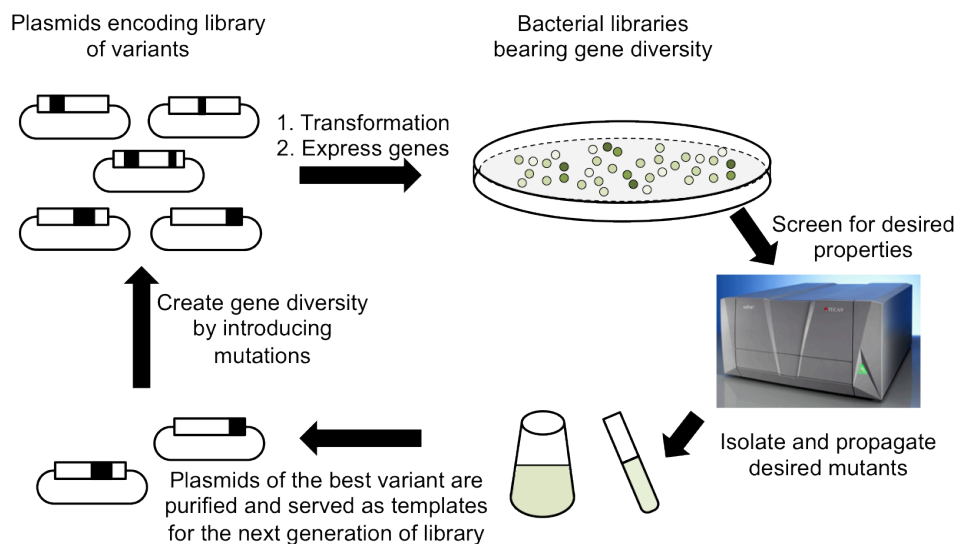


Figure 1.13 Schematic representation of the process of directed evolution.

The popularization of protein engineering was contributed by the advent of new DNA recombinant methods, including sited-directed mutagenesis, random mutagenesis and DNA hybridization. The development of site-directed mutagenesis [120] enabled researchers to effectively incorporate specific amino acids at specific sites in proteins according to their rational design. Moreover, this also allows the creation of a small scale library with randomized all 20 or a subset of predefined amino acids at specific positions of a protein sequence [118]. Protein engineers first adopted site-directed mutagenesis to mutate active site

residues in enzymes. For instance, the activity of thiol- β -lactamase was largely defected by the mutations introduced within the active site [121]. The applications were not limited to alter the function of the protein, but also expand to the generation of proteins with desired functional improvements, such as selectivity [122] and stability [123,124].

In addition to site-directed mutagenesis, DNA diversification for directed evolution can also be achieved by random mutagenesis and gene hybridization. Both of these methods are capable of creating libraries of great genetic complexity, which potentially increase the chances to find the one with desired property comparing to site-directed mutagenesis [125]. Libraries of random mutagenesis are performed on a gene template (or pool of gene templates) by amplifying genes using the polymerase chain reaction (PCR) with error prone reaction conditions (i.e., using low fidelity polymerases in the buffer with high Mg^{2+} concentration, Mn^{2+} and unbalanced dNTPs) [126,127]. The error rate of the reaction can often be adjusted through the change of buffer conditions [128,129]. However, the size of the library is constrained by the fact that beneficial mutations decreases with increasing mutation rate due to accumulation of detrimental mutations [128]. Thus random mutagenesis used in directed evolution depends on a large number of evolution cycles to accumulate the small improvements gained from each cycle.

Gene hybridization is a powerful strategy to gain beneficial mutations by assembling hybrid genes from several gene templates. Commonly used template sequences can be a group of naturally occurring homologous genes [130,131] or a mixture of mutagenized genes derived from a single progenitor [132]. Many techniques of gene recombination have been developed and used in directed evolution (reviewed in [118,133]), among which, DNA-shuffling [131] and staggered extension PCR (StEP) [132] are the most widely used methods. DNA shuffling utilizes the gene fragmentations of improved variants as templates, which also act as primers and anneal to each other in a PCR amplification to achieve the crossover events [131]. In contrast, StEP utilized full-length sequences as templates, which simplify the procedure without sacrificing the

effective accumulation of mutations. Specifically, the crossover events in StEP are created by the staggered DNA fragments, which are generated in a modified PCR with highly abbreviated annealing and extension steps [132].

Beyond the generation of library diversity, the development of screening strategy is of equal importance in directed evolution. For an effective screening method, the desired properties should be read out as a noticeable signal, such as survival, binding efficiency, enzymatic activity, or fluorescence [134]. Following screening, the next step is the physical separation of the desirable variants from the pool. Common strategies include picking isolated bacteria colonies on agar plates, trapping variants via affinity tag (*e.g.*, Phage display) [135], or collecting from a fluorescence activated cell sorter [136].

Although the success of directed evolution is well established in engineering a wide variety of enzymes [118], antibodies [135] and FPs [29,54-56]; it suffers from highly intensive labor work and the requirements of diversity and effective screening [137]. In contrast, the relative small workload of rational design is benefit from its specificity, logical deduction and statistical support. However, practically, rational designs are typically not as optimal as protein engineers envision [138]. Therefore, protein engineering is significantly benefited from a combination of both rational design and random mutagenesis [139,140]. This combination has successfully yielded in the improvements of protein's intended function, such as enzyme engineering [139], the development of FP [39,54,56,141] and FP-based biosensor [60,106,142], as well as the optimization of FRET biosensors [14,62,143].

1.5 The scope of the thesis

In this thesis, we describe our efforts on engineering FRET and ddFP-based biosensors and applying them in live cells to detect multiple dynamic activities.

Chapter 2 describes multiparameter ratiometric imaging with two spectrally distinct FRET pairs. By using biosensors made from these two FRET pairs, we successfully detected Ca^{2+} dynamics in different subcellular compartments in

single cells and observed Ca^{2+} dynamics in conjunction with protease activation concurrently. The research involving the engineering, optimization, characterization and application of the FRET-based biosensors has been published in *Analytical Chemistry* [14].

Chapter 3 focuses on the development of ddFP-based protease biosensors, which can be categorized into two major groups based on colour or location readout. One group of protease biosensors reports protease activity via a loss of fluorescence intensity. The other group indicates protease activity via a translocation of fluorescence from cytoplasm to nucleus with or without colour switch between red and green. The work related to the first group of protease biosensors was published in conjunction with Dr. Spencer Alford's work in *Chemistry & Biology* [60] and *ACS Synthetic Biology* [61]. The work related to the second group of biosensors has been submitted to *Nature Methods*.

Chapter 4 describes my efforts on labeling of the mitochondria associated membrane (MAM) mediated contacts sites via ddFP technology. Multiple membrane domains from mitochondria and endoplasmic reticulum (ER) were investigated to achieve the contacts between the fused ddFP partners. This part of work was also published in *ACS Synthetic Biology* [61]. Unpublished efforts to exploit fatty acid coenzyme A synthase 4 (FACL4) as a marker for MAM are also described.

Chapter 5 describes the attempted development of biosensing strategies for poly(ADP-ribose) polymerase 1 (PARP1) activity via the recruitment process induced by polyADP-ribose (PAR) and both FRET and ddFP technologies. We hypothesized that PAR binding molecules would be in close proximity upon recruitment and thus might lead to a change in FRET or association of ddFP partners. However, we did not observe any positive signal among our many thorough attempts, which indicated that there is likely no direct interaction between the binding molecules even though they were recruited together.

The final Chapter is a summary of this thesis work and an outlook for the future developments in the field of engineering FP-based biosensors.

There is also an appendix in which I describe efforts to construct a high throughput assay for screening the conformational change of a photosensitive domain. Both FRET and single FP-based biosensors were explored as readouts for this assay.

Chapter 2: FRET biosensors for multiparameter imaging in live cells²

2.1 Introduction

Engineering of FP variants that are active reporters of cellular biochemistry (i.e., intracellular biosensors) has required the development of strategies that enable the fluorescence intensity or colour of a FP-containing construct to be modulated in response to a change in its environment [144,145]. One strategy that has proven particularly useful is Förster resonance energy transfer (FRET) [74] from a more blue-shifted donor FP to a more red-shifted acceptor FP. A change in FRET efficiency, due to a change in distance or relative orientation between the two FPs [75], causes the ratiometric change in emission that is imaged in a typical FP-based FRET experiment. The most common approach for achieving the change in distance or orientation is to sandwich a ‘sensing’ domain between donor and acceptor FPs in a gene construct that is ultimately translated to a single polypeptide chain. The prototypical FRET-based Ca^{2+} biosensors are collectively known as cameleons and are created by genetically fusing calmodulin (CaM) and the CaM-binding region of chicken myosin light chain kinase (M13) between the two FPs of a FRET pair [10]. Binding of Ca^{2+} to CaM leads to the intramolecular binding of CaM and M13 and a change in the orientation and/or distance between the linked FPs.

² A version of this chapter has been published. Ding, Y., et al. 2012 *Anal. Chem.*, **83**, 9687-9693. Optimization of CaYang and CaYin by domain rearrangements (Section 2.2.1) is credit to Dr. Huiwang Ai. The variant of mAmetrine1.2 with improved photostability is credit to Dr. Hiofan Hoi. Experiments performed by me include *in vitro* characterization of the best variants from Dr. Ai’s work, optimization of CaYin by linker length modification and demonstration of the optimized biosensors in live cell imaging and related analysis of the spectral bleed through.

Although there is a growing demand for FP-based methods that for monitoring multiple biological parameters in a single live cell [2,28], the broad spectral profiles of FP FRET pairs has, in most cases, meant that only a single biosensor could be individually and ratiometrically imaged in a single cell. To achieve multiparameter imaging, researchers have tended to take hybrid approaches such as the combined use of cyan FP (CFP)-yellow FP (YFP) FRET-based biosensors and appropriate hues of synthetic dye-based probes [28,146]. Yet other solutions to achieve multiparameter imaging forgo the advantages of ratiometric imaging and rely instead on multiple intensimetric probes [106] or spectral unmixing of the emission from multiple ratiometric probes [48]. Arguably, these alternative methods each sacrifice some key advantages of ratiometric imaging of FP biosensors. Specifically, it is inherently quantitative, it is technically simple, it is inexpensive and uses common equipment, and it can be applied to a multitude of biological questions.

As part of our ongoing efforts to reconcile multiparameter imaging with FP-based imaging, we have previously developed a pair of spectrally distinct FP FRET pairs, mAmetrine-tdTomato (**Figure 2.1A**) and mTFP1-mCitrine (**Figure 2.1B**), that both provide strong sensitized emission and, with appropriate filter choice, can be uniquely excited in each other's presence [19]. For the sake of brevity, we refer to the mAmetrine-tdTomato pair as 'Yin' and the mTFP1-mCitrine pair as 'Yang'. To explore the utility of these spectrally distinct FRET pairs, Dr. Huiwang Ai previously constructed caspase-3 activity biosensors (DEVYin and DEVYang) and used them to accurately determine the delay between the onset of caspase-3 activity in the cytoplasm and the nucleus during apoptosis [19]. Other workers have explored the usage of two FRET pairs with a shared acceptor [23,147], or a combination of CFP-YFP and a red FRET pair based on an orange FP (OF) and a red FP (RF) [24,148,149], as spectrally distinct FRET pairs. Such pairs have enabled multiparameter imaging, though their utility tends to be limited by the relatively poor sensitized emission of the RF acceptors.

In this Chapter, I describe the construction, optimization, and application of cameleon-type Ca^{2+} biosensors based on an improved version of the Yin FRET pair combined with the original Yang FRET pair. Using these optimized biosensors, we have demonstrated that it is feasible to image Ca^{2+} dynamics in two distinct subcellular compartments or Ca^{2+} and caspase-3 activity in the same subcellular compartment.

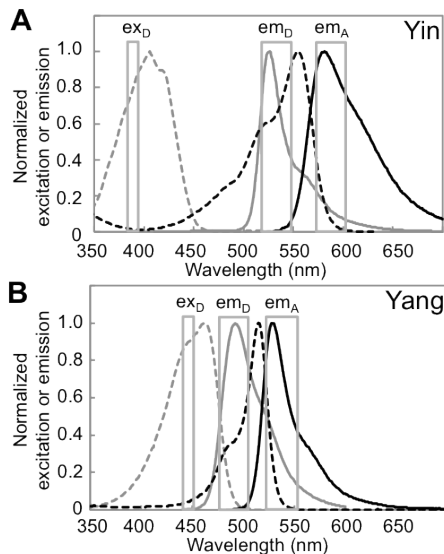


Figure 2.1 Excitation and emission spectra of the FPs that compose the spectrally distinct FRET pairs used in this work.

On each chart is represented the excitation (dashed line) and emission (solid line) spectra of both the donor (gray) and acceptor (black) FPs. For each panel, the bandpasses for a typical donor excitation filter (ex_D), donor emission filter (em_D), and acceptor emission filter (em_A) are represented. (A) The Yin FRET pair based on a mAmetrine donor and a tdTomato acceptor. (B) The Yang FRET pair based on a mTFP1 donor and a mCitrine acceptor.

2.2 Results and discussion

2.2.1 Optimization of CaYang and CaYin by domain rearrangements

We have designated our previously reported Ca^{2+} biosensor, originally constructed by replacing the CFP portion of YC3.3 with mTFP1 [55], as CaYang0.1, which has 35% change in the intensity ratio of acceptor to donor upon Ca^{2+} binding. In an effort to improve the performance of the CaYang

construct, Dr. Huiwang Ai replaced the YC3.3-derived Ca²⁺ sensing domain (with CaM E104Q) with the analogous domains of YC4.3 (with CaM E31Q) [10] to produce CaYang0.2. He also inserted the D1-derived Ca²⁺ sensing domain (engineered to have 4 charge-reversed salt-bridges) [150] to produce CaYang0.3 (**Figure 2.2**). The variant containing the D1 binding domain (CaYang0.3) showed improved dynamic range of 57%.

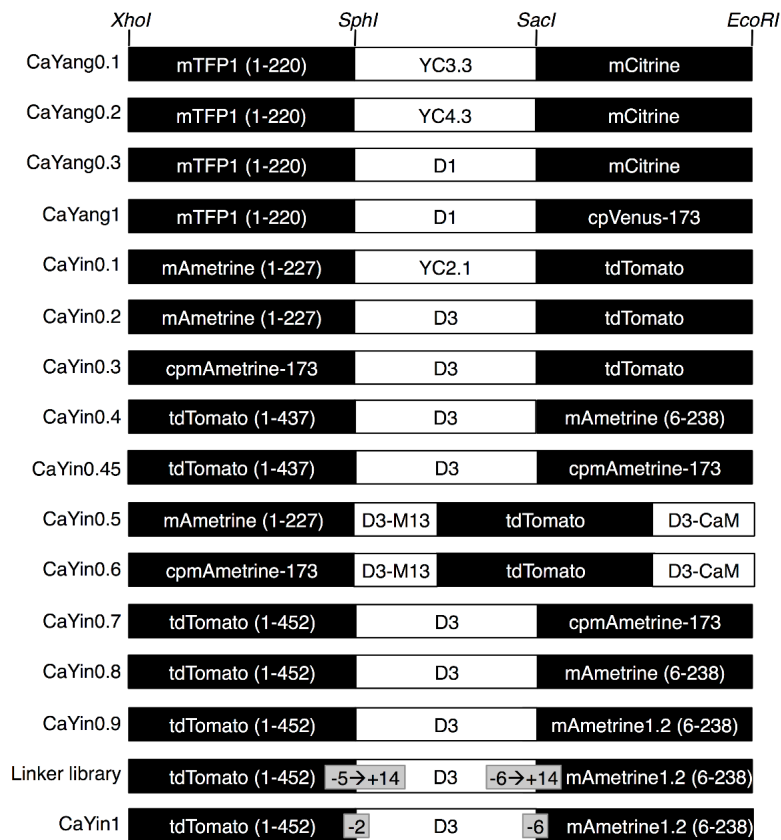


Figure 2.2 Domain arrangements tested during the optimization of CaYang and CaYin.

All variants are designated using an alphabetic character. The intermediate portion of the gene, labeled as YC2.1, YC3.3, YC4.3, D1, or D3, refers to the CaM-M13 region of the corresponding cameleon construct [10,88,95,150].

In an attempt to further improve the FRET response, the YFP acceptor, a YFP known as Citrine [88], was replaced with a circularly permuted YFP known as cp173Venus [67,95]. The rationale for attempting this replacement is that it introduced a new dipole-dipole orientation that may (or may not) provide

improved dynamic range [67]. Fortunately, this replacement did result in an increased dynamic range of 151% (**Table 2.1 and Figure 2.3A**) and so the resulting construct was designated as CaYang1.

Table 2.1 Optimization of CaYang and CaYin constructs by domain swapping.

Name	Emission ratio (acceptor emission/donor emission)		% change
	- Ca ²⁺	+ Ca ²⁺	
CaYang0.1	1.37	1.84	+35
CaYang0.2	1.07	1.18	+10
CaYang0.3	0.99	1.55	+57
CaYang1	0.97	2.44	+151
CaYin0.1	0.46	0.59	+26
CaYin0.2	0.49	0.58	+17
CaYin0.3	0.44	0.58	+33
CaYin0.4	N/A ^a	N/A	N/A
CaYin0.45	N/A	N/A	N/A
CaYin0.5	0.78	0.66	-15
CaYin0.6	0.77	0.59	-23
CaYin0.7	0.81	1.0	+24
CaYin0.8	0.58	0.84	+45
CaYin0.9	0.62	1.05	+70
*Not applicable: construct was not expressed in soluble form.			

To construct a Ca²⁺-specific biosensor that would be spectrally distinct from CaYang, Dr. Ai developed several cameleon-type constructs using the Yin FRET pair. As with the CaYang biosensor, we initially attempted a variety of domain combinations, with particular emphasis placed on exploring different arrangements of tdTomato, the binding domain of D3 [95], and the various versions of mAmetrine we now had in hand (**Figure 2.2**). The D3 binding domain has been reported to have a K_d that is well matched to the detection of Ca²⁺ in the

cytoplasm, and has the added advantage of being engineered to not bind to endogenous CaM [95,151]. Of the 9 variations tested, the construct with the largest ratio change (45%; **Table 2.1**) was CaYin0.8, a biosensor composed of tdTomato followed by the D3 Ca²⁺ binding motif and mAmetrine.

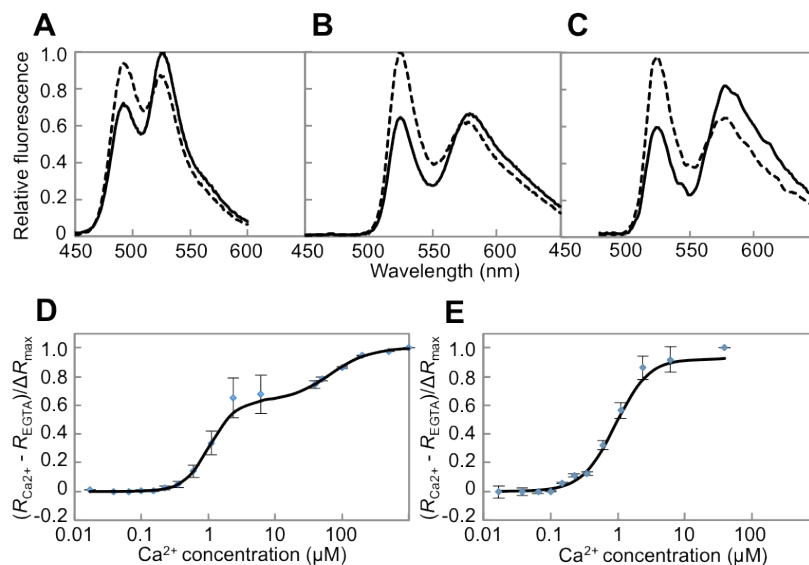


Figure 2.3 Characterization of optimized Ca²⁺ biosensors.

(A-C) The Ca²⁺-dependent emission ratio change for CaYang1 (A); CaYin0.9 (B); and CaYin1 (C). The solid and dashed lines represent the fluorescence of proteins in the presence of 500 mM Ca²⁺ and 200 μ M EGTA, respectively. (D) Fluorescence emission ratio versus concentration of Ca²⁺ for CaYang1. The K_d values are 1.04 ± 0.03 and 66.8 ± 4.6 μ M for the high and low affinity portions of the biphasic binding curve, respectively. (E) Emission ratio versus concentration of Ca²⁺ for CaYin1. The K_d is 0.87 ± 0.07 μ M.

My work started with *in vitro* characterization of CaYang1, which revealed that the biosensor had a biphasic response to Ca²⁺ (**Figure 2.3D**), similar to that reported for the parent D1 cameleon based on CFP and YFP [150]. Fitting the data to a two-site binding model gave K_d values of 1.04 ± 0.03 and 66.8 ± 4.6 μ M. Regarding to CaYin, I replaced mAmetrine from CaYin 0.8 with an improved variant, mAmetrine 1.2 (engineered by Dr. Hiofan Hoi), to create CaYin0.9, with a increased ratio change to 70% upon Ca²⁺ binding (**Table 2.1** and **Figure 2.3B**). However, we remained unsatisfied with the 70% ratio change of CaYin0.9.

2.2.2 Optimization of CaYin by linker length modification

In an effort to further improve the ratio change, we turned to linker adjustment as an alternative method to optimize biosensor performance [75]. Accordingly, we individually constructed, purified, and tested 17 additional variants of CaYin0.9 in which the linker between tdTomato and CaM and the linker between M13 and mAmetrine1.2 was varied in length (**Table 2.2** and **Figure 2.4**). In the CaYin construct, there is no extra linker sequence added between the FPs and CaM/M13. However, the N- and C-terminal ends of FPs and CaM/M13 tend to be unstructured and thus act as ‘built-in’ flexible linkers. In order to explore a variety of different orientation factors which could modulate the FRET efficiency, short flexible amino acids sequence (a sequence rich in Gly, Thr, Ala and Ser) were added in these built-in linkers. In other words, we explored different linker length combinations before CaM and after M13.

Table 2.2 Residues appended or deleted in the linker library.

Number of residues added or deleted	Amino acid sequence between tdTomato and CaM	Amino acid sequence between M13 and mAmetrine
-6	N/A*	KKI-----EL
-5	MH-----EQI	N/A
-3	N/A	KKISSS-----EL
-2	MH-----LTEEQI	N/A
0	MH-----DQLTEEQI	KKISSSGAL-----EL
+2	**MH----- <u>GSDQLTEEQI</u>	KKISSSGAL <u>GS</u> -----EL
+4	MH----- <u>ATGSDQLTEEQI</u>	KKISSSGAL <u>GSTA</u> -----EL
+6	MH----- <u>GSATGSDQLTEEQI</u>	KKISSSGAL <u>GSTAGS</u> -----EL
+8	MH----- <u>TAGSATGSDQLTEEQI</u>	KKISSSGAL <u>GSTAGSGT</u> -----EL
+10	MH----- <u>TGTAGSATGSDQLTEEQI</u>	KKISSSGAL <u>GSTAGSGTGA</u> -----EL
+14	MHAGSGTG <u>TAGSATGSDQLTEEQI</u>	KKISSSGAL <u>GSTAGSGTGASGTAE</u> L

*Not applicable: linker was not tested.
**Underlined residues represent added linker. The residues at each end that are not underlined belong to tdTomato, CaM, M13, or mAmetrine.

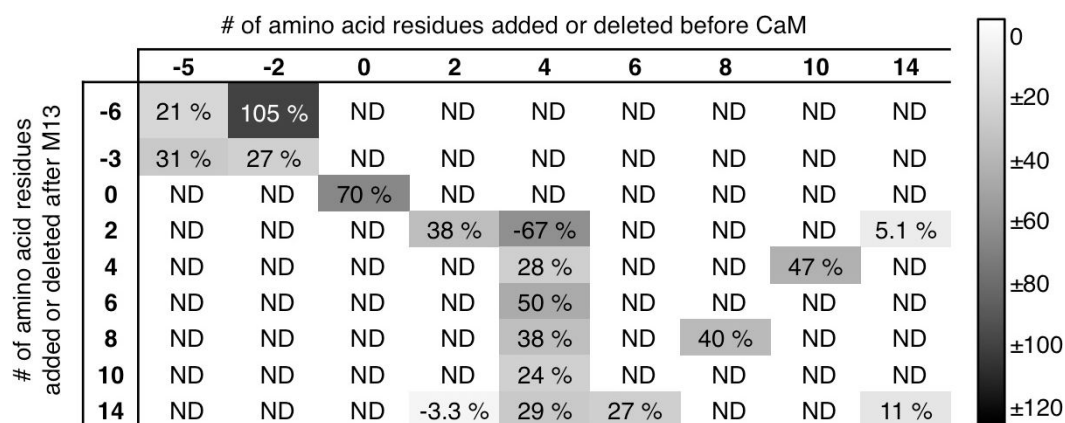


Figure 2.4 Optimization of the CaYin emission ratio change by testing of selected combinations of two linkers.

Numbers shown in percentage indicate the emission ratio change of biosensors in response to Ca^{2+} . Emission ratio change = $(\text{Ratio}_{\text{EGTA}} - \text{Ratio}_{\text{Ca}}) / \text{Ratio}_{\text{EGTA}}$. $\text{Ratio}_{\text{EGTA}}$ and Ratio_{Ca} stand for the intensity ratio of acceptor to donor in EGTA buffer and Ca^{2+} buffer, respectively. The combinations of linkers are shown in Table 2.2. ND = not determined, because linker combination was not tested.

As previously reported for an analogous optimization effort [13], there was no clear trend in the observed responses to Ca^{2+} as a function of linker length. Most variants had a decreased ratiometric response compared with the original construct (70%, **Figure 2.4**) and some of them even gave inverted (negative) responses to Ca^{2+} . An inverse response indicates that FRET is less efficient following Ca^{2+} binding due to unfavourable distances or orientation caused by the changes in the linker residues (**Figure 2.4**).

To further explore the effect of linkers on FRET performance, we also truncated residues from flexible “built-in” linkers. Since the flexible C-terminal end of tdTomato (YGMDELYK) and the N-terminal end of mAmetrine (MVSKGEEL) have been deleted already, we deleted up to five residues from the N-terminal end of CaM and up to six residues from the C-terminal end of M13 (**Table 2.2**). On the basis of **Figure 2.4**, the decrease of ratio change (from 105% to 21%, **Figure 2.4**), in the variants with two and five residues deleted from the N-terminal end of CaM, might be the result of deleted the functional crucial residues of CaM, since only about five residues were before the first crucial helix

of CaM (PDB 2BBM [152]). Regarding to M13, the deletion of six residues might lead to a closer distance between FPs, compared to the deletion of three residues, since an increase of ratio change (from 27% to 105%, **Figure 2.4**) was observed.

Therefore, among all the variants, the one with two residues deleted from the N-terminal end of CaM and six residues deleted from the C-terminal end of M13, designated as CaYin1, yielded the largest ratio change (105%; **Figure 2.3C**). Further *in vitro* characterization of CaYin1 revealed a K_d for Ca^{2+} of $0.87 \pm 0.07 \mu\text{M}$ (**Figure 2.3E**).

2.2.3 Multiparameter imaging of Ca^{2+} in different cellular compartments

To test the utility of CaYin1 and CaYang1 for multiparameter imaging, we co-expressed both biosensors in HeLa cells and performed ratiometric fluorescence imaging with appropriate filter combinations (**Table 2.3**). Similar to our previously reported imaging experiments with DEVYin and DEVYan [19], CaYin1 was targeted to the cytoplasm using a nuclear-exclusion sequence (NES) and CaYang1 was targeted to the nucleus using a nuclear localization sequence (NLS). Upon stimulation of Ca^{2+} release by treatment with histamine, intermittent increases in the acceptor to donor ratio were observed in both the cytoplasm and nucleus (**Figure 2.5A-D**), consistent with our expectations based on *in vitro* results. The oscillations lasted about 20 minutes before the cells reverted back to the resting condition.

Table 2.3 Filter sets used for dual FRET imaging.

Filter	Yin		Yang	
	mAmetrine	mAmetrine/tdTomato FRET	mTFP1	mTFP1/YFP (cpVenus) FRET
excitation	387/11 nm	387/11 nm	455/10 nm	455/10 nm
dichroic	455 nm	515 nm	470 nm	495 nm
emission	535/30 nm	585/29 nm	495/30 nm	545/30 nm

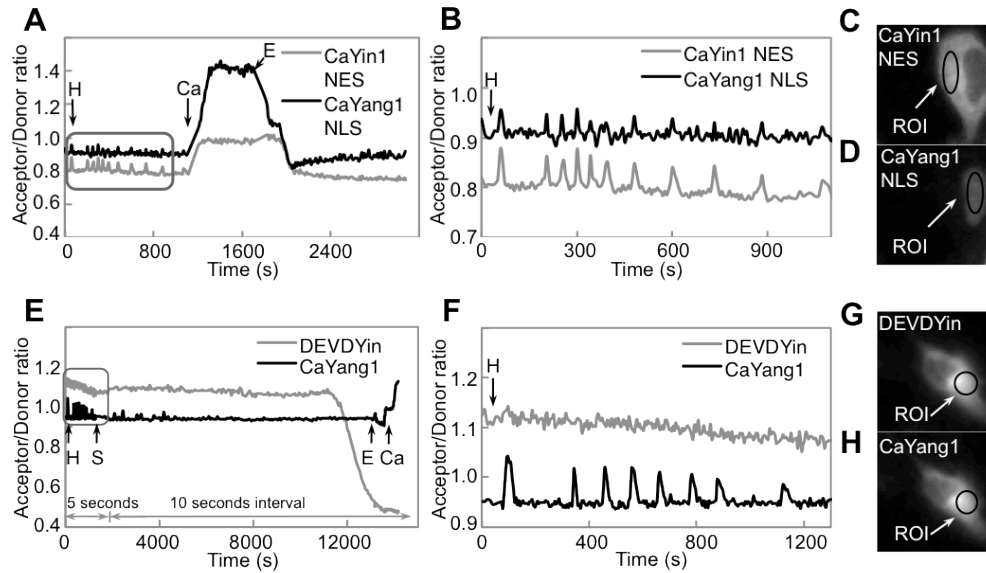


Figure 2.5 Dual FRET imaging of Ca^{2+} concentration and caspase-3 activity. (A) Imaging of Ca^{2+} concentration in two compartments of a single cell. Arrows indicate time points at which the composition of culture medium was altered. Single letter codes represent the addition or exchange of medium to give the following final concentrations: H, 30 μM histamine; Ca, 5 mM Ca^{2+} and 5 μM ionomycin; E, 10 mM EGTA and 5 μM ionomycin. (B) Zoom in on the boxed area from A. (C and D) Representative images in the mAmetrine (C) and mTFP1 (D) emission channels of the cell that was imaged in (A). ROI = region of interest from which the time-dependent average intensity was calculated. (E) Imaging of Ca^{2+} concentration and caspase-3 activity in the same compartment of a single cell. Single letter codes H, E, and C represent the same solutions as in (A), while S represents 2 μM staurosporine (final concentration). (F) Zoom in on the boxed area from E. (G and H) Representative images in the mAmetrine (G) and mTFP1 (H) emission channels of the cell imaged in E.

After approximately 40 min, cells were treated with concentrated Ca^{2+} /ionomycin buffer, with the purpose of equilibrating the intracellular Ca^{2+} concentration with the high extracellular Ca^{2+} concentration and achieving the maximum ratio signal associated with Ca^{2+} binding. Finally, cells are treated with ethylene glycol-bis(2-aminoethylether)-N,N,N',N'-tetraacetic acid (EGTA)/ionomycin buffer which chelates Ca^{2+} , such that the CaM/M13 interaction is released and the FRET ratio signal reaches its minimum value. This procedure allows the maximum and minimum FRET ratio corresponding to Ca^{2+} saturated and Ca^{2+} free conditions to be recorded for each cell. These values can

then be used to calibrate the intracellular Ca^{2+} concentrations observed in the experiment. The different maximum and minimum FRET ratios for CaYin1 and CaYang1 resulted from the different dynamic range of these two FRET pairs. Overall, these results demonstrate that both CaYin1 and CaYang1 are suitable for use in multiparameter live cell Ca^{2+} imaging experiments.

2.2.4 Multiparameter imaging with Ca^{2+} and caspase biosensors

To assess whether biosensors based on the Yin and Yang FRET pairs could be used in the same cellular compartment, we co-expressed both DEVDYin and CaYang1 in HeLa cells and performed ratiometric imaging as with the CaYin1 and CaYang1 combination (**Figure 2.5E-H**). This experiment directly assessed the spectral orthogonality of the two sensors, since Ca^{2+} spikes following histamine treatment were expected to be visualized as increases in the Yang emission ratio, but not in the Yin emission ratio. Likewise, the loss of FRET following cleavage of DEVDYin by caspase-3 was expected to be visualized as a decrease in the Yin emission ratio, but not in the Yang emission ratio. Satisfyingly, we observed that Ca^{2+} -dependent ratio changes in the Yang emission ratio resulted in no concomitant change in the Yin emission ratio (**Figure 2.5F**) and the dramatic decrease in Yin emission ratio that followed caspase-3 dependent cleavage resulted in no substantial change in Yang emission ratio (**Figure 2.5E**). At the end of each experiment all the cells are treated with EGTA/ionomycin and Ca^{2+} /ionomycin to achieve the minimum and maximum FRET ratio for CaYang1. As expected, the ratio for CaYang1 altered with no change in DEVDYin signal. Therefore, we conclude that there is minimal cross-talk between DEVDYin and CaYang1 and ratiometric imaging of both biosensors in single cells is feasible and practical

2.2.5 Correction factor for bleed through between FRET pairs

Based on the results illustrated in **Figure 2.5**, no substantial bleed through between the emission channels of the two FRET pairs. However, we know from

in vitro studies that there is some degree of cross-excitation between the two FRET pairs (Table 2.4). For example, the filter set used to excite mAmetrine gives some excitation to mTFP1 (2.13% of mTFP1 excitation as measured by convolving and integrating the excitation spectrum of mTFP1 for each filter).

Table 2.4 Analysis of spectral crosstalk for calculation of correction factors.

Name	ex mTFP1; em mTFP1	ex mTFP1; em YFP	ex mAm; em mAm	ex mAm; em tdTom
mTFP1	100%	31.34%	2.13%	0.49%
YFP	3.80%	100%	6.23%	1.99%
mAmetrine	4.50%	6.09%	100%	26.28%

Abbreviations: ex = excitation, em = emission, mAm = mAmetrine, and tdTom = tdTomato.

For each protein, the emission intensity using the most appropriate filter set is set to 100%.

The YFP used for these measurements was cpVenus, though we expect that the results would be very similar for other YFP variants such as mCitrine and Venus.

The crosstalk of tdTomato in other channels is less than 1%.

Fortunately, due to differences in fluorescent protein emission profiles, this cross-excitation is much less of a problem than it might first appear and it can be accounted for with a straightforward mathematical correction factor. Using the values provided in this table we calculated the following correction formulas:

$$I_{\text{Ame cor}} = 1.002 * I_{\text{Ame}} - 0.019 * I_{\text{cpVenus}} - 0.015 * I_{\text{TFP}};$$

$$I_{\text{TFP cor}} = 1.012 * I_{\text{TFP}} - 0.038 * I_{\text{cpVenus}} - 0.017 * I_{\text{Ame}};$$

$$I_{\text{cpVenus cor}} = 1.012 * I_{\text{cpVenus}} - 0.316 * I_{\text{TFP}} - 0.068 * I_{\text{Ame}};$$

$$I_{\text{tdTomato cor}} = I_{\text{tdTomato}} - 0.263 * I_{\text{Ame}} + 0.005 * I_{\text{cpVenus}} + 0.004 * I_{\text{TFP}}.$$

In these equations $I_{\text{Ame,cor}}$, $I_{\text{YFP,cor}}$, and $I_{\text{TFP,cor}}$ are the corrected values and I_{Ame} , I_{YFP} , and I_{TFP} are the raw experimental values.

These correction factors can be used to scale each image in a time-lapse series on a time-point by time-point basis. It is important to note that these simple correction factors are specific for the fluorescent proteins and filters used in this work but are general with respect to the FRET construct and FRET efficiency. Applying this correction to the images acquired in this work did not significantly change the timing or magnitude of the FRET changes. As shown in **Figure 2.6**, correcting the emission intensities for inter-FRET pair spectral crosstalk [19], produced time course traces that were qualitatively similar to the uncorrected traces.

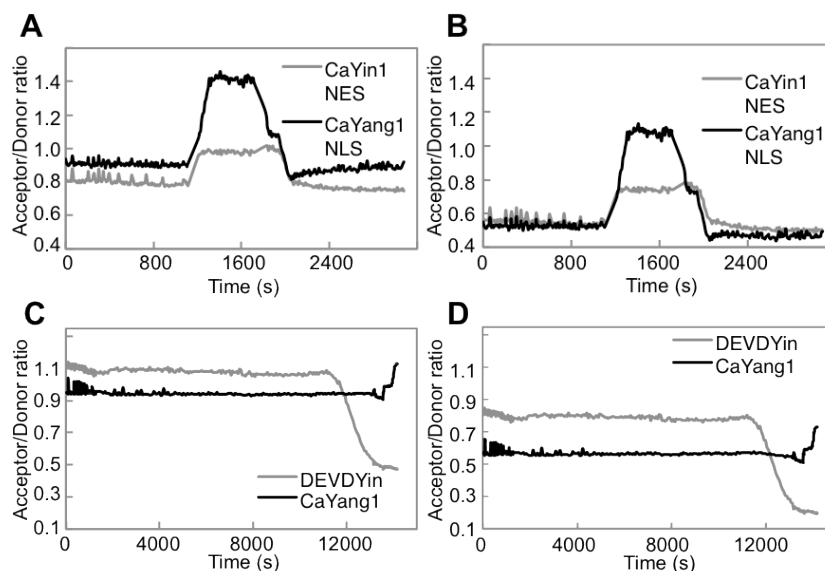


Figure 2.6 Dual FRET imaging of Ca^{2+} concentration and caspase-3 activity with application of a correction factor for spectral crosstalk.

(A) Background corrected intensity versus time data as represented in Figure 2.5A. (B) Same data as in A, following application of a correction factor for spectral crosstalk. The equations used for the correction are provided in Section 2.2.5. (C) Background corrected intensity versus time data as represented in Figure 2.5E. (D) Same data as in C, following application of the correction factor.

2.3 Conclusions

We have described the development and optimization of a pair of FP-based Ca^{2+} biosensors that are spectrally distinct and can be imaged in the same cell. We

have also demonstrated that one of these Ca^{2+} biosensors, paired with one of the previously reported caspase-3 biosensors based on the same FRET pairs, enables ratiometric imaging of both Ca^{2+} and caspase-3 activity in the cytoplasm of a single cell. With the recent development of the intensimetric red-fluorescent FP-based Ca^{2+} indicator R-GECO1 [106], analogous multiparameter imaging could now be accomplished with the combined use of R-GECO1 and a CFP-YFP FRET-based Ca^{2+} indicator [151] or caspase-3 indicator [153]. Relative to this alternative approach, the use of the Yin and Yang FRET pairs provides two advantages. The first advantage is that both biosensors can be imaged ratiometrically, thus providing greater ease of quantitation. The second advantage is that, in principle, any pair of biosensors from the vast number of existing CFP-YFP FRET-based biosensors could be converted to the Yin and Yang FRET pairs. In contrast, there are very few examples of intensimetric biosensors that could be converted to an R-GECO1-like design, severely limiting the versatility of this approach.

As highlighted by the present work, the primary disadvantage of the Yin and Yang FRET pairs (or any other novel FRET pair) is the substantial challenge associated with converting an optimized CFP-YFP FRET-based biosensor to an alternate FRET pair. As others have shown, the FRET response of a particular biosensor is critically dependent on the physical properties of the FPs [79]. Accordingly, switching to a different FRET pair, particularly one in which the FPs are derived from different species, may require the heavy task of biosensor optimization to be repeated. In the case of Yin and Yang, the necessary re-optimization effort is doubled. For these reasons, we suggest that the development and optimization of an effective OFP-RFP FRET pair is an important future direction, as it could be used in conjunction with previously optimized CFP-YFP biosensors.

2.4 Materials and methods

2.4.1 General methods

Synthetic DNA oligonucleotides were purchased from Integrated DNA Technologies (Coralville, IA). PCR products and products of restriction digestion were purified by gel electrophoresis and extracted using either the GeneJET gel extraction kit (Fermentas, ON) or the QIAquick gel extraction kit (QIAGEN, Valencia, CA). Plasmid DNA was purified using either the GeneJET Plasmid Miniprep Kit (Fermentas, ON) or the QIAprep Spin Miniprep kit (QIAGEN, Valencia, CA). Restriction endonucleases were purchased from either Invitrogen or New England Biolabs. Dye terminator cycle sequencing using the BigDye (Applied Biosystems) was used to confirm the complete cDNA sequences for all fusion constructs. Sequencing reactions were analyzed at the University of Alberta Molecular Biology Service Unit (MBSU). All filters for fluorescence screening and imaging were purchased from Chroma Technology (Rockingham, VT), Omega Filters (Brattleboro, VT), or Semrock (Rochester, NY).

2.4.2 Construction of Ca²⁺ biosensors (CaYang and CaYin)

We previously reported a version of yellow cameleon 3.3 (YC3.3) [88] in which CFP has been replaced with mTFP1 [55]. This mTFP1-YC3.3 (i.e., CaYang0.1) coding sequence is between the *XhoI* (5' end) and *EcoRI* (3' end) sites of pBAD/His B and contains a *SphI* site after mTFP1 (1-220; numbered as in Ref. [55]) and a *SacI* before Citrine (a YFP). Routine plasmid digestion and ligation with appropriately digested PCR product was used to replace Citrine with mCitrine [88] or cpVenus-173 [67]. Variants with the YC3.3 CaM/M13 portion replaced with the analogous portion from either YC4.3 or D1 were similarly constructed [150].

To generate CaYin0.1, a series of sequential digestions and ligations of the CaYang0.1 in pBAD/His B were performed. Specifically, mTFP1 was swapped with mAmetrine [19], the YC3.3-derived CaM/M13 portion was swapped with

the analogous portion of YC2.1 [10], and Citrine was swapped with tdTomato [49]. The domain organization of all CaYang and CaYin variants is provided in **Figure 2.2**. All constructs are credit to Dr. Huiwang Ai.

2.4.3 Optimization of Ca²⁺ biosensors by linker modification

To optimize the FRET efficiency change of CaYin0.9 (**Figure 2.2**), the length of the linkers between tdTomato and the D3 domain and between the D3 domain and mAmetrine1.2 were varied. The amino acid sequences of all linkers tested is provided in **Table 2.2**. Linkers were modified using a PCR procedure in which the cDNA encoding the D3 domain of CaYin0.9 was amplified with appropriately modified forward and reverse primers that contained a *SphI* site and a *SacI* site, respectively. PCR products were double digested and ligated (T4 ligase, Invitrogen) into a similarly digested pBAD/His B CaYin0.9 vector.

2.4.4 Protein purification and characterization

For production of protein, *E. coli* strain ElectroMAX™ DH10B (Invitrogen) was transformed by electroporation with a pBAD/His B expression vector containing the gene encoding the protein of interest. A single colony was used to inoculate a 4 mL culture that was grown overnight (37°C, 225 rpm) before being diluted into 0.5 L of LB medium supplemented with ampicillin. This culture was grown (37°C, 225 rpm) until it reached an OD of 0.6, induced by addition of 0.02% L-arabinose, and the cultured for 24 h at 28°C (FRET constructs) or 37°C (mAmetrine variants). Cells were harvested by centrifugation and lysed by cell disruptor (Constant Systems). All proteins were purified by Ni-NTA chromatography (Amersham) from the supernatant of the lysate and dialyzed into phosphate buffer saline (pH 7.4). FRET constructs were further purified by size exclusion column chromatography (Amersham Superdex 75 prep) in Tris-buffered saline (pH 7.4). Fluorescence measurements were recorded on a QuantaMaster spectrofluorometer (Photon Technology International) and

absorption measurements were recorded on a DU-800 UV-visible spectrophotometer (Beckman).

The fluorescence response of Ca^{2+} indicators was determined by mixing the FRET construct (300 nM) with an equal volume of 500 mM CaCl_2 or 200 μM EGTA in Tris-buffered saline (pH 7.4). To determine the K_d for Ca^{2+} , the fluorescence response of Ca^{2+} indicators was determined in buffers having free Ca^{2+} ranging from 0 μM to 1 mM. Protocol from 'Molecular Probes' calcium calibration buffer kits was used to make buffers with free Ca^{2+} ranging from 0 μM to 39 μM . Specifically, buffers were made by mixing of two solutions which are 10 mM K_2EGTA and 10 mM CaEGTA solutions containing 100 mM KCl and 30 mM MOPS, pH 7.2 in deionized water. Buffers with free Ca^{2+} above 100 μM were made from diluting 1 mM Ca^{2+} buffer.

2.4.5 Construction of mammalian expression vectors

A modified pcDNA3 vector was used for mammalian cell expression of FRET constructs. The modified pcDNA3 has a *XhoI* site (immediately preceded by a Kozak sequence) and *EcoRI* site in the same reading frame as the same sites in the pBAD/HisB vector. The CaYin1 and CaYang1 constructs in pBAD/HisB were treated with *XhoI* and *EcoRI*, and ligated with similarly treated pcDNA3. For targeting to the nucleus, three tandem copies of the nuclear localization sequence (NLS) DPKKKRKV were genetically fused to the C-terminus of the FRET construct. For targeting to the cytoplasm, a nuclear export sequence (NES) LALKLAGLDIGS was added to the C-terminus of the FRET construct.

2.4.6 General methods for live cell imaging.

All DNA for mammalian cell transfection was purified by Plasmid Midiprep kit (Qiagen). HeLa cells were cultured in DMEM (Invitrogen) supplemented with 10% FBS (Sigma) at 37°C. Cells in 35 mm imaging dishes were incubated with 1 ml DMEM (FBS free) for 30 min and then transfected with 2 μg plasmid DNA

(i.e., 1 μg of each plasmid for dual parameter imaging) that had been mixed with 2 μl Turbofect™ Protein Transfection Reagent (Fermentas) in 0.1 ml DMEM (FBS free). The culture media was changed back to DMEM with 10% FBS after 2.5 h incubation at 37°C. All imaging was conducted 24 to 36 h post-transfection with cells at room temperature in HEPES buffered Hanks' Balanced Salt Solution (HHBSS) with 25 mM HEPES, 2 g/L D-glucose, 490 μM MgCl_2 and 450 μM MgSO_4 , containing no phenol red or Ca^{2+} . Imaging was carried on an inverted Nikon Eclipse Ti microscope equipped with a 150 W Lumen 200 metal halide lamp (Prior Scientific) with a 25% neutral density filter, a 40 \times objective (NA = 0.95, air), and a 16-bit 512SC QuantEM CCD (Photometrics). Images were acquired at a frequency of 5-10 s and the exposure time was adjusted between 100-300 ms to obtain suitable intensities in each emission channel. The NIS-Elements AR 3.0 software package (Nikon) was used for automated computer control and for quantitative image analysis. Filters used for imaging are provided in **Table 2.3**.

2.4.7 Ca^{2+} imaging and induction of apoptosis

HeLa cells were treated as described above and then imaged for 2 min prior to addition of histamine (30 μM). The cells were then imaged for 15-20 min before the buffer was exchanged 3 \times with HHBSS and finally replaced with HHBSS containing 5 mM Ca^{2+} and 5 μM ionomycin. The cell were imaged 15 min before the buffer was once again exchanged and replaced with HHBSS containing 10 mM EGTA and 5 μM ionomycin. Imaging was then continued for another 15 min. To induce apoptosis, staurosporine was added into culture medium to the final concentration of 2 μM between 24 to 48 hours post-transfection. Cells were maintained in HHBSS and subjected to imaging with 1 min interval for 4-6 hours.

Chapter 3: Dimerization dependent fluorescent protein-based biosensors for imaging of caspase activity³

3.1 Introduction

While the strategies for using fluorescent proteins (FPs) as markers of gene expression, protein localization, and organelle structure are well-established, current methods for converting FPs into active biosensors of live cell biochemistry remain few in number and are technically challenging. The three most common methods for converting FPs into active biosensors include: Förster resonance energy transfer (FRET) between two different hues of FP [10,18]; engineering of a single FP to be responsive to an analyte of interest [63,65]; and bimolecular complementation of a split FP [99,101]. Over the last decade, each of these methods has been exploited in a variety of applications that have led to numerous important biological insights. However, taken as a group, these methods do suffer from a few shortcomings. For example, FRET-based biosensors tend to have relatively small fluorescent responses and are challenging to implement with multiple fluorescent probes; single FP approaches have proven difficult to generalize beyond calcium ion (Ca^{2+}) biosensors; and the irreversible nature of FP complementation has limited this approach to the detection of protein-protein interactions. The recently introduced dimerization-dependent

³ The research involving the imaging of caspase-3 activity via ddRFP and ddGFP described in this chapter has been published in Alford, S.C., et al. 2012 *Chem. Biol.* **19**, 353-360 and Alford, S.C. et al. 2012 *ACS Synth. Biol.* **1**, 569-575. Another paper describing the color switch biosensors has been submitted. Constructs of red, green and yellow caspase-3 biosensors (described in Section 3.2.1-3.2.3) and the tandem dual caspase biosensor (described in Figure 3.12) are credit to Dr. Spencer Alford. Experiments related to monitoring caspase-3 activation in neurons (described in Section 3.2.7) are credit to Jiao Li, from Dr. Yan Zhang's group. All live imaging experiments in HeLa cells and the construction of the translocation- and colour switching-based biosensors are performed by me.

fluorescent protein (ddFP) technology as a versatile method could potentially address some of these issues and provide new opportunities for the construction of biosensors of live cell applications [60,61].

A ddFP is a pair of quenched or non-fluorescent FP monomers that can associate to form a fluorescent heterodimer (**Figure 3.1**) [60,61]. One of the dark monomers (copy A) contains a fully formed chromophore that is quenched in the monomeric state. The second dark monomer (copy B) does not form a chromophore itself and only acts to substantially increase the fluorescence of copy A upon formation of the AB heterodimer. In the green and red fluorescent versions of ddFP the A copy is referred to as GA and RA, respectively. We previously reported different variants of B optimized to pair with either GA or RA. However, we later discovered that different versions of B can interchangeably complement both GA and RA (**Figure 3.1**).

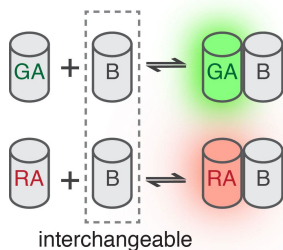


Figure 3.1 Schematic of reversibly associated ddFPs.

Traditionally, caspase-3 biosensors have relied on FRET from a donor FP to an acceptor FP that are linked by a peptide containing the substrate sequence [14,18,19]. Following cleavage the free acceptor diffuses away from the donor, resulting in a decrease in energy transfer efficiency and a ratiometric change in fluorescence emission. We hypothesized that ddFP-based biosensors could be used as an alternative to FRET-based biosensors. Advantages of ddFP-based caspase sensors could be larger intensimetric changes and a wider selection of colour choices. A potential advantage of FRET-based biosensors relative to their ddFP-based counterparts is that their ratiometric, as opposed to intensimetric, change in fluorescence emission is more amenable to quantitative analysis.

In the present work, we demonstrate the construction of caspase-3 biosensors based on a linker containing the substrate sequence Asp-Glu-Val-Asp (DEVD) [18] and green, red and yellow ddFPs [60,61]. For these biosensors, protease activity is indicated by the intensimetric loss of the initially bright fluorescence due to cleavage of the linker and dissociation of the AB heterodimer (**Figure 3.2**). We have also expanded the utility and versatility of ddFP-based protease sensors by exploiting protein translocation and the fact that the same B copy can be used to complement either GA or RA. These tactics have enabled us monitor caspase-3 activity in single cells with dramatic green-to-red and red-to-green colour switches and translocation from the cytoplasm to the nucleus. Beyond detection of a single caspase, we further achieved the simultaneous detection of both caspase-3 and caspase-8 with coexpression of two ddFP-based biosensors or a single biosensor containing two substrate and three ddFP domains. Finally, we applied a ddFP caspase biosensor to investigate the differences between two pathways of caspase-3 activation in neurons: canonical apoptosis and non-apoptotic neurite pruning.

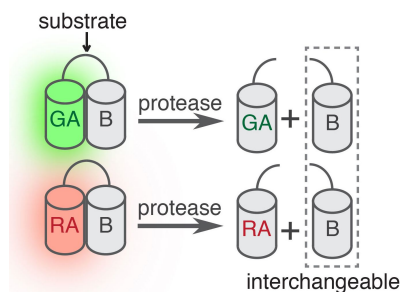


Figure 3.2 General design of ddFP-based protease biosensors.

3.2 Results and discussion

3.2.1 Protease activity monitored by a red ddFP (ddRFP)-based caspase-3 biosensor

For our initial attempt at using a ddFP for sensing protease activity, we proposed a strategy in which RA and B were fused in tandem with the well-characterized caspase-3 substrate sequence (DEVD) in the linker region.

Accordingly, this construct was designated as RA-DEVD-B. To monitor induced caspase-3 activation in live mammalian cells, HeLa cells were transfected with a plasmid encoding RA-DEVD-B, treated with either staurosporine or tumor necrosis factor- α (TNF- α) [154], and imaged through time. As shown in the schematic of **Figure 3.3A**, cleavage of the substrate sequence during apoptosis resulted in a loss of fluorescence after the disassociation of B. We reliably observed a decrease in red fluorescence intensity (dynamic range of 8.6 ± 4.3 ; N = 9), just prior to the cell shrinkage and blebbing associated with the end stages of apoptosis [155] (**Figure 3.3B**).

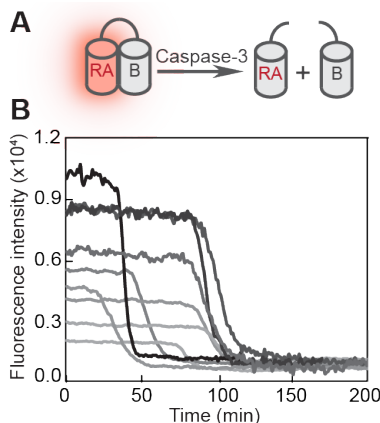


Figure 3.3 Imaging of caspase-3 activity with a ddRFPs.

(A) Schematic illustration of a ddRFP-based caspase-3 biosensor. (B) Transfected HeLa cells were treated with TNF- α ($t = 0$) to initiate apoptosis, and red fluorescence was imaged as a function of time.

The rate of the transition from the bright to dim state was comparable to the rate previously observed for a FRET-based biosensor of caspase-3 activity [14,19], indicating that heterodimer association and dissociation is not a rate limiting step on the relatively slow timescale (minutes) of this experiment. Overall, these results confirm that the affinity of RA and B is sufficiently low to allow protease detection and imply that the tandem heterodimer is sufficiently bright for imaging at intracellular concentrations well below its K_d of $33 \mu\text{M}$ [60].

3.2.2 Concurrently monitoring Ca²⁺ flux and caspase-3 via a Ca²⁺ biosensor and a ddRFP-based caspase-3 biosensor

As mentioned previously, intensimetric biosensors are preferred in multiparameter imaging, since they occupy narrower space in the limited visible wavelengths when compared to ratiometric biosensors. In Chapter 2, we discussed the multiparameter imaging of Ca²⁺ flux and caspase-3 with two spectrally distinct FRET pairs [14]. Here, we demonstrate a similar multiparameter imaging performed by a newly developed Ca²⁺ biosensor (G-GECO1) [106] together with the ddRFP-based caspase-3 biosensor. The Ca²⁺ biosensor, G-GECO1, reports Ca²⁺ fluctuation via the change of green fluorescence intensity. The key feature of Ca²⁺ sensing relies on the Ca²⁺ sensitive domains, calmodulin (CaM) and M13, whose conformational change due to the binding of Ca²⁺, can shield the chromophore from solvent and increase the green fluorescence intensity (**Figure 3.4A**).

Both the ddRFP caspase-3 biosensor and G-GECO1 were coexpressed in HeLa cells and fluorescence intensity in the green and red emission channels was monitored over time after treatment with apoptosis inducer. Since Ca²⁺ flux and caspase activation are known to be associated with cell apoptosis [156,157], we expected to detect change from both biosensors after the treatment of apoptosis inducers, staurosporine or TNF- α . As shown in **Figure 3.4B**, green spikes represented the sudden change of Ca²⁺ concentration in cytosol occurring during apoptosis. The loss of red fluorescence signal in **Figure 3.4B** indicated the cleavage of substrate sequence by caspase-3 that was activated during apoptosis. Although our observation was similar to our observations with FRET-based biosensors as discussed in Chapter 2, apoptotic Ca²⁺ flux has not been well studied and its infrequent occurrences could be at seemingly anytime after treatment with inducer. Overall, we successfully observed occasional Ca²⁺ flux and the activation of caspase-3 during induced apoptosis via the usage of G-GECO1 and ddRFP-based caspase-3 biosensor.

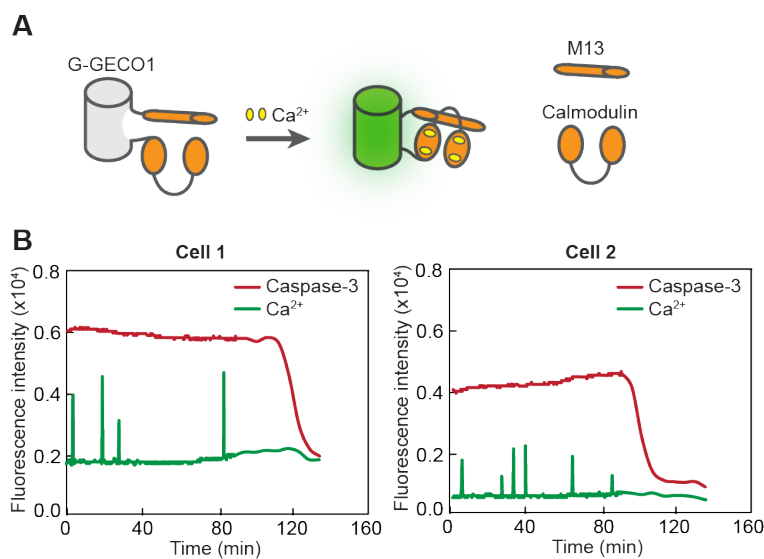


Figure 3.4 Imaging of Ca^{2+} concentration and caspase-3 activity. (A) Schematic of Ca^{2+} biosensor G-GECO1. (B) Intensity vs. time for Ca^{2+} concentration and caspase-3 activity. X-axis is time elapsed after cells were treated with staurosporine to induce apoptosis.

3.2.3 Protease activity monitored by a green ddFP (ddGFP)- or a yellow ddFP (ddYFP)-based caspase-3 biosensor

To construct a green ddFP-based caspase-3 biosensor, we introduced the caspase-3 substrate sequence into the linker joining the ddGFP partners. Expression of this construct in mammalian cells revealed 3.6 ± 1.0 -fold ($N = 39$) and 2.8 ± 0.6 -fold ($N = 10$) decrease in fluorescence following caspase-3 mediated cleavage (**Figure 3.5A,B**). The observed loss of fluorescence signal upon cleavage was reduced relative to the ~ 20 -fold contrast observed *in vitro* via trypsinolysis [61]. We speculate the concentration of monomers following cleavage is sufficient to cause noncovalent dimerization ($K_d = 9 \mu\text{M}$), and thus the observed contrast is decreased. Similar results were obtained for expression of the yellow fluorescent ddYFP-based caspase-3 biosensor (**Figure 3.5C,D**).

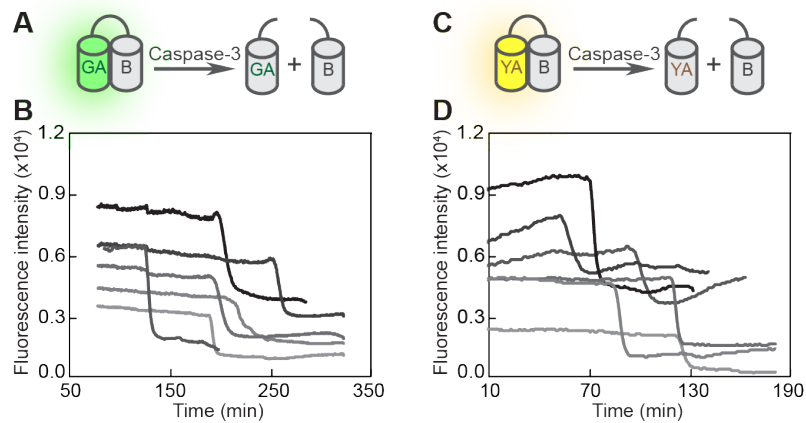


Figure 3.5 Imaging of caspase-3 activity with a ddGFPs.

Schematic illustration of a caspase-3 biosensor based on ddGFP (A) or ddYFP (C). HeLa cells, expressing a ddGFP (B) or a ddYFP (D)-based caspase-3 biosensor, were treated with TNF- α ($t = 0$) to initiate apoptosis, and green fluorescence was monitored as a function of time.

3.2.4 Engineering a single colour translocation-based biosensor

To convert the intensimetric ddFP-based caspase biosensors described above into a single colour translocation-based biosensor, we aimed to construct a system whereby cleavage of a cytoplasmic ddFP caspase indicator (A-DEVD-B) would result in a loss of fluorescence and allow untethered copy A to translocate to the nucleus while copy B is retained in the cytoplasm. A second copy B targeted to the nucleus would then complement the translocated copy A, resulting in an increase in nuclear fluorescence. To confer the translocation feature, we exploited a naturally occurring nuclear localization sequence (NLS) [158] and a nuclear export signal (NES) [159].

In our initial design, we constructed a green fluorescent tandem heterodimer (GA^{NLS} -DEVD- B^{NES}) in which GA plus an NLS (GA^{NLS}) is linked via a DEVD substrate sequence to a fusion of B plus an NES (B^{NES}) (**Figure 3.6A**). When expressed alone, GA^{NLS} -DEVD- B^{NES} was located in both the cytoplasm and nucleus at low expression levels and located primarily in the nucleus at high expression levels. However, when this construct was co-expressed with B^{NLS} ,

GA^{NLS} -DEVD- B^{NES} was distributed mainly in the cytoplasm, likely due to increased competition for binding to importins [160].

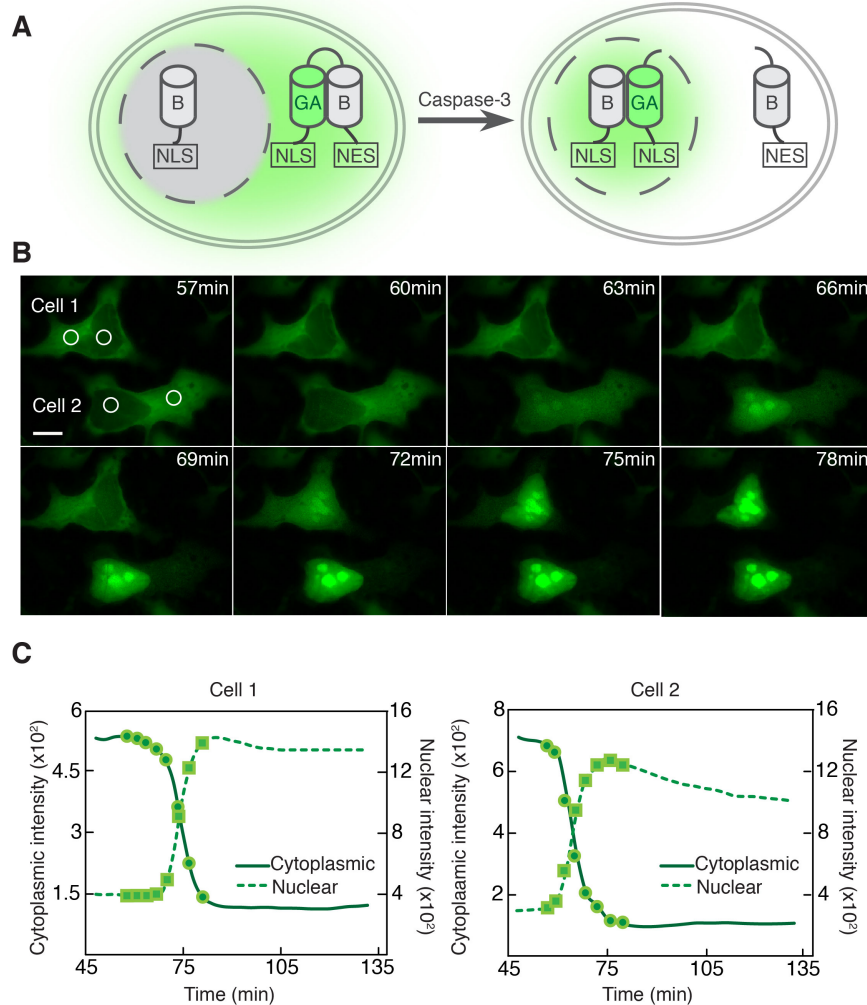


Figure 3.6 Biosensors based on translocation of fluorogenic ddGFP partner.

(A) Schematic illustration of monitoring caspase-3 activity with translocation of the fluorogenic GA partner. (B) Selected frames from imaging of HeLa cells co-expressing GA^{NLS} -DEVD- B^{NES} and B^{NLS} while undergoing staurosporine-induced apoptosis. Scale bar represents 10 μ m. Images were collected from Axiovert 200M (Zeiss) with 40x objective lens (NA = 1.3, oil). (C) Intensity vs. time for the cytoplasmic and nuclear ROIs indicated in B with markers to indicate the time points for the images. X-axis is time elapsed from 1 h after cells were treated with staurosporine.

In cells where GA^{NLS} -DEVD- B^{NES} and B^{NLS} were co-expressed, activation of caspase-3 during staurosporine-induced apoptosis was associated with a loss of

green fluorescence in the cytoplasm and a concurrent increase in green fluorescence in the nucleus (**Figure 3.6B**). As illustrated in **Figure 3.6C**, the cytoplasmic intensity decreased approximately 4-fold and the nuclear intensity increased approximately 3-fold. Subsequent apoptosis-associated fragmentation of the nucleus led to a decrease in the green fluorescence intensity in the nucleus. Similar results were obtained for co-expression of the red fluorescent RA^{NLS}-DEVD-B^{NES} and B^{NLS} (**Figure 3.7A,B**).

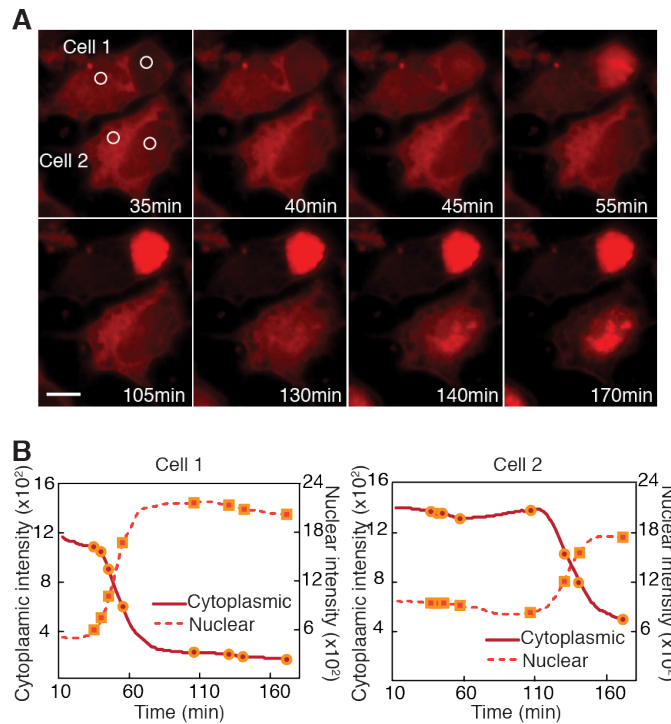


Figure 3.7 Biosensors based on translocation of fluorogenic ddrFP partner. (A) Selected frames from imaging of HeLa cells co-expressing RA^{NLS}-DEVD-B^{NES} and B^{NLS} while undergoing staurosporine-induced apoptosis. Scale bar represents 10 μ m. Images were collected from Axiovert 200M (Zeiss) with 40x objective lens (NA = 1.3, oil). (B) Intensity vs. time for the cytoplasmic and nuclear ROIs indicated in A with markers to indicate the time points for the images. X-axis is time elapsed from 1 h after cells were treated with staurosporine.

Attempts to perform an analogous fluorogenic translocation from the nucleus to the cytoplasm were not successful. Transfection of cells with either GA^{NES}-DEVD-B^{NLS} or RA^{NES}-DEVD-B^{NLS}, either with or without co-transfection

with B^{NES}, led to a primarily nuclear localization of fluorescence. Activation of caspase-3 was associated with a decrease of both nuclear fluorescence and the already dim cytoplasmic fluorescence (**Figure 3.8A-D**).

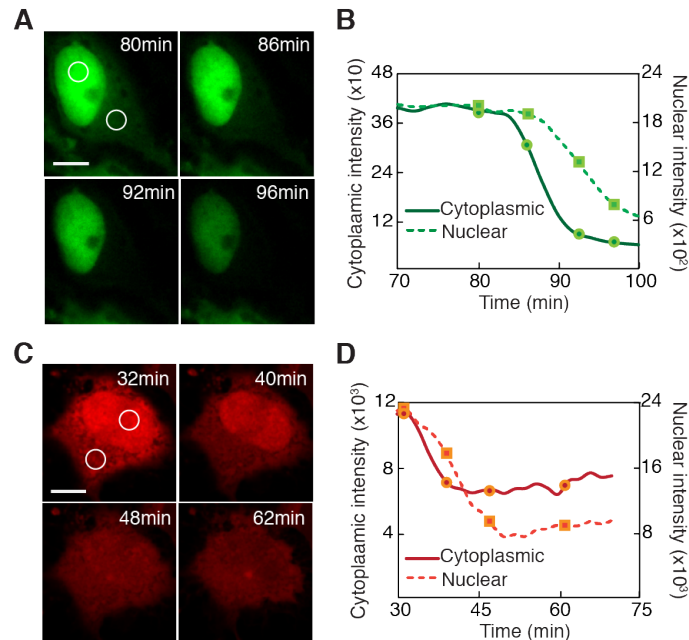


Figure 3.8 Attempted caspase-dependent ddFP translocation from the nucleus to the cytoplasm.

(A) Selected frames from imaging of HeLa cells expressing GA^{NES}-DEVD-B^{NLS} and B^{NES} during staurosporine-induced apoptosis. (B) Intensity vs. time for the ROIs shown in A. (C) Selected frames from imaging of HeLa cells expressing RA^{NES}-DEVD-B^{NLS} and B^{NES} and undergoing staurosporine-induced apoptosis. Images were collected from Axiovert 200M (Zeiss) with 40x objective lens (NA = 1.3, oil). (D) Intensity vs. time for ROIs shown in C. X-axis is time elapsed from 1 h after cells were treated with staurosporine.

The result indicates that A^{NES} (G or R) either cannot be exported from the nucleus following caspase-3 cleavage of the tandem ddFP, or that it can be exported but the heterodimer does not form. We currently favor the latter explanation, since the larger volume of the cytoplasm relative to the nucleus could dilute the A copy to a concentration well below the K_d of the heterodimer (GA-B and RA-B have K_d s of $\sim 9 \mu\text{M}$ and $\sim 30 \mu\text{M}$, respectively) [61]. However we cannot rule out the possibility that delayed activation of caspase-3 in the nucleus

relative to the cytoplasm [19] is associated with a critical compromise in the integrity of the nuclear pore complex that prevents nuclear export [161-163].

3.2.5 Engineering a colour switch and translocation-based biosensor

Given our successful design of a single colour translocation-based biosensor, we next attempted to engineer a translocation-based biosensor exhibiting a colour switch. To accomplish both colour switch and translocation, we designed an alternative system in which cleavage of a cytoplasmic ddFP-based caspase indicator (A-DEVD-B) would result in a loss of the full length biosensor fluorescence, permitting free copy B to translocate into the nucleus while copy A is retained in the cytoplasm. To illustrate how this could result in a colour switch, a nuclear-localized GA could complement a translocated red B partner (freed from RA by caspase cleavage), resulting in an increase in green fluorescence in the nucleus.

Initially, we constructed a red fluorescent tandem heterodimer (RA^{NES}-DEVD-B^{NLS}) in which RA plus an NES (RA^{NES}) was linked via the DEVD substrate to B plus an NLS (B^{NLS}) (**Figure 3.9A**). When co-expressed with another nuclear-localized protein (GA^{NLS}), RA^{NES}-DEVD-B^{NLS} was mainly distributed in cytoplasm, as shown as red fluorescence signal (**Figure 3.9B**). Relative weak green fluorescence signal was detected in nucleus, likely from quenched GA^{NLS} alone. In cells co-expressing RA^{NES}-DEVD-B^{NLS} and GA^{NLS}, activation of caspase-3 during staurosporine-induced apoptosis triggered a loss of red fluorescence in the cytoplasm and a concurrent increase in green fluorescence in the nucleus (**Figure 3.9B**). As illustrated in **Figure 3.9C**, the cytoplasmic red intensity decreased approximately 3-fold and the nuclear green intensity increased approximately 7-fold.

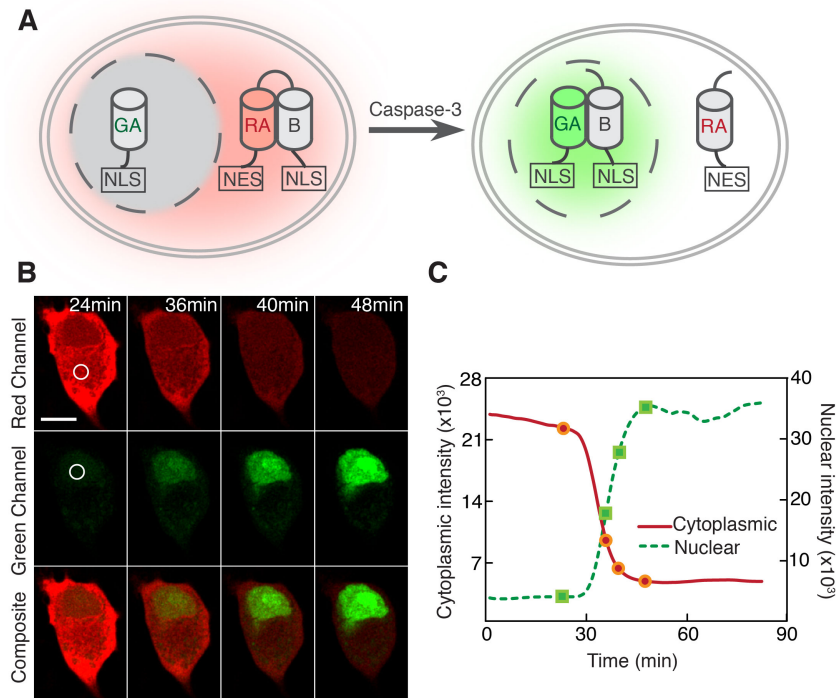


Figure 3.9 Red to green colour-switching biosensors based on translocation of the dark ddFP partner.

(A) Schematic illustration of a colour switching translocation-based biosensor. (B) Selected frames from two-colour imaging of staurosporine-treated HeLa cell co-expressing RA^{NES} -DEVD- B^{NLS} and GA^{NLS} . Scale bar represents 10 μ m. Images were collected from LSM-700 (Zeiss) with 63x objective lens (NA=1.40, oil). (C) Intensity vs. time for the cytoplasmic and nuclear ROIs indicated in B with markers to indicate the time points for the images. X-axis is time elapsed one hour after cells were treated with staurosporine to induce apoptosis.

Similar results were obtained in HeLa cells co-expressing the green fluorescent tandem heterodimer (GA^{NLS} -DEVD- B^{NES}) and nucleus targeted RA^{NLS} , in which a 8-fold decrease in cytoplasmic green intensity and a 3-fold increase in nuclear red intensity were observed after caspase-3 cleavage (**Figure 3.10**).

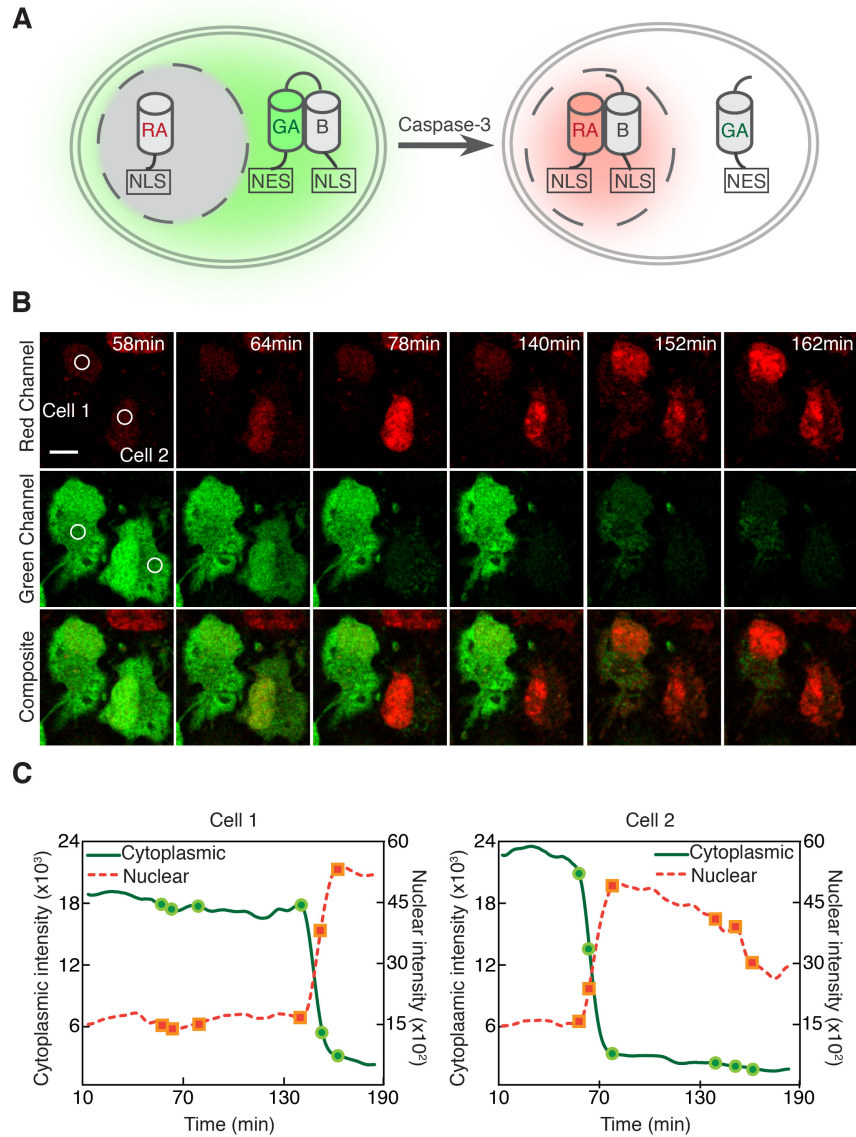


Figure 3.10 Green to red colour-switching biosensors based on translocation of the dark ddFP partner.

(A) Schematic of colour switching translocation-based biosensor. (B) Selected frames from imaging of staurosporine-treated HeLa cells co-expressing GA^{NES}-DEVD-B^{NLS} and RA^{NLS}. Scale bar represents 10 μm . Images were collected from LSM-700 (Zeiss) with 63x objective lens (NA=1.40, oil). (C) Intensity vs. time for the cytoplasmic and nuclear ROIs indicated in B with markers to indicate the time points for the images. X-axis is time elapsed one hour after cells were treated with staurosporine to induce apoptosis.

3.2.6 Detection of both caspase-8 and caspase-3 in single cells

We next investigated the ability of translocation-based biosensors to detect the activity of different caspases in live cells. To achieve detection of caspase-8, we constructed a red translocation-based caspase-8 indicator (RA^{NLS} -IETD- B^{NES}) by using caspase-8 substrate sequence (IETD) to replace the caspase-3 DEVD substrate from RA^{NLS} -DEVD- B^{NES} [154]. To accomplish concurrent monitoring of both caspase-3 and 8, we carried out a 3-plasmid co-transfection of green caspase-3 indicator (GA^{NLS} -DEVD- B^{NES}), red caspase-8 indicator (RA^{NLS} -IETD- B^{NES}) and nucleus targeted BNLS (**Figure 3.11A**). In transfected live cells, both green and red fluorescent signals were observed with primarily cytoplasmic distribution, as shown in **Figure 3B**. Cleavage of caspase-3 or caspase-8 led to a decreased cytoplasmic signal and increased nuclear signal in green or red fluorescence, respectively (**Figure 3.11B,C**). Consistent with reported data [26], we observed an extensive amount of caspase-8 and 3 activity after induction of apoptosis. A similar result was achieved for co-detection of caspase-3 and caspase-9, in which a caspase-9 substrate sequence (LEHD) [98] replaced DEVD from RA^{NLS} -DEVD- B^{NES} to create a red caspase-9 biosensor (**Figure 3.11D**).

Inspired by previous efforts to detect two cellular activities with a single polypeptide FRET-based biosensor (i.e., containing 3 FPs linked by two functional domains) [26,97,147], we constructed an analogous ddFP-based biosensor for simultaneous detection of caspase-3 and caspase-8 activity. This biosensor was a tandem heterotrimer (RA^{NES} -IETD-B-DEVD-GA) in which RA with an NES is linked via an IETD caspase-8 substrate to the B copy, which is in turn linked to GA via a DEVD caspase-3 substrate (**Figure 3.12A**). Consistent with our expectation that both RA and GA would compete for formation of a fluorescent heterodimer with copy B, cells expressing RA^{NES} -IETD-B-DEVD-GA exhibited both green and red cytoplasmic fluorescence (**Figure 3.12B**).

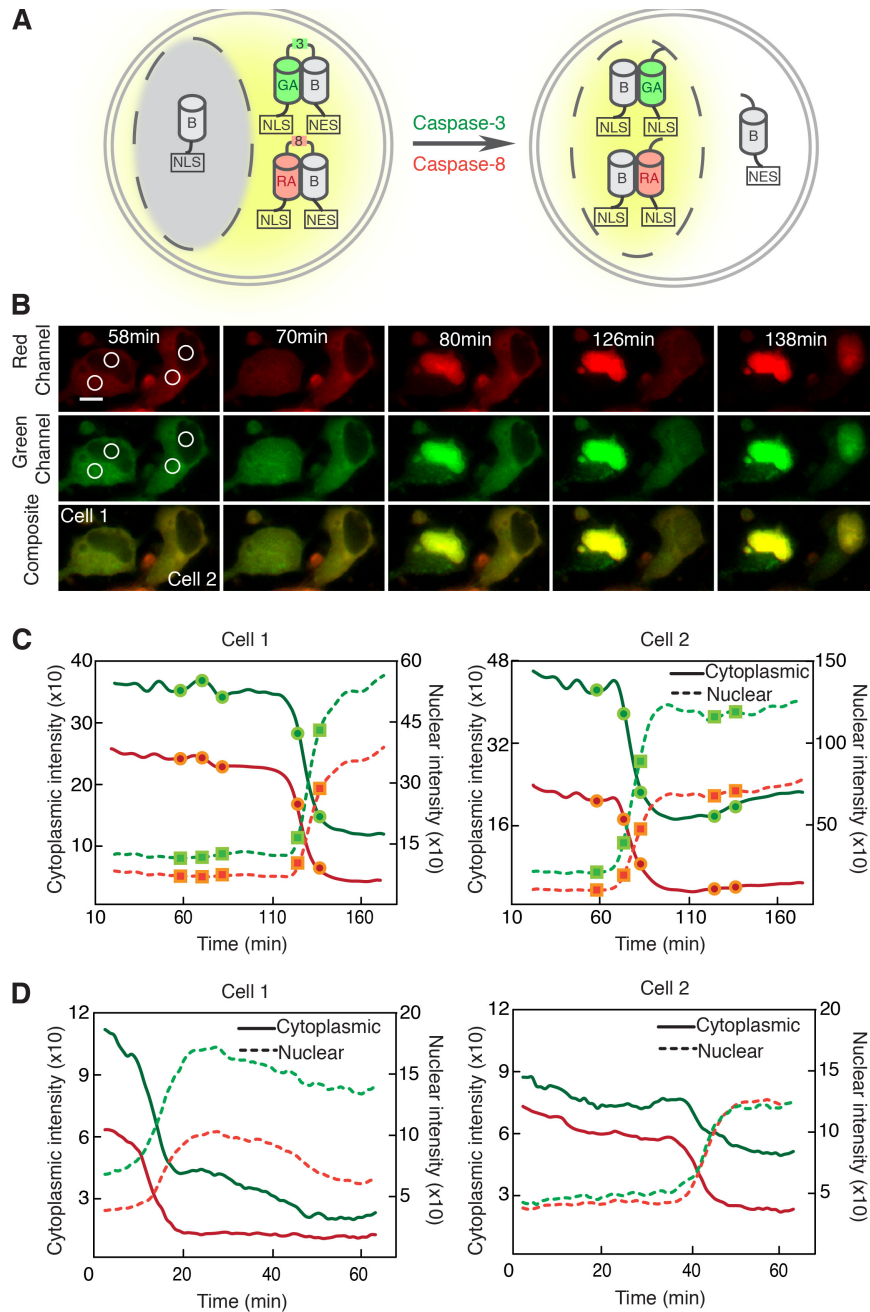


Figure 3.11 Concurrent monitoring caspase-3 and caspase-8 activity
 (A) Schematic of translocation-based caspase-3 and caspase-8 biosensors. (B) Selected frames from imaging of staurosporine-treated HeLa cells co-expressing red caspase-8 sensor (RA^{NLS} -IETD- B^{NES}), green caspase-3 sensor (GA^{NLS} -DEVD- B^{NES}) and B^{NLS} . Scale bar represents 10 μ m. Images were collected from Axiovert 200M (Zeiss) with 40x objective lens (NA = 1.3, oil). (C) Intensity vs. time for the cytoplasmic and nuclear ROIs indicated in B. (D) Intensity vs. time of concurrently imaging of HeLa cells were co-expressing a green caspase-3 and a red caspase-9 biosensor.

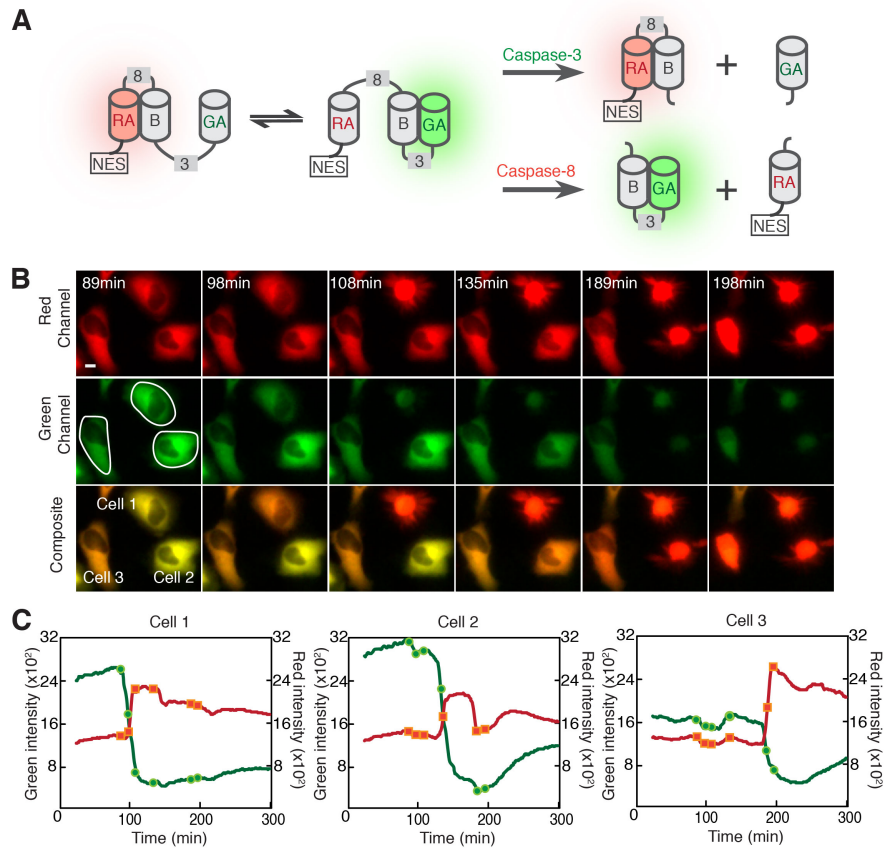


Figure 3.12 Concurrent monitoring of two caspase activities with a two-colour single polypeptide biosensor.

(A) Schematic representation of the single polypeptide ddFP-based biosensor for both caspase-3 and caspase-8. (B) Selected frames from imaging of HeLa cells expressing RA^{NES}-IETD-B-DEVD-GA and undergoing SIA. Scale bar represents 10 μm . (C) Intensity vs. time of green and red fluorescence. X-axis represents time elapsed from 1 h after cells were treated with staurosporine. Time points corresponding to the frames of green and red channel in b are represented as circles and squares, respectively.

We further expected that caspase-3 catalyzed release of GA or caspase-8 catalyzed release of RA, would lead to an increase in red fluorescence (and loss of green) or increase in green fluorescence (loss of red), respectively, due to decreased competition for binding to B. Accordingly, such an implementation should enable the order of caspase activation to be determined with greater confidence than the dual reporter construct strategy described above. Imaging of transfected cells undergoing staurosporine-induced apoptosis revealed that the eventual process of caspase activation was associated with a rapid increase of red

and loss of green fluorescence (**Figure 3.12C**), which suggests that caspase-3 activation might occur prior to caspase-8 activation or caspase-3 cleaves its substrate more effectively. Following the initial rapid change, red fluorescence was observed to decrease and green fluorescence to increase, likely due the ongoing release of RA through the action of caspase-8, which frees up more of the B copy to bind to previously released GA.

Caspase-8 and caspase-3 have well-established roles as initiator and effector caspases, respectively, for Fas-induced apoptosis [164]. In contrast, inhibitors of caspase-8 do not prevent staurosporine-induced apoptosis [165,166], and cleavage of procaspase-8 occurs after caspase-3 activation [165], indicating that staurosporine-induced apoptosis is independent of caspase-8. The caspase-8 activation we observed using two colours of our ddFP translocation biosensor (**Figure 3.11**) is most likely attributable to the previously reported feedback loop between caspase-3 and caspase-8 [26]. The unique feature of the tandem heterotrimer strategy for probing multiple protease activities is that it provides a simple and robust green-to-red or red-to-green colour switch depending upon which protease is activated first. This feature distinguishes this approach from alternative heterotrimeric FRET strategies where cleavage of one of the two substrates leads to more complex and typically subtle spectral changes.

3.2.7 Detection of caspase-3 activation during neuritic pruning

The successful detection of caspase-3 activity with translocation-based biosensors illustrated that our design was suitable for detecting apoptotic caspase activities. To further explore the suitability of these tools for detection of caspase-3 in non-apoptotic roles, we investigated the process of caspase-3-triggered neuritic pruning of cultured rat hippocampal neurons [167-169].

To detect caspase-3 activation after the onset of neuritic pruning, we utilized the green-to-red colour switching translocation-based caspase-3 biosensor. In rat hippocampal neurons, we co-expressed GA^{NES} -DEVD-B^{NLS} and RA^{NLS}, as illustrated in **Figure 3.10**.

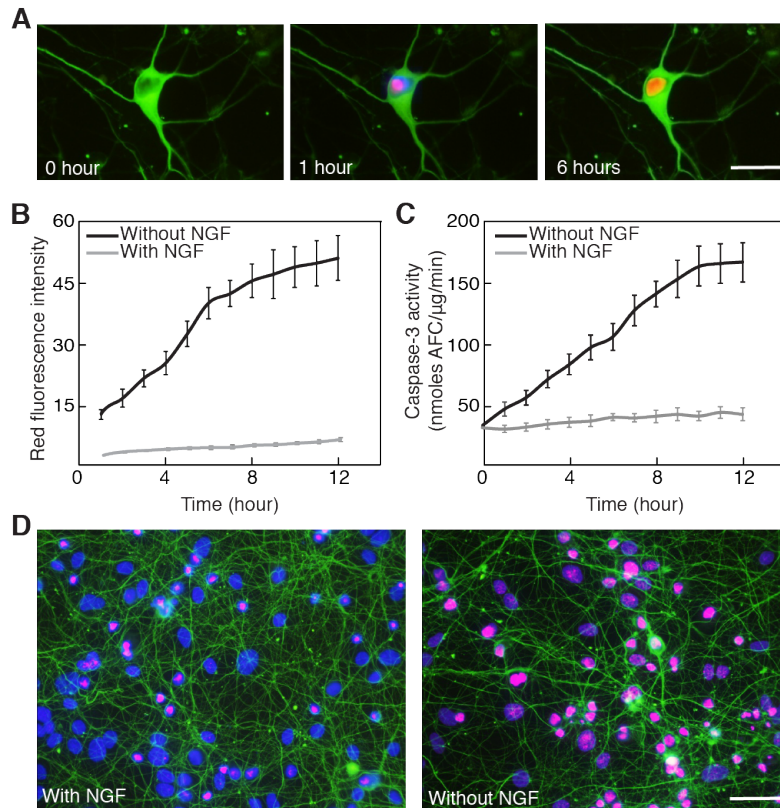


Figure 3.13 Monitoring caspase-3 activity associated with neurite pruning. (A) Composite fluorescence images of a Hoechst (blue) stained neuron co-expressing GA^{NES}-DEVD-B^{NLS} and RA^{NLS} during NGF deprivation. Scale bar represents 20 μm . (B) Nuclear red fluorescence intensity vs. time for neurons cultured with and without NGF ($p < 0.01$). Error bars represent mean \pm SE. The diminished rate of increase from ~ 6 h (relative to *in vitro* measured caspase-3 activity as shown in C) is attributed to depletion of free RA^{NLS}. (C) *In vitro* measured caspase-3 activity vs. time for neurons cultured with and without NGF ($p < 0.01$). Error bars represent mean \pm SE. (D) Images of neurons cultured with or without NGF for 24 h. Scale bar represents 50 μm . The data is credit to Jiao Li from Dr. Yan Zhang's group.

Prior to stimulating neuritic pruning, green fluorescence was detected in both the cytoplasm and nucleus (Figure 3.13A). To trigger neuritic pruning, nerve growth factor (NGF) was depleted from the culture medium [168,169]. During the early stage of non-apoptotic neuritic pruning, the morphology of neurites remained unchanged, but the activation of caspase-3 was visualized as the accumulation of red fluorescence in the nucleus with time (Figure 3.13A). The increase in red fluorescence (Figure 3.13B) was correlated with the caspase-3

activity measured for cell extracts *in vitro* (Figure 3.13C). Following 24 h of NGF deprivation, neurons exhibited substantially fewer neurites relative to control, and much brighter red fluorescence in the nucleus relative to control (Figure 3.13D).

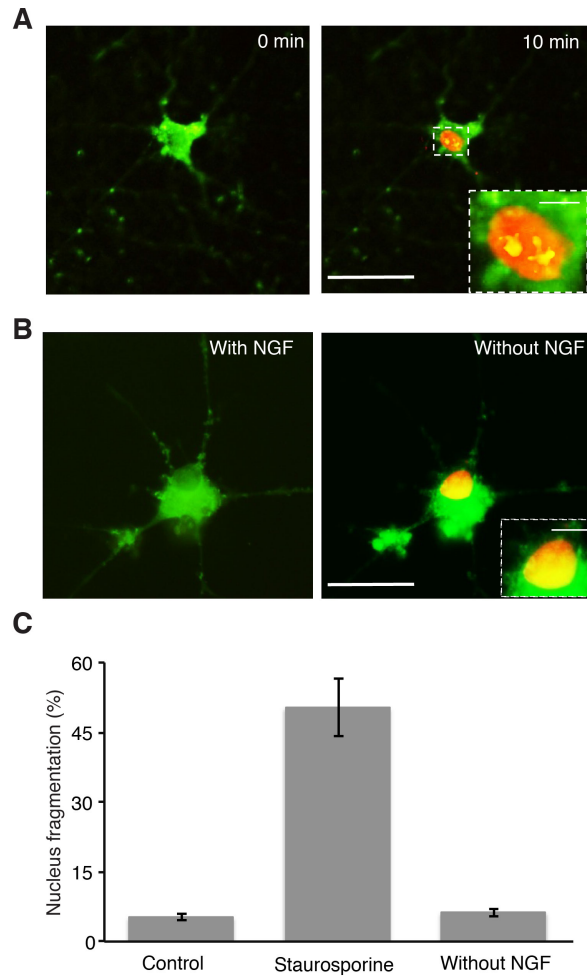


Figure 3.14 Nuclear fragmentation and caspase-3 activation in apoptotic and NGF-deprived neurons.

(A) Composite images of a neuron during staurosporine-induced apoptosis. Scale bar represents 20 μm . Inset: Zoom-in showing nucleus fragmentation. Scale bar represents 2 μm . (B) Images of a neuron before and after 24 h of NGF deprivation. Scale bar represents 10 μm . Inset: Zoom-in showing preserved nucleus integrity. Scale bar represents 2 μm . (C) Quantification of the nucleus fragmentation during apoptosis vs. NGF deprivation. The data is credit to Jiao Li from Dr. Yan Zhang's group.

To compare non-apoptotic and apoptotic caspase-3 activity in neurons, caspase-3 activation during neuronal apoptosis was monitored following staurosporine treatment [170]. Consistent with the observation of non-apoptotic caspase-3 activation during neuritic pruning, red fluorescence was detected in the nucleus after caspase-3 activation upon triggering neuronal apoptosis. Furthermore, punctate red fluorescence was only observed in neurons treated with staurosporine, which represented the apoptotic fragmentation of the nucleus (**Figure 3.14A** inset). In contrast, when caspase-3 was activated during induced neuritic pruning, the nucleus retained its integrity, exhibiting a prototypic elliptical shape (**Figure 3.14B** inset). Quantification of fluorescence confirmed that nucleus fragmentation was more prevalent in cells treated with staurosporine than those cells deprived of NGF to induce neuritic pruning (**Figure 3.14C**).

3.3 Conclusions

In this chapter, we have described the development and applications of ddFP-based protease biosensors that can be used to monitor protease activity in live cells. We demonstrated that the ddRFP-based protease biosensor, paired with one of the previously reported green Ca^{2+} biosensor [106], enables intensimetric imaging of both Ca^{2+} and caspase-3 activity concurrently in single cells. With the development of the translocation-based protease biosensors, we successfully reported dual caspase activity concurrently via translocation of fluorescence signal from cytoplasm to nucleus in single cells. Furthermore, the newly developed colour switching translocation-based protease biosensors enable reporting both apoptotic and non-apoptotic protease activity in neurons through two readouts, which are translocation from cytoplasm to nucleus and colour switching between red and green. In summary, ddFPs are a versatile biosensing platform technology that is particularly useful for monitoring of intracellular protease activities when the partner-swapping feature of the ddFPs is used in either a colour switching or competitive modality.

3.4 Materials and methods

3.4.1 General methods and materials

All synthetic DNA oligonucleotides were purchased from Integrated DNA Technologies (Coralville, IA). Pfu polymerase (Fermentas; Pittsburgh, PA) was used for standard PCR. PCR products and products of restriction digests were purified by gel electrophoresis and extracted by spin column (GeneJET gel extraction kit; Fermentas) according to the manufacturer's protocols. Restriction enzymes were purchased from New England Biolabs or Fermentas. The cDNA sequences were confirmed by dye terminator cycle sequencing using the BigDye Terminator v3.1 Cycle Sequencing Kit (Applied Biosystems - Invitrogen; Grand Island, NY). Sequencing reactions were resolved at the University of Alberta Molecular Biology Service Unit.

3.4.2 Construction of the ddFP caspase biosensor

The gene sequence encoding the nuclear exclusion sequence (LALKLAGLDIGS) [159] or a triplicate copy of the nuclear localization sequence (DPKKKRKVDPKKKRKVDPKKKRKV) [158] was appended to either the 5' or 3' end of the ddFP gene. ddFP fusions containing NES or NLS were PCR amplified with primers containing 5' *XhoI* site and a 3' *KpnI* site. The gene sequences encoding ddFP^{NES} and ddFP^{NLS} were also PCR amplified with a 5' primer that appended a *KpnI* site followed by a sequence encoding 'HSTHSHSSHTASHDEVDGA', and a 3' primer with a *HindIII* site. These DEVD containing fusions were oriented at the C-terminus of tandem ddFP. The tandem ddFP construct was built by ligating *XhoI/KpnI* digested fusions with *KpnI/HindIII* digested DEVD containing fusions into pcDNA3.1(+)(Invitrogen) through three-part ligation. Tandem ddFP of caspase-8 and caspase-9 biosensors were constructed in the same manner, except the DEVD sequence was replaced by IETD and LEHD sequence, respectively. To construct ddFP monomer fusions, genes of ddFP^{NES} or ddFP^{NLS} were amplified by primers encoding 5' *XhoI* site

and 3' *HindIII* site. *XhoI/HindIII* digested fusions were then ligated into pcDNA3.1(+). The general cloning details for each construct is outlined in **Table 3.1**.

3.4.3 HeLa cell culture and imaging

HeLa cells were maintained in Dulbecco's Modified Eagle Medium (DMEM) supplemented with 10% fetal bovine serum and Glutamax (Invitrogen) at 37°C and 5% CO₂. Transient transfections of pcDNA3.1 (+) expression plasmids were performed using Turbofect (Thermoscientific). HeLa cells in 35 mm imaging dishes were incubated with 1 mL of DMEM (FBS free) for 10 min and then transfected with 1 µg of plasmid DNA that had been mixed with 2 µL of Turbofect (Fermentas) in 0.1 mL of DMEM (FBS free). The culture media was changed back to DMEM with 10% FBS after 2 h incubation at 37°C. Apoptosis was initiated by treatment with 2 µM staurosporine at 24 to 48 h post-transfection. Cells were maintained in HEPES-buffered Hank's balanced salt solution (HHBSS) and subjected to imaging at 1 or 2 min intervals for 4-6 h. Transfected HeLa cells were imaged using an Axiovert 200M (Zeiss) microscope or a laser scanning confocal LSM-700 (Zeiss) motorized microscope. Axiovert 200M (Zeiss) was equipped with a 75 W xenon-arc lamp, 40x objective lens (NA = 1.3, oil) and a 14-bit CoolSnap HQ2 cooled CCD camera (Photometrics), driven by open source Micro-Manager software. LSM-700 (Zeiss) was equipped with 10mW 488nm and 555nm solid-state laser, 63x objective lens (NA=1.40, oil) and two high-sensitivity, low-noise adjustable PMTs, driven by Zeiss's Zen software.

Table 3.1 Details of the gene constructs used in this work.

Name	Gene (Restriction sites in italics and substrate sequences in bold)	Description
GA ^{NLS} -DEVD- B ^{NES}	<i>XhoI</i> -ddGFP A-NLS- <i>KpnI</i> - DEVD -ddFP B-NES- <i>HindIII</i>	Plasmid 1 for green translocation- based caspase-3 biosensor
RA ^{NLS} -DEVD- B ^{NES}	<i>XhoI</i> -ddRFP A-NLS- <i>KpnI</i> - DEVD -ddFP B-NES- <i>HindIII</i>	Plasmid 1 for red translocation- based caspase-3 biosensor
RA ^{NLS} -IETD- B ^{NES}	<i>XhoI</i> -ddRFP A-NLS- <i>KpnI</i> - IETD -ddFP B-NES- <i>HindIII</i>	Plasmid 1 for red translocation- based caspase-8 biosensor
RA ^{NLS} -LEHD- B ^{NES}	<i>XhoI</i> -ddRFP A-NLS- <i>KpnI</i> - LEHD -ddFP B-NES- <i>HindIII</i>	Plasmid 1 for red translocation- based caspase-9 biosensor
B ^{NLS}	<i>XhoI</i> -ddFP B-NLS- <i>HindIII</i>	Plasmid 2 for any translocation- based biosensor
GA ^{NES} -DEVD- B ^{NLS}	<i>XhoI</i> -ddGFP A-NES- <i>KpnI</i> - DEVD -ddFP B-NLS- <i>HindIII</i>	Plasmid 1 for green-to-red colour switch caspase-3 biosensor & Plasmid 1 for attempted nucleus to cytoplasm green translocation
RA ^{NLS}	<i>XhoI</i> -ddRFP A-NLS- <i>HindIII</i>	Plasmid 2 for green-to-red colour switch caspase-3 biosensor
RA ^{NES} -DEVD- B ^{NLS}	<i>XhoI</i> -NES-ddRFP A- <i>KpnI</i> - DEVD -ddFP B-NLS- <i>HindIII</i>	Plasmid 1 for red-to-green colour switch caspase-3 biosensor & Plasmid 1 for attempted nucleus to cytoplasm red translocation
GA ^{NLS}	<i>XhoI</i> -ddGFP A-NLS- <i>HindIII</i>	Plasmid 2 for red-to-green colour switch caspase-3 biosensor
B ^{NES}	<i>XhoI</i> -ddFP B-NES- <i>HindIII</i>	Plasmid 2 for attempted nucleus to cytoplasm translocation
RA ^{NES} -IETD-B- DEVD-GA	<i>HindIII</i> -NES-ddRFP A- <i>KpnI</i> - IETD - ddFP B- <i>BamHI</i> - DEVD -ddGFP A- <i>XhoI</i>	Tandem heterotrimer biosensor

Chapter 4: Dimerization-dependent FP based indicator for close contacts between membranes⁴

4.1 Introduction

Close contacts between membranes of different organelles are often crucial for modulating cellular functions and signaling cascades, either because they regulate the production or transportation of critical components, or because they represent sites of signal transduction. One of the best-known contacts are the contacts between the membranes of endoplasmic reticulum (ER) and mitochondria, which is the basis of a bidirectional communication regulating a number of physiological processes ranging from energy and lipid metabolism to signaling and cell death [171].

The study of the close contacts between the ER and mitochondria membranes can be traced back to the 1970s, when observations from electron microscopy (EM) suggested continuity between outer mitochondrial membrane and ER membrane [172]. Almost at the same time, another piece of evidence was reported by a subcellular fractionation study, in which ER membranes were co-purified with mitochondrial fractions [173]. Since then the enthusiasm for gaining a better understanding of the mechanism and the function of ER-mitochondria membrane contacts has never shrunk. In the 1990s, data from digital 3D fluorescent microscopy indicates that as much as 20% of the mitochondrial surface is in direct contact with ER [174]. A few years later, modern EM techniques revealed that mitochondria are surrounded by membranes of the ER in a distance below 200 nm [175]. Recently, high-resolution three-dimensional

⁴ The results of the MAM labeling described in this chapter has been published Alford, S.C. et al. 2012 *ACS Synth. Biol.* **1**, 569-575. Constructs with Tom20 mutants described in Section 4.2.2 are credit to Dr. Spencer Alford. Other constructs related to MAM or FAFL4 are prepared by me.

electron tomography has shown the existence of physical contacts between the two organelles, whose size are between 10 and 25 nm [176].

To better describe these physical contacts, the contact region associated with the ER membrane was designated as mitochondria-associated ER membrane (MAM) [177]. Along with the discovery of the MAM, researchers started to understand the molecular basis and related functions. Specifically, MAM facilitates inter-organelle lipid transfer [177] by eliminating the energetically unfavourable transfer of hydrophobic lipids through the water rich cytosol [178]. Furthermore, the MAM plays essential roles in intracellular Ca^{2+} homeostasis [179,180], apoptosis progression [181] and the regulation of metabolism [182]. Due to the enrichment of Ca^{2+} channels, the MAM directly facilitates rapid Ca^{2+} transmission between the ER and mitochondria, and thus regulates mitochondrial metabolism. Yet, overloading Ca^{2+} in mitochondria can lead to impairment of mitochondrial function and opening of the permeable transition channels, followed by the disruption of the membrane potential, and finally, cell death [171,183-186].

Given the importance of the MAM in cell function, it is important to find proper MAM markers that could be utilized in the detection of changes in MAM composition and the movement of MAM under various stimulations [176,182]. Since the MAM is the major platform for metabolism and transportation of lipids between the ER and mitochondria [178], the traditional MAM markers are lipid metabolism enzymes. For example, one of the reported markers is the long chain fatty acid coenzyme A ligase 4, also called fatty acid coenzyme A synthase 4 (FACL4/ACSL4), which is involved in the ligation of fatty acids to coenzyme A and the following regulation of lipid metabolism (**Figure 4.1**) and cell signalling [187,188].

However, the traditional MAM markers commonly suffer from nonspecific labeling. For instance, FACL4 is reported not only on MAM but also on peroxisomes [189]. Furthermore, lipid metabolism enzymes may not tolerate FP fusions. Specifically, the localization of these enzymes might be altered if fused with a FP [190], or the localizations of fusion proteins are not fully reproducible

[186]. Lastly, currently available MAM markers are often characterized based on membrane purification from cell extract, which may not fully reflect the performance of the MAM markers in live cells.

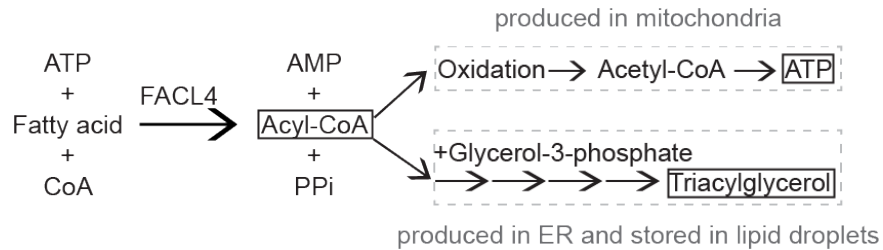


Figure 4.1 Schematic illustration of FAACL4's function in lipid metabolism.

Given the drawbacks of current MAM markers, we aimed to construct a genetically encoded FP-based MAM marker that could be utilized to study MAM in live cells with good reproducibility. Due to the diverse distribution of MAM proteins along the membranes of ER and mitochondria, we aimed to specifically highlight the close contact region between the two organelles, which is the definition of MAM. To selectively label the close contact region, dimerization-dependent FPs (ddFPs) were exploited for marker design. As discussed previously, ddFP technology relies on the reversible binding of two dark monomers, copy A and copy B, to form a fluorescent heterodimer (**Figure 4.2**). The fluorogenic response associated with the formation of heterodimer can be employed as an indicator of the close proximity between proteins of interest. In this study, green ddFP (ddGFP) monomers, GA and GB, were fused to MAM protein markers to enable the visualization of close contacts between membranes of ER and mitochondria.



Figure 4.2 Schematic of ddFP technology

4.2 Results and discussion

4.2.1 ddGFP labeling of MAM in live cells

Our strategy for labeling of the MAM was to coexpress GA and GB fusions in which each partner was fused to a MAM enriched protein. Specifically, we fused the ddFP monomers to the mitochondrial protein translocase of outer membrane-20 (Tom20) and the ER protein calnexin. Tom20 is an outer membrane protein of the mitochondria that functions as a receptor during protein import [191,192]. Since Tom20 is bound to the outer membrane through the N-terminal transmembrane domain [193], the fusion of GB to the C-terminus of Tom20 (Tom20-GB) would place GB partners on the cytosolic face of mitochondria (**Figure 4.3A**). Calnexin is a Ca^{2+} binding ER folding chaperone that is enriched on the MAM, where it modulates Ca^{2+} homeostasis [194-197]. Since calnexin contains a large N-terminal Ca^{2+} -binding luminal domain, a single transmembrane helix and a C-terminal cytosolic tail [196], the fusion of GA to the C-terminus of calnexin (Calnexin-GA) would place the ddGFP partners on the cytosolic side of the ER (**Figure 4.3A**).

When the gene fusions of Tom20-GB and Calnexin-GA were expressed independently, no substantial fluorescence signal was detected above autofluorescence (**Figure 4.3B,C**). However, when cells were cotransfected with genes encoding both fusions, we observed prominent green fluorescence localized in the perinuclear region of cells (**Figure 4.3D**). The perinuclear region was defined as discrete fluorescent labeling at points of mitochondria-ER contacts (**Figure 4.3D**), consistent with previous reports of MAM staining [197].

As a control, we cotransfected a knockout mouse embryonic fibroblast (MEF) cell line (a kind gift from Dr. Thomas Simmen), which is deficient for mitofusin-2, a protein that physically tethers ER membrane to mitochondria [179]. Transfected wild-type MEFs exhibited MAM labeling similar to that observed in HeLa cells (**Figure 4.3E**). In contrast, MAM labeling was rarely observed in mitofusin-2 knockout MEFs (**Figure 4.3F**), in which the fluorescence intensity of the MAM labeling was diminished relative to wild-type MEFs. This result is

consistent with impaired formation of ER-mitochondria membrane juxtaposition in MEFs lacking mitofusin-2 [179].

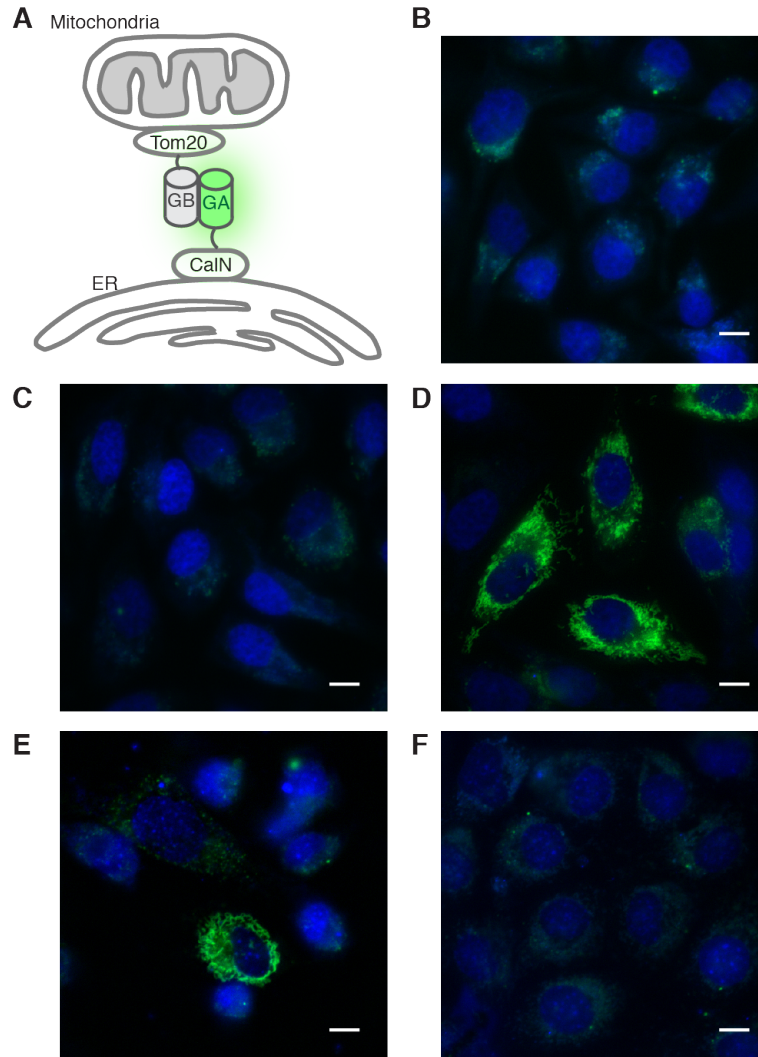


Figure 4.3 ddGFP labeling of MAM in live cells.

(A) MAM labeling strategy. (B) Expression of Calnexin-GA or (C) Tom20-GB alone in HeLa cells. (D) Coexpression of calnexin-GA and Tom20-GB in HeLa cells. Fluorescent images of wild-type (E) or mitofusin-2 knockout (F) MEFs cotransfected with Calnexin-GA and Tom20-GB. Cell nuclei (blue) are stained with DAPI. Scale bar represents 10 μ m.

To confirm that we observed genuine MAM-mediated contact sites with the combination of calnexin and Tom20, we performed a control experiment with cotransfection of mCherry targeted to either the mitochondria or ER. The images

in **Figure 4.4** demonstrated that the green fluorescence from MAM-associated ddGFP heterodimers colocalized with both the mitochondria and the ER.

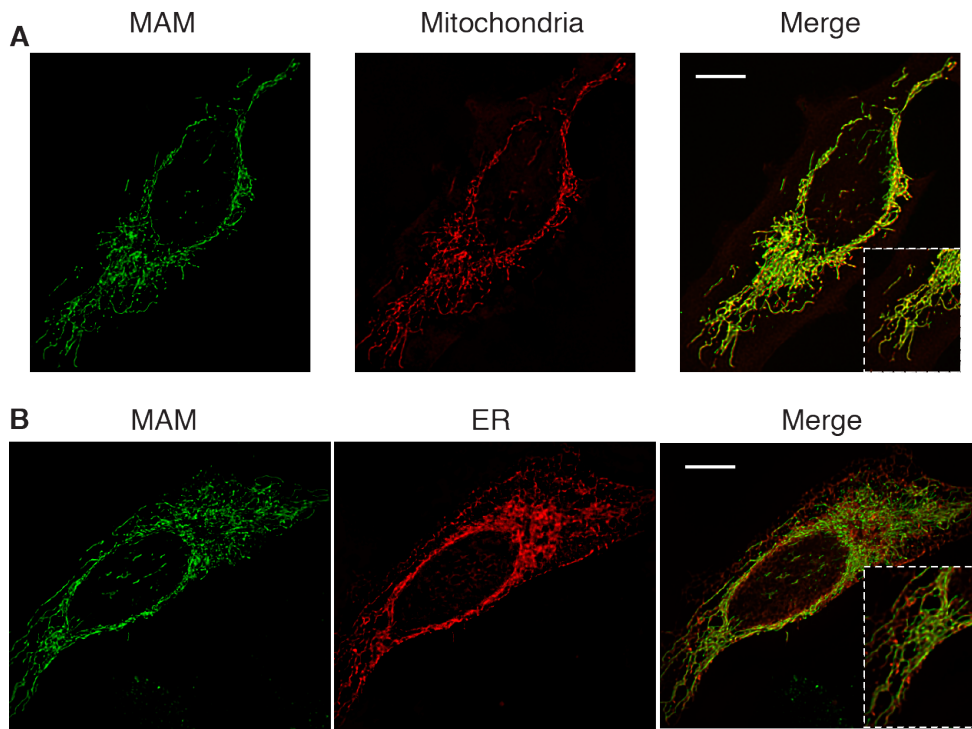


Figure 4.4 ddGFP MAM label colocalizes with mitochondria (A) and ER (B). HeLa cells were transfected with three plasmids encoding Calnexin-GA, Tom20-GB, and either a mCherry-ER or a mCherry-mitochondria marker. Left panel is ddGFP fluorescence, middle panel is red mCherry fluorescence, and right panel depicts merge. Manders coefficient (M1) for ER was 0.881 and for mitochondria was 0.865. M1 coefficients were determined using Volocity software (Perkin Elmer). Images were acquired on an Olympus IX-81 motorized microscope spinning-disk confocal microscope. Scale bar represents 10 μm .

Furthermore, we attempted to employ our MAM markers to detect the dissociation and the reassociation of MAM and mitochondria under conditions of low Ca^{2+} (<100 nM) and high Ca^{2+} (>1 μM), respectively [175]. Since ionomycin [175,198] and tunicamycin [176] have been reported to cause Ca^{2+} fluctuations in live cells, they were used in an attempt to perturb the associated state of ddGFP heterodimers in MAM labeling. Unfortunately, we didn't observe any detectable change in green fluorescence signal, though a change in the overall shape of the organelles was observed. One possible explanation for this negative result is that

the ddFP-based MAM labeling strategy is insensitive to the relatively subtle changes in the membrane-membrane distance that are expected to occur. Another possible explanation is that, much like a molecular Velcro, the ddFPs have effectively forced the membranes to remain associated. For future work, it might be possible to use phosphorylation [196] or palmitoylation [197] of calnexin to visualize the dissociation of MAM from mitochondria.

4.2.2 MAM labeling is dependent on the proximity

To confirm the dependence of proximity in MAM labeling and to eliminate the possibility of artefacts due to nonspecific aggregation of ddGFPs, we performed various control experiments.

We first utilized Tom20 mutants that have been reported to delocalize from the mitochondria [193]. Expression of these Tom20 mutants as mCherry fusions confirmed that these chimeras redistributed to the cytoplasm and Golgi (**Figure 4.5A-D**). Fusion of these Tom20 mutants to GB and coexpression with Calnexin-GA resulted in a loss of green fluorescent labeling of MAM mitochondria contacts (**Figure 4.5E,F**).

Another control experiment was performed with two distinct ER targeting and mitochondria targeting constructs that are not known to lead to MAM enrichment. One of ER targeting construct utilized the signal recognition particle receptor β (SR β) (residues 1–85 of the *Rattus norvegicus* gene product) [199,200], which is known to facilitate protein translocation across and insertion into membranes. Since SR β is bound to the ER membrane with a C-terminal cytosolic tail [200,201], the fusion of GB to the C-terminus of SR β (SR β -GB) would place GB partners on the cytosolic face of ER membrane. When cotransfected with cytosolic GA (**Figure 4.6A**), green fluorescent heterodimers formed between SR β -GB and cytosolic GA and colocalized with ER, which validated that the localization of SR β is on the cytosolic side of ER membrane (**Figure 4.6B**).

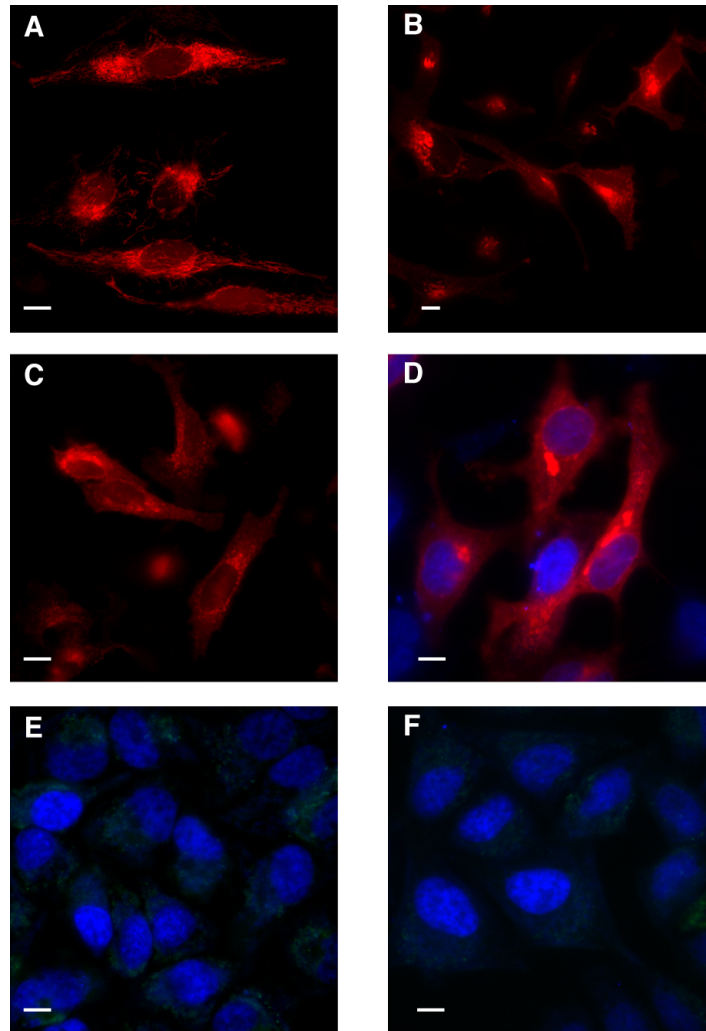


Figure 4.5 Tom20 truncation mutants delocalize from the mitochondria and prevent fluorescent labeling of the MAM.

(A) Native Tom20-mCherry fusions localize to the mitochondrial network. (B) mCherry-Golgi localization control. Tom20 ($\Delta 25-31$)-mCherry (C) and Tom 20 ($\Delta 34-51$; K27S/R28S/R29S)-mCherry (D) delocalize to exhibit a random distribution or Golgi localization. HeLa cells co-transfected with Calnexin-GA and delocalized Tom20 ($\Delta 25-31$)-GB truncation (E) or Tom20 ($\Delta 34-51$; K27S/R28S/R29S)-GB truncation (F). Cell nuclei (blue) are stained with DAPI. Scale bar represents 10 μm . All fusions with Tom20 mutants transfected in this experiment are credit Dr. Spencer Alford.

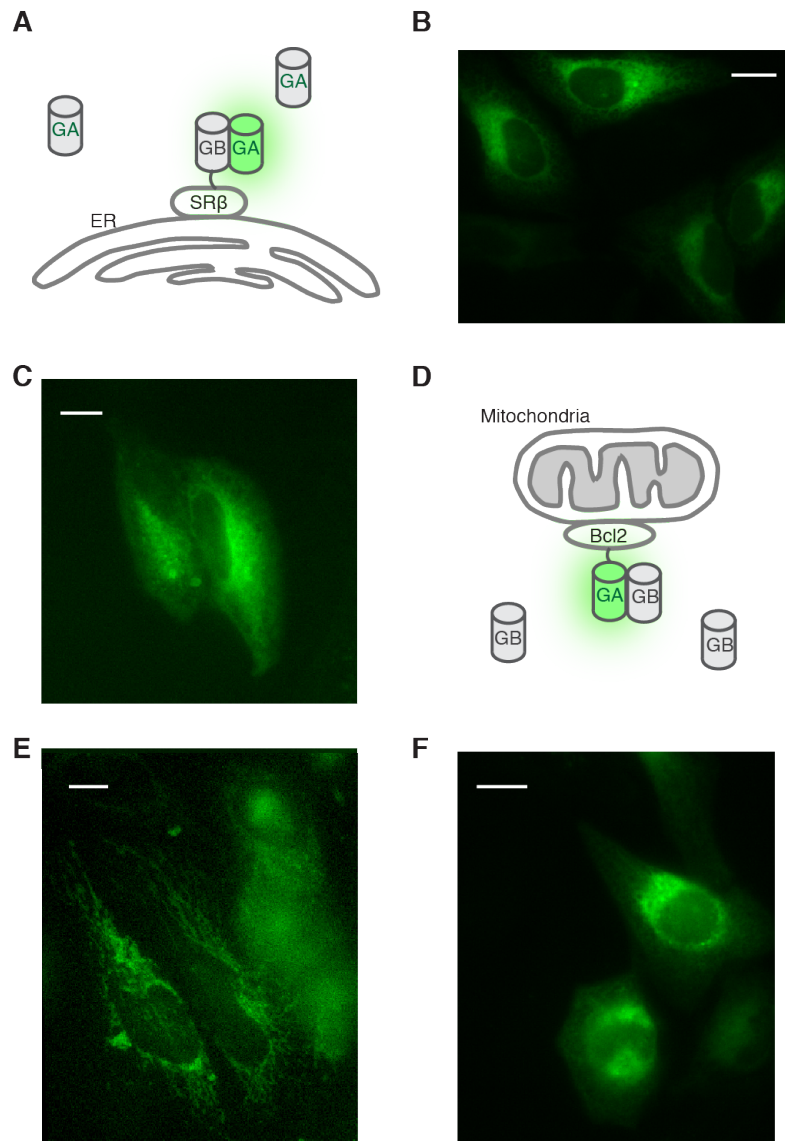


Figure 4.6 Control experiments with non-MAM proteins

Strategy used for determining whether the domains are on the cytosolic side of either ER (A) or mitochondria (D) membrane. HeLa cells were transfected with two plasmids encoding a cytosolic GA and an ER targeted fusion, either SRβ-GB (B) or GB-Bcl2-Cb5 (C). (E) HeLa cells were transfected with two plasmids encoding a cytosolic GB and a mitochondria targeted fusion, GA-Bcl2-ActA. (F) HeLa cells were transfected with two plasmids encoding SRβ-GB and SRα-GA fusion. Images were acquired on Nikon Eclipse Ti microscope. Scale bar represents 10 μm.

The other ER targeting construct was built by fusing GB to the N-terminus of Homo sapiens B-cell lymphoma 2 (Bcl2, residues 1–218) followed by a cytochrome-b5 (cb5) transmembrane domain [202,203]. This construct was

designated as GB-Bcl2-Cb5. A cotransfection of cytosolic GA and GB-Bcl2-Cb5 was performed to verify the correct localization of GB-Bcl2-Cb5. As shown in **Figure 4.6C**, green fluorescence signal colocalized with ER, which indicated that GB was placed on the cytosolic side of ER membrane through the Bcl2-Cb5 domain. When each of the ER targeting fusions was expressed independently, no fluorescent labeling was detected above autofluorescence.

To build a construct targeting the cytosolic side of the mitochondrial membrane, Bcl2 was fused to the membrane-anchoring domain of actin assembly inducing protein (ActA), namely Bcl2-ActA [202,203]. To visualize the localization of Bcl2-ActA, GA was fused to the N-terminus of Bcl2-ActA to construct fusion of GA-Bcl2-ActA. Expression of fusion GA-Bcl2-ActA in conjunction with cytosolic GB (**Figure 4.6D**), gave strong green fluorescent signal that localized with mitochondria (**Figure 4.6E**). Expression of GA-Bcl2-ActA alone didn't exhibit any fluorescent labeling above autofluorescence.

When coexpressing fusion GA-Bcl2-ActA with either SR β -GB or GB-Bcl2-Cb5 in HeLa cells, no positive fluorescence signal above autofluorescence was detected. An unstructured linker sequence, corresponding to residues 95 to 135 of phage λ repressor [204,205], was inserted between GA and Bcl2-ActA of fusion GA-Bcl2-ActA to increase the chance for the association of ddGFPs. Yet, we didn't detect any fluorescence signal above the autofluorescence. This observation is not entirely unexpected, since membrane markers used in this experiment are not known to be enriched in MAM and are probably not in close proximity. The control experiments with SR β and Bcl2 domains indicated that the formation of the heterodimer was dependent on the proximity of targeted membrane proteins.

Finally, a positive control was performed to further test the emerging conclusion that direct interaction between proteins of interest could cause the formation of ddGFP heterodimers on membranes. Since signal recognition particle receptors are membrane-associated heterodimeric proteins, including subunits of SR α and SR β , the control experiment was to detect the dimerization of the receptors via fusions with ddGFPs. After coexpressing fusions SR β -GB and SR α -GA, green fluorescence signal from heterodimers was detected and

colocalized with ER (**Figure 4.6F**). Yet, no fluorescence signal was detected above autofluorescence, when each fusion was expressed independently. This result served as a positive control to validate the formation of green fluorescent heterodimers on the membrane.

4.2.3 Investigating the localization of FACL4

Although we were able to demonstrate the effective labeling of MAM via fusions of ddGFP monomers to calnexin and Tom20 (**Section 4.2.1**), we could not demonstrate the detection of dynamic dissociation of MAM and mitochondria under conditions of low Ca^{2+} [175]. To search for alternative MAM markers that may serve as dynamic indicators, we investigated one of the most reliable MAM-associated proteins, fatty acid coenzyme A synthase 4 (FACL4) [187], as recommended by our collaborator Dr. Thomas Simmen. FACL4 has been reported to localize to ER (as part of MAM), peroxisomes [206], microsomes, mitochondria [207] and cytosol [208]. However, most of the localization information was based on experimental data from lipid purification with little work done using imaging of live cells. Notably, none of the mammalian FACL4 genes have classical targeting sequences for endoplasmic reticulum, mitochondria, or peroxisomes [209]. Thus, the localization of FACL4 in live cells is still an open question.

To investigate the localization of FACL4 in live cells, HeLa cells were transfected with a gene encoding the fusion of a yellow fluorescent protein (mCitrine) fused to the C-terminus of FACL4 (FACL4-mCitrine). Surprisingly, we found that the FACL4-mCitrine fusion localized mainly on the plasma membrane (**Figure 4.7A**) and also on putative microsomes (**Figure 4.7B**). No distinctive fluorescence signal was detected that would be consistent MAM. However, weak fluorescence signals from the perinuclear region were observed. In an attempt to identify the nature of this localization around the perinuclear region, we cotransfected cells with a gene encoding a fusion of FACL4 and EGFP, in conjunction with a gene encoding a red fluorescent mitochondria

marker. As shown in **Figure 4.7C**, the green fluorescence signal from FACL4 fusion did not fully colocalize with the red mitochondria marker, which convinced us that the fusion of FACL4 and a FP does not localize specifically to the mitochondria in HeLa cells.

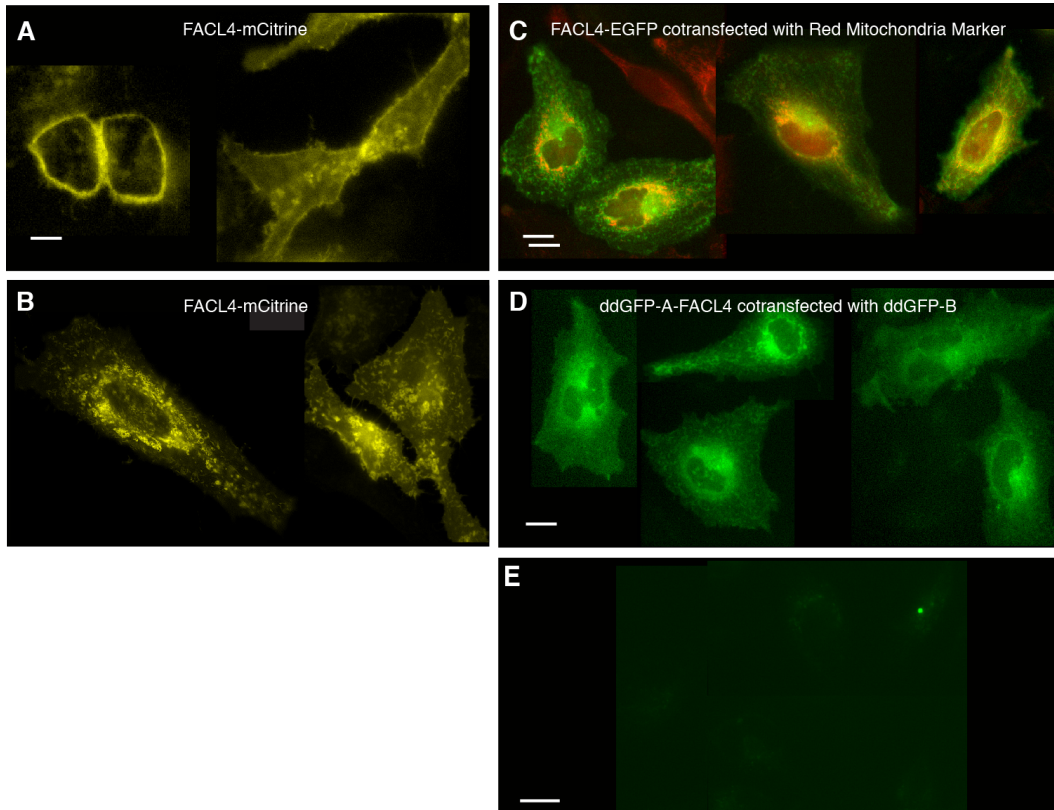


Figure 4.7 Localization of FACL4 in live HeLa cells.

FACL4-mCitrine fusion localizes mainly on cytoplasmic membrane (A) and possible microsomes (B). (C) Images of HeLa cells coexpressing fusion FACL4-EGFP and a red mitochondria marker. (D) Images of HeLa cells coexpressing fusions GA-FACL4 and a cytosolic GB. Green fluorescence of ddGFP heterodimers is detected. (E) Images of HeLa cells coexpressing fusions FACL4-GA and a cytosolic GB. No fluorescence of ddGFP heterodimers is detected above autofluorescence. Scale bars represents 10 μm.

To better understand the positions of protein termini across the membrane, the ddFP-based strategy was employed. Specifically, GA was fused to either the N- or the C-terminus of FACL4 to create fusions of GA-FACL4 or FACL4-GA, respectively. Similar to the strategy shown in **Figure 4.6A and D**, a cytoplasmic

GB was coexpressed with either GA-FACL4 or FACL4-GA in HeLa cells. The key to this strategy is the formation of heterodimers between cytosolic GB and the accessible GA exposed to cytoplasm via fusion with FACL4. If the GA monomer is indeed exposed to the cytoplasm, it could form a dimer with the free cytoplasmic GB and form green fluorescent heterodimers. We observed green fluorescence signal from the coexpression of GA-FACL4 and cytoplasmic GB (**Figure 4.7D**) but not from FACL4-GA and cytoplasmic GB (**Figure 4.7E**), leading us to conclude that only N-terminus of FACL4 was exposed to cytoplasm.

Due to the inconsistencies between previous studies and our observations of FACL4 localization, we started to search for an explanation for our data. A literature search led our attention to an isoform of FACL4 (isoform 2), which is expressed in human brain [210] and related to mental retardation [208]. The protein of isoform 2 differs from our initial FACL4 construct (isoform 1) by the inclusion of a 41-residue N-terminal hydrophobic sequence derived from alternative splicing of the gene [208]. The additional 41-residue peptide (711 a.a vs. 670 a.a) in isoform 2 is the most hydrophobic domain of the molecule [209] and has been reported to shift the intracellular localization of the enzyme from cytosol to the membrane of the ER in neurons [208].

To visualize the localization of isoform 2 in live cells, we fused mCitrine to the C-terminus of isoform 2. When expressed in live HeLa cells, we observed yellow fluorescence signal from ER (**Figure 4.8A-C**) and putative peroxisomes, which are visible as small strongly puncta in the inset of **Figure 4.8C**. The ER localization of isoform 2 was consistent to the hypothesis from a computational prediction [208], even though our experiments were done in HeLa cells rather than neurons. In addition, the colocalization of isoform 2 and a mitochondria marker was investigated by coexpressing fusions of isoform 2-EGFP and a red mitochondria marker. As shown in **Figure 4.8D**, the green fluorescence signal did not colocalize with the red signal, which indicated that isoform 2 was not localized to the mitochondria.

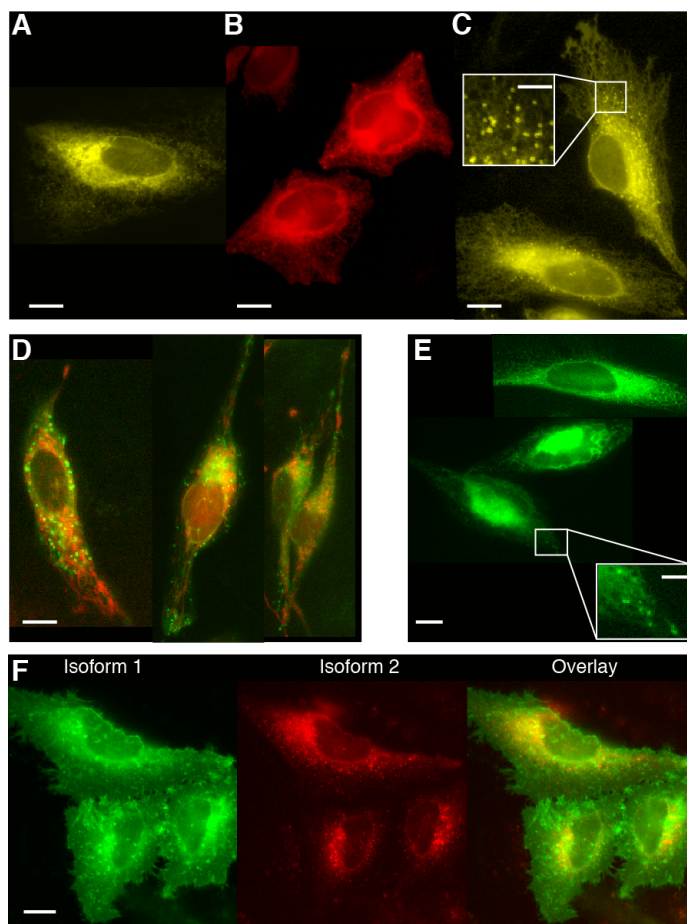


Figure 4.8 Localization of FACL4 isoform 2 in live HeLa cells.

Images of HeLa cells expressing fusions of isoform 2-mCitrine (A), mRuby2-isoform 2 (B) and mVenus-isoform 2 (C). (D) Images of HeLa cells coexpressing green isoform 2-EGFP and a red mitochondria marker. (E) Images of HeLa cells coexpressing fusion GA-isoform 2 and a cytosolic GB. (F) Images of HeLa cells coexpressing fusions of isoform 2-mCitrine and FACL4-ECFP (isoform 1), indicated by red and green, respectively. Overlay of both channels is shown on the right. Scale bar represents 10 μm in the image and 3 μm in the insets.

As with isoform 1, a ddFP-strategy was utilized to study the position of the termini of isoform 2. GA was fused to either the N- or the C-terminus of isoform 2 to create fusions of GA-isoform 2 and isoform 2-GA, respectively, which were then each coexpressed with cytosolic GB. Similar to the study of isoform 1, we only observed green fluorescence signal from coexpression of GA-isoform 2 and cytosolic GB, which indicated that isoform 2 was present on the cytosolic surface of ER membrane with its N-terminus exposed to the cytoplasm (**Figure 4.8E**).

Surprisingly, fluorescent puncta were also visualized in ddFP-based experiments (inset of **Figure 4.8E**), which demonstrated that the N-terminus of isoform 2 was exposed to cytoplasm no matter where it was localized. Since the C-terminus of isoform 2 was not accessible to the cytoplasm in ddFP-based experiment, we reasoned that the C-terminus might be inside ER lumen. To test this hypothesis, isoform 2-GA was coexpressed with an ER luminal-GB, which was created by attaching an ER retention sequence to the gene of GB. Imaging of transfected cells did not reveal any fluorescence signal above autofluorescence, which indicated that C-terminus of isoform 2 was either not inside the ER or inside the ER but not accessible to GA.

To study the colocalization of isoform 1 and 2, fusions of both isoforms fused to different colours of FP were coexpressed in HeLa cells. Specifically, isoform 2-mCitrine and FACL4-ECFP (isoform 1) were coexpressed. This experiment revealed that yellow fluorescence signal was observed mainly from ER and cyan fluorescence signal was primarily associated with the cytoplasmic membrane (**Figure 4.8F**). In **Figure 4.8F**, red and green colour was used to represent fluorescence signal from fusions with isoform 2 and isoform 1, respectively. There are relatively few yellow regions apparent in these cells, indicating that the two isoforms are not colocalized.

Overall, we discovered that FACL4 isoform 1 localizes primarily on the cytoplasmic membrane and we confirmed the localization of isoform 2 on the ER membrane. In addition, we determined that the N-termini of both isoforms are exposed to the cytoplasm regardless of their localization. However, no convincing imaging data was found to support MAM localization of either isoform.

4.3 Conclusion

Collectively, our results demonstrate that a ddFP approach using a MAM-enriched ER portion together with a mitochondrial portion provides an effective label of the MAM. Specifically, calnexin and Tom20 fusions with ddGFPs were proven to be effective in labeling MAM. Other membrane proteins, such as SR β

and Bcl2, could not be utilized in labeling MAM, since they only presented on ER or mitochondria membrane and are not enriched in MAM.

In addition, FA CL4 was also intensively studied as a candidate for labeling MAM. Distinctive preferences regarding to its localization were observed for two isoforms of FA CL4. The majority of isoform 1 was found on the cytoplasmic membrane and putative microsomes. Isoform 2 exhibited mainly ER membrane localization (**Figure 4.9**), consistent to the hypothesis from a computational prediction [208]. Using ddFP-based strategies, it was revealed that both isoforms have cytosolic exposed N-termini (**Figure 4.9**). Although FA CL4 has been reported as a well-characterized MAM protein, we didn't observe any convincing MAM localization with fusions of FA CL4 fused to FPs. The majority of previous reports on MAM-localized proteins were proteomic studies based on membrane purification from cell extract. Our results indicate that researchers should treat such results with caution and follow up studies using FP fusions and live cell imaging are warranted.

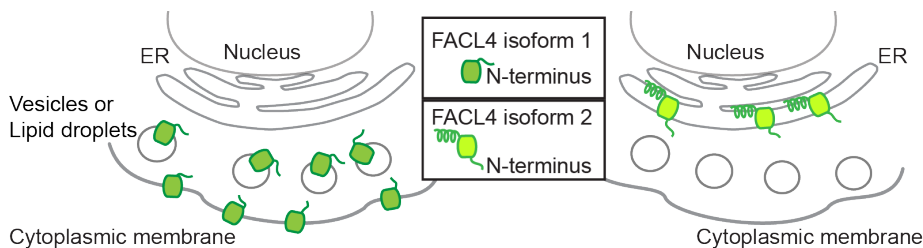


Figure 4.9 Schematic illustration of FA CL4 localization.

The localization of FA CL4 (isoform 2) on ER is adapted from reviews of MAM [211] and lipid synthesis [212].

4.4 Material and methods

4.4.1 General methods and materials

All synthetic oligonucleotides for cloning were purchased from Integrated DNA Technologies (IDT, Coralville, IA). Polymerase chain reaction (PCR) was performed using Pfu DNA polymerase (Fermentas) according to the provided

manufacturers' protocols. FastDigest restriction endonucleases (Fermentas) were used for restriction digests of PCR products and analytical DNA digestion. GeneJET gel extraction kit (Fermentas) or QIAquick Gel-Extraction kit (Qiagen) was used for DNA purification following agarose gel electrophoresis. DNA ligation was carried out using T4 DNA ligase (Invitrogen). *E. coli* strain ElectroMAX DH10B (Invitrogen) was used for routine plasmid propagation, library construction and screening, and recombinant protein production. The cDNA sequences were confirmed by dye terminator cycle sequencing using the BigDye® (Applied Biosciences) cycle Sequencing Kit. Sequencing reactions were analyzed at the University of Alberta Molecular Biology Service Unit (MBSU) at the University of Alberta.

4.4.2 Construction of mammalian expression plasmids

A modified pcDNA3.1(+) (Invitrogen) plasmid, with an *XhoI* and an *HindIII* sites in the same reading frame as the equivalent sites of the pBAD/His B plasmid, was used for mammalian cell expression. Genes of SR α , SR β , Bcl2, Cb5, and ActA were kind gifts from Dr. David Andrews. Genes of calnexin and Tom20 were kind gifts of Michael Davidson. The gene of human FACL4 was kind gift from Dr. Thomas Simmen. Brief cloning scheme for each construct is outlined in **Table 4.1**. Generally, three-part ligations were used to incorporate the *XhoI/KpnI* and *KpnI/HindIII* digested genes of membrane proteins or FPs into *XhoI/HindIII* digested pcDNA3.1(+) vector.

Localization markers were mCherry-mito-7 (mitochondria), mCherry-SiT-N-15 (Golgi), which were gifts from Michael Davidson. ER markers were ER-mCherry, ER-GB and ER-mRuby, which were made by fusing FP to calreticulin signal peptide and a KDEL retention sequence.

4.4.3 Mammalian cell culture and imaging

All DNA for mammalian cell transfection was purified by the Plasmid Mini-prep kit (Fermentas). HeLa cells were maintained in Dulbecco's Modified

Eagle Medium (DMEM) supplemented with 10% fetal bovine serum and glutamax (Invitrogen) at 37°C and 5% CO₂. Transient transfections of pcDNA3.1 (+) expression plasmids were performed using Turbofect Protein Transfection Reagent (Thermoscientific). Cells in 35 mm imaging dishes were incubated with 1 mL of DMEM (FBS free) for 10 min and then transfected with 1 µg of plasmid DNA that had been mixed with 2 µL of Turbofect (Fermentas) in 0.1 mL of DMEM (FBS free). When multiple plasmids were co-transfected, equal mass of each plasmid was used. The culture media was changed back to DMEM with 10% FBS after 2 h incubation at 37°C. Twenty-four hours post-transfection, cells were imaged in HEPES-buffered Hank's balanced salt solution (HHBSS). To induce dissociation of MAM and mitochondria membrane, one method was to add Ionomycin (Invitrogen) and EGTA into imaging buffer (HHBSS) with a final concentration of 10 µM and 10 mM [175], respectively. The other method we have tried was to treat transfected cells with 10 µg/ml tunicamycin (Sigma-Aldrich) during imaging [176].

Imaging was performed either on an inverted Nikon Eclipse Ti microscope or a Zeiss Axiovert 200M microscope. Nikon Eclipse Ti was equipped with a 200W metal halide lamp (PRIOR Lumen), a 60 × objective (NA = 1.4 oil) and a QuantEM: 512SC 16-bit cooled CCD camera (Photometrics), driven by the NIS-Elements AR 3.2 software package (Nikon). Zeiss Axiovert 200M microscope was equipped with a 75 W xenon-arc lamp, 40x objective lens (NA = 1.3, oil) and a 14-bit CoolSnap HQ2 cooled CCD camera (Photometrics), driven by open source Micro-Manager software. Exposure times were adjusted between 100 ms to 400ms to obtain suitable intensities in each channel.

Confocal colocalization data was collected using a spinning-disk confocal Olympus IX-81 motorized microscope. Green and red excitations were conducted with 50mW 491 and 561 nm pumped diode lasers. LMM5 from Spectral Applied Research was used for laser merging. The two lasers were coupled to the spinning disk confocal head (CSU10; Yokogawa) mounted with a Sedat dichroic mirror (Semrock). The lasers were processed with appropriate filter sets (Semrock) to

capture fluorescence images with an EMCCD (C9100–13, Hamamatsu), driven by Perkin-Elmer’s Volocity software.

Table 4.1 Cloning strategies for DNA constructs described in Chapter 4.

Construct ¹	Gene assembly (restriction sites in italics)
Calnexin-GA	<i>XhoI-Calnexin-KpnI-GA-HindIII</i>
Tomm20-GB	<i>XhoI-Tomm20-KpnI-GB-HindIII</i>
Tomm20-mecherry	<i>XhoI-Tomm20-KpnI-mCherry-HindIII</i>
GB (cytosolic)	<i>XhoI-GB-HindIII</i>
SRβ-GB	<i>XhoI-SRβ-KpnI-GB-HindIII</i>
GB-Bcl2-Cb5	<i>XhoI-GB-KpnI-Bcl2-cb5-HindIII</i>
GA-Bcl2-ActA	<i>XhoI-GA-KpnI-Bcl2-ActA-HindIII</i>
SRα -GA	<i>XhoI-SRα-KpnI-GA-HindIII</i>
SRβ-linker-GB	<i>XhoI-SRβ-BglII-linker-KpnI-GB-HindIII</i>
GA-linker-Bcl2-ActA	<i>XhoI-GA-BglII-linker-KpnI-Bcl2-ActA-HindIII</i>
FACL4-mCitrine	<i>XhoI-FACL4-KpnI-mCitrine-HindIII</i>
ddGFP A-FACL4	<i>XhoI-GA-KpnI-FACL4-HindIII</i>
FACL4-ddGFP A	<i>XhoI-FACL4-KpnI-GA-HindIII</i>
FACL4-EGFP	<i>XhoI-FACL4-KpnI-EGFP-HindIII</i>
FACL4-ECFP	<i>XhoI-FACL4-KpnI-ECFP-HindIII</i>
ECFP-FACL4	<i>XhoI-ECFP-KpnI-FACL4-HindIII</i>
isoform 2-mCitrine	<i>XhoI-isoform 2-KpnI-mCitrine-HindIII</i>
isoform 2-ddGFP A	<i>XhoI-isoform 2-KpnI-GA-HindIII</i>
ddGFP A-isoform 2	<i>XhoI-GA-KpnI-isoform 2-HindIII</i>
ECFP-isoform 2	<i>XhoI-ECFP-KpnI-isoform 2-HindIII</i>
mVenus-isoform 2	<i>XhoI-mVenus (residue 1-229)-KpnI-isoform 2-HindIII</i>
mRuby2-isoform 2	<i>XhoI-mRuby2-KpnI-isoform 2-HindIII</i>
EGFP-isoform 2	<i>XhoI-EGFP-KpnI-isoform 2-HindIII</i>
¹ All constructs are in pcDNA3.1(+).	

Chapter 5: Biosensing strategies for PARP1 activity

5.1 Introduction

Living organisms rely on elaborate systems to recognize and repair gene damage. When these systems fail, DNA damage accumulates, ultimately leading to cancer or cell death. Breakage of the DNA backbone is one of the primary forms of DNA damage and may occur as single-strand breaks or double-strand breaks (DSBs) [213]. These breaks are highly cytotoxic and disturb genome stability, thus necessitating repair mechanisms. The DNA damage response (DDR) pathway recognizes DNA damage and recruits DNA repair factors to damaged sites. The majority of DDR factors are protein kinases, poly(ADP-ribose) polymerases (PARPs), or ubiquitin ligases. These proteins post-translationally modify their targets (*e.g.*, phosphorylation, poly-ADP-ribosylation, and ubiquitination), which triggers the DDR cascade and recruitment of the repair machinery [214].

Poly(ADP-ribose) polymerase 1 (PARP1) is one of the key factors in the DDR cascade and becomes activated through its interaction with DNA breaks. The regulatory domain of PARP1 recognizes and binds to a DNA break (**Figure 5.1**). Once activated, PARP1 covalently modifies itself and other proteins with long branched polymers of ADP-ribose (PAR). These polymers, in turn, recruit additional DNA repair factors [215,216] (**Figure 5.1**).

Given the essential role of PARP1 in DNA repair, it is generally thought that PARP1 inhibitors could be useful as anti-cancer agents. Specifically, they may enhance the cytotoxic effects of cytotoxic alkylating agents [217]. PARP1 inhibitors generally function by trapping PARP1 in a protein-DNA complex, preventing poly-ADP-ribosylation, and effectively abolishing DNA repair. Consequently, accumulated DNA damage induces cell death, thus potentially eliminating cancer cells. Several studies suggest PARP1 inhibition is particularly

toxic to cancer cell lines and human tumors exhibiting compromised DNA repair systems [217-219]. PARP1 inhibitors may also be utilized to prevent necrotic cell death resulting from PARP1-mediated depletion of nicotinamide adenine dinucleotide (NAD⁺) and ATP energy stores [220].

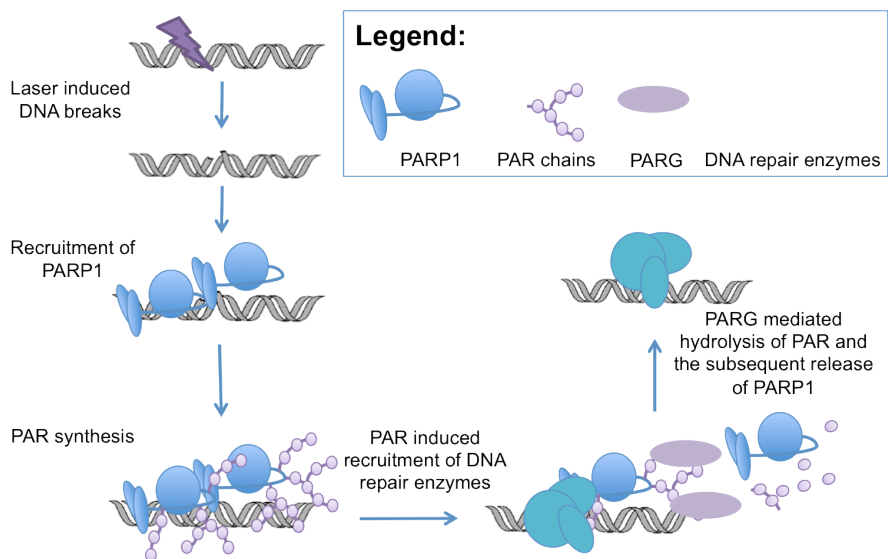


Figure 5.1 Schematic of the PARP1-assisted DNA repair pathway.

Small-molecule inhibitors of PARP1 have been widely investigated for use in anticancer therapies and preventing necrotic diseases. Standard assays for monitoring PARP1 activity rely on antibody-mediated detection of the PARP1's enzymatic end product [221], measurement of the depletion of labeled substrate [222,223], or conversion of NAD⁺ into a highly fluorescent compound [224]. Since these assays require specialized labeling reagents or antibodies, screening small-molecule libraries for inhibitors is costly or impractical. Further, the non-native NAD⁺ substrate analogues may yield non-physiologically relevant results. Therefore, additional bioanalytical tools are required to assess PARP1 activity and facilitate high throughput inhibitor screening in live cells.

We aimed to develop a fluorescent protein (FP)-based biosensor sensitive to PARP1 activity. Since PARP1 mediates recruitment of PAR-binding molecules via PAR chains, we hypothesized that changes in fluorescence intensity or colour

could be coupled to the protein-protein interactions associated with PAR-binding molecules.

In addition to PAR-binding molecules, we investigated interactions mediated by phosphorylation and ubiquitination. Phosphorylation of chromatin proteins by the ataxia telangiectasia mutated (ATM) kinase is triggered by recognition of DNA lesions by PARP1. Phosphorylation, in turn, initiates an ubiquitination-mediated cascade at the sites of DNA damage. Both phosphorylation and ubiquitination amplify the recruiting signal for assembly of the DNA repair complex. Protein-protein interactions related to phosphorylation and ubiquitination will be discussed further in Sections 5.2.5 and 5.2.6.

5.2 Results and discussion

5.2.1 Detection of PARP1 activity *in vitro*

Inspired by an intramolecular FRET-based histone H3 lysine 27 trimethylation biosensor [143], we designed a multi-component biosensor comprised of a FRET pair, a PARP1 substrate domain, and a PAR-binding protein domain. Initially, the substrate and binding domain were linked in tandem and flanked at the N- and C-terminus with fluorescent proteins that participate in FRET (**Figure 5.2**).

Branched PAR is typically linked to PARP1 substrates. We predicted that when PARP1 substrate and PAR-binding proteins are expressed as a single polypeptide, the binding of PAR-binding protein to ‘PAR-ylated’ substrate would cause a conformational change within the fusion protein and thus alter the FRET efficiency (**Figure 5.2**). To design the corresponding fusion protein, mouse histone H2A protein [225] was used as the PARP1 substrate [226], and a mutant of poly(ADP-ribose) glycohydrolase (PARG), which specifically binds to PAR with high micromolar affinity [227], was used as the PAR-binding domain. Specifically, we utilized a catalytically deficient mutant of human PARG (mPARG) that retains high affinity binding to PAR [227]. Furthermore, we tested ECFP-mCitrine and mTFP1-mCitrine fluorescent protein FRET pairs [14]. We

hypothesized that PARP1 activation would trigger PAR modification of H2A, and consequently, the binding of mPARG to PAR would change the distance or orientation between donor and acceptor FPs and lead to a change in emission ratio (**Figure 5.2**). To search for large changes in distance or conformation, different linear arrangements of the H2A, mPARG, and FP domains were investigated. As for illustration, one of the FRET constructs, designated as donor-mPARG-H2A-acceptor is illustrated in **Figure 5.2**. A similar construct without mPARG, namely donor-H2A-acceptor, was also utilized as a control.

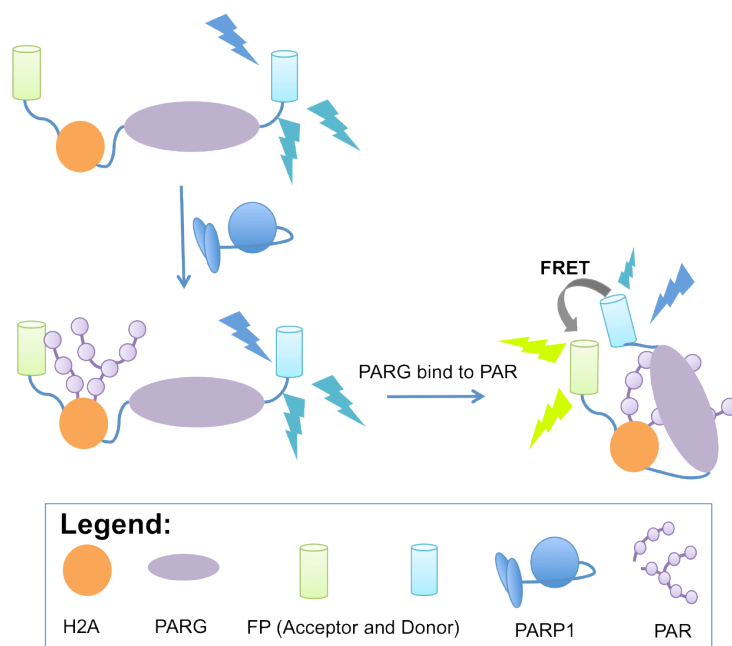


Figure 5.2 Schematic for FRET-based PARP1 biosensor strategy.

A custom dual expression plasmid (credit to Andreas Ibraheem) was used to express the FRET construct and PARP1 together in *E. coli* [143]. The FRET construct and PARP1 were under control of the P_{Tac} and P_{BAD} promoters, respectively. This permitted constitutive expression of the FRET construct and inducible expression of PARP1. After PARP1 induction, the donor FP was excited and emission spectra were collected. Initial experiments showed a significant decrease in the acceptor fluorescence when mPARG was incorporated, relative to when it was left out, suggesting that either the big size of mPARG prevented FRET or the constructs are susceptible to proteolysis (**Figure 5.3A**).

The differences in emission profiles of constructs with or without PARG resulted from the different quantum yield of FP donors, mTFP1 and ECFP, and a larger quantum yield of mTFP1 led to a higher emission intensity.

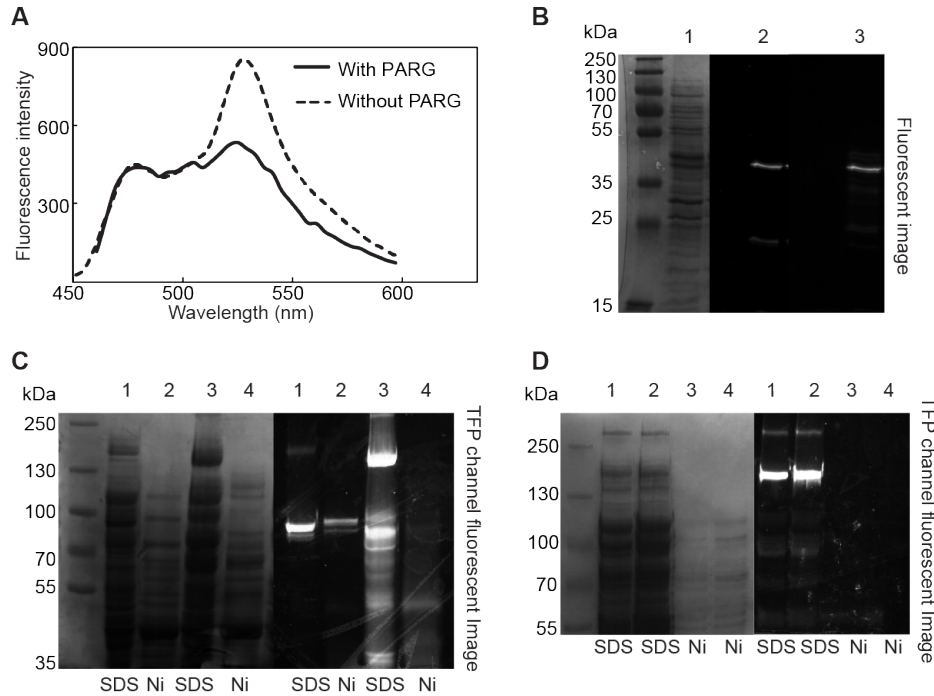


Figure 5.3 Proteolysis of PARP1 and mPARG expressed in *E. coli*.

(A) Emission spectra of donor-mPARG-H2A-acceptor and donor-H2A-acceptor at excitation of 425nm. (B) SDS-PAGE of H2A-donor-acceptor-mPARG (C) and (D) are SDS-PAGE of *E. coli* cell lysates expressing constructs 3 and 4. (C) SDS-PAGE of fusions with catalytic domain of mPARG(397-976) and full-length mPARG(0-976). Lane 1 and 2 are mTFP1-PARG(397-976). Lane 3 and 4 are mTFP1-PARG(0-976). (D) SDS-PAGE of EYFP-PARP1 with and without D214A mutation. Lane 1 and 3 are with D214A mutations and lane 2 and 4 are without D214A mutation. Image on the right is the fluorescent image of the same gel on the left. SDS, cell lysate from SDS treatment. Ni, Ni-NTA purified protein from mild cell lysis.

To investigate the possibility of proteolysis of these biosensor constructs when expressed in *E. coli*, pseudo-native SDS-PAGE was performed. Briefly, protein samples were not boiled prior to electrophoresis, permitting visualization of in-gel fluorescence. In addition, construct H2A-donor-acceptor-mPARG was used in this assay to exclude the possibility of proteolysis of FP pairs. The full-

length FRET construct has an expected molecular weight of 178 kDa. However, we observed one band of lower molecular weight that was fluorescent in both the mTFP1 and YFP channels, indicating the intact fusion of FPs and the presence of a proteolyzed mPARG (**Figure 5.3B left**). The proteolysis of mPARG and PARP1 in *E. coli* led to free diffusing FP donor and acceptor, which accounts for the loss of FRET emission at 535 nm after excitation at 425 nm (**Figure 5.3A**).

Further experiments demonstrated that the PARG-containing constructs were ending up primarily in inclusion bodies when expressed in *E. coli*. Cell lysates from SDS-assisted cell lysis and proteins harvested by mild cell lysis with B-PER and Ni-NTA purification were analyzed by SDS-PAGE. Soluble proteins could be isolated by Ni-NTA purification, while insoluble proteins were released from inclusion bodies by harsh SDS-assisted cell lysis. mTFP1-mPARG was only detected from cell lysate and not the soluble fraction (**lanes 3 and 4, Figure 5.3C**). Thus, we concluded that full-length mPARG was effectively insoluble and was sequestered in inclusion bodies (**Figure 5.3C, lane 3 and 4**). Similarly, PARP1 proteolysis was also detected by SDS-PAGE, as the majority of the protein bands electrophoresed at molecular weights lower than the predicted 137 kDa for EYFP-PARP1 [228].

Various strategies were tested to try and improve bacterial expression and purification of mPARG and PARP1 constructs. First, two putative protease cleavage sites within mPARG were abolished by installing the D253A and D307A mutations [229]. However, these mutations were not sufficient to prevent proteolysis. Second, we expressed only the catalytic domain of mPARG (residues 397-976), which has been reported to be soluble and functional [230]. By fusing mTFP1 to the catalytic domain of mPARG, the expression of intact protein was confirmed by a single fluorescent band ~100 kDa on pseudo-native SDS-PAGE (**Figure 5.3C, lane 1 and 2**). While we were able to successfully express the catalytic domain of mPARG, its recruitment by PAR was lost. This will be discussed further in Section 5.2.2.

To try and improve the bacterial expression of the PARP1 enzyme, we installed the D214A mutation which has been previously reported to block

proteolysis [231,232]. Unfortunately, pseudo-native SDS-PAGE showed the full-length protein was not present in the soluble fraction (**Figure 5.3D, lane 3 and 4**). Similar to mPARG, we only detected full-length PARP1 after strong SDS-assisted lysis, indicating inclusion body sequestration (**Figure 5.3D, lane 1 and 2**). This observation was not entirely a surprise to us, since reports of soluble PARP1 proteins expressed in *E. coli* have been limited to soluble subdomains, such as the DNA binding domain [228].

In addition to the aforementioned obstacles, our intended strategy for designing FRET constructs was also limited by the poor expression of histone H2A. The majority of H2A was found in *E. coli* inclusion bodies, necessitating complicated denaturation and renaturation to arrive at pure proteins [233]. Given their large size and poor solubility, we concluded the expression of full-length FRET biosensor was not tractable. As an alternative, we next aimed to engineer a live cell FP-based biosensor of PARP1 activity.

5.2.2 Confirmation of PARP1 activity in live cells

An existing method to assay PARP1 activity was developed by Trevigen [234]. This assay measures cellular PAR levels using capture ELISA with a monoclonal antibody raised against PAR. The disadvantage of this technique is that it requires the use of cell extracts, which is not conducive to imaging and may not reflect PARP1 activity in live cells. Our goal was to build a biosensor that reports PARP1 activity using a change in fluorescence intensity in live cells. The basis for our design was the protein complex formed at sites of DNA damage. Within the complex, a large number of PARP1, PARG and other DNA damage-associated proteins are assembled in close proximity. Due to the close proximity, we hypothesized the recruited proteins could be utilized to design a FRET-type or ddFP-type biosensor for reporting PARP1 activity.

Before constructing biosensors, we wanted to first validate the recruitment of PARP1 and mPARG after DNA damage was induced. Both PARP1 and mPARG were fused to FPs (YFP and mTFP, respectively) to enable real-time

visualization of PARP1 recruitment and activation. DNA lesions were introduced by microirradiating live cells with a violet laser.

HeLa cells were transfected with the plasmids encoding the EYFP-PARP fusion and yellow fluorescence was observed throughout the nucleus (**Figure 5.4C**). After microirradiation with 405 nm laser light, a rapid increase in fluorescence was observed and discretely localized at the site of irradiation, indicating the accumulation of EYFP-PARP1 at damaged DNA sites (**Figure 5.4A,C**). A decrease in fluorescence intensity was observed in non-irradiated areas (**Figure 5.4B,C**). These results are consistent with previous reports [235]. Localized accumulation of EYFP-PARP1 was transient and the protein redistributed away from the irradiated site over a timescale of minutes. Specifically, fluorescence intensity decreased after reaching a maximum at 1 min after microirradiation (**Figure 5.4A inset**), matching the reported *in vivo* half-life of PAR [236]. We also aimed to visualize the accumulation of mutated PARG (mPARG). In HeLa cells transfected with a plasmid encoding a mTFP1-mPARG fusion, we observed a 2.5-fold increase in fluorescence intensity after microirradiation (**Figure 5.4D,E,F**), indicating the quick synthesis of PAR chains followed by recruitment of mPARG to these sites [237]. Compared to PARP1, mPARG accumulated with slower kinetics (*i.e.*, 2 min for mPARG versus 1 min for PARP1) and did not redistribute as rapidly. mPARG also accumulated but to a larger extent as indicated by the larger increase in fluorescence intensity observed for mPARG relative to PARP1 (**Figure 5.4D,E**). Since PARG was more efficiently recruited than PARP1, we speculate that the rapid disassembly of the PAR chain by native PARG caused the release of EYFP-PARP1 [237].

In addition to the mTFP1-mPARG fusion, we also generated fusions with the FP component oriented at the C-terminus (*e.g.*, mPARG-mCitrine), and tested these fusions with live cell imaging. As with the N-terminal fusions, rapid accumulation of the fusion protein was observed in the irradiated area (**Figure 5.5A**). However, these fusions accumulated to a lesser extent relative to mTFP1-mPARG. Thus, only fusions with N-terminal FP fusions (*i.e.*, FP-mPARG) were used in subsequent experiments.

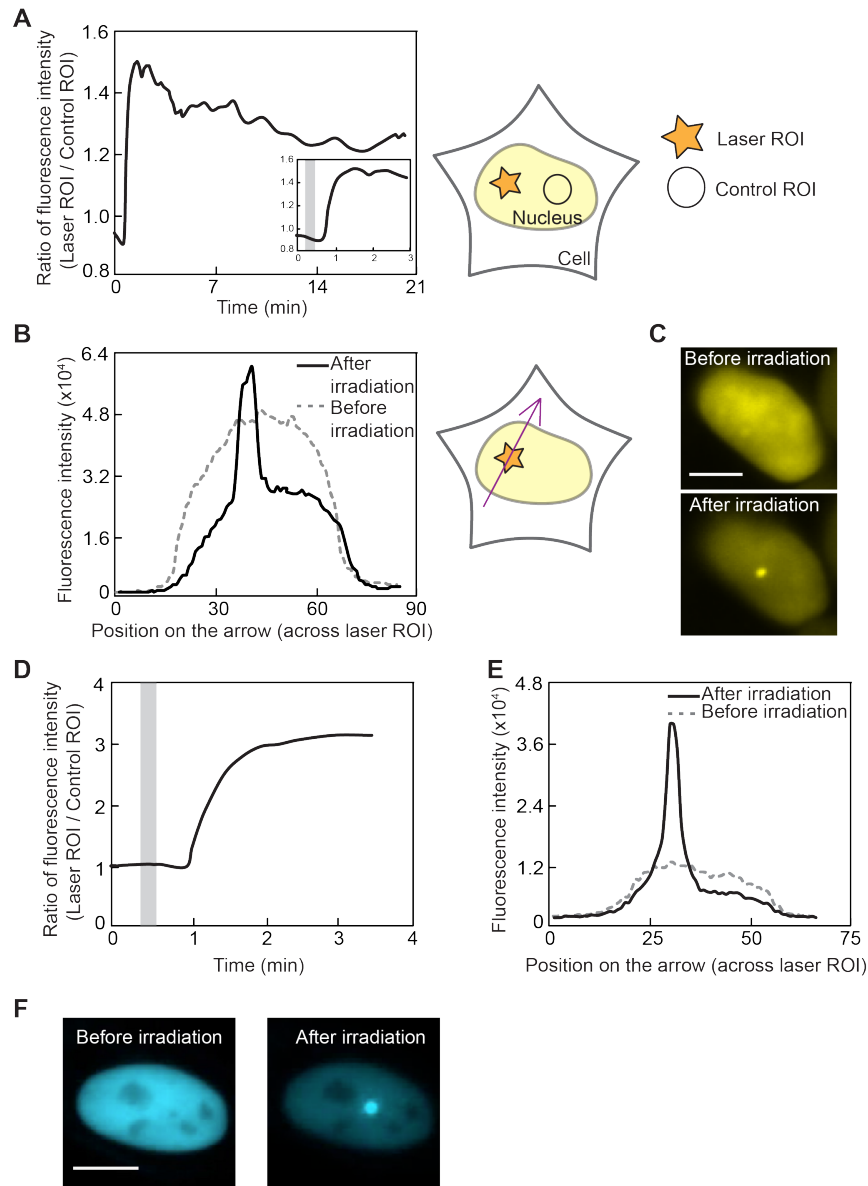


Figure 5.4 Recruitment of PARP1 and mPARG after microirradiation.

(A), (B) and (C) Recruitment of EYFP-PARP1 after microirradiation. (D), (E) and (F) Recruitment of mTFP1-mPARG after microirradiation. (A) and (C) Intensity ratio vs. time for the regions of interest (ROIs) indicated in schematic on the right. X-axis is time elapsed since the cells were treated by microirradiation in the laser ROI. Time of microirradiation is shown in the grey area. (B) and (D) Intensity profile of transfected HeLa cells. Area of intensity profile is indicated by an arrow across the DNA damage site as illustrated in the schematic. (C) and (E) Live cell images before and after microirradiation. Scale bar represents 10 μm .

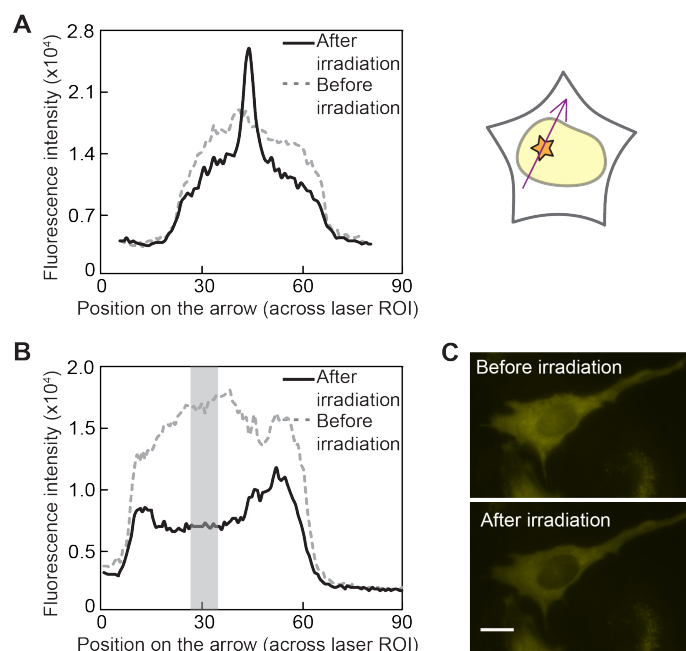


Figure 5.5 Recruitment of C-terminus FP fusions and catalytic domain of mPARG after microirradiation.

(A) and (B) Intensity profile of the area indicated by an arrow. The arrow is across the DNA damage site as indicated in the schematic. (A) Intensity profile of mPARG-mCitrine. Area of the peak matches the DNA damage site. (B) Intensity profile of mCitrine-mPARG(397-976). Area of microirradiation is shown in the grey area. (C) Live cell images of mCitrine-mPARG(397-976) before and after microirradiation. Scale bar represents 10 μ m.

The catalytic domain of mPARG (residues 397-976, as discussed in section 5.2.1) was also assessed for its recruitment to PAR chains at DNA damage sites. Briefly, mPARG (397-976) was fused to mCitrine and the gene was expressed in cells. Since it lacks a regulatory domain, mCitrine-mPARG(397-976) was ubiquitously distributed in the cell rather than only in the nucleus (**Figure 5.5B**) as was observed for full length mPARG. After microirradiation, mCitrine-mPARG(397-976) did not exhibit the expected localization pattern, but was instead photobleached (**Figure 5.5C**). For this reason, mPARG(397-976) was not used in subsequent experiments in favor of the full-length mPARG fusion.

5.2.3 Detection of PARP1 activity via FRET in live cells

In section 5.2.2 we showed the recruitment of PARP1 or mPARG in response to DNA damage. However, this redistribution of the FPs does not alter the overall fluorescence intensity from the cell and is therefore not useful for high-throughput assays of PARP1 activity. Preferably, the potential interactions between recruited proteins should be reported as an overall change in total intensity for the whole cell or a change in emission ratio. A FRET-based biosensor represents one approach for developing an indicator that could change its emission ratio and thus be useful for high-throughput screening.

We first attempted to generate a FRET biosensor utilizing the potential protein-protein interactions among the PAR binding protein, mPARG. Two types of FRET designs were implemented. In both designs mTFP1 and mCitrine were used as donor and acceptor, respectively. The first design relied on intermolecular FRET between two independent fusions: mTFP1-mPARG and mCitrine-mPARG. The second design utilized a single fusion of mTFP1-mPARG-mCitrine that could presumably participate in both intra- and intermolecular FRET.

To test the first (intermolecular) design, we coexpressed mTFP1-mPARG and mCitrine-mPARG fusions in HeLa cells. Prior to illumination, we observed an even distribution of cyan and yellow fluorescence throughout the nucleus (similar to **Figure 5.4F**). Furthermore, we consistently observed the accumulation of mPARG after microirradiation as indicated by a 2.5-fold increase in both mTFP1 and mCitrine fluorescence intensity in irradiated areas relative to non-irradiated areas (**Figure 5.6A**). We had expected that, after recruitment to the site of the DNA damage, mTFP1 to mCitrine FRET would be observed. This would be indicated by a decrease in mTFP1 intensity and an increase in sensitized emission from mCitrine. Disappointingly, we observed only a very small change in the intensity ratio of FRET and donor, relative to the ratio outside of the area of DNA damage (shown in the grey area of **Figure 5.6B**). We speculate that the FRET between N-terminally fused FPs could be hindered from the relatively large size of the mPARG protein.

To address this potential problem, we turned to our second design consisting of a single mTFP1-mPARG-mCitrine fusion. By fusing FPs to both termini of mPARG, we expected to increase the likelihood of bringing donors and acceptors into close proximity upon binding of multiple copies of mPARG to PAR at the site of DNA damage. Unfortunately, this biosensor design also failed to exhibit a substantial change in emission intensity ratios (**Figure 5.6C,D**).

Although we did not observe the large changes in emission ratio that we had hoped for, a small increase in ratio of approximately 15~20% was consistently detected at the site of illumination. To distill the cause of this increase, we performed control experiments in which only mTFP1-mPARG was expressed but the mTFP1 and FRET emission channels were monitored (**Figure 5.6E,F**). As previously reported (Section 2.2.5), a 35% bleedthrough of mTFP1 signal into the FRET channel was detected (**Figure 5.6E**). In contrast to the FRET constructs (**Figure 5.6B,D**), we noticed a 5% drop in the intensity ratio at sites of DNA damage following microirradiation (**Figure 5.6F**). We attributed the 5% drop to photobleaching both of mTFP1 and endogenous autofluorescent molecules that contribute to the fluorescent background. Together, the 5% drop in the control and the 20% increase in emission ratio due to FRET led us to conclude that recruited the FPs fused to the mPARG molecules were being brought together at a distance close to the 10 nm functional detection range limit for FRET.

In addition to trying to use FRET to detect the close proximity of mPARG proteins, we also tried to determine if mPARG was in close proximity to PARP1 at DNA damage sites. Fusions of EYFP-PARP1 and mTFP1-mPARG were coexpressed in HeLa cells followed by microirradiation. Both fusion proteins accumulated in irradiated areas, with mTFP1-mPARG accumulating to a greater extent (**Figure 5.7A**). Comparison of the emission intensity ratios for each fluorescent channel (**Figure 5.7B**) revealed a larger increase of intensity ratio over time for the mTFP1-mPARG fusion, indicating that this protein is recruited to a greater extent (**Figure 5.7B**). We also compared the intensity ratios of the FRET channel divided by the donor channel in either irradiated or non-irradiated control areas (**Figure 5.7C**). A gradually decrease of FRET/mTFP1 ratio in the

irradiated area and a relatively constant FRET/mTFP1 ratio in non-irradiated control area was detected (**Figure 5.7C**).

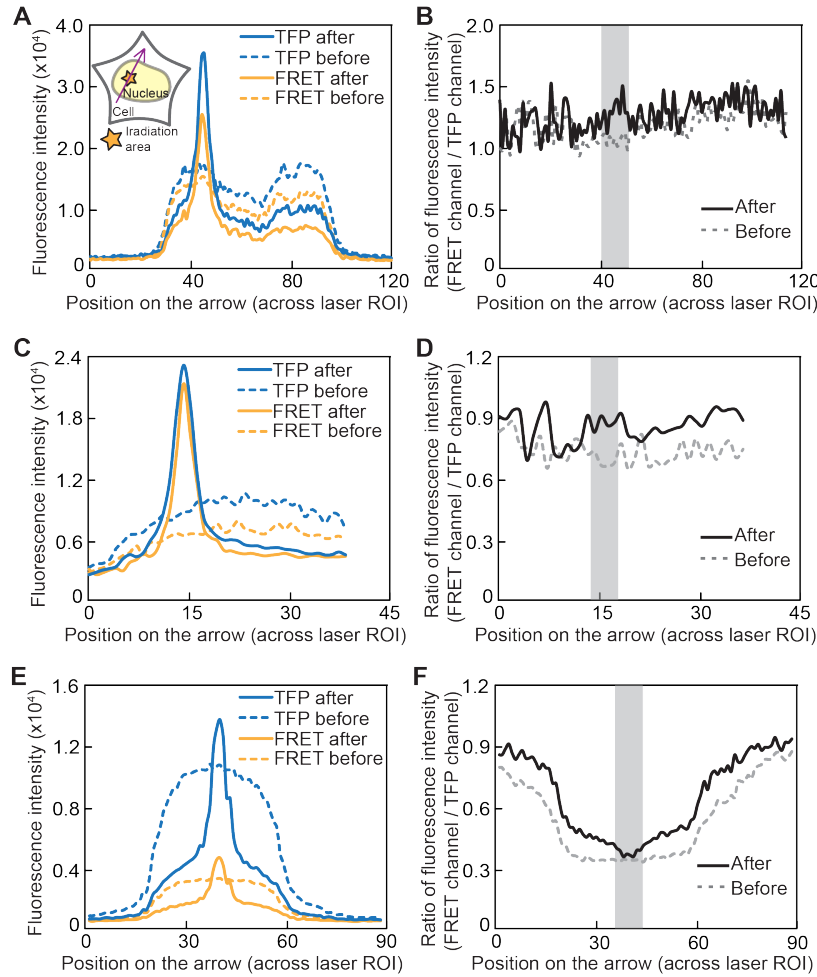


Figure 5.6 FRET analysis with protein fusions of FP and mPARG

(A) Intensity profile of cells co-transfected with mTFP1-mPARG and mCitrine-mPARG shown in both mTFP1 and FRET channel. An arrow indicates profile area across the DNA damage site as indicated in the schematic. (B) Intensity ratio of (A). (C) Intensity profile of cells transfected with mTFP1-mPARG-mCitrine is shown in both mTFP1 and FRET channel. (D) Intensity ratio of (C). (E) Intensity profile of cells transfected with mTFP1-mPARG is shown in both mTFP1 and FRET channel. (F) Intensity ratio of (E). Area of microirradiation is shown in the grey area.

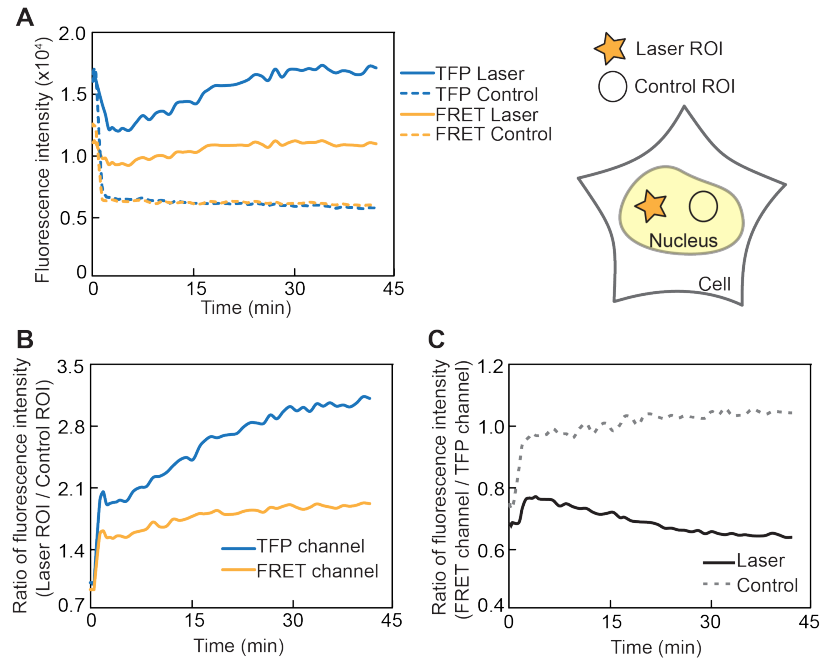


Figure 5.7 FRET analysis of cells coexpressing EYFP-PAPP1 and mTFP1-mPARG before and after microirradiation.

(A) Intensity vs. time is shown in both mTFP1 and FRET channel. Laser and control ROIs are indicated in the schematic. (B) Intensity ratio vs. time is plotted by different channel. ‘TFP channel’ equals intensity of ‘TFP laser’ divided by ‘TFP control’ from (A). ‘FRET channel’ is calculated by the same method. (C) Intensity ratio vs. time is plotted by different ROIs. ‘Laser’ equals intensity of ‘FRET laser’ divided by ‘TFP laser’ from (A). ‘Control’ is calculated by the same method.

We speculated that the decrease in the irradiated area was due to release of EYFP-PARP1 proteins after hydrolysis of PAR chains by endogenous PARG. Unfortunately, due to the imbalance of recruited molecules and different kinetics, we could not confidently conclude that FRET between mTFP1-mPARG and EYFP-PARP1 molecules was occurring.

5.2.4 Detection of PARP1 activity using dimerization-dependent fluorescent protein technology in live cells

Since we were unable to use FRET as a robust readout for clustering of mPARG and PARP1 at sites of DNA damage, we turned to our dimerization-dependent FPs (ddFPs) as an alternative detection strategy. DdFP biosensors rely

on the reversible binding of two non- (or weakly) fluorescent monomeric FP partners to form a strongly fluorescent heterodimer [60,61] (Section 3.1). When ddFP partners are expressed at concentrations well below their K_d , the heterodimer does not form to a significant extent and so little fluorescence results. However, if the ddFP partners are spatially confined (*e.g.*, due to clustering of mPARG at sites of DNA damage) and their effective concentration exceeds their K_d , they will heterodimerize with an intensimetric increase in fluorescence. DdFP partners are designated as copy A and copy B, with the heterodimer designated as AB. We fused copy A and copy B independently to mPARG to generate two fusions. These fusions should be brought into close proximity when recruited to sites of DNA damage, increasing the concentration of both copy A and copy B, thus driving fluorogenic heterodimerization. By monitoring the intensimetric change, this biosensor should enable detection PARP1 activity.

ddFPs have been engineered as red and green colour variants [60,61]. We fused both the red and green ddFP monomers to the N-terminus of mPARG, creating the following fusions: ddRFP A-mPARG, ddRFP B-mPARG, ddGFP A-mPARG and ddGFP B-mPARG. When we co-expressed ddGFP A-mPARG and ddGFP B-mPARG in HeLa cells, we observed only a weak fluorescence signal before microirradiation, as expected. After microirradiation, a 5-fold increase in fluorescence intensity was detected at DNA damage site as shown in **Figure 5.8A**. A similar result was captured using the red ddFP variants (**Figure 5.8B**). Unfortunately, the 5-fold increase is approximately the same as what we observed for accumulation of an FP-PARG fusion (as described in Section 5.4.2). This led us to conclude that the increases we were observing were due simply to the increased concentration of the weakly fluorescent A copy at the site of DNA damage. If heterodimerization were occurring, we would have expected to observe an additional increase (possibly ~10-fold) above and beyond the increase due to localization alone.

We hypothesized that the linker between the ddFP monomer and mPARG was limiting the ability of the ddFP monomers to access each other and form heterodimers. To test this idea, a 40-residue unstructured linker (~10 nm)

[204,205] was inserted between ddFP and mPARG. Promisingly, this design moderately increased the intensity change to approximately 9-fold in some cells (**Figure 5.8C**). This improvement inspired us to try longer linkers. Accordingly, we made concatenated linkers of the existing linker to generate both 80- and 160-residue linkers. Unfortunately, these extended linker fusions did not further improve the intensimetric change. Taking all variants with 40-, 80- or 160-residue linker into consideration, the best fluorescence intensity increases were limited to ~8-fold changes, with average fluorescence intensity increases of 6.2 ± 2.4 -fold (n=14 cells) with ddGFP fusions and 5.6 ± 2.0 -fold (n=12 cells) with ddRFP fusions. Both results paralleled the 5.5 ± 1.8 -fold increase (n=12 cells) achieved using mTFP1-mPARG. Thus, we concluded that the use of ddFPs did not improve the detection of PARP1 activity.

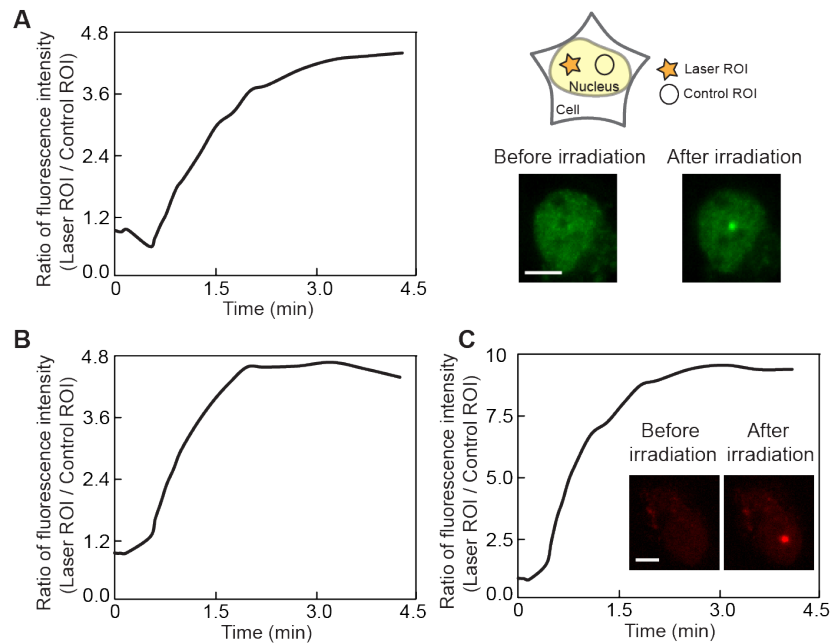


Figure 5.8 Recruitment of ddFP-mPARG proteins after microirradiation.

(A) Intensity ratio vs. time of cell cotransfected with ddGFP A-mPARG and ddGFP B-mPARG. (B) Intensity ratio vs. time of cell cotransfected with ddRFP A-mPARG and ddRFP B-mPARG. ROIs are indicated in schematic of (A). X-axis is time elapsed since the cells were treated by microirradiation in the laser ROI. (A) Intensity ratio vs. time of cell cotransfected with ddGFP A-linker-mPARG and ddGFP B-linker-mPARG. Scale bar represents 10 μ m.

5.2.5 Validation DNA damage with ATM and PARP1 inhibitors

The failure of both FRET and ddFP-type biosensors to robustly detect PARP1 activity fostered a concern that microirradiation was not generating DNA breaks. To confirm the presence of DNA damage, we tested the behavior of our biosensors in the presence of PARP1 inhibitors.

HeLa cells expressing EYFP-PARP1 were treated with the PARP1 inhibitor, AG14361 [238,239], and analyzed for intensimetric changes upon laser-induced DNA damage. After microirradiation, we did not observe a significant change in EYFP-PARP1 recruitment (**Figure 5.9A**) in the presence of the inhibitor relative to cells not treated with inhibitor (**Figure 5.4A inset**). We did, however, observe a delay in reaching the maximum accumulation of PARP1 in the presence of the inhibitor (**Figure 5.9A**). To test its inhibitory effect on poly-ADP ribosylation, we treated HeLa cells expressing mTFP1-mPARG with AG14361. We observed a slower accumulation of mTFP1-mPARG, which is consistent with decreased PARP1 activity due to inhibition [238,239] (**Figure 5.9B**).

To further enhance the inhibitory effect, a kinase inhibitor, specific for inhibiting ataxia telangiectasia mutated (ATM) kinase, was used in combination with AG14361. During the DNA damage response, ATM initiates and amplifies the recruiting signal by phosphorylating H2A at serine 139. This initiates a complex cascade leading to PARP1 activation [240]. Accordingly, the ATM inhibitor, Ku 0055933 [241,242], was expected to block PARP1 activation and thus prevent mPARG recruitment. We monitored the response of FP-PARP1 and FP-mPARG fusions to microirradiation in the presence of AG14361 and Ku 0055933. We did not observe any effect on the recruitment of EYFP-PARP1 (**Figure 5.9C**), but we did detect a delay in mTFP1-mPARG recruitment. This indicated that the activity of PARP1 was inhibited but it was still being recruited to the site of damage, as expected (**Figure 5.9D, Table 5.1**).

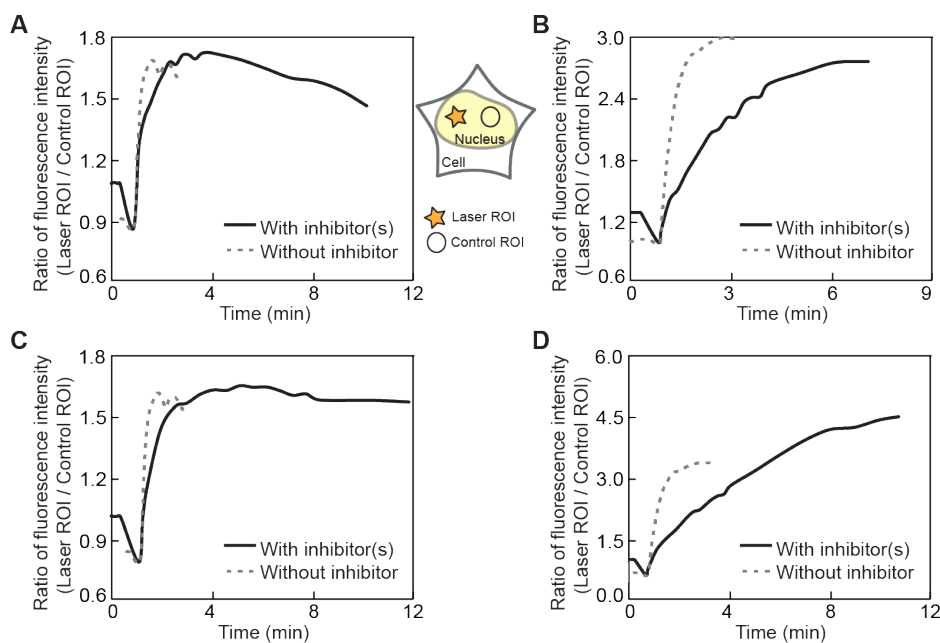


Figure 5.9 Recruitment of PARP1 and mPARG fusions with the treatment of inhibitors.

(A) Intensity ratio vs. time of cell transfected with EYFP-PARP1 and treated by PARP1 inhibitor. (B) Intensity ratio vs. time of cell transfected with mTFP1-mPARG and treated by PARP1 inhibitor. (C) Intensity ratio vs. time of cell transfected with EYFP-PARP1 and treated by both ATM and PARP1 inhibitor. (D) Intensity ratio vs. time of cell transfected with mTFP1-mPARG and treated by both ATM and PARP1 inhibitor. ROIs are indicated in schematic of (A). X-axis is time elapsed since the cells were treated by microirradiation in the laser ROI. Time of microirradiation is shown in the grey area. Data for the control experiments without inhibitors are adapted from Figure 5.4A and D.

Table 5.1 Comparison of DNA damage response with and without inhibitors

Inhibitor used	Time to reach maximum intensity*		
	None	PARP1 inhibitor	ATM inhibitor, PARP1 inhibitor
EYFP-PARP	< 1min	1min	1min
mTFP1-PARG	1.5min	6min	8~10min

*After microirradiation; All numbers are approximate.

In general, the inhibitors only slightly reduced PARP1 accumulation after DNA damage, but substantially inhibited the PAR synthesis and, thus, delayed the accumulation of additional proteins. Collectively, our observations were consistent with reported inhibitor studies [238-240], thus confirming our microirradiation method was inducing DNA damage and the PARP1-catalyzed formation of PAR.

5.2.6 Detection of polyubiquitin chains in live cells

Similar to how we had attempted to detect PARP1 activity in live cells by binding proteins to the polymeric PAR chain, we next attempted to detect an alternative polymeric chain, polyubiquitin ($n > 10$) [243]. As a small protein-modifier, ubiquitin acts as a versatile cellular signal in degradative and nondegradative biological processes, such as protein degradation, DNA repair, transcription, and inflammation [244]. This ubiquitin signaling is achieved by conjugated modification of substrates with monoubiquitin or polyubiquitin assembled by the linkage through the C-terminus lysine. Specifically, polyubiquitination on lysine 48 leads to degradation of the substrate protein [245], whereas, lysine 63-linked polyubiquitin and monoubiquitin mainly participate in nondegradative signaling pathways (*e.g.*, endocytosis and DNA repair) [246]. For the scope of this chapter, we focused on polyubiquitination on lysine 63 of H2Ax, which plays an essential role responding to DNA damage by recruiting DNA repair enzymes to polyubiquitinated sites [214].

To determine if the size of the recruited molecules affected the interactions of the ddFPs, we utilized two differently sized polyubiquitin-binding proteins. The first protein, called receptor-associated protein 80 (RAP80) [247], is a nuclear protein containing two ubiquitin-interacting motifs (UIMs) and is comprised of 720 amino acids [248,249]. The second protein, called SuperUIMs [250], is a tandem repeat of three UIMs comprising just 113 amino acids [248]. RAP80 exhibits high micromolar affinity for ubiquitin, while SuperUIMs exhibit nanomolar affinity [248,250]. Given its smaller size and higher affinity, we expected SuperUIMs would pack more densely than RAP80, and the

corresponding close proximity would enable detection using FRET or ddFP-based biosensors.

To test our hypothesis, both RAP80 and SuperUIMs were fused to the N-terminus of FPs. When Rap80-mCitrine was expressed in HeLa cells, fluorescence was localized to the nucleus (**Figure 5.10A inset**). After microirradiation, recruitment of RAP80 to the DNA damage site was observed after 20 min and increased with time (**Figure 5.10A**). Compared to the non-irradiated area, a 1.3-fold increase of intensity was observed in the irradiated area, indicating the recruitment of RAP80 (**Figure 5.10B**). A similar result was observed in HeLa cells expressing both RAP80-ddGFP A and RAP80-ddGFP B (**Figure 5.10C**). In addition, no increase in FRET was observed from HeLa cells co-expressing both Rap80-ECFP and Rap80-mCitrine (data not shown). Due to the large size of RAP80 (80kDa) [247], the poor intensity changes associated with RAP80 were not unexpected. We next evaluated the ability of SuperUIMs to behave as polyubiquitination sensors.

We fused SuperUIM to FPs to generate SuperUIM-FP fusions and the localization of the fusions was imaged before and after microirradiation. These fusions accumulated at DNA damage sites after microirradiation, but only exhibited a 2-fold increase in fluorescence intensity (**Figure 5.10D**). This was comparable to the 1.3-fold fluorescence increase of RAP80-FP fusions (**Figure 5.10B**). Co-expression of SuperUIMs-ddGFP A and SuperUIMs-ddGFP B in HeLa cells, failed to detect increases in fluorescence intensity above 2-fold (**Figure 5.10E**), indicating relocalization of existed heterodimer rather than heterodimer formation in situ. Likewise, no change in FRET signal was collected from HeLa cells expressing both SuperUIMs-ECFP and SuperUIMs-mCitrine (**Figure 5.10F**).

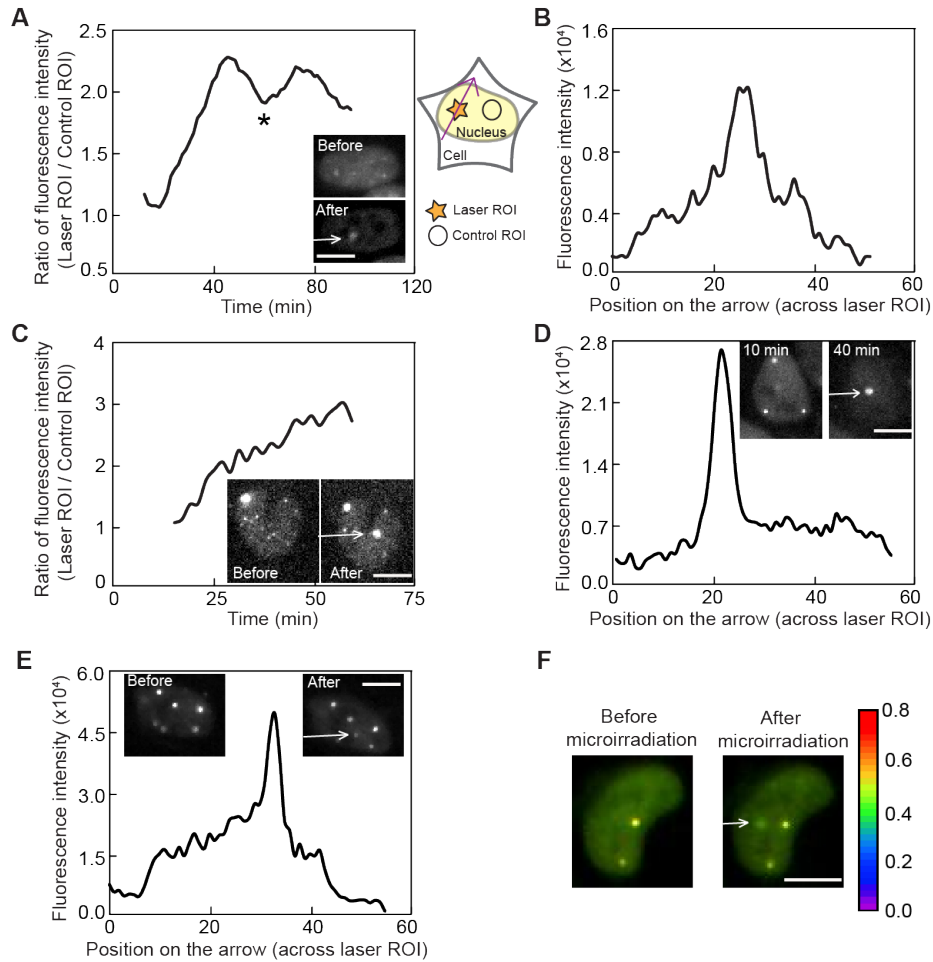


Figure 5.10 Recruitment of fusions with Rap80 or SuperUIMs after microirradiation.

All ROIs are indicated in schematic. Area of intensity profile is indicated by an arrow across the DNA damage site as illustrated in the schematic. (A) Intensity ratio vs. time of cell expressing Rap80-mCitrine. X-axis is time elapsed since the cell were treated by microirradiation in the laser ROI. The sudden drop at 60 min in the graph was due to the lost of focus over time. (B) Intensity profile of (A). (C) Intensity ratio vs. time of cell co-expressing RAP80-ddGFP A and RAP80-ddGFP B. X-axis is time elapsed since the cell were treated by microirradiation in the laser ROI. (D) Intensity profile of cell expressing SuperUIMs-mCitrine. (E) Intensity profile of cell coexpressing SuperUIMs-ddGFP A and SuperUIMs-ddGFP B. (F) Ratiometric images of cell co-expressing SuperUIMs-ECFP and SuperUIMs- mCitrine. Scale bar represents 10 μ m.

5.3 Conclusion

Our initial goal was to develop a PARP1 biosensor suitable for either *in vitro* or cell-based high-throughput screening of anti-cancer PARP1 inhibitors. We designed biosensors based on FRET- and ddFP-type strategies, but unfortunately our designs failed to provide sufficient changes in FRET efficiency or fluorescence intensity to make them practically useful.

Although our biosensors did not provide optimal fluorescent reporter characteristics, they did prove successful to visualize recruitment of PARP1 and mPARG to sites of DNA damage. Thorough biochemical analysis confirmed the distance between recruited proteins was close to the limits of the functional detection range of FRET. Experiments with polyubiquitin binding proteins suggested that the size of the recruited protein size was not the crucial issue that was limiting FRET or the formation of heterodimers. Indeed, even when we introduced extremely long linkers we were unable to find evidence of heterodimer formation.

The major puzzle to emerge from this work is why did the attempted biosensor designs fail. We suspect that for the FRET-based biosensors, the FPs were simply too far apart to engage in efficient FRET. However, this same issue should not have prevented the ddFPs from working under similar situations, since the two proteins retain affinity for each other and very long linkers were used. The major assumptions that led us to believe that the ddFPs should have been successful are: 1) the concentrations of the ddFPs monomers in the dim fluorescent cells that we imaged were below the *in vitro* measured K_d s of the ddFPs (*i.e.*, $\sim 30 \mu\text{M}$ for ddGFP and $\sim 1 \mu\text{M}$ for ddRFP); 2) the concentration of ddFP-mPARG fusions at the site of DNA damage is substantially higher than the free concentration in the nucleus; and 3) the intracellular K_d is the same as the *in vitro* K_d . Our currently preferred explanation for why this strategy failed is that the 3rd assumption does not hold due to macromolecular crowding effects [251]. Accordingly, even though the ddFP proteins are expressed at concentrations below their K_d , they are already largely heterodimerized even before DNA

damage is induced. It is for this reason that we do not see the ‘extra’ fluorescence increase due to heterodimerization at the site of DNA damage.

5.4 Material and methods

5.4.1 General methods and materials

All synthetic oligonucleotides for cloning were purchased from Integrated DNA Technologies (IDT, Coralville, IA). Polymerase chain reaction (PCR) was performed using Pfu DNA polymerase (Fermentas) according to the provided manufacturers’ protocols. FastDigest restriction endonucleases (Fermentas) were used for restriction digests of PCR products and analytical DNA digestion. GeneJET gel extraction kit (Fermentas) or QIAquick Gel-Extraction kit (Qiagen) was used for DNA purification following agarose gel electrophoresis. DNA ligation was carried out using T4 DNA ligase (Invitrogen). *E. coli* strain ElectroMAX DH10B (Invitrogen) was used for routine plasmid propagation, library construction and screening, and recombinant protein production. The cDNA sequences were confirmed by dye terminator cycle sequencing using the BigDye (Applied Biosciences) cycle Sequencing Kit. Sequencing reactions were analyzed at the University of Alberta Molecular Biology Service Unit (MBSU) at the University of Alberta.

5.4.2 Construction of *in vitro* PARP1 biosensors

Genes of human PARP1, mutated human PARG (mPARG) and mouse histone H2A were kind gifts of Dr. Michael J. Hendzel. Before the amplification of genes encoding PARP1 and mPARG, QuikChange Site-Directed Mutagenesis Kit (Agilent Technologies) was used to perform site-directed mutations to remove the build-in restriction sites. Gene of PARP1 was then cloned between 5’ *EcoRI* and 3’ *BglII* sites and ligated into an *EcoRI/BglII* digested dual expression plasmid (credit to Andreas Ibraheem). This custom *E. coli* dual expression

plasmid contained an *EcoRI/BglIII* polylinker under control of P_{BAD} and an *XhoI/HindIII* polylinker under control of P_{Tac}.

The constructs of FRET biosensors were built by fusing genes of two FPs (mTFP1 and mCitrine), mouse H2A and mPARG together. Using the assembly of construct 1 as example, H2A gene was amplified using a 5' primer with an *XhoI* site and a 3' primer with an *XbaI* site followed by an 18 bp overhang of 5' mTFP1 sequence, while mTFP1 was cloned between 5' *XbaI* and 3' *Sall* sites. To anneal H2A and mTFP1 together, an over extension PCR was performed. A mixture of PCR products from cloning H2A and mTFP1 acting as template, along with the 5' H2A primer with an *XhoI* site and 3' mTFP1 primer with a *Sall* site, were used to amplify the full-length gene of H2A-TFP. The other FP, mCitrine, was amplified using a 5' primer with both *Sall* and *KpnI* sites and a 3' primer with a *HindIII* site, and was digested by *Sall/HindIII*. After a three-part ligation with the *XhoI/HindIII* digested dual expression plasmid, genes encoding H2A, mTFP1 and mCitrine was incorporated into the plasmid. The final step was to insert *Sall/KpnI* digested gene of mPARG into the *Sall/KpnI* polylinker before mCitrine. Constructs were designed with convenient restriction sites to permit swapping of genes as required. The general cloning strategy for other construct is outlined in **Table 5.2**. Restriction enzyme sites used to clone the designated constructs are provided in the table.

Plasmids were transformed into electrocompetent DH10B *E. coli* and plated to LB agar media supplemented with 400 µg/ml ampicillin and L-arabinose (0.02%). Colonies were picked and cultured in LB supplemented with 100 µg/ml ampicillin and L- arabinose (0.02%) overnight at 37°C.

5.4.3 Protein purification

To obtain purified proteins, the genes for the four FRET constructs from dual expression vectors were sub-cloned into a pBAD/HisB vector and used to transform *E. coli*. Cultures at an optical density of 0.5-0.7 were induced with 0.02% L-arabinose and allowed to incubate a further 12-16 hrs with shaking at

28°C. Cell pellets were resuspended in 10 mM Tris-Cl and 0.5 M NaCl pH 7.4 and lysed using a cell disrupter (Constant Systems Ltd.). Cleared lysates were obtained by centrifugation at 13,000 rpm in 50 ml conical tubes for 50 minutes. Lysates were incubated with Nickel-NTA on ice with agitation for 30 minutes and then batch purified through a fritted column using a vacuum manifold. Protein-bound resin was washed several times with a total of 50 mL 5 mM Tris-Cl, 0.5 M NaCl, 20 mM imidazole pH 8.0. The final 10 mL of wash was performed by gravity flow. Proteins were eluted using 5 mM Tris-Cl, 0.5 M NaCl, 250 mM imidazole pH 8.0 and analyzed by SDS-PAGE.

Sodium dodecyl sulfate polyacrylamide gel electrophoresis (SDS-PAGE) was performed (5% stacking gel/10% resolving gel) according to reported method [252], except samples were not heated prior to electrophoresis. Protein samples were prepared with 1x sample buffer (62.5 mM Tris-Cl pH 6.8, 2% SDS, 7.5% glycerol, 0.02% bromophenol blue). Gels were analyzed for in-gel fluorescence using digital imaging with appropriate filters (excitation 436/20 nm; emission 480/40 and 535/30 nm).

5.4.4 Construction of mammalian expression plasmids

A modified pcDNA3.1(+) (Invitrogen) plasmid, with an *XhoI* and an *HindIII* sites in the same reading frame as the equivalent sites of the pBAD/His B plasmid, was used for mammalian cell expression. Gene of RAP80 was a kind gift from Dr. J.N. Mark Glover. Reported NLS-Vx3 peptide [250] was the template for SuperUIMs and it was a kind gift from Dr. Michael J. Hendzel. Before cloning, Quikchange reactions were performed to remove the *HindIII* site from SuperUIMs gene and the *KpnI* site from RAP80 gene. The general cloning strategy for each construct is outlined in **Table 5.3**. Generally, three-part ligations were used to incorporate the fusions into pcDNA3.1(+) vector.

The unstructured 40-residue linker sequence corresponded to residues 95 to 135 of phage λ repressor [204,205] (source: *HindIII*-digested Lambda DNA, Invitrogen/Life technologies). The doublet and quadruplicated linker was created

through a ligation between compatible cohesive ends of *BamHI* and *BglIII* sites. Specifically, a plasmid encoding the 40-residue linker between between *BglIII/KpnI* sites was used as template, amplified by two sets of primers. One set of primers contained a 5' pBAD sequencing primer and a 3' *BamHI* primer, and the other set contained a 5' *BglIII* primer and 3' pBAD sequencing primer. Products from the two amplifications were digested by *BamHI* and *BglIII* restriction enzymes, respectively. Then, the doublet linker was created by fusing the two fragments together via the compatible cohesive ends. Likewise, the quadruplicated linker was made by using doublet linker as template. At the end, the products were digested by *BglIII/KpnI* and incorporated between ddGFP and mPARG in pcDNA3.1(+) vector.

5.4.5 Mammalian cell culture and imaging

All DNA for mammalian cell transfection was purified by the Plasmid Mini-prep kit (Fermentas). HeLa cells were maintained in Dulbecco's Modified Eagle Medium (DMEM) supplemented with 10% fetal bovine serum and glutamax (Invitrogen) at 37°C and 5% CO₂. Transient transfections of pcDNA3.1 (+) expression plasmids were performed using Turbofect Protein Transfection Reagent (Thermoscientific). Cells in 35 mm imaging dishes were incubated with 1 mL of DMEM (FBS free) for 10 min and then transfected with 1 µg of plasmid DNA that had been mixed with 2 µL of Turbofect (Fermentas) in 0.1 mL of DMEM (FBS free). When two plasmids were co-transfected, 0.5 µg of plasmid A and 0.5 µg of plasmid B were used. The culture media was changed back to DMEM with 10% FBS after 2 h incubation at 37°C. 24 hours post-transfection, transfected Hela cells were subject to imaging. Regarding to the experiments with inhibitors, transfected Hela cells were incubated with 2.5µM PARP inhibitor (AG 14361) or/and 10 µM ATM inhibitor (Ku 0055933) for 2, 24 or 48 hours prior to imaging [241,242,253]. During imaging, culture media were replaced by HEPES-buffered Hank's balanced salt solution (HHBSS).

Imaging was performed on an inverted Nikon Eclipse Ti microscope equipped with a 200W metal halide lamp (PRIOR Lumen), a 60 × objective (NA = 1.4 oil) and a QuantEM: 512SC 16-bit cooled CCD camera (Photometrics). Microirradiation was performed by a MicroPoint (ANDOR technology), which provided a 405 nm photo-stimulation through pulsed nitrogen pumped tunable dye laser. Cells were subjected to a 4 J/m² pulse for 10 second microirradiation and imaged with 10 sec interval for the first 2min and with 1 min interval for the next hour. Exposure times were adjusted between 100 ms to 400ms to obtain suitable intensities in each channel.

The NIS-Elements AR 3.2 software package (Nikon) was used for automated computer control and for quantitative image analysis. Ratio images were created by dividing the FRET image by the donor image, applying a pseudocolour look-up-table, and scaling each pixel intensity in the ratio image by the corresponding pixel intensity for the average of the donor and FRET channels.

Table 5.2 Cloning strategies for DNA constructs described in Chapter 5.

Name	Gene (Restriction sites in italics)	Vector		
Construct 1	<i>XhoI</i> – H2A – <i>XbaI</i> – Donor – <i>Sall</i> – PARG – <i>KpnI</i> – Acceptor – <i>HindIII</i>	Dual	pBAD	
Construct 2	<i>XhoI</i> – Donor – <i>XbaI</i> – PARG – <i>Sall</i> – H2A – <i>KpnI</i> – Acceptor – <i>HindIII</i>	Dual	pBAD	
Construct 3	<i>XhoI</i> – H2A – <i>XbaI</i> – Donor – <i>Sall</i> – Acceptor – <i>KpnI</i> – PARG – <i>HindIII</i>	Dual	pBAD	
Construct 4	<i>XhoI</i> – Donor – <i>XbaI</i> – PARG – <i>Sall</i> – Acceptor – <i>KpnI</i> – H2A – <i>HindIII</i>	Dual	pBAD	
PARP	<i>EcoRI</i> – <i>EagI</i> – PARP – <i>BglIII</i>	Dual		
EYFP-PARP	<i>XhoI</i> – EYFP – <i>EagI</i> – PARP – <i>BglIII</i> – <i>HindIII</i>		pBAD	pcDNA
EYFP-PARP (D-A)	<i>XhoI</i> – EYFP – <i>EagI</i> – PARP (D214A) – <i>BglIII</i> – <i>HindIII</i>		pBAD	
mCitrine-H2A	<i>XhoI</i> – mCitrine – <i>XbaI</i> – <i>Sall</i> – H2A – <i>HindIII</i>		pBAD	
mTFP1-PARG	<i>XhoI</i> – mTFP1 – <i>XbaI</i> – PARG – <i>HindIII</i>		pBAD	pcDNA
mTFP1-PARG (D-A)	<i>XhoI</i> – mTFP1 – <i>XbaI</i> – PARG(D253A,D307A) – <i>HindIII</i>		pBAD	
mTFP1-PARG(397-976)	<i>XhoI</i> – mTFP1 – <i>XbaI</i> – PARG(397– 976) – <i>HindIII</i>		pBAD	pcDNA
mCitrine-	<i>XhoI</i> – mCitrine – <i>XbaI</i> – PARG – <i>HindIII</i>			pcDNA

PARG				
mTFP1-PARG-mCitrine	<i>XhoI</i> - mTFP1 - <i>XbaI</i> - PARG- <i>Sall</i> - mCitrine- <i>HindIII</i>			pcDNA
ddGFP A-PARG	<i>XhoI</i> - ddGFP A - <i>KpnI</i> - PARG- <i>HindIII</i>			pcDNA
ddGFP B-PARG	<i>XhoI</i> - ddGFP B - <i>KpnI</i> - PARG- <i>HindIII</i>			pcDNA
ddGFP A-4xlinker-PARG	<i>XhoI</i> - ddGFP A - <i>BglII</i> - 4xlinker- <i>KpnI</i> - PARG- <i>HindIII</i>			pcDNA
ddGFP B-4xlinker-PARG	<i>XhoI</i> - ddGFP B - <i>BglII</i> - 4xlinker- <i>KpnI</i> - PARG- <i>HindIII</i>			pcDNA
ddRFP A-PARG	<i>XhoI</i> - ddRFP A - <i>KpnI</i> - PARG- <i>HindIII</i>			pcDNA
ddRFP B-PARG	<i>XhoI</i> - ddRFP B - <i>KpnI</i> - PARG- <i>HindIII</i>			pcDNA
ddRFP A-4xlinker-PARG	<i>XhoI</i> - ddRFP A - <i>BglII</i> - 4xlinker- <i>KpnI</i> - PARG- <i>HindIII</i>			pcDNA
ddRFP B-4xlinker-PARG	<i>XhoI</i> - ddRFP B - <i>BglII</i> - 4xlinker- <i>KpnI</i> - PARG- <i>HindIII</i>			pcDNA
RAP80-ECFP	<i>XhoI</i> - RAP80 - <i>KpnI</i> - ECFP- <i>HindIII</i>			pcDNA
RAP80-mCitrine	<i>XhoI</i> - RAP80 - <i>KpnI</i> - mCitrine- <i>HindIII</i>			pcDNA
RAP80-ddGFP A	<i>XhoI</i> - RAP80 - <i>KpnI</i> - ddGFP A- <i>HindIII</i>			pcDNA
RAP80-ddGFP B	<i>XhoI</i> - RAP80 - <i>KpnI</i> - ddGFP B- <i>HindIII</i>			pcDNA
SuperUIMs-ddGFP A	<i>XhoI</i> - SuperUIMs - <i>KpnI</i> - ddGFP A- <i>HindIII</i>			pcDNA
SuperUIMs-ddGFP B	<i>XhoI</i> - SuperUIMs - <i>KpnI</i> - ddGFP B- <i>HindIII</i>			pcDNA
SuperUIMs-ECFP	<i>XhoI</i> - SuperUIMs - <i>KpnI</i> - ECFP- <i>HindIII</i>			pcDNA
SuperUIMs-mCitrine	<i>XhoI</i> - SuperUIMs - <i>KpnI</i> - mCitrine- <i>HindIII</i>			pcDNA

Chapter 6: Conclusions and future directions

6.1 Summary of thesis

The development of fluorescent proteins (FPs) has resulted in a broad colour palette of genetically encoded fluorophores that facilitate live cell imaging of cellular structure and enable the development of FP-based biosensors. These biosensors have provided researchers with a valuable toolset for detecting dynamic cellular activities and molecular interactions in live cells and animals. Despite the rapid spread of biosensing tools throughout the biological research community, the invention of new biosensors with enhanced dynamic range, improved sensitivity and compatibility in multiparameter imaging, is still required. Therefore, the aim of this thesis was to develop new FP-based biosensors and demonstrate their utility in live cell imaging.

FP-based biosensors that involve the use of FRET are one of the most useful classes of live cell imaging tools. The first generation of a FP-based FRET pair, constructed with a blue FP as a donor and a green FP as an acceptor, suffered from having a dim donor that is particularly susceptible to photobleaching. Later, the discovery of the cyan FP and yellow FP, with large spectral overlap and improved brightness and photostability, ushered in a new era for the design of FP-based FRET biosensors. Although hundreds of publications have reported the use of the cyan and yellow FRET pair in biosensing, their application is generally limited to reporting on a single biochemical parameter. To expand the application of FP FRET in multiparameter imaging, a former member of the Campbell research group, Dr. Huiwang Ai, engineered two FP pairs with distinctive excitation and/or emission wavelengths that could each be imaged independently in the presence of the other [19]. Building upon Dr. Ai's research, I completed the development and optimization of a pair of FRET-based Ca^{2+} biosensors, CaYin

and CaYang, which are spectrally distinct. By expressing these FRET-based Ca^{2+} biosensors in live cells, Ca^{2+} flux in different cellular compartments of the same cell could be monitored. I also demonstrated that one of these Ca^{2+} biosensors, paired with one of the previously reported caspase-3 biosensors based on the same FRET pairs, enables ratiometric imaging of both Ca^{2+} and caspase-3 activity in the cytoplasm of a single cell. Due to the intrinsically ratiometric change of FRET-based strategies, the use of the Yin and Yang FRET pairs provides greater ease of quantitation. In principle, any pair of biosensors from the vast number of existing cyan/yellow FRET-based biosensors could be converted to the Yin and Yang FRET pairs. In this way, the Yin and Yang FRET pairs provide a new route to deciphering the relationship between multiple biological events in their native intracellular environments.

Despite these advances in FP FRET technology, FRET-based biosensors still suffer from the major disadvantage of having very broad excitation and emission profiles that limit the number of FRET pairs that can be applied in single cells. In contrast, intensimetric biosensors inherently require narrower swaths of the visible spectrum, typically occupying about half the wavelength range of a FRET pair. Accordingly, I also spent a substantial amount of time exploring intensimetric biosensors for multiparameter live cell imaging. Traditionally, intensimetric biosensors mainly referred to single FP-based biosensors. These biosensors exhibit fluorescence changes at a single wavelength in response to a change in chromophore environment caused by analyte flux, molecular interactions, or induced conformational change. With the advent of dimerization dependent FP (ddFP)-based technology developed by Dr. Spencer Alford of the Campbell group [60,61], a new entry was added to the list of strategies that can be used for creation of genetically encoded intensimetric biosensors.

The first constructed ddFP-based biosensor was a caspase biosensor, in which caspase activity was indicated by an intensimetric loss of fluorescence. In contrast to FRET-based caspase biosensors, only one emission channel is monitored when using ddFP-based biosensors. Thus, additional emission channels can be assigned to detect other parameters concurrently. So far, Dr. Alford and I

have demonstrated the activation of caspase-3 during apoptosis via green, red and yellow ddFP-based biosensors. In addition, I have also demonstrated the practicality of single colour partner swapping translocation-based biosensors, which report caspase activity with a translocation from the cytoplasm to the nucleus. With these translocation-based biosensors, I achieved the simultaneous detection of both caspase-3 and caspase-8 with coexpression of two ddFP-based biosensors of different colours.

One of the most exciting developments to come out of this research is the development of novel biosensors that report caspase activity via both colour switching and translocation. These tactics have enabled us to monitor caspase-3 activity in single cells with dramatic green-to-red or red-to-green colour switches and translocation from the cytoplasm to the nucleus. This implementation obviously sacrifices the advantages of intensimetric biosensors for multiparameter imaging, but does provide a new highly ratiometric biosensing methodology that has some advantages of its own. For example, it is particularly useful for integrating a low level of protease activity over time, since the activity can be read out using the nuclear accumulation of fluorescence in a distinct spectral channel. This advantage was demonstrated by investigating the differences between two pathways of caspase-3 activation in neurons: canonical apoptosis and non-apoptotic neurite pruning.

Beyond caspase biosensors, ddFP technology has been further explored as an indicator for mitochondria-associated endoplasmic reticulum membrane (MAM). As indicated by its name, MAM represents the physical association between the endoplasmic reticulum (ER) and mitochondria, and plays essential roles in signal transduction and functional interactions between the ER and mitochondria [184]. To report this association between ER and mitochondria membrane, we developed a ddFP approach using a MAM-enriched ER surface-targeted monomer together with a mitochondrial surface-targeted monomer. Specifically, I demonstrated that calnexin and Tom20 fusions with ddGFPs were effective in labeling MAM. To search for alternative MAM markers, I also intensively studied the long-chain acyl-CoA synthetase 4 (FACL4). However,

FACL4 possesses quite distinctive preferences regarding its localization based on the results from two isoforms. The majority of isoform 1 was found in cytoplasmic membrane, whereas isoform 2 exhibited mainly ER membrane localization, consistent with a hypothesis from a computational prediction [208].

Given these successes in biosensing of enzymatic activity and membrane association, we attempted to engineer an FP-based assay to report the activity of the DNA damage related enzyme, poly ADP-ribose polymerase 1 (PARP1). Potentially, this assay could facilitate the development of a screening platform for inhibitors of PARP1, which could lead to the discovery of promising anti-cancer molecules. Learning from our previous experience, we assembled multiple constructs on the basis of either PARP1 enzyme or poly ADP-ribose glycohydrolase (PARG). With these constructs, we demonstrated the recruitment of PARP1 after microirradiation induced DNA damage. Likewise, the enzymatic activity of PARP1 was confirmed by the formation of its products, the freshly synthesized poly ADP-ribose (PAR) chains, resulting the recruitment of PARG at the DNA damage site. We then endeavored to design an assay of PARP activity that would take advantage of the close proximity between recruited molecules at the site of DNA damage. However, we ultimately found that the recruited molecules were not in close enough proximity to enable efficient FRET between fused FPs. I was also unable to demonstrate fluorogenic ddFP heterodimerization at the site of DNA damage, likely due to preassociation of the monomers in the crowded environment of the nucleus. Further attempted experiments with polyubiquitin binding proteins also demonstrated a lack of association between ddFP molecules recruited by a DNA damage signal.

6.2 Future directions

6.2.1 FRET based biosensors in multiparameter imaging

In this work we demonstrated multiparameter imaging with FRET pairs Yin and Yang. With the recent development of the intensimetric red-fluorescent FP-based Ca^{2+} indicator R-GECO1 [106], analogous multiparameter imaging could

now be more easily accomplished with the combined use of R-GECO1 and a traditional CFP/YFP or Yang FRET-based Ca^{2+} indicator [151] or caspase-3 indicator [153]. One remaining advantage associated with Yin and Yang FRET pairs is that they can both be imaged ratiometrically. However, the primary disadvantage of the Yin and Yang FRET pairs (or any other novel FRET pair) is the substantial challenge associated with converting an optimized CFP-YFP FRET based biosensor to an alternate FRET pair. As we and others have shown, the FRET response of a particular biosensor is critically dependent on the physical properties of the FPs [79]. Accordingly, switching to a different FRET pair, particularly one in which the FPs are derived from different species, may require the heavy task of biosensor optimization to be repeated. Dauntingly, the necessary re-optimization effort is doubled for Yin and Yang, since they were designed to be used only in conjunction. It would be preferable to develop a new FRET pair that could be easily used in conjunction with the existing CFP-YFP FRET pair. For this reason we suggest that the development and optimization of an effective orange-red or red-far red FRET pair is an important future direction, as it could be used in conjunction with existing CFP-YFP based biosensors to expand the number of parameters monitored concurrently. Overall, the spectral distinctive FRET pairs could facilitate the interpretation of relative kinetics in multiple biological processes with a spatiotemporal precision that was previously inaccessible.

6.2.2 DdFP-based biosensors for multiparameter imaging

In this work I have demonstrated several new implementation and applications of ddFP technology. One thing that I did not explore in this work is the further improvement of the ddFPs themselves, but this is currently the focus of other researchers in the Campbell group. The two most important directions for improving the ddFPs are decreasing the affinity and increasing the contrast. Even incremental improvements in either one of these areas would dramatically increase the utility of ddFPs for a variety of applications.

For ddFP-based caspase biosensors, future efforts could focus on engineering the colour switch biosensors into a generic protease indicator that not only could be used in the study of signal pathway in apoptosis but also could be used as screening methods for new drug candidates targeted to the protease. Furthermore, by taking advantage of the colour switch translocation, similar systems could be explored as reporters of nucleo-cytoplasmic transportation during apoptosis or other cellular process [254].

DdFP-based biosensors can be applied not only to report enzymatic activity, but also to highlight the protein-protein interaction or proximity. By utilizing the interaction or proximity between calnexin and Tomm20, we specifically marked the mitochondria-associated ER membrane (MAM). During the investigation for alternative MAM markers, we discovered the interesting localization pattern of FACL4 isoforms, which is worth further exploration.

In addition to being used as a MAM marker, ddFP technology could be expanded to biomolecular fluorescence complementation (BiFC) related biosensors. As discussed in Chapter 1, BiFC or complementation-based biosensors are commonly utilized in the detection of protein-protein interaction, which in turn facilitate the exploration of signaling pathways in live cells. Unlike the irreversible single-FP based BiFC biosensors [21], ddFP-based biosensors benefit from their reversible nature, which will allow researchers to examine dynamic events in live cells. Furthermore, due to the fluorogenic ability of the reversible ddFP technology, it could be exploited in the study of dynamic communication between cells via the recognition and interaction of receptors. These suggestions aside, we hope that ddFP technology will gain more attention from the research community leading to an enlarged number of examples in which it is utilized for biosensor design.

6.3 Closing remarks

In summary, the research presented in this thesis described our efforts to develop FRET and dimerization-dependent fluorescent protein based biosensing

strategies that could be used for monitoring of multiple cellular activities concurrently. With this purpose in mind we developed and validated two spectrally distinctive FRET pairs for monitoring Ca^{2+} flux at different organelles of the same cell or detecting Ca^{2+} flux and caspase activation concurrently. Although these two compatible FRET pairs have been exploited only in Ca^{2+} flux and caspase activation, their potential applications could be extended to other studies of live cell dynamics. However, since each FRET pair occupies two colour channels in the available range of visible wavelength, the maximum number of FRET pairs that could be used in a single cell is likely limited to two. In contrast, intensimetric biosensors report biological events via change of fluorescence intensity in a single channel, which generally makes intensimetric biosensors a preferred choice for multiparameter imaging. Inspired by this idea, we engineered a series of dimerization-dependent FP (ddFP) based biosensors to detect closely associated membranes and caspase activity. Furthermore, ddFP-based caspase biosensors have been engineered into colour switching and translocation-based reporters, whose readouts contain both intensity and location information. Since ddFP technology has now been shown to be useful for live cell intensimetric detection of both small molecules and enzymatic activities, we believe ddFPs mark a significant addition to the FP toolkit and will facilitate the design of useful biosensors for live cell imaging. All things considered, we suggest that, for qualitative and multiparameter imaging applications, ddFP and other intensimetric FP biosensor designs will ultimately prove to be more versatile and practically useful than FRET-based designs.

Appendix: Engineering fluorescent biosensors based on the photo-responsive domain, LOV2

A.1 Introduction

Complex physiological behaviors are ultimately governed by signaling pathways that depend upon protein-protein interactions and the localizations of proteins in the cell. To decipher these signaling pathways, researchers must be able to detect and control the activity of specific proteins. One powerful technology used to control protein function, now generally known as optogenetics, involves the manipulation of protein function using light. Such optical manipulation affords non-invasive control and a high degree of temporal and spatial resolution [255].

Plants and other photosynthetic organisms (*e.g.*, algae) have evolved specialized photoreceptor proteins to detect and respond to environmental light stimuli. This ability permits modulation of metabolic activities with photosynthesis. In the last two decades, intense research in this area has described the biochemistry responsible for photoreception and photomodulation [256,257]. The resulting advances in knowledge have enabled the development of strategies for manipulating protein function at precise times and locations using light.

Recently, several photoreceptors from plants and bacteria were successfully utilized to control protein function using light. Many plants possess red light sensing phytochromes [258] as well as blue-light receptors, such as cryptochrome [259] and phototropin [260]. The latter contains a ‘Light, Oxygen and Voltage-sensing’ domain, or LOV domain, that responds to light by modulating the receptor’s function [261,262]. LOV domains were first discovered in plants, but subsequently found throughout nature as N-terminal regulatory domains on many different effector proteins [263]. In plants, the LOV domain is linked to, and regulates, a serine/threonine protein kinase domain. The kinase domain undergoes light-inducible autophosphorylation [264]. In bacteria, LOV domains regulate

histidine-kinases, helix–turn–helix DNA-binding domains, and phosphatases [265]. The broad spectrum of effector domains coupled to the LOV domain in nature suggests an opportunity to artificially combine LOV domains with different effector domains to create light-activated proteins.

To engineer a functional light-activated protein, one must consider the photochemistry and light-induced conformational changes associated with the LOV domain. Further, an appropriate effector domain must be chosen such that its activity can be controlled by the LOV conformational change [266]. Photons are captured by LOV domains with a non-covalently bound light-absorbing flavin mononucleotide (FMN) chromophore. Photon capture promotes FMN to an excited state, which in turn initiates a self-contained photocycle in which a photoadduct between FMN and a highly conserved cysteine residue is formed [261]. This photocycle triggers a conformational change in the LOV domain, which activates the linked effector domain, such as a kinase [257]. The photoadduct slowly decays back to the non-covalent ground state in the dark, deactivating the effector domain until the next photocycle is initiated. In addition to the excited state photocycle, the thermal decay process may also exert temporal control over effector proteins, since the timescale of decay varies for the LOV domains from a few seconds to many hours at room temperature [267].

The primary LOV domain photochemical reaction in the excited state is well studied, but the molecular mechanism coupling photoadduct formation to the conformational change remains controversial. X-ray crystal structures of the LOV domain in the dark and light states show only minor differences in protein conformation [268]. In contrast, an NMR analysis of a plant LOV2 domain showed that the light-induced loss of secondary structure of the C-terminal α -helix ($J\alpha$ -helix) triggered a phosphorylation reaction of the effector, phototropin [269,270]. Moreover, structural studies and other *in vitro* data suggested that the transduction of light capture in some bacterial LOV proteins might occur by rotation of the $J\alpha$ -helix [271,272]. The consensus conclusion is that the structural perturbation caused by photon capture is transmitted to the effector domain through a loss of structure or rotation of the C-terminal $J\alpha$ -helix.

Several studies have illustrated that light-dependent signal transduction mediated by LOV domains can be coupled to a variety of effectors by generating artificial hybrid proteins. For example, membrane protrusions and ruffling can be regulated using a photoactivable hybrid of a LOV domain and a GTPase known as Rac1 [273]. In this hybrid, the LOV domain of *Avena Sativa* sterically blocks the active site of the Rac1 effector enzyme. Upon irradiation, the J α -helix loses structure, thus relieving inhibition of Rac1 [273]. The LOV domain has also been utilized to control gene expression; a plant LOV domain was used to regulate the DNA binding domain of the *E. coli* tryptophan repressor protein through a shared helix [274]. Alternatively, gene expression has been controlled [275] using a fusion of a DNA binding domain and a rapidly exchanging dimer of the LOV domain known as Vivid [276-278]. Finally, gene expression has also been controlled using a peptide fused to the C-terminal J α -helix of *Avena Sativa* LOV2. Light induced J α -helix structure loss allowed the peptide to bind its target and initiate gene transcription in yeast [279]. These studies illustrate that coupling LOV domains to other proteins (effectors) is a versatile strategy to modulate protein activities in live cells.

Although several hybrid LOV-effector proteins have proven useful for modulating protein function with light, most examples used effectors whose functions were closely related to the natural LOV-coupled effector domains (*e.g.*, DNA binding domains and kinases). Only a narrow set of examples demonstrating light-dependent control of unrelated LOV effectors has been reported [266]. Whether or not LOV domains can be employed as universal light switches to control protein function remains an open question. The generality of photomodulation mediated by LOV domains may be limited due to the subtle conformational changes associated with the photoreaction. We speculated that we could use directed evolution to enhance the conformational change of a LOV domain and thereby increase its utility as a universal light-dependent switch. To screen for improved variants, our objective was to generate fluorescent protein (FP)-related library screening strategies utilizing biosensing platforms such as FRET, dimerization-dependent FPs (ddFPs), and single FP biosensors. If

successful, the improved LOV domains with enhanced conformational changes could be utilized with on a wider variety of effectors that are not naturally associated with the LOV domain.

A.2 Results and discussion

A.2.1 Characterization of LOV2 domain from *Arabidopsis*

We first investigated the LOV2 domain from phototropin 1 of *Arabidopsis thaliana*, which is naturally coupled to serine/threonine kinase domains [264,280]. The key event of the LOV2 photocycle involves the formation of a covalent adduct between a cysteine residue (**Figure A.1A,B**) and the FMN chromophore upon blue light irradiation. The incorporation of light-insensitive mutation C512A (numbering based on the LOV1 domain) prevents photocycling (**Figure A.1B**) and keeps the FMN chromophore in the ground state, capable of absorbing light and emitting fluorescence. Conversely, the LOV2 variant, I608E (**Figure A.1A**), possesses a J α -helix permanently dissociated from the LOV core [270], mimicking the unfolded structure following photoactivation.

To compare the C512A and I608E mutants to the native LOV2 domain, we collected the absorbance and emission spectra of the purified proteins (**Figure A.2A,B**). The emission spectra of LOV2 and its mutants were broad and exhibited multiple peaks. Photoconversion of LOV2 was abolished in the C512A mutant, resulting in strong absorbance and emission, which was consistent to the reported data [281,282]. Since the conjugated system of the FMN chromophore was disrupted by the newly formed covalent bond with cysteine during the photoreaction, decreased absorbance and emission were observed in wild type LOV2 relative to the C512A mutant. The I608E mutant exhibited the least absorbance and emission, likely due to the decreased conformational rigidity of the core of LOV2 domain after the dissociation of J α helix.

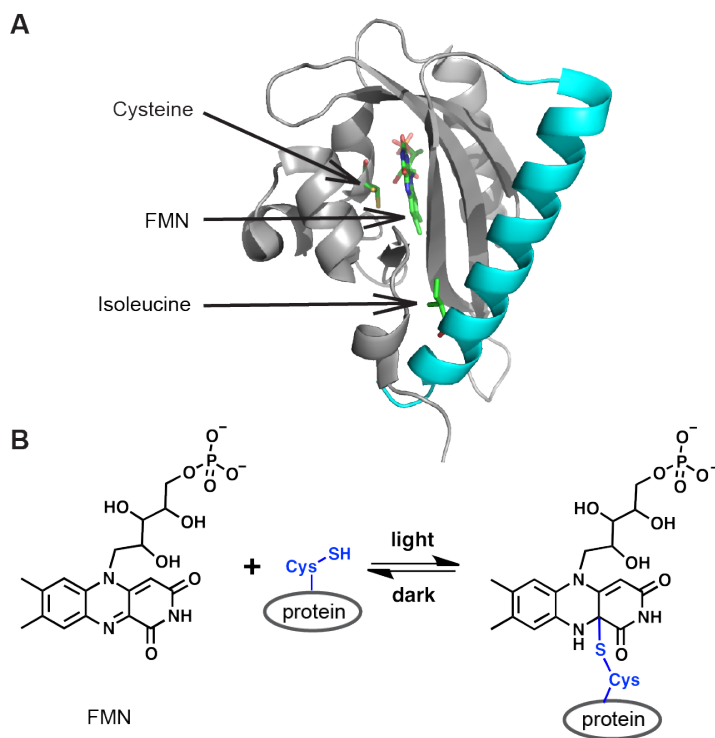


Figure A.1 LOV2 domain and the photocycle

(A) The core of LOV2 domain is shown in grey and J α -helix is shown in cyan. FMN molecule, light-insensitive residue Cys512 and dissociation related residue Ile608 are depicted using stick representation and coloured by element: carbon, green; nitrogen, blue; oxygen, red; sulfur, orange. Figure is prepared from an *Avena sativa* LOV2 domain (PDB ID 2WKP [273]). (B) Photoreaction between FMN and the cysteine of LOV2 domain.

To determine the influence of pH on the emission, we performed a pH titration for LOV2 domain, monitored with excitation at 415 nm and 370 nm, respectively. One single broad emission peak was observed at pH values below 6, without loss of the peak maximum (**Figure A.2C,D**). We attributed the single broad peak to the exposed FMN chromophore, since LOV2 might be partially denatured at low pH. Furthermore, a significant change in the emission spectrum of LOV2 was not observed between pH 7 and 10 (**Figure A.2C,D**), indicating pH-independent fluorescence. Based on the pH titration, the extent of LOV2 sheltering of FMN changed the emission profile to two peaks, but did not significantly alter fluorescence intensity.

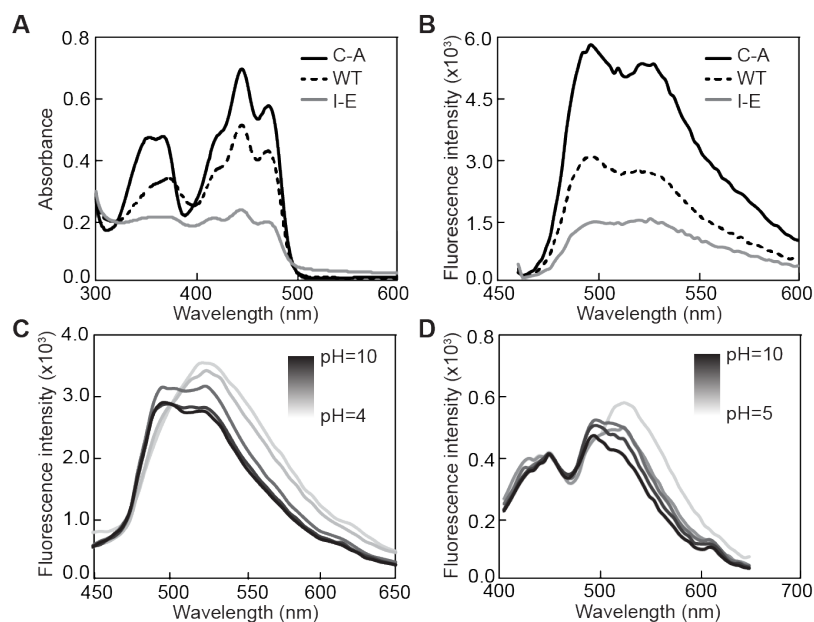


Figure A.2 Absorption and emission spectra of LOV2 mutants.

(A) Absorption spectra of LOV2 mutants and wild type (WT). Mutants C512A and I608E are shown as solid line in black and grey, respectively. Dashed line represent wild type. (B) Emission spectra of (A) are collected at 415nm excitation. Emission spectra of LOV2 under different pH conditions are collected at 415nm excitation (C) and 370nm excitation (D).

A.2.2 Attempted detection of LOV2 conformational change using FRET and ddFPs

Following our preliminary characterization of the LOV2 mutants, we aimed to use FRET as a strategy to monitor the conformational change upon blue light irradiation. We speculated the conformational change would change the FRET efficiency between a donor and an acceptor FP fused to the termini of the LOV2 domain. Given our previous successful application of the Yang FRET pair (described in Chapter 2), we used the same FRET pair (mTFP1 and cpVenus) to design a LOV2 sensor. We constructed a Yang LOV2 fusion by replacing the Ca^{2+} binding module of a Yang cameleon with the LOV2 domain, with or without C512A or I608E mutations. These hybrids were designated as Yang LOV2, Yang C512A and Yang I608E, respectively. To compare the Yang LOV2 FRET constructs and the LOV2 domain, we collected absorbance spectra of each fusion. As expected, there was a large overlap in the absorbance spectra of the LOV2

domain and mTFP1 (**Figure A.3A**), but the LOV2 mutants did not cause significant changes in the absorbance spectra of FRET constructs (**Figure A.3A**). However, emission spectra (**Figure A.3B**) revealed FRET efficiency was enhanced in the C512A mutant, as revealed by a higher intensity 535 nm peak. In contrast, a lower intensity 535 nm peak was observed for when the I608E LOV2 domain was present (**Figure A.3B**). Since the conformational change within LOV2 is caused by the unfolding or dissociation of J α -helix [269,270,283], the observation of a higher FRET efficiency in Yang C512A (locked in the dark state) and a lower efficiency in Yang I608E (with an unstructured J α -helix) was a promising result.

To study the effect of the LOV2 photoreaction on FRET efficiency, the fluorescence emission of FRET constructs was monitored during blue light irradiation. The intensity ratio of FRET/mTFP1 (535nm/490nm) decreased over time using Yang LOV2 (**Figure A.3C**). Likewise, a similar decrease was observed with the C512A and I608E mutants (**Figure A.3D**), indicative of chromophore photobleaching rather than photoreaction. Interpretation of the emission spectra was difficult due to a large spectral overlap between the emission of the LOV2 domain and the Yang FRET pair. Overall, we did not observe changes in FRET efficiency that could be unambiguously assigned to a change in structure of J α -helix.

To better resolve the effect of LOV2 conformational change on FRET, we constructed a red FRET pair to minimize spectral overlap [24,148,149]. mOrange was used as the donor and mCherry as the acceptor [49] and the pair was designated as O/Ch. Due to the red shifted spectra of the O/Ch FRET pair, absorbance of the LOV2 chromophore was clearly distinguishable from the FP absorbance (**Figure A.4A**). However, in contrast to our results with the Yang FRET pair, we did not observe a difference in the absorbance spectra between the wild type and mutant LOV FRET constructs (**Figure A.4A**). Likewise, the emission spectra of the three FRET constructs were practically indiscernible (**Figure A.4B**). For this reason, photoswitching with this construct was not further pursued.

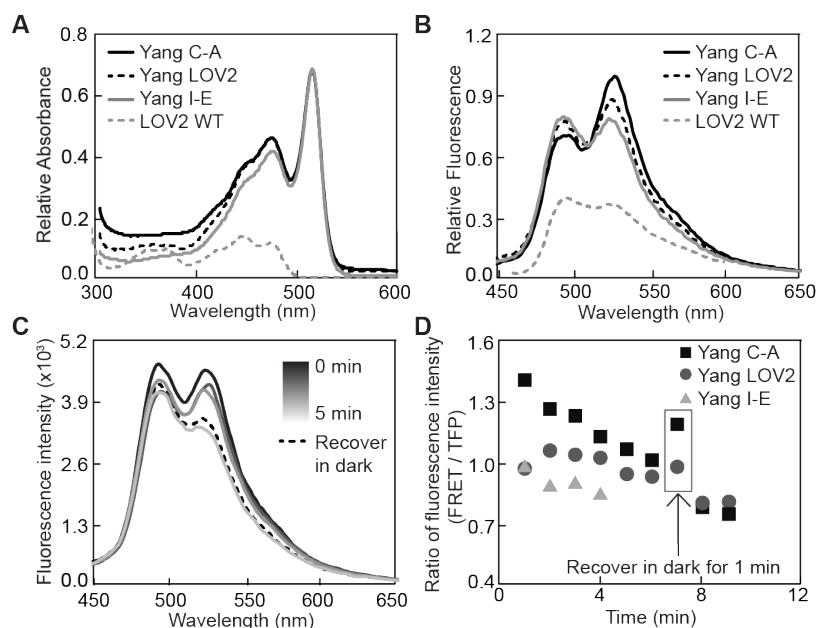


Figure A.3 Characterization of FRET constructs with LOV2 mutants. (A) Absorption spectra of FRET constructs with and without LOV2 C512A and I608E mutations. (B) Emission spectra of (A) are collected at 415 nm excitation. (C) Emission and recovery spectra of Yang LOV2 collected 5 sec after irradiation with 405 nm LED light with 90 sec intervals. After 5min irradiation, protein was kept in dark for 1 min to collect the recovery profile. (D) Intensity ratio of FRET constructs with mutations was monitored after irradiation. Y-axis represents the irradiation time on protein sample. Proteins were put back under 405 nm LED light after the recovery data was collected, highlighted in the box.

Given the inability of FRET to detect LOV2 conformational changes, we next attempted to use a dimerization-dependent FP (ddFP) strategy. DdFPs rely on the association of two dark monomeric FPs to form a brightly fluorescent heterodimer [60]. We hypothesized that the blue-light induced conformational change of the LOV2 domain could potentially disrupt the associated state of ddFP heterodimers, which could be visualized as a decrease in fluorescence intensity. To assemble ddFP-based constructs, we replaced the FRET FP pair flanking the LOV2 domain with two red ddFP monomers (ddRFPs). Unfortunately, the fluorescence intensity of the LOV2-ddFP constructs was substantially decreased relative to other ddRFP tandem heterodimers we have constructed (**Figure A.4C**). The LOV2 domain, and both the point mutants of the LOV2 domain, likely hindered the association between the ddRFP partners since a strong emission of

LOV2 was observed but only a weak emission for the ddRFP heterodimer (**Figure A.4D**). The red fluorescence intensity increased over time, but with a concurrent decrease in intensity from LOV2, possibly due to FRET. Therefore, the poor performance of LOV2-ddFP constructs prompted us to abandon further investigation of ddFP-based strategies for LOV2 sensing.

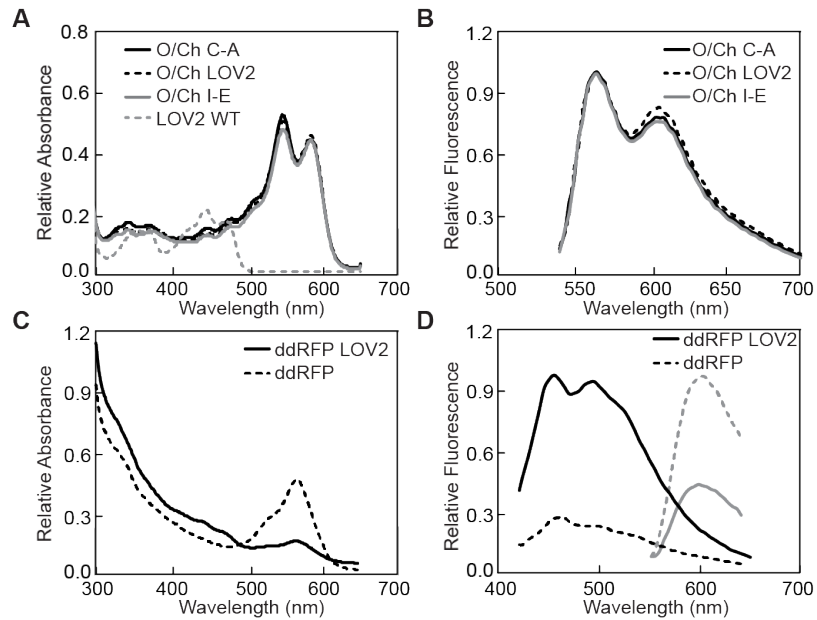


Figure A.4 Characterization of a red FRET (O/Ch) and ddRFP constructs with LOV2 mutants.

(A) Absorption spectra of red FRET constructs with and without C512A and I608E mutations. (B) Emission spectra of (A) are collected at 520 nm excitation. (C) Absorption spectra of ddRFP LOV2 construct and ddRFP. (D) Emission spectra of (C) are collected at 400 nm excitation shown in black and 540 nm excitation shown in grey.

We concluded that FRET and ddFP technology was not practically useful for reporting on the blue light-induced conformational change of the *A. thaliana* LOV2 domain.

A.2.3 Attempted engineering of an *Avena sativa* LOV2 sensor using a circularly permuted fluorescent protein.

Although numerous studies have demonstrated and investigated the conformational change dynamics of the *A. thaliana* LOV2 domain [281,284,285], relatively few examples of using this domain to control protein function have been reported. Conversely, the LOV2 domain from *Avena sativa* (Oat) has been more widely utilized and has been used to produce a photoactivable enzyme for control cell mobility [273], as well as a peptide to inducible control gene expression [279]. Thus, we speculated that *Avena sativa* LOV2 domain might be more suitable for our generalized photomodulation strategy

Comparison of the primary sequence of LOV2 domains from *A. thaliana* and *A. sativa*, revealed a stark difference in the J α -helix (highlighted in yellow in **Figure A.5**). Specifically, the J α -helix from *Avena sativa* is notably shorter in length. Furthermore, several mutations in the LOV core differentiate the two species. Some of these residues may influence the hydrophobic interaction between J α -helix and LOV core. Despite the sequence differences in the LOV2 domains, their emission spectra are essentially identical.

```

Arabidopsis  GIDLATTLERIEKNFVITDPRLPDNPPIIFASDSFLELTEYSREEILGRNCRFLQGPETDL 60
Oat          GIDLATTLERIEKNFVITDPRLPDNPPIIFASDSFQLTEYSREEILGRNCRFLQGPETDR 60
*****:*****:*****:*****:*****:*****:*****:*****:*****:
Arabidopsis  TTVKIRNAIDNQTEVTVQLINYSKGGKFFWNI FHLQPMRDQKGEVQYFIGVQLDGSKHV 120
Oat          ATVRKIRDAIDNQTEVTVQLINYSKGGKFFWNI FHLQPMRDQKGDVQYFIGVQLDGETHV 120
: ** : ** : *****:*****:*****:*****:*****:*****:*****:
Arabidopsis  EPVRNVEETAVKEGEDLVKKTAVNIIDEAVRELPDANMTPEDLWANHSKV
Oat          R-----DAAEREGVMLIKKTAENIDEAAKELPDANLRPEDLWANHSKV
.           : ** : ** * : ***** ***** : ***** : *****

```

Figure A.5 Sequence alignment of *Arabidopsis* and *Avena sativa* LOV2 domain.

Mutations found in the core of LOV2 domain are highlighted in pink. Mutants C512A and I608E related light-insensitive residue (cysteine) and J α -helix dissociation residue (isoleucine) are in cyan. J α -helices from two LOV2 variants are shown in yellow.

In an attempt to make a reporter of the conformational change of the *A. sativa* LOV2 domain, we adopted a strategy based on a circularly permuted FP (cpFP). In the permuted variant, the N- and C-termini of cpFP are in close

proximity to the chromophore. Due to the close proximity, even a small disturbance of the termini should perturb the chromophore environment and change fluorescence intensity. In this study, we utilized the FP component of a red Ca^{2+} indicator, named R-GECO1 [106], in which the change of fluorescence intensity depends on the conformational change of the directly linked Ca^{2+} binding domains. By directly linking the LOV2 domain to the N-terminus of the R-GECO1 cpFP, we constructed a fusion called LOV2-GECO (**Figure A.6A**). A dramatic decrease in the emission of LOV2 was observed with LOV2-GECO, comparable to control experiments performed with a variant of LOV2 without the $\text{J}\alpha$ -helix, namely LOV2-no $\text{J}\alpha$ (**Figure A.6B**). Similarly, a weak emission was collected for the fusion of GECO main body and LOV2 lacking the $\text{J}\alpha$ -helix (**Figure A.6B**). This indicated to us that the interaction between $\text{J}\alpha$ and the LOV2 core was disrupted through fusion to the cpFP. The disrupted interaction likely mimics the dissociated state of $\text{J}\alpha$ -helix. A relatively weak red emission was detected from LOV2-GECO, probably due to disruption of the cpFP caused by fusion to the LOV2 domain (**Figure A.6C**).

To modify the linker region between LOV2 and the cpFP part, we tried both deletions and making libraries with randomized linker sequences. Colonies, expressing the variants from the libraries with bright red fluorescence, were picked and cultured, and the protein extracts were characterized by their emission spectra. However, all fluorescent variants exhibited a similar emission profile (**Figure A.6D**), illustrating that varying the linker region did not significantly affect the LOV2-cpFP fusion. In the R-GECO1 design, a Ca^{2+} -induced conformational change in the Ca^{2+} binding domain mimics the normal interaction between the residues from $\beta 7$ strand of cpFP and the chromophore. As a negative control, we replaced the entire $\beta 7$ strand from the cpFP by $\text{J}\alpha$ -helix to build construct LOV2-GECO (no $\beta 7$). The absorbance spectrum (**Figure A.6E**) showed that the removal of $\beta 7$ further disrupted the formation of FP chromophore, which was probably caused by the poor folding of LOV2-GECO fusions. This explanation was derived from the fact that proper folding is the prerequisite for chromophore formation [31].

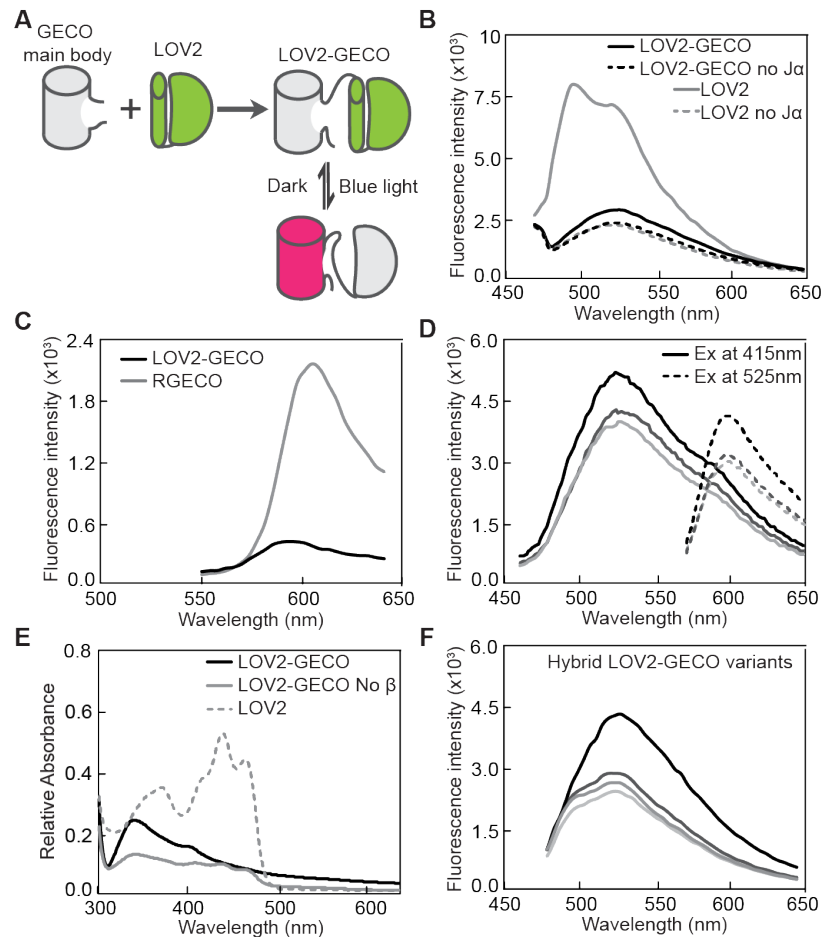


Figure A.6 Characterization of LOV2-GECO.

(A) Schematic for assembly of LOV2-GECO. Emission spectra of LOV2-GECO and controls collected at excitation wavelength of 425 nm (B) and 525 nm (C). (D) Emission spectra of linker randomized LOV2-GECO variants, indicated by different lines. (E) Absorption spectra of LOV2-GECO variants. (F) Emission spectra of hybrid LOV2-GECO variants.

To rescue folding and fluorescence, we designed a hybrid strand of J α -helix and β 7 that we predicted would reestablish the interactions with the chromophore when in a β -strand conformation but also associate with the LOV2 domain when in an α -helical conformation. From our library screening studies of LOV2-GECO variants with randomized linkers, we determined that the preferred sequence of J α -helix was KKTAENIDEAAKELXXT (X is one of a variety of amino acids). The sequence of β 7 strand (SERMYPED) was also used as the second component of the hybrid sequence (key residues Met and Pro underlined). Since both the J α helix and β 7 strand were essential for the functions, our goal was to incorporate

the key residues of both sequences in the hybrid. Accordingly, we designed the hybrid sequence, KKTAENIDEAAKMLPXT, in which the J α helix and β 7 sequences comprise the N- and C-terminal regions, respectively. After screening libraries in which residue X was randomized, we did not identify variants significant differences in emission spectra (**Figure A.6F**). Similar to original LOV2-GECO fusion, relatively weak red fluorescence was observed, indicating a weakly folded cpFP.

Even though the fluorescence emission of both the LOV2 and cpFP domains in LOV2-GECO fusions were reduced due to the destabilized J α -helix of LOV2 domain and the exposed chromophore, we attempted to screen a library of variants for their response to blue light *in vitro*. To image the changes in *E. coli* colony fluorescence, agar plates were imaged using our custom imaging system (both the green and red fluorescence channels) before illumination with blue light. The plates were then placed under blue light and imaged at 2 min intervals for 30 min. Since blue light should partially unfold the J α -helix, the folding or fluorescence intensity of the cpFP might be disturbed. We aimed to identify colonies exhibiting a large change in red fluorescence after blue light illumination. For most colonies we observed a general photobleaching phenomenon in both green and red channels. Those few colonies that exhibited a slight enhancement in red fluorescence were cultured for further characterization. However, those purified protein variants did not exhibit the desired changes upon blue light irradiation.

A.2.4 Attempted alternative design of LOV2 and cpFP fusions

As our initial design of a LOV2 and cpFP fusion was not fruitful, we attempted an alternative design in which LOV2 was split into two fragments: the J α helix and the LOV core. The LOV2 fragments were fused to each of the N- and C-terminus of GECO FP component (**Figure A.7A**). For this work we created a circularly permuted LOV2 variant (cpLOV2), in which the original termini of

LOV2 were fused to GECO main body and two new termini were created. This fusion was designated as cpLOV2-GECO (**Figure A.7A**).

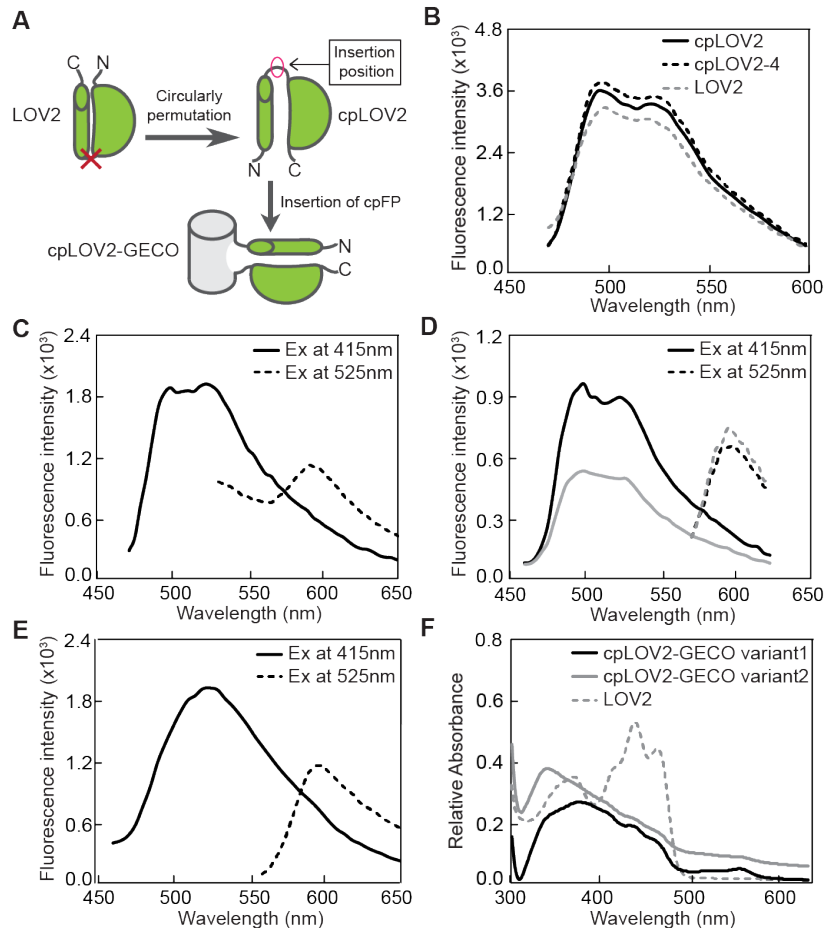


Figure A.7 Characterization of cpLOV2 and fusion of cpLOV2-GECO.

(A) Schematic for assembly of cpLOV2 and cpLOV2-GECO. (B) Emission spectra of cpLOV2 collected at excitation wavelength of 425 nm. Restriction site between the new termini encodes residues Gly and Thr (GT). Number 4 indicates addition of 4 residues between new termini. (C) Emission spectra of cpLOV2-GECO collected at excitation wavelength of 425 nm and 525 nm. (D) Emission spectra of cpLOV2-GECO variants with mutation C450A is shown in black, with mutation I539E is shown in grey. (E) Emission spectra of cpLOV2-GECO variants without any linker. (F) Absorption spectra of cpLOV2-GECO variants.

Although a LOV2 domain lacking the $J\alpha$ -helix has previously been engineered to be fluorescent [286], the cpLOV2 variant had not previously been reported. To optimize this construct before fusion to the GECO domain, we first created a small library of cpLOV2 variants with randomized residues in the linker

region between the two original termini (**Figure A.7A**). The emission spectra showed the best variants of cpLOV2 shared a similar emission profile to that of wild type (**Figure A.7B**). The small differences in the intensity were attributed to varying extents of the photoreaction.

Given the apparent associated state of J α -helix in cpLOV2, we assumed the J α -helix would have a greater probability of remaining associated with the body of the protein in cpLOV2-GECO. This could potentially enhance the emission of the FP chromophore by isolating it from the hydrophilic environment. As we expected, we observed a double peak in the emission spectrum of cpLOV2-GECO (**Figure A.7C**), corresponding to the properly folded LOV2 domain with the associated J α -helix. A weak 590 nm peak attributed to the chromophore of the cpFP was observed as well (**Figure A.7C**). We then incorporated the light-insensitive mutation, C450A, and the dissociation related mutation, I539E, into cpLOV2-GECO individually. These two variants exhibited a large difference in the LOV2 emission spectra, but were similar in terms of the red fluorescence emission from the cpFP domain (**Figure A.7D**). Although C450A and I539E represent different conformations of LOV2, these differences were not reflected in the emission profile of the cpFP.

In an attempt to make the cpFP more sensitive to structural changes in the LOV2 domain, we further manipulated the linkers between the J α -helix, the LOV2 core, and the cpFP. With the deletion of linkers, the J α -helix was observed in the dissociated state, as indicated by a single peak in the emission spectra (**Figure A.7E**). We found that the linkers mainly affected the LOV2 domain, rather than the cpFP, as indicated by absorbance spectra (**Figure A.7F**). Therefore, in variants of cpLOV2-GECO lacking linkers, it appeared folding and function of the cpFP was compromised, indicating the necessity of the linkers for maintaining LOV2 structure.

To rescue the poor folding of the cpLOV2-GECO fusions, we carried out a colony screening method (as described in Section A.2.4) to seek variants with enhanced red fluorescence. However, photobleaching was a persistent problem that prevented accurate comparisons of intensity before and after illumination.

A.3 Conclusion

The ultimate goal for this project was to use FP-based strategies to engineer LOV2 variants possessing larger conformational change upon blue light stimulation. In an attempt to achieve this goal, we constructed fusion proteins by fusing the LOV2 domain to FRET FP pairs, ddFP partners, and a single FP. The first FRET pair we investigated, mTFP1 and cpVenus, failed to perform as a reliable reporter due to the large spectra overlap with LOV2. A red FRET pair, containing mOrange and mCherry, failed to show any response and did not appear to respond to the conformational change. Further, the ddRFP-based strategy was not successful due to the poor maturation of the fusion. As an alternative, we attempted to utilize a circularly permuted FP (cpFP) to reflect the conformational change in LOV2. Unfortunately, the subtle LOV2 conformational change was not sufficient to trigger a substantial change in the chromophore environment of cpFP. The take home message from this work is that the conformational change of LOV2 domain appears to have evolved for its natural coupling to specific effector domains and it is very challenging to exploit this conformational change in unnatural contexts. Accordingly, we suspect that the set of proteins amenable to using the LOV2 domain as general mechanism for light-dependent function control is limited [266].

A.4 Materials and methods

A.4.1 General methods and materials

All synthetic oligonucleotides for cloning were purchased from Integrated DNA Technologies (IDT, Coralville, IA). Polymerase chain reaction (PCR) was performed using Pfu DNA polymerase (Fermentas) according to the provided manufacturers' protocols. FastDigest restriction endonucleases (Fermentas) were used for restriction digests of PCR products and analytical DNA digestion. GeneJET gel extraction kit (Fermentas) or QIAquick Gel-Extraction kit (Qiagen) was used for DNA purification following agarose gel electrophoresis. DNA

ligation was carried out using T4 DNA ligase (Invitrogen). *E. coli* strain ElectroMAX DH10B (Invitrogen) was used for routine plasmid propagation, library construction and screening, and recombinant protein production. Plasmid DNA for both bacterial transformation and mammalian cell transfection was isolated and purified using Fermentas GeneJET-plasmid miniprep kit following the manufacturer's protocol.

The cDNA sequences were confirmed by dye terminator cycle sequencing using the BigDye (Applied Biosciences) cycle Sequencing Kit. Sequencing reactions were analyzed at the University of Alberta Molecular Biology Service Unit (MBSU) at the University of Alberta.

A.4.2 Construction of LOV2 related fusions

Gene of *Arabidopsis* LOV2 (463-632) was amplified between *XhoI/EcoRI* to be inserted into an *XhoI/EcoRI* digested pBAD/His B vector. To construct the Yang FRET fusions, plasmid CaYang1 was employed as template and gene encoding calmodulin and M13 was replaced by gene of LOV2 domain. Likewise, to create fusion of O/Ch FRET, mOrange was used to replace mTFP1 and mCherry was to replace cpVenus. DdRFP LOV2 construct was made in a similar way with details listed in **Table A.1**.

Gene of *Avena sativa* LOV2 (404-546) was amplified from the gene encoding PA-Rac1 (plasmid 22027 from Addgene). CpLOV2 was created by a three-part ligation of the *XhoI/KpnI* digested gene of J α -helix, the gene of LOV2 core digested by *KpnI/HindIII* and *XhoI/HindIII* digested vector. Gene encoding cpFP was amplified from RGECO1 with a 5' primer encoding *XhoI* and *KpnI*, and a 3' primer encoding *BglIII* and *HindIII*. Then the PCR product was digested by *XhoI/HindIII* and ligated into a similarly digested pBAD/His B vector. To create LOV2-GECO fusions, *XhoI/KpnI* digested gene of LOV2 was inserted between *XhoI/KpnI* in the plasmid with cpFP (GECO main body) in it. To create cpLOV2-GECO fusions, gene of J α -helix was fused to gene of cpFP via an over-extension PCR and gene of LOV core was inserted between *BglIII/HindIII*. Saturation/semi-

saturation mutagenesis at specific residues was performed using over-extension PCR. In the first step, two PCR were run: one using a 5' primer for the full-length gene and a 3' primer containing the desired mutations at the target site; the other PCR using a 5' primer which shares an overhang with the 3' primer in the first reaction and anneals the target site and a 3' primer for the full-length gene. In the second step, a mixture of the PCR product from the first step were use as template and 5' and 3' primer for the full-length gene were use to amplify the full-length gene incorporating the desired mutations. Brief cloning scheme for each construct is outlined in **Table A.1**. Restriction enzyme sites used to clone the designated constructs are provided in the table.

A.4.3 Plasmid library screening

E. coli colonies expressing the libraries of LOV2-GECO fusions were grown on 10 cm Petri dishes. A custom imaging system equipped with filter sets (Chroma) for 470/40 nm excitation with 510/20 nm emission (*i.e.*, for green fluorescence) and 560/40 nm excitation with 630/60 nm emission (*i.e.*, for red fluorescence) is used to acquire both green and red fluorescence images of the Petri dish. Then, Petri dish is evenly illuminated with 405/40 nm blue light. The dish is imaged with 2 min intervals in the following 30 min using the same filters. The digital images are loaded into Image Pro plus software (Media Cybernetics, Bethesda, MD) where they are aligned and processed using a custom macro. Then, colonies with a large change in red fluorescence were picked.

A.4.4 Protein Purification and Characterization

E. coli strain ElectroMAX DH10B (Invitrogen) was transformed by electroporation with a pBAD/His B containing the gene of interest. A single colony was used to inoculate a 4 mL culture that was grown overnight (37 °C, 225 rpm) before being diluted into 0.5 L of LB medium supplemented with ampicillin. This culture was grown (37 °C, 225 rpm) to an optical density of 0.6, induced with 0.02% L-arabinose, and cultured for 24 h at 28 °C. Cells were harvested by

centrifugation and lysed by cell disruptor (Constant Systems). All proteins were purified by Ni-NTA chromatography (Amersham). Fluorescence and absorbance spectra were recorded on a QuantaMaster spectrofluorometer (Photon Technology International) and a DU-800 UV-visible spectrophotometer (Beckman), respectively.

To achieve the photoreaction of LOV2 domain, protein samples were placed in a “photoconversion chamber” evenly illuminated with the light from six 9×11 arrays of 405 nm light emitting diodes (LEDs) (OptoDiode Corporation, Newbury Park, CA). The fluorescence response of Ca^{2+} sensing was determined by mixing the LOV2-M13-CaM construct (300 nM) with 100 times volume of calcium buffers having free Ca^{2+} ranging from 17 nM to 39 μM (pH 7.4). The preparation of the buffers was stated in Section 2.4.4.

Table A.1 Cloning strategies for DNA constructs described in Appendix.

Construct ¹	Gene assembly (<i>Restriction sites in italics</i>)
LOV2 (<i>Arabidopsis</i>)	
LOV2	<i>XhoI</i> -LOV2- <i>EcoRI</i>
LOV2 C-A	<i>XhoI</i> -LOV2 (C-A)- <i>EcoRI</i>
LOV2 I-E	<i>XhoI</i> -LOV2 (I-E)- <i>EcoRI</i>
Yang LOV2 FRET	<i>XhoI</i> -mTFP1- <i>SphI</i> -LOV2- <i>KpnI</i> -cpVenus- <i>EcoRI</i>
Yang LOV2 FRET C-A	<i>XhoI</i> -mTFP1- <i>SphI</i> -LOV2 (C-A) - <i>KpnI</i> -cpVenus- <i>EcoRI</i>
Yang LOV2 FRET I-E	<i>XhoI</i> -mTFP1- <i>SphI</i> -LOV2 (I-E) - <i>KpnI</i> -cpVenus- <i>EcoRI</i>
O/Ch LOV2 FRET	<i>XhoI</i> -mOrange- <i>SphI</i> -LOV2- <i>KpnI</i> -mCherry- <i>HindIII</i>
O/Ch LOV2 FRET C-A	<i>XhoI</i> -mOrange- <i>SphI</i> -LOV2 (C-A) - <i>KpnI</i> -mCherry- <i>HindIII</i>
O/Ch LOV2 FRET I-E	<i>XhoI</i> -mOrange- <i>SphI</i> -LOV2 (I-E) - <i>KpnI</i> -mCherry- <i>HindIII</i>
ddRFP LOV2	<i>XhoI</i> -ddRFP A- <i>SphI</i> -LOV2- <i>KpnI</i> -ddRFP B- <i>HindIII</i>
ddRFP LOV2 C-A	<i>XhoI</i> -ddRFP A- <i>SphI</i> -LOV2 (C-A) - <i>KpnI</i> -ddRFP B- <i>HindIII</i>
ddRFP LOV2 I-E	<i>XhoI</i> -ddRFP A- <i>SphI</i> -LOV2 (I-E)- <i>KpnI</i> -ddRFP B- <i>HindIII</i>
LOV2 (<i>Avena sativa</i>)	
LOV2	<i>XhoI</i> -LOV2- <i>HindIII</i>
LOV2 C-A	<i>XhoI</i> -LOV2 (C-A)- <i>HindIII</i>
LOV2 I-E	<i>XhoI</i> -LOV2 (I-E)- <i>HindIII</i>
LOV2-GECO	<i>XhoI</i> -LOV2)- <i>KpnI</i> -GECO main body (cpFP)- <i>BglII</i> - <i>HindIII</i>
LOV2-GECO No PVV	<i>XhoI</i> -LOV2-GECO main body (cpFP)- <i>BglII</i> - <i>HindIII</i>
LOV2-GECO No β 7	<i>XhoI</i> -LOV2-GECO main body (cpFP) - <i>BglII</i> - <i>HindIII</i>
LOV2-GECO Hybrid helix	<i>XhoI</i> -LOV core-hybrid helix of $J\alpha$ and β 7-GECO main body (cpFP) - <i>BglII</i> - <i>HindIII</i>
cpLOV2 variant 1	<i>XhoI</i> - $J\alpha$ -helix)- <i>KpnI</i> -LOV core- <i>HindIII</i>
cpLOV2 variant 2	<i>XhoI</i> - $J\alpha$ -helix)- <i>KpnI</i> - <i>BglII</i> -LOV core- <i>HindIII</i>
cpLOV2-GECO	<i>XhoI</i> - $J\alpha$ -helix)- <i>KpnI</i> -GECO main body (cpFP) - <i>BglII</i> -LOV core- <i>HindIII</i>
¹ All constructs are in pBAD/His B	

Bibliography

1. Newman R. H., Fosbrink M. D., Zhang J. Genetically Encodable Fluorescent Biosensors for Tracking Signaling Dynamics in Living Cells. *Chem. Rev.* **2011**, 111(5), 3614-3666.
2. Depry C., Mehta S., Zhang J. Multiplexed visualization of dynamic signaling networks using genetically encoded fluorescent protein-based biosensors. *Pflugers Arch.* **2012**, 465(3), 373-381.
3. Frommer W. B., Davidson M. W., Campbell R. E. Genetically encoded biosensors based on engineered fluorescent proteins. *Chem. Soc. Rev.* **2009**, 38(10), 2833-2841.
4. Ntziachristos V. Fluorescence molecular imaging. *Annu. Rev. Biomed. Eng.* **2006**, 8, 1-33.
5. Wang Y., Shyy J. Y.-J., Chien S. Fluorescence proteins, live-cell imaging, and mechanobiology: seeing is believing. *Annu. Rev. Biomed. Eng.* **2008**, 10, 1-38.
6. Fernandez-Suarez M., Ting A. Y. Fluorescent probes for super-resolution imaging in living cells. *Nat. Rev. Mol. Cell Biol.* **2008**, 9(12), 929-943.
7. Terai T., Nagano T. Fluorescent probes for bioimaging applications. *Curr. Opin. Chem. Biol.* **2008**, 12(5), 515-521.
8. Grynkiewicz G., Poenie M., Tsien R. Y. A new generation of Ca²⁺ indicators with greatly improved fluorescence properties. *J. Biol. Chem.* **1985**, 260(6), 3440-3450.
9. Helm P. J., Patwardhan A., Manders E. M. A study of the precision of confocal, ratiometric, Fura-2-based [Ca²⁺] measurements. *Cell Calcium* **1997**, 22(4), 287-298.
10. Miyawaki A., Llopis J., Heim R., McCaffery J. M., Adams J. A., Ikura M., Tsien R. Y. Fluorescent indicators for Ca²⁺ based on green fluorescent proteins and calmodulin. *Nature* **1997**, 388(6645), 882-887.
11. Shaner N. C., Steinbach P. A., Tsien R. Y. A guide to choosing fluorescent proteins. *Nat. Methods* **2005**, 2(12), 905-909.
12. Kogure T., Karasawa S., Araki T., Saito K., Kinjo M., Miyawaki A. A fluorescent variant of a protein from the stony coral *Montipora* facilitates dual-color single-laser fluorescence cross-correlation spectroscopy. *Nat. Biotechnol.* **2006**, 24(5), 577-581.

13. Hires S. A., Zhu Y., Tsien R. Y. Optical measurement of synaptic glutamate spillover and reuptake by linker optimized glutamate-sensitive fluorescent reporters. *Proc. Natl. Acad. Sci. U. S. A.* **2008**, 105(11), 4411-4416.
14. Ding Y., Ai H. W., Hoi H., Campbell R. E. Förster resonance energy transfer-based biosensors for multiparameter ratiometric imaging of Ca²⁺ dynamics and caspase-3 activity in single cells. *Anal. Chem.* **2011**, 83(24), 9687-9693.
15. DiPilato L. M., Cheng X., Zhang J. Fluorescent indicators of cAMP and Epac activation reveal differential dynamics of cAMP signaling within discrete subcellular compartments. *Proc. Natl. Acad. Sci. U. S. A.* **2004**, 101(47), 16513-16518.
16. van der Krogt G. N. M., Ogink J., Ponsioen B., Jalink K. A comparison of donor-acceptor pairs for genetically encoded FRET sensors: application to the Epac cAMP sensor as an example. *PLoS One* **2008**, 3(4), e1916.
17. Zhang J., Allen M. D. FRET-based biosensors for protein kinases: illuminating the kinome. *Mol. Biosyst.* **2007**, 3(11), 759-765.
18. Xu X., Gerard A. L., Huang B. C., Anderson D. C., Payan D. G., Luo Y. Detection of programmed cell death using fluorescence energy transfer. *Nucleic Acids Res.* **1998**, 26(8), 2034-2039.
19. Ai H. W., Hazelwood K. L., Davidson M. W., Campbell R. E. Fluorescent protein FRET pairs for ratiometric imaging of dual biosensors. *Nat. Methods* **2008**, 5(5), 401-403.
20. Shyu Y. J., Hu C. D. Fluorescence complementation: an emerging tool for biological research. *Trends Biotechnol.* **2008**, 26(11), 622-630.
21. Kerppola T. K. Bimolecular fluorescence complementation (BiFC) analysis as a probe of protein interactions in living cells. *Annu. Rev. Biophys.* **2008**, 37, 465-487.
22. Kerppola T. K. Visualization of molecular interactions using bimolecular fluorescence complementation analysis: Characteristics of protein fragment complementation. *Chem. Soc. Rev.* **2009**, 38(10), 2876.
23. Aye-Han N.-N., Allen M. D., Ni Q., Zhang J. Parallel tracking of cAMP and PKA signaling dynamics in living cells with FRET-based fluorescent biosensors. *Mol. Biosyst.* **2012**, 8(5), 1435.
24. Ouyang M., Huang H., Shaner N. C., Remacle A. G., Shiryaev S. A., Strongin A. Y., Tsien R. Y., Wang Y. Simultaneous visualization of

- protumorigenic Src and MT1-MMP activities with fluorescence resonance energy transfer. *Cancer Res.* **2010**, 70(6), 2204-2212.
25. Bates M., Huang B., Dempsey G. T., Zhuang X. Multicolor Super-Resolution Imaging with Photo-Switchable Fluorescent Probes. *Science* **2007**, 317(5845), 1749-1753.
 26. Kominami K., Nagai T., Sawasaki T., Tsujimura Y., Yashima K., Sunaga Y., Tsuchimochi M., Nishimura J., Chiba K., Nakabayashi J., et al. In vivo imaging of hierarchical spatiotemporal activation of caspase-8 during apoptosis. *PLoS One* **2012**, 7(11), e50218.
 27. Kawai H., Suzuki T., Kobayashi T., Sakurai H., Ohata H., Honda K., Momose K., Namekata I., Tanaka H., Shigenobu K., et al. Simultaneous real-time detection of initiator- and effector-caspase activation by double fluorescence resonance energy transfer analysis. *J. Pharmacol. Sci.* **2005**, 97(3), 361-368.
 28. Carlson H. J., Campbell R. E. Genetically encoded FRET-based biosensors for multiparameter fluorescence imaging. *Curr. Opin. Biotechnol.* **2009**, 20(1), 19-27.
 29. Day R. N., Davidson M. W. The fluorescent protein palette: tools for cellular imaging. *Chem. Soc. Rev.* **2009**, 38(10), 2887.
 30. Zimmer M. GFP: from jellyfish to the Nobel prize and beyond. *Chem. Soc. Rev.* **2009**, 38(10), 2823.
 31. Tsien R. Y. The green fluorescent protein. *Annu. Rev. Biochem.* **1998**, 67, 509-544.
 32. Prasher D. C., Eckenrode V. K., Ward W. W., Prendergast F. G., Cormier M. J. Primary structure of the *Aequorea victoria* green-fluorescent protein. *Gene* **1992**, 111(2), 229-233.
 33. Inouye S., Tsuji F. I. *Aequorea* green fluorescent protein. Expression of the gene and fluorescence characteristics of the recombinant protein. *FEBS Lett.* **1994**, 341(2-3), 277-280.
 34. Chalfie M., Tu Y., Euskirchen G., Ward W. W., Prasher D. C. Green Fluorescent Protein as a Marker for Gene Expression. *Science* **1994**, 263(5148), 802-805.
 35. Matz M. V., Fradkov A. F., Labas Y. A., Savitsky A. P., Zaraisky A. G., Markelov M. L., Lukyanov S. A. Fluorescent proteins from nonbioluminescent Anthozoa species. *Nat. Biotechnol.* **1999**, 17(10), 969-973.

36. Labas Y. A., Gurskaya N. G., Yanushevich Y. G., Fradkov A. F., Lukyanov K. A., Lukyanov S. A., Matz M. V. Diversity and evolution of the green fluorescent protein family. *Proc. Natl. Acad. Sci. U. S. A.* **2002**, 99(7), 4256-4261.
37. Salih A., Larkum A., Cox G., Kühl M., Hoegh-Guldberg O. Fluorescent pigments in corals are photoprotective. *Nature* **2000**, 408(6814), 850-853.
38. Matz M. V., Marshall N. J., Vorobyev M. Are corals colorful? *Photochem. Photobiol.* **2006**, 82(2), 345-350.
39. Shaner N. C., Lambert G. G., Chamma A., Ni Y., Cranfill P. J., Baird M. A., Sell B. R., Allen J. R., Day R. N., Israelsson M., et al. A bright monomeric green fluorescent protein derived from *Branchiostoma lanceolatum*. *Nat. Methods* **2013**, 10(5), 407-409.
40. Ormo M., Cubitt A. B., Kallio K., Gross L. A., Tsien R. Y., Remington S. J. Crystal structure of the *Aequorea victoria* green fluorescent protein. *Science* **1996**, 273(5280), 1392-1395.
41. Yang F., Moss L. G., Phillips G. N., Jr. The molecular structure of green fluorescent protein. *Nat. Biotechnol.* **1996**, 14(10), 1246-1251.
42. Barondeau D. P., Kassmann C. J., Tainer J. A., Getzoff E. D. Understanding GFP posttranslational chemistry: structures of designed variants that achieve backbone fragmentation, hydrolysis, and decarboxylation. *J. Am. Chem. Soc.* **2006**, 128(14), 4685-4693.
43. Heim R., Prasher D. C., Tsien R. Y. Wavelength mutations and posttranslational autoxidation of green fluorescent protein. *Proc. Natl. Acad. Sci. U. S. A.* **1994**, 91(26), 12501-12504.
44. Rosenow M. A., Patel H. N., Wachter R. M. Oxidative chemistry in the GFP active site leads to covalent cross-linking of a modified leucine side chain with a histidine imidazole: implications for the mechanism of chromophore formation. *Biochemistry* **2005**, 44(23), 8303-8311.
45. Wachter R. M., Watkins J. L., Kim H. Mechanistic diversity of red fluorescence acquisition by GFP-like proteins. *Biochemistry* **2010**, 49(35), 7417-7427.
46. Strack R. L., Strongin D. E., Mets L., Glick B. S., Keenan R. J. Chromophore formation in DsRed occurs by a branched pathway. *J. Am. Chem. Soc.* **2010**, 132(24), 8496-8505.
47. Subach O. M., Malashkevich V. N., Zencheck W. D., Morozova K. S., Piatkevich K. D., Almo S. C., Verkhusha V. V. Structural characterization

- of acylimine-containing blue and red chromophores in mTagBFP and TagRFP fluorescent proteins. *Chem. Biol.* **2010**, 17(4), 333-341.
48. Tomosugi W., Matsuda T., Tani T., Nemoto T., Kotera I., Saito K., Horikawa K., Nagai T. An ultramarine fluorescent protein with increased photostability and pH insensitivity. *Nat. Methods* **2009**, 6(5), 351-353.
 49. Shaner N. C., Campbell R. E., Steinbach P. A., Giepmans B. N. G., Palmer A. E., Tsien R. Y. Improved monomeric red, orange and yellow fluorescent proteins derived from *Discosoma* sp. red fluorescent protein. *Nat. Biotechnol.* **2004**, 22(12), 1567-1572.
 50. Ai H. W., Shaner N. C., Cheng Z., Tsien R. Y., Campbell R. E. Exploration of new chromophore structures leads to the identification of improved blue fluorescent proteins. *Biochemistry* **2007**, 46(20), 5904-5910.
 51. Drobizhev M., Tillo S., Makarov N. S., Hughes T. E., Rebane A. Color hues in red fluorescent proteins are due to internal quadratic Stark effect. *J. Phys. Chem. B* **2009**, 113(39), 12860-12864.
 52. Shu X., Shaner N. C., Yarbrough C. A., Tsien R. Y., Remington S. J. Novel chromophores and buried charges control color in mFruits. *Biochemistry* **2006**, 45(32), 9639-9647.
 53. Baird G. S., Zacharias D. A., Tsien R. Y. Biochemistry, mutagenesis, and oligomerization of DsRed, a red fluorescent protein from coral. *Proc. Natl. Acad. Sci. U. S. A.* **2000**, 97(22), 11984-11993.
 54. Campbell R. E., Tour O., Palmer A. E., Steinbach P. A., Baird G. S., Zacharias D. A., Tsien R. Y. A monomeric red fluorescent protein. *Proc. Natl. Acad. Sci. U. S. A.* **2002**, 99(12), 7877-7882.
 55. Ai H. W., Henderson J. N., Remington S. J., Campbell R. E. Directed evolution of a monomeric, bright and photostable version of *Clavularia* cyan fluorescent protein: structural characterization and applications in fluorescence imaging. *Biochem. J.* **2006**, 400(3), 531-540.
 56. Hoi H., Howe E. S., Ding Y., Zhang W., Baird M. A., Sell B. R., Allen J. R., Davidson M. W., Campbell R. E. An engineered monomeric *Zoanthus* sp. yellow fluorescent protein. *Chem. Biol.* **2013**, Accepted.
 57. Strack R. L., Strongin D. E., Bhattacharyya D., Tao W., Berman A., Broxmeyer H. E., Keenan R. J., Glick B. S. A noncytotoxic DsRed variant for whole-cell labeling. *Nat Methods* **2008**, 5(11), 955-957.

58. Zacharias D. A., Violin J. D., Newton A. C., Tsien R. Y. Partitioning of lipid-modified monomeric GFPs into membrane microdomains of live cells. *Science* **2002**, 296(5569), 913-916.
59. Ai H. W., Olenych S. G., Wong P., Davidson M. W., Campbell R. E. Hue-shifted monomeric variants of *Clavularia* cyan fluorescent protein: identification of the molecular determinants of color and applications in fluorescence imaging. *BMC Biol.* **2008**, 6(1), 13.
60. Alford S. C., Abdelfattah A. S., Ding Y., Campbell R. E. A fluorogenic red fluorescent protein heterodimer. *Chem. Biol.* **2012**, 19(3), 353-360.
61. Alford S. C., Ding Y., Simmen T., Campbell R. E. Dimerization-dependent green and yellow fluorescent proteins. *ACS Synth. Biol.* **2012**, 1(12), 569-575.
62. Grunberg R., Burnier J. V., Ferrar T., Beltran-Sastre V., Stricher F., van der Sloot A. M., Garcia-Olivas R., Mallabiabarrena A., Sanjuan X., Zimmermann T., et al. Engineering of weak helper interactions for high-efficiency FRET probes. *Nat. Methods* **2013**, advance online publication.
63. Baird G. S., Zacharias D. A., Tsien R. Y. Circular permutation and receptor insertion within green fluorescent proteins. *Proc. Natl. Acad. Sci. U. S. A.* **1999**, 96(20), 11241-11247.
64. Topell S., Hennecke J., Glockshuber R. Circularly permuted variants of the green fluorescent protein. *FEBS Lett.* **1999**, 457(2), 283-292.
65. Nagai T., Sawano A., Park E. S., Miyawaki A. Circularly permuted green fluorescent proteins engineered to sense Ca²⁺. *Proc. Natl. Acad. Sci. U. S. A.* **2001**, 98(6), 3197-3202.
66. Kawai Y., Sato M., Umezawa Y. Single color fluorescent indicators of protein phosphorylation for multicolor imaging of intracellular signal flow dynamics. *Anal. Chem.* **2004**, 76(20), 6144-6149.
67. Nagai T., Yamada S., Tominaga T., Ichikawa M., Miyawaki A. Expanded dynamic range of fluorescent indicators for Ca²⁺ by circularly permuted yellow fluorescent proteins. *Proc. Natl. Acad. Sci. U. S. A.* **2004**, 101(29), 10554-10559.
68. Lukyanov K. A., Chudakov D. M., Lukyanov S., Verkhusha V. V. Innovation: Photoactivatable fluorescent proteins. *Nat. Rev. Mol. Cell Biol.* **2005**, 6(11), 885-891.
69. Patterson G. H., Lippincott-Schwartz J. A photoactivatable GFP for selective photolabeling of proteins and cells. *Science* **2002**, 297(5588), 1873-1877.

70. McEvoy A. L., Hoi H., Bates M., Platonova E., Cranfill P. J., Baird M. A., Davidson M. W., Ewers H., Liphardt J., Campbell R. E. mMaple: a photoconvertible fluorescent protein for use in multiple imaging modalities. *PLoS One* **2012**, 7(12), e51314.
71. Ando R., Hama H., Yamamoto-Hino M., Mizuno H., Miyawaki A. An optical marker based on the UV-induced green-to-red photoconversion of a fluorescent protein. *Proc. Natl. Acad. Sci. U. S. A.* **2002**, 99(20), 12651-12656.
72. Shaner N. C., Patterson G. H., Davidson M. W. Advances in fluorescent protein technology. *J. Cell Sci.* **2007**, 120(Pt 24), 4247-4260.
73. Zapata-Hommer O., Griesbeck O. Efficiently folding and circularly permuted variants of the Sapphire mutant of GFP. *BMC Biotechnol.* **2003**, 3, 5.
74. Förster T. Zwischenmolekulare Energiewanderung und Fluoreszenz. *Annalen der Physik* **1948**, 437(1-2), 55-75.
75. Campbell R. E. Fluorescent-protein-based biosensors: modulation of energy transfer as a design principle. *Anal. Chem.* **2009**, 81(15), 5972-5979.
76. Patterson G. H., Piston D. W., Barisas B. G. Forster distances between green fluorescent protein pairs. *Anal. Biochem.* **2000**, 284(2), 438-440.
77. Sun Y., Booker C. F., Kumari S., Day R. N., Davidson M., Periasamy A. Characterization of an orange acceptor fluorescent protein for sensitized spectral fluorescence resonance energy transfer microscopy using a white-light laser. *J. Biomed. Opt.* **2009**, 14(5), 054009.
78. Niino Y., Hotta K., Oka K. Blue fluorescent cGMP sensor for multiparameter fluorescence imaging. *PLoS One* **2010**, 5(2), e9164.
79. Kotera I., Iwasaki T., Imamura H., Noji H., Nagai T. Reversible dimerization of *Aequorea victoria* fluorescent proteins increases the dynamic range of FRET-based indicators. *ACS Chem. Biol.* **2010**, 5(2), 215-222.
80. Ohashi T., Galiacy S. D., Briscoe G., Erickson H. P. An experimental study of GFP-based FRET, with application to intrinsically unstructured proteins. *Protein Sci.* **2007**, 16(7), 1429-1438.
81. Vinkenburg J. L., Evers T. H., Reulen S. W., Meijer E. W., Merkx M. Enhanced sensitivity of FRET-based protease sensors by redesign of the GFP dimerization interface. *ChemBioChem* **2007**, 8(10), 1119-1121.

82. Nguyen A. W., Daugherty P. S. Evolutionary optimization of fluorescent proteins for intracellular FRET. *Nat. Biotechnol.* **2005**, 23(3), 355-360.
83. Heim R., Tsien R. Y. Engineering green fluorescent protein for improved brightness, longer wavelengths and fluorescence resonance energy transfer. *Curr. Biol.* **1996**, 6(2), 178-182.
84. Yang T. T., Sinai P., Green G., Kitts P. A., Chen Y. T., Lybarger L., Chervenak R., Patterson G. H., Piston D. W., Kain S. R. Improved fluorescence and dual color detection with enhanced blue and green variants of the green fluorescent protein. *J. Biol. Chem.* **1998**, 273(14), 8212-8218.
85. Rizzo M. A., Springer G. H., Granada B., Piston D. W. An improved cyan fluorescent protein variant useful for FRET. *Nat. Biotechnol.* **2004**, 22(4), 445-449.
86. Goedhart J., van Weeren L., Hink M. A., Vischer N. O., Jalink K., Gadella T. W., Jr. Bright cyan fluorescent protein variants identified by fluorescence lifetime screening. *Nat. Methods* **2010**, 7(2), 137-139.
87. Day R. N., Booker C. F., Periasamy A. Characterization of an improved donor fluorescent protein for Forster resonance energy transfer microscopy. *J. Biomed. Opt.* **2008**, 13(3), 031203.
88. Griesbeck O., Baird G. S., Campbell R. E., Zacharias D. A., Tsien R. Y. Reducing the environmental sensitivity of yellow fluorescent protein. Mechanism and applications. *J. Biol. Chem.* **2001**, 276(31), 29188-29194.
89. Nagai T., Ibata K., Park E. S., Kubota M., Mikoshiba K., Miyawaki A. A variant of yellow fluorescent protein with fast and efficient maturation for cell-biological applications. *Nat. Biotechnol.* **2002**, 20(1), 87-90.
90. Weissleder R. A clearer vision for in vivo imaging. *Nat. Biotechnol.* **2001**, 19(4), 316-317.
91. Davidson M. W., Campbell R. E. Engineered fluorescent proteins: innovations and applications. *Nat. Methods* **2009**, 6(10), 713-717.
92. Lam A. J., St-Pierre F., Gong Y., Marshall J. D., Cranfill P. J., Baird M. A., McKeown M. R., Wiedenmann J., Davidson M. W., Schnitzer M. J., et al. Improving FRET dynamic range with bright green and red fluorescent proteins. *Nat. Methods* **2012**, 9(10), 1005-1012.
93. Lukasiewicz S., Faron-Gorecka A., Dobrucki J., Polit A., Dziedzicka-Wasylewska M. Studies on the role of the receptor protein motifs possibly involved in electrostatic interactions on the dopamine D1 and D2 receptor oligomerization. *FEBS J.* **2009**, 276(3), 760-775.

94. Marcaggi P., Mutoh H., Dimitrov D., Beato M., Knopfel T. Optical measurement of mGluR1 conformational changes reveals fast activation, slow deactivation, and sensitization. *Proc. Natl. Acad. Sci. U. S. A.* **2009**, 106(27), 11388-11393.
95. Palmer A. E., Giacomello M., Kortemme T., Hires S. A., Lev-Ram V., Baker D., Tsien R. Y. Ca²⁺ indicators based on computationally redesigned calmodulin-peptide pairs. *Chem. Biol.* **2006**, 13(5), 521-530.
96. Dittmer P. J., Miranda J. G., Gorski J. A., Palmer A. E. Genetically encoded sensors to elucidate spatial distribution of cellular zinc. *J. Biol. Chem.* **2009**, 284(24), 16289-16297.
97. Wu X., Simone J., Hewgill D., Siegel R., Lipsky P. E., He L. Measurement of two caspase activities simultaneously in living cells by a novel dual FRET fluorescent indicator probe. *Cytometry A* **2006**, 69(6), 477-486.
98. Figueroa R. A., Ramberg V., Gatsinzi T., Samuelsson M., Zhang M., Iverfeldt K., Hallberg E. Anchored FRET sensors detect local caspase activation prior to neuronal degeneration. *Mol. Neurodegener.* **2011**, 6(1), 35.
99. Ghosh I., Hamilton A. D., Regan L. Antiparallel leucine zipper-directed protein reassembly: application to the green fluorescent protein. *J. Am. Chem. Soc.* **2000**, 122(23), 5658-5659.
100. Shyu Y. J., Liu H., Deng X., Hu C. D. Identification of new fluorescent protein fragments for bimolecular fluorescence complementation analysis under physiological conditions. *BioTechniques* **2006**, 40(1), 61-66.
101. Hu C. D., Chinenov Y., Kerppola T. K. Visualization of interactions among bZIP and Rel family proteins in living cells using bimolecular fluorescence complementation. *Mol. Cell* **2002**, 9(4), 789-798.
102. Jach G., Pesch M., Richter K., Frings S., Uhrig J. F. An improved mRFP1 adds red to bimolecular fluorescence complementation. *Nat. Methods* **2006**, 3(8), 597-600.
103. Fan J. Y., Cui Z. Q., Wei H. P., Zhang Z. P., Zhou Y. F., Wang Y. P., Zhang X. E. Split mCherry as a new red bimolecular fluorescence complementation system for visualizing protein-protein interactions in living cells. *Biochem. Biophys. Res. Commun.* **2008**, 367(1), 47-53.
104. Hu C. D., Kerppola T. K. Simultaneous visualization of multiple protein interactions in living cells using multicolor fluorescence complementation analysis. *Nat. Biotechnol.* **2003**, 21(5), 539-545.

105. Ottmann C., Weyand M., Wolf A., Kuhlmann J., Ottmann C. Applicability of superfolder YFP bimolecular fluorescence complementation in vitro. *Biol. Chem.* **2009**, 390(1), 81-90.
106. Zhao Y., Araki S., Wu J., Teramoto T., Chang Y. F., Nakano M., Abdelfattah A. S., Fujiwara M., Ishihara T., Nagai T., et al. An expanded palette of genetically encoded Ca²⁺ indicators. *Science* **2011**, 333(6051), 1888-1891.
107. Miesenbock G., De Angelis D. A., Rothman J. E. Visualizing secretion and synaptic transmission with pH-sensitive green fluorescent proteins. *Nature* **1998**, 394(6689), 192-195.
108. Li Y., Tsien R. W. pHTomato, a red, genetically encoded indicator that enables multiplex interrogation of synaptic activity. *Nat. Neurosci.* **2012**, 15(7), 1047-1053.
109. Jayaraman S., Haggie P., Wachter R. M., Remington S. J., Verkman A. S. Mechanism and cellular applications of a green fluorescent protein-based halide sensor. *J. Biol. Chem.* **2000**, 275(9), 6047-6050.
110. Dooley C. T., Dore T. M., Hanson G. T., Jackson W. C., Remington S. J., Tsien R. Y. Imaging dynamic redox changes in mammalian cells with green fluorescent protein indicators. *J. Biol. Chem.* **2004**, 279(21), 22284-22293.
111. Hanson G. T., Aggeler R., Oglesbee D., Cannon M., Capaldi R. A., Tsien R. Y., Remington S. J. Investigating mitochondrial redox potential with redox-sensitive green fluorescent protein indicators. *J. Biol. Chem.* **2004**, 279(13), 13044-13053.
112. Akerboom J., Rivera J. D., Guilbe M. M., Malave E. C., Hernandez H. H., Tian L., Hires S. A., Marvin J. S., Looger L. L., Schreier E. R. Crystal structures of the GCaMP calcium sensor reveal the mechanism of fluorescence signal change and aid rational design. *J. Biol. Chem.* **2009**, 284(10), 6455-6464.
113. Park J. S., Cochran R. J. *Protein Engineering and Design 2010*, Boca Raton: CRC Press.
114. Boas F. E., Harbury P. B. Potential energy functions for protein design. *Curr. Opin. Struct. Biol.* **2007**, 17(2), 199-204.
115. Regmi C. K., Bhandari Y. R., Gerstman B. S., Chapagain P. P. Exploring the diffusion of molecular oxygen in the red fluorescent protein mCherry using explicit oxygen molecular dynamics simulations. *J. Phys. Chem. B* **2013**, 117(8), 2247-2253.

116. Chica R. A., Moore M. M., Allen B. D., Mayo S. L. Generation of longer emission wavelength red fluorescent proteins using computationally designed libraries. *Proc. Natl. Acad. Sci. U. S. A.* **2010**, 107(47), 20257-20262.
117. Bloom J. D., Arnold F. H. In the light of directed evolution: pathways of adaptive protein evolution. *Proc. Natl. Acad. Sci. U. S. A.* **2009**, 106 Suppl 1, 9995-10000.
118. Yuan L., Kurek I., English J., Keenan R. Laboratory-directed protein evolution. *Microbiol. Mol. Biol. Rev.* **2005**, 69(3), 373-392.
119. Hibbert E. G., Dalby P. A. Directed evolution strategies for improved enzymatic performance. *Microb. Cell Fact.* **2005**, 4, 29.
120. Hutchison C. A., 3rd, Phillips S., Edgell M. H., Gillam S., Jahnke P., Smith M. Mutagenesis at a specific position in a DNA sequence. *J. Biol. Chem.* **1978**, 253(18), 6551-6560.
121. Sigal I. S., Harwood B. G., Arentzen R. Thiol-beta-lactamase: replacement of the active-site serine of RTEM beta-lactamase by a cysteine residue. *Proc. Natl. Acad. Sci. U. S. A.* **1982**, 79(23), 7157-7160.
122. Park S., Morley K. L., Horsman G. P., Holmquist M., Hult K., Kazlauskas R. J. Focusing mutations into the *P. fluorescens* esterase binding site increases enantioselectivity more effectively than distant mutations. *Chem. Biol.* **2005**, 12(1), 45-54.
123. Estell D. A., Graycar T. P., Wells J. A. Engineering an enzyme by site-directed mutagenesis to be resistant to chemical oxidation. *J. Biol. Chem.* **1985**, 260(11), 6518-6521.
124. von der Osten C., Branner S., Hastrup S., Hedegaard L., Rasmussen M. D., Bisgard-Frantzen H., Carlsen S., Mikkelsen J. M. Protein engineering of subtilisins to improve stability in detergent formulations. *J. Biotechnol.* **1993**, 28(1), 55-68.
125. Tobin M. B., Gustafsson C., Huisman G. W. Directed evolution: the 'rational' basis for 'irrational' design. *Curr. Opin. Struct. Biol.* **2000**, 10(4), 421-427.
126. Beckman R. A., Mildvan A. S., Loeb L. A. On the fidelity of DNA replication: manganese mutagenesis in vitro. *Biochemistry* **1985**, 24(21), 5810-5817.
127. Cirino P. C., Mayer K. M., Umeno D. Generating mutant libraries using error-prone PCR. *Methods Mol. Biol.* **2003**, 231, 3-9.

128. Drummond D. A., Iverson B. L., Georgiou G., Arnold F. H. Why high-error-rate random mutagenesis libraries are enriched in functional and improved proteins. *J. Mol. Biol.* **2005**, 350(4), 806-816.
129. Wang L., Jackson W. C., Steinbach P. A., Tsien R. Y. Evolution of new nonantibody proteins via iterative somatic hypermutation. *Proc. Natl. Acad. Sci. U. S. A.* **2004**, 101(48), 16745-16749.
130. Cramer A., Raillard S. A., Bermudez E., Stemmer W. P. DNA shuffling of a family of genes from diverse species accelerates directed evolution. *Nature* **1998**, 391(6664), 288-291.
131. Stemmer W. P. Rapid evolution of a protein in vitro by DNA shuffling. *Nature* **1994**, 370(6488), 389-391.
132. Zhao H., Zha W. In vitro 'sexual' evolution through the PCR-based staggered extension process (StEP). *Nat. Protoc.* **2006**, 1(4), 1865-1871.
133. Sen S., Venkata Dasu V., Mandal B. Developments in directed evolution for improving enzyme functions. *Appl. Biochem. Biotechnol.* **2007**, 143(3), 212-223.
134. Lin H., Cornish V. W. Screening and selection methods for large-scale analysis of protein function. *Angew. Chem. Int. Ed. Engl.* **2002**, 41(23), 4402-4425.
135. O'Neil K. T., Hoess R. H. Phage display: protein engineering by directed evolution. *Curr. Opin. Struct. Biol.* **1995**, 5(4), 443-449.
136. Cormack B. P., Valdivia R. H., Falkow S. FACS-optimized mutants of the green fluorescent protein (GFP). *Gene* **1996**, 173(1 Spec No), 33-38.
137. Schmidt-Dannert C. Directed evolution of single proteins, metabolic pathways, and viruses. *Biochemistry* **2001**, 40(44), 13125-13136.
138. Schmidt-Dannert C., Arnold F. H. Directed evolution of industrial enzymes. *Trends Biotechnol.* **1999**, 17(4), 135-136.
139. Chica R. A., Doucet N., Pelletier J. N. Semi-rational approaches to engineering enzyme activity: combining the benefits of directed evolution and rational design. *Curr. Opin. Biotechnol.* **2005**, 16(4), 378-384.
140. Fox R. J., Huisman G. W. Enzyme optimization: moving from blind evolution to statistical exploration of sequence-function space. *Trends Biotechnol.* **2008**, 26(3), 132-138.
141. Chica R. A., Moore M. M., Allen B. D., Mayo S. L. Generation of longer emission wavelength red fluorescent proteins using computationally

- designed libraries. *Proc. Natl. Acad. Sci. U. S. A.* **2010**, 107(47), 20257-20262.
142. Hoi H., Matsuda T., Nagai T., Campbell R. E. Highlightable Ca²⁺ indicators for live cell imaging. *J. Am. Chem. Soc.* **2013**, 135(1), 46-49.
 143. Ibraheem A., Yap H., Ding Y., Campbell R. E. A bacteria colony-based screen for optimal linker combinations in genetically encoded biosensors. *BMC Biotechnol.* **2011**, 11(1), 105.
 144. Ibraheem A., Campbell R. E. Designs and applications of fluorescent protein-based biosensors. *Curr. Opin. Chem. Biol.* **2010**, 14(1), 30-36.
 145. VanEngelenburg S. B., Palmer A. E. Fluorescent biosensors of protein function. *Curr. Opin. Chem. Biol.* **2008**, 12(1), 60-65.
 146. Violin J. D., Zhang J., Tsien R. Y., Newton A. C. A genetically encoded fluorescent reporter reveals oscillatory phosphorylation by protein kinase C. *J. Cell Biol.* **2003**, 161(5), 899-909.
 147. Ni Q., Ganesan A., Aye-Han N. N., Gao X., Allen M. D., Levchenko A., Zhang J. Signaling diversity of PKA achieved via a Ca²⁺-cAMP-PKA oscillatory circuit. *Nat. Chem. Biol.* **2011**, 7(1), 34-40.
 148. Grant D. M., Zhang W., McGhee E. J., Bunney T. D., Talbot C. B., Kumar S., Munro I., Dunsby C., Neil M. A., Katan M., et al. Multiplexed FRET to image multiple signaling events in live cells. *Biophys. J.* **2008**, 95(10), L69-71.
 149. Piljic A., Schultz C. Simultaneous recording of multiple cellular events by FRET. *ACS Chem. Biol.* **2008**, 3(3), 156-160.
 150. Palmer A., Jin C., Reed J., Tsien R. Bcl-2-mediated alterations in endoplasmic reticulum Ca²⁺ analyzed with an improved genetically encoded fluorescent sensor. *Proc. Natl. Acad. Sci. U. S. A.* **2004**, 101(50), 17404-17409.
 151. Palmer A. E., Tsien R. Y. Measuring calcium signaling using genetically targetable fluorescent indicators. *Nat. Protoc.* **2006**, 1(3), 1057-1065.
 152. Ikura M., Clore G. M., Gronenborn A. M., Zhu G., Klee C. B., Bax A. Solution structure of a calmodulin-target peptide complex by multidimensional NMR. *Science* **1992**, 256(5057), 632-638.
 153. Luo K. Q., Yu V. C., Pu Y., Chang D. C. Application of the fluorescence resonance energy transfer method for studying the dynamics of caspase-3 activation during UV-induced apoptosis in living HeLa cells. *Biochem. Biophys. Res. Commun.* **2001**, 283(5), 1054-1060.

154. Luo K. Q., Yu V. C., Pu Y., Chang D. C. Measuring dynamics of caspase-8 activation in a single living HeLa cell during TNF- α induced apoptosis. *Biochem. Biophys. Res. Commun.* **2003**, 304(2), 217-222.
155. Bortner C. D., Cidlowski J. A. Apoptotic volume decrease and the incredible shrinking cell. *Cell Death Differ.* **2002**, 9(12), 1307-1310.
156. McConkey D. J., Orrenius S. The role of calcium in the regulation of apoptosis. *Biochem. Biophys. Res. Commun.* **1997**, 239(2), 357-366.
157. Pu Y., Luo K., Chang D. A Ca²⁺ signal is found upstream of cytochrome c release during apoptosis in HeLa cells. *Biochem. Biophys. Res. Commun.* **2002**, 299(5), 762-769.
158. Kalderon D., Roberts B. L., Richardson W. D., Smith A. E. A short amino acid sequence able to specify nuclear location. *Cell* **1984**, 39(3 Pt 2), 499-509.
159. Wen W., Meinkoth J. L., Tsien R. Y., Taylor S. S. Identification of a signal for rapid export of proteins from the nucleus. *Cell* **1995**, 82(3), 463-473.
160. Kakar M., Davis J. R., Kern S. E., Lim C. S. Optimizing the protein switch: altering nuclear import and export signals, and ligand binding domain. *J. Control. Release* **2007**, 120(3), 220-232.
161. Ferrando-May E. Nucleocytoplasmic transport in apoptosis. *Cell Death Differ.* **2005**, 12(10), 1263-1276.
162. Kramer A., Liashkovich I., Oberleithner H., Ludwig S., Mazur I., Shahin V. Apoptosis leads to a degradation of vital components of active nuclear transport and a dissociation of the nuclear lamina. *Proc. Natl. Acad. Sci. U. S. A.* **2008**, 105(32), 11236-11241.
163. Chan K. S., Wong C. H., Huang Y. F., Li H. Y. Survivin withdrawal by nuclear export failure as a physiological switch to commit cells to apoptosis. *Cell Death Dis.* **2010**, 1(7), e57-59.
164. Danial N. N., Korsmeyer S. J. Cell death: critical control points. *Cell* **2004**, 116(2), 205-219.
165. Zhang X. D., Gillespie S. K., Hersey P. Staurosporine induces apoptosis of melanoma by both caspase-dependent and -independent apoptotic pathways. *Mol. Cancer Ther.* **2004**, 3(2), 187-197.
166. Imao T., Nagata S. Apaf-1- and Caspase-8-independent apoptosis. *Cell Death Differ.* **2013**, 20(2), 343-352.

167. Williams D. W., Kondo S., Krzyzanowska A., Hiromi Y., Truman J. W. Local caspase activity directs engulfment of dendrites during pruning. *Nat. Neurosci.* **2006**, 9(10), 1234-1236.
168. Simon D. J., Weimer R. M., McLaughlin T., Kallop D., Stanger K., Yang J., O'Leary D. D., Hannoush R. N., Tessier-Lavigne M. A caspase cascade regulating developmental axon degeneration. *J. Neurosci.* **2012**, 32(49), 17540-17553.
169. Kuo C. T., Zhu S., Younger S., Jan L. Y., Jan Y. N. Identification of E2/E3 ubiquitinating enzymes and caspase activity regulating *Drosophila* sensory neuron dendrite pruning. *Neuron* **2006**, 51(3), 283-290.
170. Qin X. Y., Lv J. H., Cui J., Fang X., Zhang Y. Curcumin protects against staurosporine toxicity in rat neurons. *Neurosci. Bull.* **2012**, 28(5), 606-610.
171. de Brito O. M., Scorrano L. An intimate liaison: spatial organization of the endoplasmic reticulum-mitochondria relationship. *EMBO J.* **2010**, 29(16), 2715-2723.
172. Franke W. W., Kartenbeck J. Outer mitochondrial membrane continuous with endoplasmic reticulum. *Protoplasma* **1971**, 73(1), 35-41.
173. Lewis J. A., Tata J. R. A rapidly sedimenting fraction of rat liver endoplasmic reticulum. *J. Cell Sci.* **1973**, 13(2), 447-459.
174. Rizzuto R., Pinton P., Carrington W., Fay F. S., Fogarty K. E., Lifshitz L. M., Tuft R. A., Pozzan T. Close contacts with the endoplasmic reticulum as determinants of mitochondrial Ca²⁺ responses. *Science* **1998**, 280(5370), 1763-1766.
175. Wang H. J., Guay G., Pogan L., Sauve R., Nabi I. R. Calcium regulates the association between mitochondria and a smooth subdomain of the endoplasmic reticulum. *J. Cell Biol.* **2000**, 150(6), 1489-1498.
176. Csordas G., Renken C., Varnai P., Walter L., Weaver D., Buttle K. F., Balla T., Mannella C. A., Hajnoczky G. Structural and functional features and significance of the physical linkage between ER and mitochondria. *J. Cell Biol.* **2006**, 174(7), 915-921.
177. Vance J. E. Phospholipid synthesis in a membrane fraction associated with mitochondria. *J. Biol. Chem.* **1990**, 265(13), 7248-7256.
178. Voelker D. R. New perspectives on the regulation of intermembrane glycerophospholipid traffic. *J. Lipid Res.* **2003**, 44(3), 441-449.
179. de Brito O. M., Scorrano L. Mitofusin 2 tethers endoplasmic reticulum to mitochondria. *Nature* **2008**, 456(7222), 605-610.

180. Rizzuto R., Marchi S., Bonora M., Aguiari P., Bononi A., De Stefani D., Giorgi C., Leo S., Rimessi A., Siviero R., et al. Ca²⁺ transfer from the ER to mitochondria: When, how and why. *Biochim. Biophys. Acta* **2009**, 1787(11), 1342-1351.
181. Boehning D., Patterson R. L., Sedaghat L., Glebova N. O., Kurosaki T., Snyder S. H. Cytochrome c binds to inositol (1,4,5) trisphosphate receptors, amplifying calcium-dependent apoptosis. *Nat. Cell Biol.* **2003**, 5(12), 1051-1061.
182. Bravo R., Vicencio J. M., Parra V., Troncoso R., Munoz J. P., Bui M., Quiroga C., Rodriguez A. E., Verdejo H. E., Ferreira J., et al. Increased ER-mitochondrial coupling promotes mitochondrial respiration and bioenergetics during early phases of ER stress. *J. Cell Sci.* **2011**, 124(Pt 13), 2143-2152.
183. Pizzo P., Pozzan T. Mitochondria–endoplasmic reticulum choreography: structure and signaling dynamics. *Trends Cell Biol.* **2007**, 17(10), 511-517.
184. Hayashi T., Rizzuto R., Hajnoczky G., Su T.-P. MAM: more than just a housekeeper. *Trends Cell Biol.* **2009**, 19(2), 81-88.
185. Lebedzinska M., Szabadkai G., Jones A. W. E., Duszynski J., Wieckowski M. R. Interactions between the endoplasmic reticulum, mitochondria, plasma membrane and other subcellular organelles. *Int. J. Biochem. Cell Biol.* **2009**, 41(10), 1805-1816.
186. Raturi A., Simmen T. Where the endoplasmic reticulum and the mitochondrion tie the knot: the mitochondria-associated membrane (MAM). *Biochim. Biophys. Acta* **2013**, 1833(1), 213-224.
187. Lewin T. M. Acyl-CoA Synthetase Isoforms 1, 4, and 5 Are Present in Different Subcellular Membranes in Rat Liver and Can Be Inhibited Independently. *J. Biol. Chem.* **2001**, 276(27), 24674-24679.
188. Faergeman N. J., Knudsen J. Role of long-chain fatty acyl-CoA esters in the regulation of metabolism and in cell signalling. *Biochem. J.* **1997**, 323 (Pt 1), 1-12.
189. Hoepfner D., Schildknecht D., Braakman I., Philippsen P., Tabak H. F. Contribution of the endoplasmic reticulum to peroxisome formation. *Cell* **2005**, 122(1), 85-95.
190. Horner S. M., Liu H. M., Park H. S., Briley J., Gale M., Jr. Mitochondrial-associated endoplasmic reticulum membranes (MAM) form innate immune synapses and are targeted by hepatitis C virus. *Proc. Natl. Acad. Sci. U. S. A.* **2011**, 108(35), 14590-14595.

191. Pfanner N., Craig E. Mitochondrial preprotein translocase. *Annu. Rev. Cell Dev. Biol.* **1997**, 13, 25-57.
192. Abe Y., Shodai T., Muto T., Mihara K., Torii H., Nishikawa S., Endo T., Kohda D. Structural basis of presequence recognition by the mitochondrial protein import receptor Tom20. *Cell* **2000**, 100(5), 551-560.
193. Kanaji S., Iwahashi J., Kida Y., Sakaguchi M., Mihara K. Characterization of the signal that directs Tom20 to the mitochondrial outer membrane. *J. Cell Biol.* **2000**, 151(2), 277-288.
194. Roderick H. L., Lechleiter J. D., Camacho P. Cytosolic phosphorylation of calnexin controls intracellular Ca(2+) oscillations via an interaction with SERCA2b. *J. Cell Biol.* **2000**, 149(6), 1235-1248.
195. Schrag J. D., Bergeron J. J., Li Y., Borisova S., Hahn M., Thomas D. Y., Cygler M. The Structure of calnexin, an ER chaperone involved in quality control of protein folding. *Mol. Cell* **2001**, 8(3), 633-644.
196. Chevet E., Smirle J., Cameron P. H., Thomas D. Y., Bergeron J. J. M. Calnexin phosphorylation: Linking cytoplasmic signalling to endoplasmic reticulum lumenal functions. *Semin. Cell Dev. Biol.* **2010**, 21(5), 486-490.
197. Lynes E. M., Bui M., Yap M. C., Benson M. D., Schneider B., Ellgaard L., Berthiaume L. G., Simmen T. Palmitoylated TMX and calnexin target to the mitochondria-associated membrane. *EMBO J.* **2012**, 31(2), 457-470.
198. Goetz J. G., Genty H., St-Pierre P., Dang T., Joshi B., Sauve R., Vogl W., Nabi I. R. Reversible interactions between smooth domains of the endoplasmic reticulum and mitochondria are regulated by physiological cytosolic Ca²⁺ levels. *J. Cell Sci.* **2007**, 120(20), 3553-3564.
199. Ogg S. C., Barz W. P., Walter P. A functional GTPase domain, but not its transmembrane domain, is required for function of the SRP receptor β -subunit. *J. Cell Biol.* **1998**, 142(2), 341-354.
200. Schwartz T., Blobel G. Structural basis for the function of the beta subunit of the eukaryotic signal recognition particle receptor. *Cell* **2003**, 112(6), 793-803.
201. Fulga T. A., Sinning I., Dobberstein B., Pool M. R. SRbeta coordinates signal sequence release from SRP with ribosome binding to the translocon. *EMBO J.* **2001**, 20(9), 2338-2347.
202. Zhu W., Cowie A., Wasfy G. W., Penn L. Z., Leber B., Andrews D. W. Bcl-2 mutants with restricted subcellular location reveal spatially distinct pathways for apoptosis in different cell types. *EMBO J.* **1996**, 15(16), 4130-4141.

203. Hwang Y. T. Novel targeting signals mediate the sorting of different isoforms of the tail-anchored membrane protein cytochrome b5 to either endoplasmic reticulum or mitochondria. *Plant Cell* **2004**, 16(11), 3002-3019.
204. Gorke B. Activity of Lac repressor anchored to the Escherichia coli inner membrane. *Nucleic Acids Res.* **2005**, 33(8), 2504-2511.
205. Stayrook S., Jaru-Ampornpan P., Ni J., Hochschild A., Lewis M. Crystal structure of the λ repressor and a model for pairwise cooperative operator binding. *Nature* **2008**, 452(7190), 1022-1025.
206. Lewin T. M., Van Horn C. G., Krisans S. K., Coleman R. A. Rat liver acyl-CoA synthetase 4 is a peripheral-membrane protein located in two distinct subcellular organelles, peroxisomes, and mitochondrial-associated membrane. *Arch. Biochem. Biophys.* **2002**, 404(2), 263-270.
207. Smith M. a. E., Saraceno G. E., Capani F., Castilla R. Long-chain acyl-CoA synthetase 4 is regulated by phosphorylation. *Biochem. Biophys. Res. Commun.* **2013**, 430(1), 272-277.
208. Meloni I., Muscettola M., Raynaud M., Longo I., Bruttini M., Moizard M. P., Gomot M., Chelly J., des Portes V., Fryns J. P., et al. FAACL4, encoding fatty acid-CoA ligase 4, is mutated in nonspecific X-linked mental retardation. *Nat. Genet.* **2002**, 30(4), 436-440.
209. Piccini M., Vitelli F., Bruttini M., Pober B. R., Jonsson J. J., Villanova M., Zollo M., Borsani G., Ballabio A., Renieri A. FAACL4, a new gene encoding long-chain acyl-CoA synthetase 4, is deleted in a family with Alport syndrome, elliptocytosis, and mental retardation. *Genomics* **1998**, 47(3), 350-358.
210. Cao Y., Traer E., Zimmerman G. A., McIntyre T. M., Prescott S. M. Cloning, expression, and chromosomal localization of human long-chain fatty acid-CoA ligase 4 (FAACL4). *Genomics* **1998**, 49(2), 327-330.
211. Schon E. A., Area-Gomez E. Mitochondria-associated ER membranes in Alzheimer disease. *Mol. Cell. Neurosci.* **2013**, 55, 26-36.
212. Issop L., Rone M. B., Papadopoulos V. Organelle plasticity and interactions in cholesterol transport and steroid biosynthesis. *Mol. Cell. Endocrinol.* **2013**, 371(1-2), 34-46.
213. Coquelle N., Glover J. N. M. PARP pairs up to PARsylate. *Nat. Struct. Mol. Biol.* **2012**, 19(7), 660-661.
214. Ciccia A., Elledge S. J. The DNA damage response: making it safe to pay with knives. *Mol. Cell* **2010**, 40(2), 179-204.

215. Ali A. A. E., Timinszky G., Arribas-Bosacoma R., Kozlowski M., Hassa P. O., Hassler M., Ladurner A. G., Pearl L. H., Oliver A. W. The zinc-finger domains of PARP1 cooperate to recognize DNA strand breaks. *Nat. Struct. Mol. Biol.* **2012**, 19(7), 685-692.
216. D'Amours D., Desnoyers S., D'Silva I., Poirier G. G. Poly(ADP-ribose)ylation reactions in the regulation of nuclear functions. *Biochem. J.* **1999**, 342 (Pt 2), 249-268.
217. Rouleau M., Patel A., Hendzel M. J., Kaufmann S. H., Poirier G. G. PARP inhibition: PARP1 and beyond. *Nat. Rev. Cancer* **2010**, 10(4), 293-301.
218. Farmer H., McCabe N., Lord C. J., Tutt A. N., Johnson D. A., Richardson T. B., Santarosa M., Dillon K. J., Hickson I., Knights C., et al. Targeting the DNA repair defect in BRCA mutant cells as a therapeutic strategy. *Nature* **2005**, 434(7035), 917-921.
219. Fong P. C., Boss D. S., Yap T. A., Tutt A., Wu P., Mergui-Roelvink M., Mortimer P., Swaisland H., Lau A., O'Connor M. J., et al. Inhibition of poly(ADP-ribose) polymerase in tumors from BRCA mutation carriers. *N. Engl. J. Med.* **2009**, 361(2), 123-134.
220. Szabo C., Dawson V. L. Role of poly(ADP-ribose) synthetase in inflammation and ischaemia-reperfusion. *Trends Pharmacol. Sci.* **1998**, 19(7), 287-298.
221. Decker P., Miranda E. A., de Murcia G., Muller S. An improved nonisotopic test to screen a large series of new inhibitor molecules of poly(ADP-ribose) polymerase activity for therapeutic applications. *Clin. Cancer Res.* **1999**, 5(5), 1169-1172.
222. Dillon K. J., Smith G. C., Martin N. M. A FlashPlate assay for the identification of PARP-1 inhibitors. *J. Biomol. Screen.* **2003**, 8(3), 347-352.
223. Brown J. A., Marala R. B. Development of a high-throughput screening-amenable assay for human poly(ADP-ribose) polymerase inhibitors. *J. Pharmacol. Toxicol. Methods* **2002**, 47(3), 137-141.
224. Putt K. An enzymatic assay for poly(ADP-ribose) polymerase-1 (PARP-1) via the chemical quantitation of NAD⁺: application to the high-throughput screening of small molecules as potential inhibitors. *Anal. Biochem.* **2004**, 326(1), 78-86.
225. Redon C., Pilch D., Rogakou E., Sedelnikova O., Newrock K., Bonner W. Histone H2A variants H2AX and H2AZ. *Curr. Opin. Genet. Dev.* **2002**, 12(2), 162-169.

226. Ahel I., Ahel D., Matsusaka T., Clark A. J., Pines J., Boulton S. J., West S. C. Poly(ADP-ribose)-binding zinc finger motifs in DNA repair/checkpoint proteins. *Nature* **2008**, 451(7174), 81-85.
227. Slade D., Dunstan M. S., Barkauskaite E., Weston R., Lafite P., Dixon N., Ahel M., Leys D., Ahel I. The structure and catalytic mechanism of a poly(ADP-ribose) glycohydrolase. *Nature* **2011**, 477(7366), 616-620.
228. Molinete M., Vermeulen W., Burkle A., Ménissier-de Murcia J., Küpper J. H., Hoeijmakers J. H., de Murcia G. Overproduction of the poly(ADP-ribose) polymerase DNA-binding domain blocks alkylation-induced DNA repair synthesis in mammalian cells. *EMBO J.* **1993**, 12(5), 2109-2117.
229. Affar E. B., Germain M., Winstall E., Vodenicharov M., Shah R. G., Salvesen G. S., Poirier G. G. Caspase-3-mediated processing of poly(ADP-ribose) glycohydrolase during apoptosis. *J. Biol. Chem.* **2001**, 276(4), 2935-2942.
230. Okita N., Ohta R., Ashizawa D., Yamada Y., Abe H., Abe T., Tanuma S.-i. Bacterial production of recombinant human poly(ADP-ribose) glycohydrolase. *Protein Expr. Purif.* **2011**, 75(2), 230-235.
231. Gagnon S. N., Desnoyers S. Single amino acid substitution enhances bacterial expression of PARP-4D214A. *Mol. Cell. Biochem.* **2003**, 243(1-2), 15-22.
232. Nossa C. W., Jain P., Tamilselvam B., Gupta V. R., Chen L.-F., Schreiber V., Desnoyers S., Blanke S. R. Activation of the abundant nuclear factor poly(ADP-ribose) polymerase-1 by *Helicobacter pylori*. *Proc. Natl. Acad. Sci. U. S. A.* **2009**, 106(47), 19998-20003.
233. Tanaka Y., Tawaramoto-Sasanuma M., Kawaguchi S., Ohta T., Yoda K., Kurumizaka H., Yokoyama S. Expression and purification of recombinant human histones. *Methods* **2004**, 33(1), 3-11.
234. Liu X., Palma J., Kinders R., Shi Y., Donawho C., Ellis P. A., Rodriguez L. E., Colon-Lopez M., Saltarelli M., LeBlond D., et al. An enzyme-linked immunosorbent poly(ADP-ribose) polymerase biomarker assay for clinical trials of PARP inhibitors. *Anal. Biochem.* **2008**, 381(2), 240-247.
235. Mortusewicz O., Ame J. C., Schreiber V., Leonhardt H. Feedback-regulated poly(ADP-ribosylation) by PARP-1 is required for rapid response to DNA damage in living cells. *Nucleic Acids Res.* **2007**, 35(22), 7665-7675.
236. Putt K. S., Hergenrother P. J. A nonradiometric, high-throughput assay for poly(ADP-ribose) glycohydrolase (PARG): application to inhibitor identification and evaluation. *Anal. Biochem.* **2004**, 333(2), 256-264.

237. Schreiber V., Dantzer F., Ame J.-C., de Murcia G. Poly(ADP-ribose): novel functions for an old molecule. *Nat. Rev. Mol. Cell Biol.* **2006**, 7(7), 517-528.
238. Calabrese C. R., Almasy R., Barton S., Batey M. A., Calvert A. H., Canan-Koch S., Durkacz B. W., Hostomsky Z., Kumpf R. A., Kyle S., et al. Anticancer chemosensitization and radiosensitization by the novel poly(ADP-ribose) polymerase-1 inhibitor AG14361. *J. Natl. Cancer Inst.* **2004**, 96(1), 56-67.
239. Curtin N. J., Wang L.-Z., Yiakouvaki A., Kyle S., Arris C. A., Canan-Koch S., Webber S. E., Durkacz B. W., Calvert H. A., Hostomsky Z., et al. Novel poly(ADP-ribose) polymerase-1 inhibitor, AG14361, restores sensitivity to temozolomide in mismatch repair-deficient cells. *Clin. Cancer Res.* **2004**, 10(3), 881-889.
240. Kotova E., Lodhi N., Jarnik M., Pinnola A. D., Ji Y., Tulin A. V. Drosophila histone H2A variant (H2Av) controls poly(ADP-ribose) polymerase 1 (PARP1) activation in chromatin. *Proc. Natl. Acad. Sci. U. S. A.* **2011**, 108(15), 6205-6210.
241. Bryant H. E. Inhibition of poly (ADP-ribose) polymerase activates ATM which is required for subsequent homologous recombination repair. *Nucleic Acids Res.* **2006**, 34(6), 1685-1691.
242. Chen B. P. C., Uematsu N., Kobayashi J., Lerenthal Y., Krempler A., Yajima H., Löbrich M., Shiloh Y., Chen D. J. Ataxia telangiectasia mutated (ATM) is essential for DNA-PKcs phosphorylations at the Thr-2609 cluster upon DNA double strand break. *J. Biol. Chem.* **2007**, 282(9), 6582-6587.
243. Kim H. C., Huibregtse J. M. Polyubiquitination by HECT E3s and the determinants of chain type specificity. *Mol. Cell. Biol.* **2009**, 29(12), 3307-3318.
244. Husnjak K., Dikic I. Ubiquitin-binding proteins: decoders of ubiquitin-mediated cellular functions. *Annu. Rev. Biochem.* **2012**, 81(1), 291-322.
245. Pickart C. M., Fushman D. Polyubiquitin chains: polymeric protein signals. *Curr. Opin. Chem. Biol.* **2004**, 8(6), 610-616.
246. Sun L., Chen Z. J. The novel functions of ubiquitination in signaling. *Curr. Opin. Cell Biol.* **2004**, 16(2), 119-126.
247. Yan J., Kim Y. S., Yang X. P., Li L. P., Liao G., Xia F., Jetten A. M. The ubiquitin-interacting motif containing protein RAP80 interacts with BRCA1 and functions in DNA damage repair response. *Cancer Res.* **2007**, 67(14), 6647-6656.

248. Sims J. J., Cohen R. E. Linkage-Specific Avidity Defines the Lysine 63-Linked Polyubiquitin-Binding Preference of Rap80. *Mol. Cell* **2009**, 33(6), 775-783.
249. Sato Y., Yoshikawa A., Mimura H., Yamashita M., Yamagata A., Fukai S. Structural basis for specific recognition of Lys 63-linked polyubiquitin chains by tandem UIMs of RAP80. *EMBO J.* **2009**, 28(16), 2461-2468.
250. Sims J. J., Scavone F., Cooper E. M., Kane L. A., Youle R. J., Boeke J. D., Cohen R. E. Polyubiquitin-sensor proteins reveal localization and linkage-type dependence of cellular ubiquitin signaling. *Nat. Methods* **2012**, 9(3), 303-309.
251. Zimmerman S. B., Minton A. P. Macromolecular crowding: biochemical, biophysical, and physiological consequences. *Annu. Rev. Biophys. Biomol. Struct.* **1993**, 22, 27-65.
252. Laemmli U. K. Cleavage of structural proteins during the assembly of the head of bacteriophage T4. *Nature* **1970**, 227(5259), 680-685.
253. Shaheen F. S., Znojek P., Fisher A., Webster M., Plummer R., Gaughan L., Smith G. C. M., Leung H. Y., Curtin N. J., Robson C. N. Targeting the DNA Double Strand Break Repair Machinery in Prostate Cancer. *PLoS One* **2011**, 6(5), e20311.
254. R., Mizuno H., Miyawaki A. Regulated fast nucleocytoplasmic shuttling observed by reversible protein highlighting. *Science* **2004**, 306(5700), 1370-1373.
255. Gorostiza P., Isacoff E. Y. Optical switches for remote and noninvasive control of cell signaling. *Science* **2008**, 322(5900), 395-399.
256. Briggs W. R. A wandering pathway in plant biology: from wildflowers to phototropins to bacterial virulence. *Annu. Rev. Plant Biol.* **2010**, 61(1), 1-20.
257. Losi A., Gartner W. Old Chromophores, New Photoactivation Paradigms, Trendy Applications: Flavins in Blue Light-Sensing Photoreceptors. *Photochem. Photobiol.* **2011**, 87(3), 491-510.
258. Han I. S., Tseng T. S., Eisinger W., Briggs W. R. Phytochrome A regulates the intracellular distribution of phototropin 1-green fluorescent protein in *Arabidopsis thaliana*. *Plant Cell* **2008**, 20(10), 2835-2847.
259. Ohgishi M., Saji K., Okada K., Sakai T. Functional analysis of each blue light receptor, cry1, cry2, phot1, and phot2, by using combinatorial multiple mutants in *Arabidopsis*. *Proc. Natl. Acad. Sci. U. S. A.* **2004**, 101(8), 2223-2228.

260. Thompson C. L., Sancar A. Photolyase/cryptochrome blue-light photoreceptors use photon energy to repair DNA and reset the circadian clock. *Oncogene* **2002**, 21(58), 9043-9056.
261. Christie J. M., Salomon M., Nozue K., Wada M., Briggs W. R. LOV (light, oxygen, or voltage) domains of the blue-light photoreceptor phototropin (NPH1): binding sites for the chromophore flavin mononucleotide. *Proc. Natl. Acad. Sci. U. S. A.* **1999**, 96(15), 8779-8783.
262. Briggs W. R. The LOV domain: a chromophore module servicing multiple photoreceptors. *J. Biomed. Sci.* **2007**, 14(4), 499-504.
263. Crosson S., Rajagopal S., Moffat K. The LOV domain family: photoresponsive signaling modules coupled to diverse output domains *Biochemistry* **2003**, 42(1), 2-10.
264. Huala E., Oeller P. W., Liscum E., Han I. S., Larsen E., Briggs W. R. Arabidopsis NPH1: a protein kinase with a putative redox-sensing domain. *Science* **1997**, 278(5346), 2120-2123.
265. Losi A., Gartner W. Bacterial bilin- and flavin-binding photoreceptors. *Photochem. Photobiol. Sci.* **2008**, 7(10), 1168-1178.
266. Krauss U., Lee J., Benkovic S. J., Jaeger K.-E. LOVely enzymes - towards engineering light-controllable biocatalysts. *Microb. Biotechnol.* **2010**, 3(1), 15-23.
267. Losi A. Flavin-based Blue-Light photosensors: a photobiophysics update. *Photochem. Photobiol.* **2007**, 83(6), 1283-1300.
268. Halavaty A. S., Moffat K. N- and C-terminal flanking regions modulate light-induced signal transduction in the LOV2 domain of the blue light sensor phototropin 1 from *Avena sativa*. *Biochemistry* **2007**, 46(49), 14001-14009.
269. Harper S. M. Structural basis of a phototropin light switch. *Science* **2003**, 301(5639), 1541-1544.
270. Harper S. M., Christie J. M., Gardner K. H. Disruption of the LOV-J α Helix Interaction Activates Phototropin Kinase Activity *Biochemistry* **2004**, 43(51), 16184-16192.
271. Moglich A., Ayers R. A., Moffat K. Design and signaling mechanism of light-regulated histidine kinases. *J. Mol. Biol.* **2009**, 385(5), 1433-1444.
272. Moglich A., Moffat K. Structural basis for light-dependent signaling in the dimeric LOV domain of the photosensor YtvA. *J. Mol. Biol.* **2007**, 373(1), 112-126.

273. Wu Y. I., Frey D., Lungu O. I., Jaehrig A., Schlichting I., Kuhlman B., Hahn K. M. A genetically encoded photoactivatable Rac controls the motility of living cells. *Nature* **2009**, 461(7260), 104-108.
274. Strickland D., Moffat K., Sosnick T. R. Light-activated DNA binding in a designed allosteric protein. *Proc. Natl. Acad. Sci. U. S. A.* **2008**, 105(31), 10709-10714.
275. Wang X., Chen X., Yang Y. Spatiotemporal control of gene expression by a light-switchable transgene system. *Nat. Methods* **2012**, 9(3), 266-269.
276. Zoltowski B. D., Schwerdtfeger C., Widom J., Loros J. J., Bilwes A. M., Dunlap J. C., Crane B. R. Conformational switching in the fungal light sensor Vivid. *Science* **2007**, 316(5827), 1054-1057.
277. Lamb J. S., Zoltowski B. D., Pabit S. A., Crane B. R., Pollack L. Time-resolved dimerization of a PAS-LOV protein measured with photocoupled small angle X-ray scattering. *J. Am. Chem. Soc.* **2008**, 130(37), 12226-12227.
278. Zoltowski B. D., Crane B. R. Light activation of the LOV protein vivid generates a rapidly exchanging dimer. *Biochemistry* **2008**, 47(27), 7012-7019.
279. Lungu O. I., Hallett R. A., Choi E. J., Aiken M. J., Hahn K. M., Kuhlman B. Designing photoswitchable peptides using the AsLOV2 domain. *Chem. Biol.* **2012**, 19(4), 507-517.
280. Christie J. M. Arabidopsis NPH1: a flavoprotein with the properties of a photoreceptor for phototropism. *Science* **1998**, 282(5394), 1698-1701.
281. Nakasone Y., Eitoku T., Matsuoka D., Tokutomi S., Terazima M. Dynamics of conformational changes of Arabidopsis phototropin 1 LOV2 with the linker domain. *J. Mol. Biol.* **2007**, 367(2), 432-442.
282. Jones M. A., Feeney K. A., Kelly S. M., Christie J. M. Mutational analysis of phototropin 1 provides insights into the mechanism underlying LOV2 signal transmission. *J. Biol. Chem.* **2007**, 282(9), 6405-6414.
283. Pfeifer A., Mathes T., Lu Y., Hegemann P., Kottke T. Blue Light Induces Global and Localized Conformational Changes in the Kinase Domain of Full-Length Phototropin. *Biochemistry* **2010**, 49(5), 1024-1032.
284. Eitoku T., Nakasone Y., Matsuoka D., Tokutomi S., Terazima M. Conformational dynamics of phototropin 2 LOV2 domain with the linker upon photoexcitation. *J. Am. Chem. Soc.* **2005**, 127(38), 13238-13244.

285. Nakasone Y., Eitoku T., Matsuoka D., Tokutomi S., Terazima M. Kinetic measurement of transient dimerization and dissociation reactions of Arabidopsis phototropin 1 LOV2 domain. *Biophys. J.* **2006**, 91(2), 645-653.
286. Chapman S., Faulkner C., Kaiserli E., Garcia-Mata C., Savenkov E. I., Roberts A. G., Oparka K. J., Christie J. M. The photoreversible fluorescent protein iLOV outperforms GFP as a reporter of plant virus infection. *Proc. Natl. Acad. Sci. U. S. A.* **2008**, 105(50), 20038-20043.